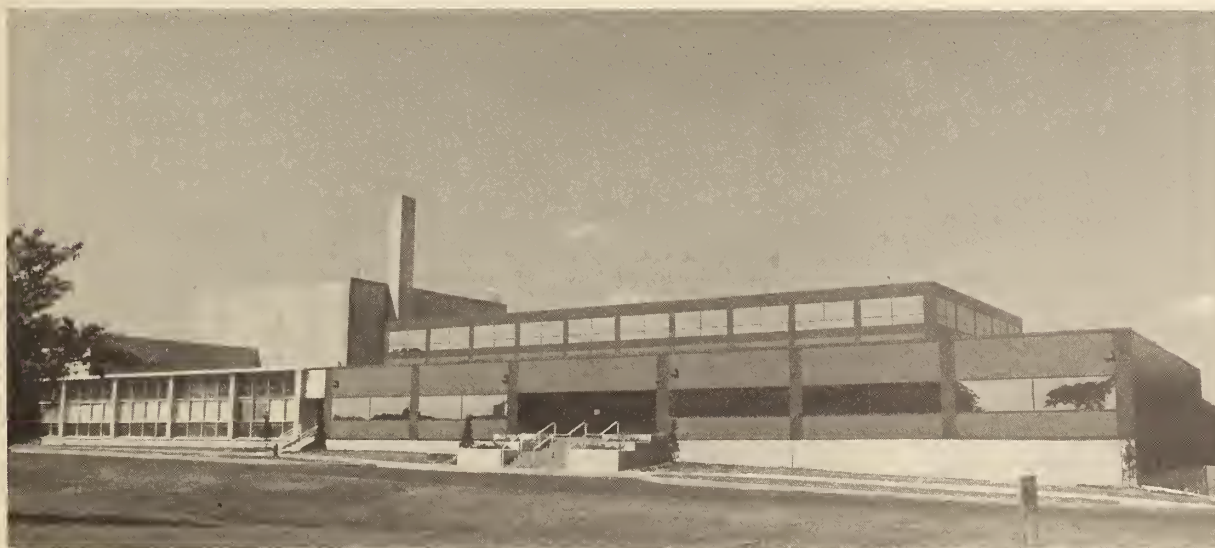




A11103 599032

NIST
PUBLICATIONSNIST TECHNICAL NOTE **1272**

U.S. DEPARTMENT OF COMMERCE/National Institute of Standards and Technology

**NIST Reactor:
Summary of Activities
July 1988 Through June 1989**

QC

100

.U5753

NO. 1272

1989

**NATIONAL INSTITUTE OF STANDARDS &
TECHNOLOGY**

Research Information Center
Gaithersburg, MD 20899

NIST Reactor: Summary of Activities July 1988 Through June 1989

Carol O'Connor, Editor

Reactor Radiation Division
Institute for Materials Science and Engineering
National Institute of Standards and Technology
Gaithersburg, MD 20899

December 1989



U.S. Department of Commerce
Robert A. Mosbacher, Secretary
National Institute of Standards and Technology
Raymond G. Kammer, Acting Director

NISTC
QC100
U5753
1988/
11989
C.2

National Institute of Standards and Technology Technical Note 1272
Natl. Inst. Stand. Technol. Tech. Note 1272, 324 pages (Dec. 1989)
CODEN: NTNOEF

U.S. GOVERNMENT PRINTING OFFICE
WASHINGTON: 1989

For sale by the Superintendent of Documents, U.S. Government Printing Office, Washington, DC 20402-9325

FOREWORD

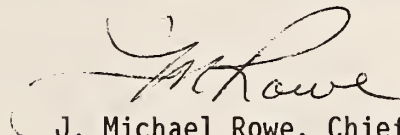
The National Institute of Standards and Technology (NIST) research reactor serves the needs of NIST, other government agencies, universities, and industries as a national center for the application of neutron methods to a broad range of problems of national interest. The Reactor Radiation Division has a threefold mission: to operate the reactor in the most cost effective manner possible while protecting the public safety; to perform research on a broad range of problems in materials-related science and to develop new or improved methods for the application of neutrons; and to operate a national user center, providing state-of-the-art neutron measurement capabilities to U.S. researchers. The Division staff works closely with many other organizations both within NIST and outside on research of mutual interest. The extent of these cooperative and collaborative programs has expanded steadily since the reactor came on line. They can be expected to grow even further as the Cold Neutron Research Facility, which will provide 15 additional instruments, comes on line over the next 3 years.

The reactor operates at 20 MW and supports over 25 research facilities, with an additional 15 becoming available as part of the Cold Neutron Project. During the period covered by this report, over 1160 irradiations were performed, and more than 350 researchers made use of the facilities, in spite of an operating schedule that was seriously curtailed as a result of construction activities.

This report summarizes the work done which is dependent on the reactor including a large number of programs outside the Division. The first section summarizes the programs carried out by scientists in the Reactor Radiation Division and their collaborators. The second section summarizes NIST work originating outside NIST for which the Division provides reactor facilities and irradiation services. The remaining sections are self-explanatory.

Appreciation is extended to C. O'Connor for her contributions to the editing, organization, and preparation of this report; E. Altman, N. Repetti, J. Spillman, and S. von Feck for typing the manuscripts.

Finally, this is the first report in the history of the Division prepared by anyone but Dr. R. S. Carter, who retired in December 1988. All that has been accomplished over the years is a direct result of the foresight and dedication of Bob. We wish him well in his retirement.



J. Michael Rowe, Chief
Reactor Radiation Division
National Institute of Standards
and Technology

ABSTRACT

This report summarizes all those programs which use the NIST reactor. It covers the period for July 1988 through June 1989. The programs range from the use of neutron beams to study the structure and dynamics of materials through nuclear physics and neutron standards to sample irradiations for activation analysis, isotope production, neutron radiography, and nondestructive evaluation.

KEY WORDS: activation analysis; cold neutrons; crystal structure; diffraction; isotopes; molecular dynamics; neutron; neutron radiography; nondestructive evaluation; nuclear reactor; radiation.

DISCLAIMER

Certain trade names and company products are identified in order to adequately specify the experimental procedure. In no case does such identification imply recommendation or endorsement by the National Institute of Standards and Technology, nor does it imply that the products are necessarily the best available for the purpose.

CONTENTS

FOREWORD	iii
ABSTRACT	iv
A. REACTOR RADIATION DIVISION AND COLLABORATIVE PROGRAMS	1
Neutron Scattering Study of the Vibrations and Dynamics of Trimethylsilyl Adsorbates on Silica	1
Hydrogen Vibrational Modes and Anisotropic Potential in α -Sch _x	3
Neutron Spectroscopic Studies of Adsorbates on Ruthenium Sulfide Catalysts	6
Neutron Scattering Study of the Molecular Dynamics of Ammonium Fluoroberyllate	8
Inelastic Neutron Scattering Studies of Nonlinear Optical Materials: p-Nitroaniline Adsorbed in ALPO-5	9
Dynamics of Molecular Hydrogen Adsorbed in Transition-Metal Exchanged Zeolites	11
The Dependence of the OH ⁻ Librations on the Octahedral Site Occupancies in 2:1 Layered Silicates	12
Neutron Scattering Studies of Trimethylammonium Pillared Vermiculite Clays	14
Structural Studies of Stage 1 Metal-Dichloride Graphite Intercalation Compounds	17
Application of Maximum Entropy to Phase Refinement in Macromolecular Crystallography	18
Background Contributions and Quantitative Phase Determination in Rietveld Structure Refinement	21
Neutron Rietveld Analysis of Anion and Cation Disorder in the Fast-Ion Conducting Pyrochlore System $Y_2(Zr_xTi_{1-x})_2O_7$	23
Crystal Structure of 11,23-di-tert-butyl-1,9,11,13,21,23-hexa- azapentacyclo[19.3.1 ^{3,7} .1 ^{9,13} .1 ^{15,19}]octacos-3,5,7(28), 15,17,19 (26)-hexaene-25,27-dione, (C ₃₀ H ₄₂ N ₆ O ₂)	24
Neutron Diffraction Studies of the Martensitic Transformation in Sodium Metal	26
Structure of AlCuFe Alloys Exhibiting the Icosahedral Phase	29
Evolution of the Magnetic Structure in Tb _x Y _{1-x} Ag	32
Magnetic Order in A Tb _{0.5} Dy _{0.5} Single Crystal	34
Orientation Dependence of the Magnetic Structure in Dy/Y Superlattices	35
Magnetoelasticity in Rare-Earth Superlattices and Films	37
Neutron Diffraction Studies of Cd _{1-x} Mn _x Se Films and ZnSe/MnSe Multilayers	42
Exchange Interactions in Co-Based II-VI Diluted Magnetic Semiconductors	45

CONTENTS

Characterization of the Quasicrystalline State of $\text{Al}_{73}\text{Mn}_{21}\text{Si}_6$	
From Neutron Scattering Experiments	47
Antiferromagnetic Order in $\text{YBa}_2\text{Cu}_{3-x}\text{Co}_x\text{O}_{6+y}$	49
Oxygen Dependence of the Magnetic Phase Transitions in	
$\text{YBa}_2\text{Cu}_{2.8}\text{Co}_{0.2}\text{O}_{6+y}$	52
Magnetic Properties of $\text{Bi}_2\text{A}_2\text{TO}_6$: A = MSr,Ca and T = Co,Mn	54
The Defective Structures of $\text{Ba}_2\text{YCu}_3\text{O}_{6+x}$ and	
$\text{Ba}_2\text{YCu}_{3-y}\text{M}_y\text{O}_{6+z}$ (M = Fe, Co, Al, Ga)	56
Magnetic Order of Nd in $\text{NdBa}_2\text{Cu}_3\text{O}_{6+x}$	57
Two- and Three-Dimensional Magnetic Behavior of Er in $\text{ErBa}_2\text{Cu}_3\text{O}_7$	59
Effect of Superconductivity on the Small Angle Neutron	
Scattering in $\text{ErBa}_2\text{Cu}_3\text{O}_7$	63
Magnetic Order of Pr in $\text{PrBa}_2\text{Cu}_3\text{O}_7$	67
Pressure Dependence of the Cu Magnetic Order in $\text{RBa}_2\text{Cu}_3\text{O}_{6+x}$	70
Two- and Three-Dimensional Magnetic Order in $\text{RBa}_2\text{Cu}_4\text{O}_8$	73
Magnetic Order of the Cu Planes and Chains in $\text{RBa}_2\text{Cu}_3\text{O}_{6+x}$	76
Antiferromagnetic Order of the Cu in Nd_2CuO_4	82
Superconducting $\text{Tl}_{2.0}\text{Ba}_{2.0}\text{CuO}_{6+\delta}$: A High Resolution	
Neutron Powder Investigation.	85
Neutron Powder Diffraction Study of $\text{Pb}_2\text{Sr}_2\text{YCu}_3\text{O}_8$, The	
Prototype of a New Family of Superconductors	89
Sans Study of $\text{YBa}_2\text{Cu}_3\text{O}_{7-x}$ Sol-Gel Processing	89
Interplanar-Boson-Exchange Models of High-Temperature	
Superconductivity--Theoretical Comparisons and Possible	
Experimental Tests.	90
Texture Study of Magnetically Aligned $\text{YBa}_2\text{Cu}_3\text{O}_7$ by Neutron	
Diffraction	95
Grazing-Angle Neutron Diffraction Study of Cr/Nb/ Al_2O_3 Film	97
Neutron Reflectivity Study of GD-Y Interface	99
Determination of Hydrogen Density Profiles in Thin Films and	
Multilayers by Neutron Reflection	101
The Morphology of Symmetric Diblock Copolymers as Revealed by	
Neutron Reflectivity	102
Temperature Dependence of the Morphology of Thin Diblock	
Copolymer Films as Revealed by Neutron Reflectivity	109
Neutron Reflectivity Study of the Density Profile of an Adsorbed	
Diblock Copolymer at the Solution-Quartz Interface	115
SANS Studies of Blends of Crosslinked PSD With Linear PSH	119
The Effect of Radiation Crosslinking on the Scattering Function	
in Weakly Interacting Miscible Polymer Blends	121
Grafted Interpenetrating Polymer Networks	123
Microstructure and Isotopic Labeling Effects on the Miscibility	
of Polybutadiene Blends Studied by the Small Angle Neutron	
Scattering Technique	125

CONTENTS

Shear Effects on the Phase Separation Behavior of a Polymer Blend in Solution by Small Angle Neutron Scattering	132
Concentration Fluctuations in Mixtures of Linear and Star Shaped Polymers	137
Chain Conformation of a Block Polymer in a Microphase-Separated Structure	138
SANS Study of Order and Disorder in a Model Diblock Copolymer . .	144
Molecular Structure of Bimodal Polymer Network	146
Small Angle Neutron Scattering Studies on Chain Asymmetry of Coextruded Poly(Vinylalcohol) Film	150
In-Situ Neutron Diffraction on Deuterium Loaded Palladium in an Electrochemical Cell	151
Comments on Cold Fusion in Metals	155
Cavity Growth Rates in Fatigued Copper	156
Textures of Specially Fabricated Metals	158
Residual Stress Measurements in Metallurgical Samples	162
Microstresses in Ceramic Composites	166
Multiple Small Angle Neutron Scattering Characterization of the Densification of Alumina	168
Neutron Scattering and Its Effect on Reaction Rates in Neutron Absorption Experiments	171
Characterization of Molecular Network of Epoxies Using Neutron Scattering	174
Shearing Apparatus for SANS: Preliminary Results From Sheared Colloidal Suspensions	177
Analysis of SANS From Controlled Pore Glasses	180
Physical Gels of Aqueous Polyvinylalcohol Solutions - A Small Angle Neutron Scattering Study	182
Small Angle Neutron Scattering From Bacterial Magnetite	183
SANS Study of Mixed Lecithin-Bile Salt Micelles and Vesicles . . .	187
NIST Crystal Data Center	189
A New Method for Identification of Solid-State Materials	190
Autoradiography Study of Paintings	192
Cold Neutron Project	195
Center for High Resolution Neutron Scattering	198
Spin Polarized Inelastic Neutron Scattering Spectrometer (SPINS). .	199
Cold Neutron Triple Axis Spectrometer	200
High Resolution Time-of-Flight Spectrometer	201
Analytical Calculations of the Performance of Neutron Guide Systems	202
On the Use of Multiply Channeled Guides to Increase Intensity on the Sample in a Multiple Disk Chopper Time-of-Flight Spectrometer.	207
Focused Neutron Beams for Materials Analysis	211
Design Studies for the Prompt Gamma-Ray Activation Analysis Instrument	212
Cold Neutron Depth Profiling	214
High Resolution Small Angle Scattering Spectrometer	215
Design of Cold Neutron Backscattering Spectrometer	217
Supermirror Development	218

CONTENTS

B. NON-RRD PROGRAMS.	219
Neutron Interactions and Dosimetry Group	219
Nuclear Methods Group: Overview	233
INAA Homogeneity Measurements on the New NIST Leaf	
Reference Materials	238
Prompt Gamma Activation Analysis of Gaseous Samples	244
Instrumental Neutron Activation Analysis of Marine Samples	246
Determination of B and Li in Dietary Samples using NA-MS	249
Exhumation Confirms Lead Analyses Results	250
Instrumental Neutron Activation Analysis of Microscopic Samples.	251
Low-Background Gamma Ray Assay Laboratory for Activation	
Analysis	252
Investigation of Reported Cold Nuclear Fusion	258
Facilities for Activation Analysis	261
Atmospheric, Environmental Biological Studies by Instrumental and	
Neutron-Capture Prompt γ -Ray Activation Analysis	262
Effects of Neutron Scattering by Hydrogen on Neutron-Capture	
Prompt γ -Ray Activation Analysis (PGAA)	263
Submicrometer Size Distributions of Airborne Particles Bearing	
Various Trace Elements	265
California Air Resources Board Air-Filter Samples	269
Stable Isotope Tracing of Zinc in Infants	271
Investigation of the Gamma-Ray Spectrum for the $^{128}\text{Te}(\text{n},\text{g})$ and	
$^{130}\text{Te}(\text{n},\text{g})$ Reactions	274
Fundamental Physics	275
Neutron Activation Analysis at the Food and Drug Administration	275
Germanium Detector Optimization of MDA for Efficiency vs. Low	
Intrinsic Background	278
 C. REACTOR OPERATIONS AND ENGINEERING SERVICES	 280
Reactor Operations and Services	280
Reactor Operations and Engineering	281
 D. PERSONNEL ROSTER.	 284
 E. PUBLICATIONS.	 295

A. REACTOR RADIATION DIVISION AND COLLABORATIVE PROGRAMS

NEUTRON SCATTERING STUDY OF THE VIBRATIONS AND DYNAMICS OF TRIMETHYLSILYL ADSORBATES ON SILICA

T. J. Udovic, D. A. Neumann, and J. J. Rush

L. C. Sander
(Organic Analytical Research Division)

and

I. S. Anderson
(Paul Scherrer Institut, Villigen, Switzerland)

The nature of trimethylsilyl ($(\text{CH}_3)_3\text{Si}$ -, TMS) adsorbates bonded to silica surface oxygens, via the reaction of trimethylchlorosilane with surface silanol groups, has been probed using neutron scattering methods. The TMS vibrational spectra in the range 10 - 230 meV were obtained as a function of temperature by incoherent inelastic neutron scattering (IINS) using the BT-4 triple-axis spectrometer with both the Be-filter and Be-graphite-Be-filter analyzers. The region below 12 meV was investigated using the cold-neutron time-of-flight (TOF) spectrometer in order to characterize the temperature dependence of both low-energy vibrational transitions and quasielastic neutron scattering processes.

Figure 1 shows high-resolution vibrational spectra of TMS/SiO_2 at 4 and 80 K. Both spectra reflect the same general features: an intense mode at ~ 20 meV due to the methyl torsional modes, weak scattering intensity between 30 and 80 meV due to the different skeletal modes, and the more pronounced peaks between 80 and 120 meV due mainly to the Si-C-H bending modes. Additional scattering features at ~ 160 and 180 meV observed under low-resolution conditions (i.e., Be-filter analysis, spectrum not illustrated) are representative of H-C-H bending modes. Acceptable spectral fits by normal coordinate analysis required the inclusion of off-diagonal force-constant matrix elements (i.e., intramolecular interactions). The IINS spectral features at 80 K are noticeably broader than the corresponding features at 4 K, indicative of significant TMS rotational motions on a neutron timescale down to 80 K or below.

Figure 2 shows the corrected TOF spectra of TMS/SiO_2 at 4 and 10 K on an energy scale. An energy loss feature at ca. 2.5 meV at 4 K shows up as both

REACTOR RADIATION DIVISION AND COLLABORATIVE PROGRAMS

energy loss and energy gain features at 10 K due to the population of the 2.5 meV level above the ground state as the temperature is raised. This low-energy feature is assigned to the torsional vibration of the entire trimethylsilyl group around the O-Si axis, since the relatively large moment of inertia of this group would predict torsional modes in this region.

Quasielastic neutron scattering spectra between 4 and 300 K confirm that trimethylsilyl group rotational motions are responsible for the broadening of the IINS vibrational features at 80 K, with the methyl group rotational motions (observable at higher temperatures) already virtually frozen out ($\tau \geq 10^{-10}$ s) at this temperature.

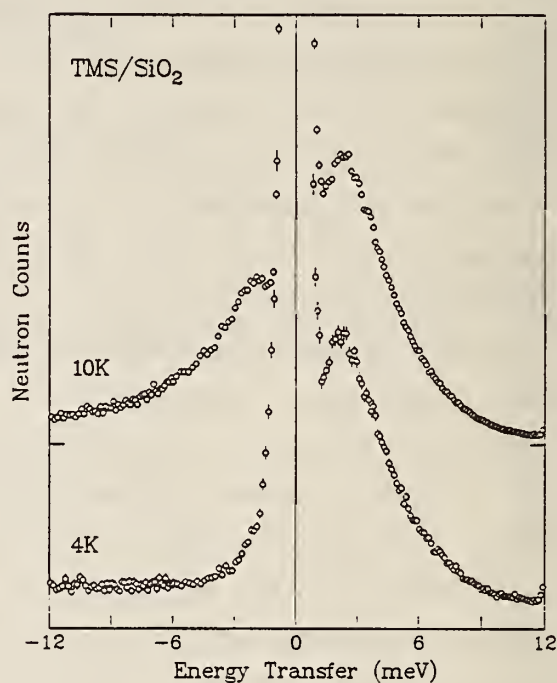
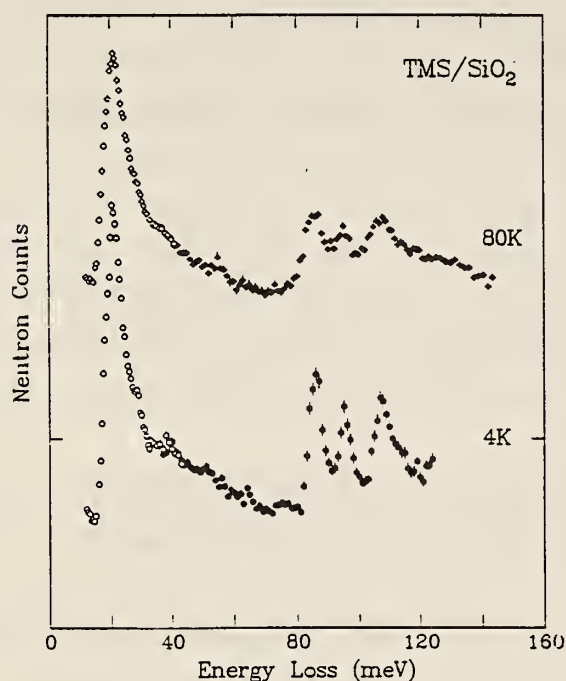


Figure 1. (left) IINS spectra of TMS/SiO₂ as a function of temperature taken on the BT-4 spectrometer using the Be-graphite-Be-filter analyzer.

Figure 2. (right) Low-energy IINS spectra of TMS/SiO₂ as a function of temperature taken on the TOF spectrometer with 13.8 meV incident energy. Positive energy transfers correspond to neutron energy loss.

REACTOR RADIATION DIVISION AND COLLABORATIVE PROGRAMS
HYDROGEN VIBRATIONAL MODES AND ANISOTROPIC POTENTIAL IN α -ScH_x

T. J. Udovic and J. J. Rush

I. S. Anderson
(Paul Scherrer Institut, Villigen, Switzerland)

and

R. G. Barnes
(Iowa State University, Ames, IA)

The hydrogen vibrational spectra of single-crystal α -ScH_x ($x = 0.05$, 0.16 , and 0.25) have been measured using incoherent inelastic neutron scattering (IINS) methods in order to characterize the bonding potential of hydrogen in the tetrahedral interstices (i.e., t sites) of the Sc metal lattice. Alignment of the momentum transfer vector Q either perpendicular or parallel to the c -axis permitted selective enhancement of the scattering sensitivity of the different hydrogen normal modes. Low-resolution IINS spectra, obtained using the BT-4 spectrometer with the Be-filter analyzer, show that the c -axis vibration peak (at ~ 103 meV) is over 30% lower in energy than the doubly-degenerate basal-plane modes (at ~ 148 meV) and is substantially anharmonic, as reflected by the ratio (1.76) of the second- to first-excited-state energies.

High-resolution IINS spectra of the c -axis mode at the different hydrogen concentrations, obtained using the BT-4 spectrometer with the Be-graphite-Be-filter analyzer, are shown in figure 1. The observed downward shift of the c -axis mode from 102.9 meV at $x \geq 0.16$ to 101 meV at $x = 0.05$ is similar to the hydrogen concentration dependence of the c -axis mode found for α -YH_x [1], which has been attributed to the relaxation of coherent strain ordering as the hydrogen concentration decreases, resulting in a larger average metal-hydrogen separation as more alternative hydrogen configurations become accessible. All hydrogen concentrations reveal a peak that is much broader (~ 14 meV fwhm intrinsic linewidth, $x = 0.25$) than the instrumental resolution. The peak, however, is devoid of any resolved fine structure indicative of a distinct local-mode splitting induced by the dynamic coupling of hydrogen pairs across metal atoms along the c -axis, as was observed previously for α -YH_x [1].

A comparison of the high-resolution spectra of the c -axis mode for α -ScH_{0.25} and α -YH_{0.18} in figure 2 illustrates the difference in lineshapes.

In contrast to the Gaussian-shaped peak for $\alpha\text{-ScH}_{0.25}$, a definite 4 meV splitting is observed for $\alpha\text{-YH}_{0.18}$, despite its narrower apparent overall linewidth. Even if a splitting is present for $\alpha\text{-ScH}_{0.25}$, it would not necessarily be observable if the component peaks were considerably broadened. Indeed, the $\alpha\text{-ScH}_{0.25}$ spectrum can be fit just as well with two broad Gaussian components, each ~ 10 meV fwhm and separated by 4 meV at positions of 102.9 ± 2 meV. In contrast, the visible splitting in the $\text{YH}_{0.18}$ spectrum, necessitates the presence of much narrower component peaks. Attempts to fit the complex-shaped spectrum with two Gaussians required peakwidths of ~ 4 meV to reproduce the degree of observed separation in the central portion of the spectrum.

In short, the overall broadness of the $\alpha\text{-ScH}_x$ spectra is consistent with the presence of H pairing across Sc atoms along the c-axis, similar to the hydrogen pairing that occurs in $\alpha\text{-YH}_x$. The lack of visible splitting in the $\alpha\text{-ScH}_x$ spectra suggests that the individual components of the c-axis spectra are more broadened than in $\alpha\text{-YH}_x$ due to a larger distribution of H-pair environments (i.e., less extended ordering of H pairs in the c-direction) or a greater variety of intra- and interline arrangements. Thus, it appears that the hydrogen pairs in $\alpha\text{-ScH}_x$ are more disordered than in $\alpha\text{-YH}_x$, which is consistent with the suggestion from recent NMR studies [2] that the hydrogen arrangements in $\alpha\text{-ScH}_x$ are, in some sense, akin to a "proton glass."

Previous vibrational spectroscopic measurements of $\alpha\text{-YD}_{0.17}\text{H}_{0.019}$ [1], in which the H atoms are sufficiently dilute that they can effectively pair only with D atoms across an Y atom, yielded a single narrowed peak at 100 meV instead of the expected doublet at 99 and 103 meV found for H-H pairs in $\alpha\text{-YH}_{0.18}$. This observed behavior confirmed that the c-axis mode splitting in $\alpha\text{-YH}_x$ is caused by a dynamic coupling mechanism rather than by vibrations in a local potential statically perturbed by pairing. Similar isotope dilution experiments, utilizing $\alpha\text{-ScD}_{0.25}$ doped with a small percentage of H, are planned in order to further probe the nature of dynamically-coupled hydrogen pairing in this system. Experiments are also under way to study the local c-axis diffusion of hydrogen in the $\alpha\text{-ScH}_x$ system.

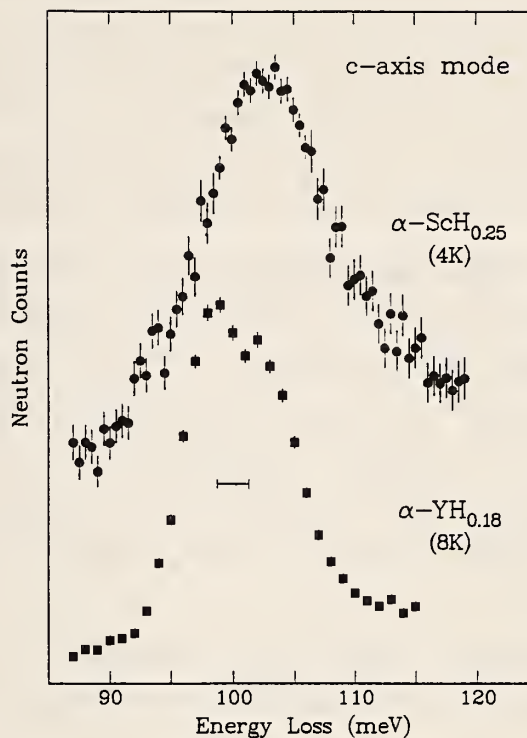
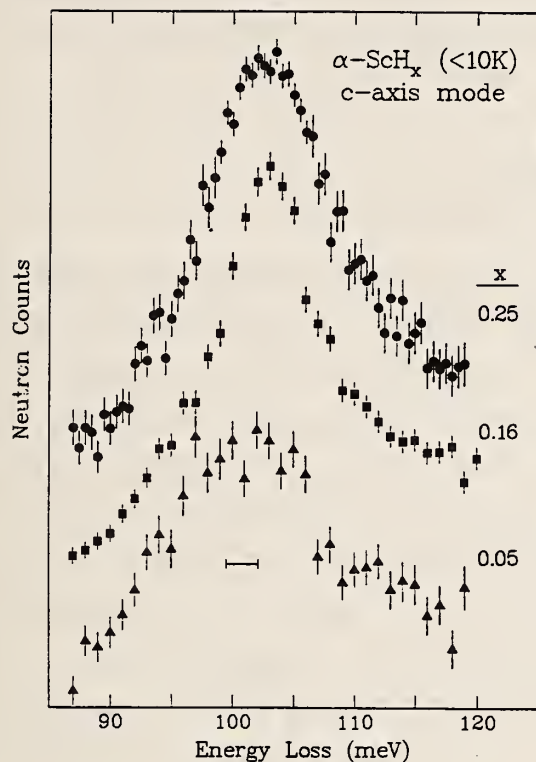


Figure 1. (left) High-resolution IINS spectra of the c-axis mode at $T < 10\text{ K}$ for $\alpha\text{-ScH}_x$ as a function of H concentration. The instrumental resolution (fwhm) is illustrated by the horizontal bar beneath the spectra.

Figure 2. (right) High-resolution IINS spectra of the c-axis mode at $T < 10\text{ K}$ for single-crystals of $\alpha\text{-ScH}_{0.25}$ and $\alpha\text{-YH}_{0.18}$ [1]. The instrumental resolution (fwhm) is illustrated by the horizontal bar beneath the spectra.

References

- [1] Anderson, I. S.; Berk, N. F.; Rush, J. J.; Udovic, T. J. Phys. Rev. B37, 4358 (1988).
- [2] Lichty, L. R.; Han, J.-W.; Ibanez-Meier, R.; Torgeson, D. R.; Barnes, R. G.; Seymour, E. F. W.; Sholl, C. A. Phys. Rev. B39, 2012 (1989).

NEUTRON SPECTROSCOPIC STUDIES OF ADSORBATES ON RUTHENIUM SULFIDE CATALYSTS

T. J. Udovic and J. J. Rush

and

B. J. Tatarchuk
(Auburn University, Auburn, AL)

Ruthenium sulfide (RuS_2) is an active catalyst for hydrodesulfurization (HDS) reactions. As a result, there has been interest in investigating the adsorption properties of this material, particularly with respect to hydrogen. A previous incoherent inelastic neutron scattering (IINS) study [1] of hydrogen adsorption on RuS_2 has indicated that hydrogen adsorbs dissociatively forming surface sulfhydryl (SH) groups. The likely sites for hydrogen dissociation and adsorption are coordinatively unsaturated S-S anion pairs which provide both the necessary electron density and dual-site geometry. The H/RuS_2 vibrational spectrum at 80 K is shown in figure 1a. The main scattering feature, assigned to the Ru-S-H bending modes, appears as a complex doublet at 74 and 88 meV with the corresponding second harmonics evident at higher energy.

A corresponding isotope dilution experiment [1] utilizing a 15% H_2 /85% D_2 adsorbate mixture yielded the H/RuS_2 spectrum at 80 K in figure 1b, indicating no significant change in the H vibrational peak structure except for some additional increase in scattering intensity at ~104 meV. Assuming that complete isotopic mixing of H and D occurred, this spectrum would be a measure of isolated SH groups surrounded by SD groups, effectively breaking up any possible H-H dynamic coupling. Hence, the conclusion from the isotope dilution experiment would be that the complex peakshape in figures 1a and 1b is due to a distribution of bending-mode energies rather than the phonon dispersion of a single bending mode via H-H dynamic coupling interactions.

Recent secondary ion mass spectrometry (SIMS) data at Auburn University have suggested that, contrary to the original assumption, no significant isotopic mixing occurs when H_2 and D_2 are coadsorbed on RuS_2 , even at 373 K. In other words, the dissociation and adsorption of H-H and D-D onto the S-S anion pairs results in a stable configuration of (H)S-S(H) and (D)S-S(D) groups with no (H)S-S(D) groups created by exchange processes. This suggests that the complex bending-mode peakshape may be due to H-H interactions

between hydrogens on the same S-S anion pair and clouds the conclusions of the previous isotope dilution results.

To investigate this further, another isotope experiment was performed by measuring the vibrational spectrum after adsorption of HD onto the RuS_2 surface. This would ensure that the amount of (H)S-S(D) groups is maximized. The resulting IINS spectrum is shown in figure 1c, again indicating no significant changes in the H vibrational peak structure except for additional scattering intensity at 104 meV. Hence, it still appears that the complex peakshape is due to a distribution of bending-mode energies rather than a dispersion effect induced by dynamic coupling interactions between near-neighbor hydrogens. The origin of the 104 meV feature is still under investigation but may be due to the presence of O impurity atoms which lead to the formation of surface OH groups possessing bending mode energies in this region.

Experiments are in progress for investigating other adsorbates on RuS_2 , such as thiophene, which are of interest from the viewpoint of HDS surface chemistry.

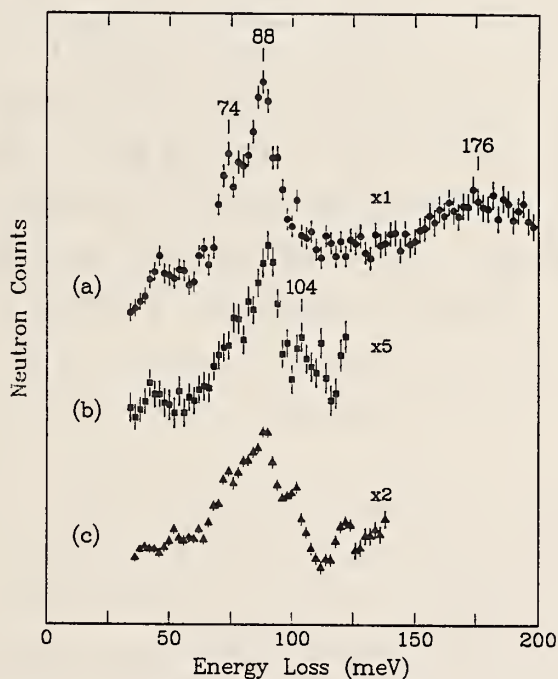


Figure 1. IINS spectra of RuS_2 at 80 K taken on the BT-4 spectrometer using the Be-filter analyzer after saturation adsorption of H_2 (a), 15% H_2 /85% D_2 (b), and HD (c).

Reference

- [1] Heise, W. H.; Lu, K.; Kuo, Y.-J.; Udovic, T. J.; Rush, J. J.; Tatarchuk, B. J. J. Phys. Chem. 92, 5184 (1988).

NEUTRON SCATTERING STUDY OF THE MOLECULAR DYNAMICS OF AMMONIUM FLUOROBERYLLATE

M. Davidović

("Boris Kidrič" Institute of Nuclear Sciences, Vincă, Belgrade, Yugoslavia)

and

T. J. Udovic and J. J. Rush

Inelastic neutron scattering experiments were performed to investigate the molecular dynamics of both the protonated and deuterated forms of ammonium fluoroberyllate ($(\text{NH}_4)_2\text{BeF}_4$ and $(\text{ND}_4)_2\text{BeF}_4$), an ammonium salt with a ferroelectric phase transition at ~ 180 K. The BT-4 triple-axis spectrometer with the Be-graphite-Be-filter analyzer was used to collect the density-of-states spectrum between 10 and 80 meV of both isotopic forms as a function of temperature: namely, above, at, and below the ferroelectric transition temperature. Complementary spectra covering the low-energy region below 12 meV were collected using the TOF spectrometer with 13.8 meV incident energy. Data analysis is in progress to characterize any subtle changes in the molecular dynamics accompanying the incommensurate structural phase transition which occurs upon transformation from the paraelectric to the ferroelectric state.

**INELASTIC NEUTRON SCATTERING STUDIES OF NONLINEAR OPTICAL MATERIALS:
p-NITROANILINE ADSORBED IN ALPO-5**

J. M. Nicol

(University of Maryland, College Park, MD and Reactor Radiation Division)

T. J. Udovic and J. J. Rush

and

S. D. Cox and G. D. Stucky

(University of California, Santa Barbara, CA)

Inclusion of a guest species into a host framework is a relatively new method by which new nonlinear optical materials for second harmonic generation (SHG) can be synthesized. SHG is very sensitive to symmetry restrictions; thus, for a material to exhibit SHG the crystal structure must be noncentrosymmetric. In inclusion chemistry this symmetry restriction can be imposed on a guest molecule by an acentric host or created by guest-host interactions. Therefore by careful size and shape selection of the host and guest, the inclusion of a guest molecule in a host framework can result in molecular alignment and optimization of the SHG coefficient and create a system with nonlinear optical properties that are very different from those of either the individual guest molecules or the host framework.

Recently the adsorption of para-nitroaniline (p-NA) into the channels of the molecular sieve ALPO-5 has been shown to produce SHG effects ten times larger than that of any previously reported organic or organometallic inclusion complex [1]. The acentric molecular sieve ALPO-5 has a neutral framework composed of alternating AlO_4 and PO_4 tetrahedra linked by oxygen bridges to form an array of one-dimensional 12-ring channels, into which p-NA is adsorbed.

We have used incoherent inelastic neutron scattering (IINS) to characterize the vibrational spectroscopy (below 2000 cm^{-1}) of p-NA adsorbed in ALPO-5 at both 3 and 13 wt % which represent the onset of and the maximum in the nonlinear optical coefficient, respectively. In addition, the spectra of pure p-NA and ALPO-5 were obtained for comparison.

The IINS scattering data were measured using the BT-4 spectrometer with either a Be or Be-graphite-Be filter analyzer and a Cu(220) monochromator with 40'-40' collimation before and after the monochromator or a graphite

(002) monochromator with 40'-20' collimation. Data were collected over the energy range 10-220 meV at a temperature of 80 K.

Figure 1 illustrates data in the 35-230 meV region for 3 and 13 wt % p-NA adsorbed in ALPO-5. Analysis of these data and that obtained for pure Na and ALPO-5 are currently under way. Spectral differences in the region of 30-60 and 100-150 meV are clearly seen. These differences may arise from differences in the alignment, ordering and hydrogen bonding of the p-NA molecules inside the confines of the ALPO-5 channels. From IR data [1] it is known that the extent of hydrogen bonding of p-NA in ALPO-5 is different in the low and high loading samples. The possibility also exists for clustering of p-NA in the channels. Further studies of the system are planned using quasielastic neutron scattering, SANS and neutron diffraction.

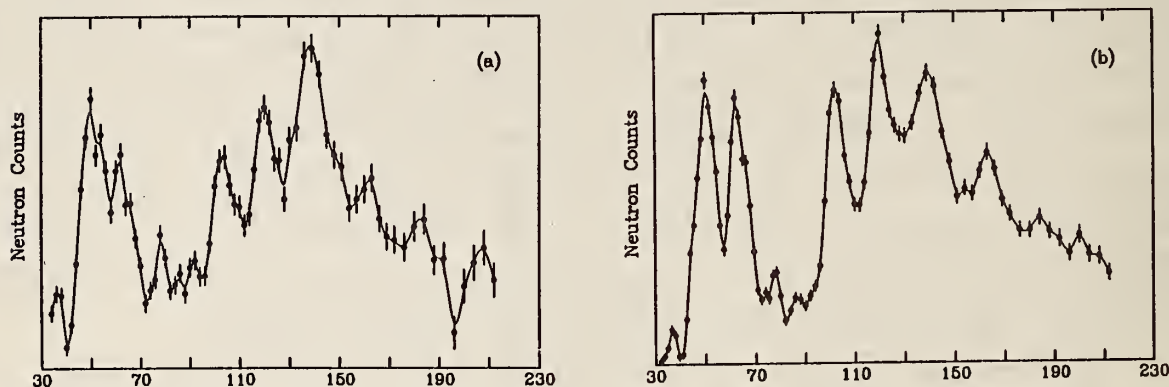


Figure 1. The IINS of (a) 3 wt % and (b) 13 wt % p-nitroaniline adsorbed in ALPO-5 at 80 K.

Reference

- [1] Cox, S. D.; Gier, T. E.; Stucky, G. D.; Bierlein, J. J. Am. Chem. Soc. 110, 2986 (1988).

**DYNAMICS OF MOLECULAR HYDROGEN ADSORBED IN TRANSITION-METAL
EXCHANGED ZEOLITES**

J. M. Nicol

(University of Maryland, College Park, MD and Reactor Radiation Division)

J. Eckert

(Los Alamos National Laboratory, Los Alamos, NM)

and

J. Howard

(Imperial Chemical Industries, Wilton, England)

The sensitivity of incoherent inelastic neutron scattering (IINS) to the rotational and vibrational transitions of molecular hydrogen, as well as the ability of neutrons to induce transitions within the librational ground state by nuclear spin flips that are generally not allowed in optical spectroscopies, makes IINS a particularly useful probe of bound hydrogen. We have previously studied the rotational and vibrational transitions of molecular hydrogen adsorbed in the cavities of partially cobalt-exchanged type A zeolite by IINS [1]. Transitions due to both rotational and vibrational excitations of the adsorbed hydrogen were identified in the spectra. Analysis of the data revealed the barrier height to rotation and details of end-on coordination of hydrogen to the Co^{2+} cations. This work has now been extended to other transition-metal ion-exchanged zeolites.

IINS spectra have been obtained for molecular hydrogen adsorbed in the cavities of partially Zn-exchanged type A zeolite as a function of both temperature and coverage. Neutron scattering data were collected in the energy-transfer range 1-12 meV using the time-of-flight (TOF) spectrometer at an incident energy of 13.8 meV. Hydrogen was adsorbed to coverages of 0.5, 1.0, and 2.0 molecules per supercage in the fully dehydrated zeolite at 50 K. The sample was then annealed at 80 K before being cooled to the data collection temperature of either 4, 50, or 80 K.

The data reveal two transitions in both neutron energy loss and gain at ~ 4 and 8.4 meV. The intensities and temperature dependence of these peaks, as well as their frequency shifts, are being analyzed to establish their origin in terms of rotational and vibrational transitions of the hydrogen molecules interacting with the cations (Zn and Na) in the framework. As in the CoNa-A case, a number of potential force fields of different symmetry are being considered; i.e., end-on vs. side-on adsorption geometry.

Reference

- [1] Nicol, J. M.; Eckert, J.; Howard, J. J. Phys. Chem. 92, 7117 (1988).

THE DEPENDENCE OF THE OH⁻ LIBRATIONS ON THE OCTAHEDRAL SITE OCCUPANCIES IN 2:1 LAYERED SILICATES

D. A. Neumann

and

J. M. Nicol

(University of Maryland, College Park, MD and Reactor Radiation Division)

Most layered silicates are composed of two basic building blocks: SiO₄⁴⁻ tetrahedra which are corner-joined, and Al(OH)₆³⁻ octahedra which are edge-joined. Different minerals are formed by the isomorphous substitutions of either or both of the Al and Si ions and by different stacking arrangements of the tetrahedrally and octahedrally coordinated layers. For instance, a 2:1 layered silicate is composed of a tetrahedral layer followed by an octahedral layer followed by another tetrahedral layer which are joined by shared O atoms. Members of this class of minerals include the micas, vermiculite, the smectites, and talc. The vastly different properties of these substances are due to the charge density on the layers which arises from the various substitutions in the octahedral sites, tetrahedral sites, or both. This charge is compensated by cations residing in the interlayer galleries. These minerals are further classified according to the degree to which the octahedral sites are occupied. If all of the octahedral sites are occupied, the mineral is referred to as trioctahedral, while if 2/3 of the these sites are occupied it is called dioctahedral. Talc and vermiculite are examples of trioctahedral 2:1 layered silicates. Muscovite, which is a mica, and montmorillonite, a smectite, are dioctahedral minerals.

Using the Be-graphite-Be filter analyzer on the BT-4 spectrometer, we have begun inelastic neutron scattering measurements on members of this class of silicates in order to determine the dependence of the OH⁻ librations on the occupancy of the octahedral site. This information will provide valuable experimental input for currently developing models of the dynamics of these minerals and may be important for the characterization of the host material in pillared clays which show promise as tailored catalysts and molecular sieves.

Figure 1 shows the inelastic spectra for talc between 20 and 140 meV. Talc is trioctahedral with an ideal chemical formula of $\text{Mg}_3\text{Si}_4\text{O}_{10}(\text{OH})_2$. The Mg has been substituted for the Al in the octahedral sites causing the charge density on the layers to be zero. Thus there are no gallery cations in talc. Here a dominant peak is observed at about 85 meV which is due to the OH^- librations. A smaller peak is observed at about 65 meV. The inelastic spectra of muscovite is shown in figure 2 over the same energy range. Muscovite is dioctahedral with an ideal chemical composition of $\text{KAl}_2(\text{AlSi}_3)\text{O}_{10}(\text{OH})_2$. The K is the gallery ion which compensates the net negative charge which arises from the substitution of Al for Si on the tetrahedral sites. Here we observe essentially three peaks of comparable intensity at about 60, 80, and 115 meV. Clearly the two spectra are vastly different.

To ascertain the degree to which charge density on the layers and tetrahedral site substitutions affect the OH^- librations in these minerals, we plan to do similar measurements on phlogopite which is a trioctahedral mica with an ideal composition of $\text{KMg}_3(\text{AlSi}_3)\text{O}_{10}(\text{OH})_2$ and pyrophyllite which is dioctahedral mineral with composition $\text{Al}_2\text{Si}_4\text{O}_{10}(\text{OH})_2$. Like talc, pyrophyllite has no net charge on the layers, so there is no gallery cation. In addition, efforts are being made to model our results using programs written by J. Gales and S. D. Mahanti of Michigan State University.

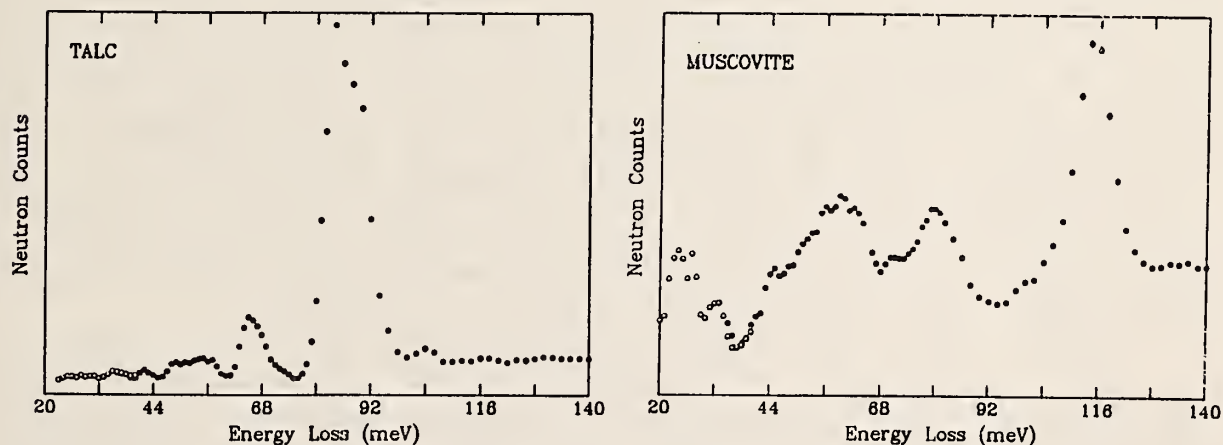


Figure 1. (left) Inelastic scattering spectra of talc taken at 80 K.

Figure 2. (right) Orientationally averaged inelastic scattering spectra of muscovite taken at 80 K.

NEUTRON SCATTERING STUDIES OF TRIMETHYLAMMONIUM
PILLARED VERMICULITE CLAYS

D. A. Neumann

Y. B. Fan, H. Kim, S. A. Solin, and T. J. Pinnavaia
(Michigan State University, East Lansing, MI)

and

S. F. Trevino
(ARDEC, Picatinny Arsenal, NJ and Reactor Radiation Division)

Layered silicates such as vermiculite are unique among lamellar solids because of their ability to be pillared by robust intercalated guest ions which occupy sites within the interlayer galleries. The enormous free volume of accessible interior space that is created by pillaring has significant practical implications for tailored catalysts and molecular sieves. In spite of this, relatively little information is available concerning the structure and dynamics of these potentially important materials. We have therefore undertaken a neutron scattering study of trimethylammonium pillared vermiculite.

The measurements were performed on the BT-4 spectrometer using the conventional triple-axis arrangement for the elastic scans and the Be-graphite-Be filter analyzer for collection of the inelastic scattering data. The samples were fabricated from natural Mg-vermiculite from Llano, Texas which were ground until the crystallites were a few microns in size to ensure that the ion exchange process would occur within a reasonable time. After the Mg ions were exchanged for tetramethylammonium in the presence of the EDTA anion, the resulting material was sedimented onto a glass plate to form a self-supported, oriented film. This film was then dried for 12 hours at 100 °C and cut into smaller pieces which were stacked so that their c-axes were aligned. The resulting samples had mosaics of about 30°.

Table 1 shows the total scattering lengths of the individual layers obtained by fitting the measured (00 ℓ) intensities compared to the scattering lengths expected for a unit cell composition of $[(CH_3)_3NH^+]_2-(Al_{0.31}Fe_{0.03}Mg_{5.66})_2(Si_{5.73}Al_{2.27})O_{20}(OH)_4$. The important point is that all of the fit scattering lengths correspond closely to the expected ones, except for those of the gallery ions. Varying other parameters in the system (i.e., bond lengths and Debye-Waller factors) does not alter this conclusion. This

implies that the trimethylammonium ions have not completely exchanged with the original gallery ions. In fact, this data is consistent with an exchange of only about 30%. Thus the available gallery space in these materials may not be uniform, a result which has implications for the possible use of these materials as catalysts, catalyst supports, and molecular sieves.

Table 1. Comparison of the total scattering lengths B_i per layer per unit cell which were derived from a fit of the (00 l) intensities to those expected for Llano vermiculite intercalated with trimethylammonium

Layer	B_i (fit)	B_i (calculated)
Mg	5.90	6.15
O(1)	2.83	2.73
Si/Al	1.89	1.60
O(2)	3.37	3.48
$(CH_3)_3NH^+$	2.63	-1.63
$(CD_3)_3ND^+$	8.50	19.19

The inelastic scattering spectra for the $(CH_3)_3NH^+$ intercalated sample are shown in figure 1 for two different orientations. Here the open symbols are data taken with the graphite monochromator and collimations of 40'-20' before and after the monochromator, respectively, and the open symbols refer to data taken with the Cu(220) monochromator and collimations of 60'-40'. In the energy range between 20 and 100 meV, four peaks were identified as being due to internal modes of the trimethylammonium ion. The symmetric and antisymmetric torsional excitations of the methyl groups were observed at 28.8 and 36.8 meV, respectively, while two bending modes were observed at energies of 51.1 and 58.0 meV. Since the data showed obvious orientational dependence, we have also performed a normal mode calculation for the trimethylammonium ion in order to determine its orientation. The best representation of the experimental data, after taking the clay modes into account, was obtained when the N-H bond was parallel to the c-axis. The result of this calculation was convoluted with the resolution and is plotted as the solid line in figure 1. Modes not reproduced by the calculation are due to excitations of the host material and mainly result from motion of the H in the OH^- groups. These features are also present in the $(CD_3)_3ND^+$

intercalated sample. The only one of these peaks which has been clearly identified is the one at 80 meV which arises from the OH^- librations. The identification of the other modes requires a detailed lattice-dynamical calculation of the host material.

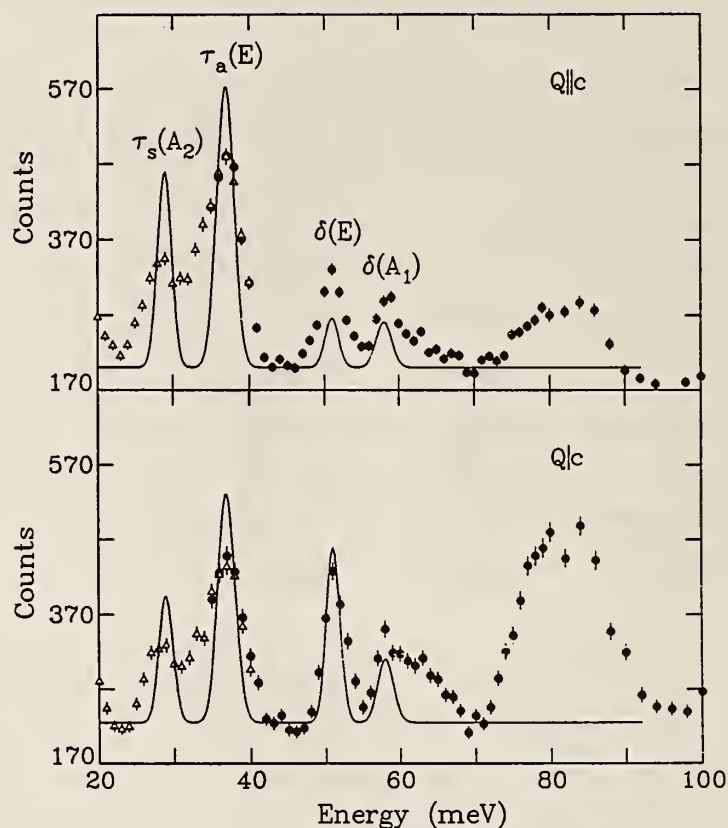


Figure 1. Inelastic neutron scattering spectra of trimethylammonium pillared vermiculite for in-plane and out-of-plane excitations taken at 80 K. The solid line represents a normal mode calculation for the trimethylammonium ion assuming that the C-H bond is oriented along the c-axis.

REACTOR RADIATION DIVISION AND COLLABORATIVE PROGRAMS

**STRUCTURAL STUDIES OF STAGE 1 METAL-DICHLORIDE GRAPHITE
INTERCALATION COMPOUNDS**

J. S. Speck, B. J. Wuensch, and M. S. Dresselhaus
(Massachusetts Institute of Technology, Cambridge, MA)

and

E. Prince

Metal-dichlorides such as CuCl_2 or CoCl_2 intercalated into graphite usually form incommensurate structures. The intercalate layer in these compounds consists of a chlorine/metal/chlorine sandwich similar to that found in the CdCl_2 structure. We have carried out extensive x-ray photographic and diffractometer studies on a series of stage 1 and stage 2 metal-dichloride graphite intercalation compounds (GICs). Although the intercalant and carbon have incommensurate in-plane structures, both species form long-range ordered three-dimensional crystals for the stage 1 compounds. In the stage 2 compounds the interlayer intercalant interactions are sufficiently attenuated by the carbon that there is no layer stacking structure. We have found that the CdCl_2 structure is preserved for CoCl_2 , MnCl_2 , and NiCl_2 in the stage 1 compounds. CuCl_2 intercalated in graphite has the structure of copper cations sitting in the octahedral sites of distorted chlorine layers. In this case the CuCl_2 stacks in an $\alpha\beta$ sequence.

The single crystal GICs used for these studies have a fwhm mosaic spread of $\sim 5^\circ$ in the best case. This is because the intercalation processes causes a $\sim 300\%$ expansion of the graphite crystals perpendicular to the layer planes. Hence the quality of data for single crystal structure refinement will be poor. To overcome this problem, we have prepared stage 1 CuCl_2 and CoCl_2 -GICs in graphite powder. We have obtained neutron powder diffraction data on the Neutron Beam Split-core (NBS) reactor in order to carry out a Rietveld structure refinement. The data analysis is currently in progress. The goal of the analysis is to refine the atomic positions, site occupancies, and thermal parameters. The current limitation in the analysis is that the carbon and intercalant have distinct reciprocal lattices and hence their respective structures must be refined separately. Additionally, different parameters are necessary to describe the linewidths of different families of reflections.

**APPLICATION OF MAXIMUM ENTROPY TO PHASE REFINEMENT
IN MACROMOLECULAR CRYSTALLOGRAPHY**

E. Prince

L. Sjölin

(Chalmers University of Technology, Göteborg, Sweden)

and

D. M. Collins

(Naval Research Laboratory, Washington, DC)

A procedure was previously described [1] for finding an everywhere-positive density distribution whose Fourier transform is in agreement with an arbitrarily large set of observed diffraction intensities. This procedure has been applied to improving the phases, and thereby elucidating details, of the crystal structures of several proteins, ribonuclease A complexed with uridine vanadate, calcium containing fragment 1 of bovine prothrombin, and Mojave toxin.

In each case the starting map was one that had been produced with phases obtained from a partial (Mojave toxin) or complete (ribonuclease and bovine prothrombin) solution of the structure of the protein molecule obtained by other means. In Mojave toxin there are two molecular subunits, in one of which the chain was well refined, while in the other it was not. After 50 cycles of sequential maximum entropy fitting of blocks of the 100 worst fitting reflections, the resulting map showed an alternative path for a part of the poorly fitting chain. Interestingly, a molecular dynamics calculation [2] of the minimum energy conformation of the chain suggests a similar alternative path.

In ribonuclease the protein chain was well refined, but details of the solvent and, particularly, the uridine vanadate complex, which was believed, on biochemical grounds, to be bound at the active site, were missing. After a maximum entropy fit of the 30 worst fitting reflections, the resulting map revealed that one region of previously uncertain density was clearly a molecule of t-butanol, that several previously located water molecules should be moved, and, most importantly, a clear picture of the uridine vanadate complex. Figure 1 shows this region of the maximum entropy map, with the uridine molecule and a nearby histidine side chain in the active site of the protein molecule.

The protein chain of calcium containing fragment 1 of bovine prothrombin was also fairly well defined, but a substantial proportion (25%) of the contents of the unit cell is carbohydrate, which had not been located, and the location of the calcium atom was also unclear. A maximum entropy fit to the 30 worst fitting reflections gave a clear picture of the calcium atom, bound, as had been expected, to a group of four residues of the unusual amino acid γ -carboxy glutamic acid on the surface of the molecule, and also revealed numerous regions of density that could be fit with carbohydrate. Figure 2a shows one of these regions, and figure 2b shows the calcium site.

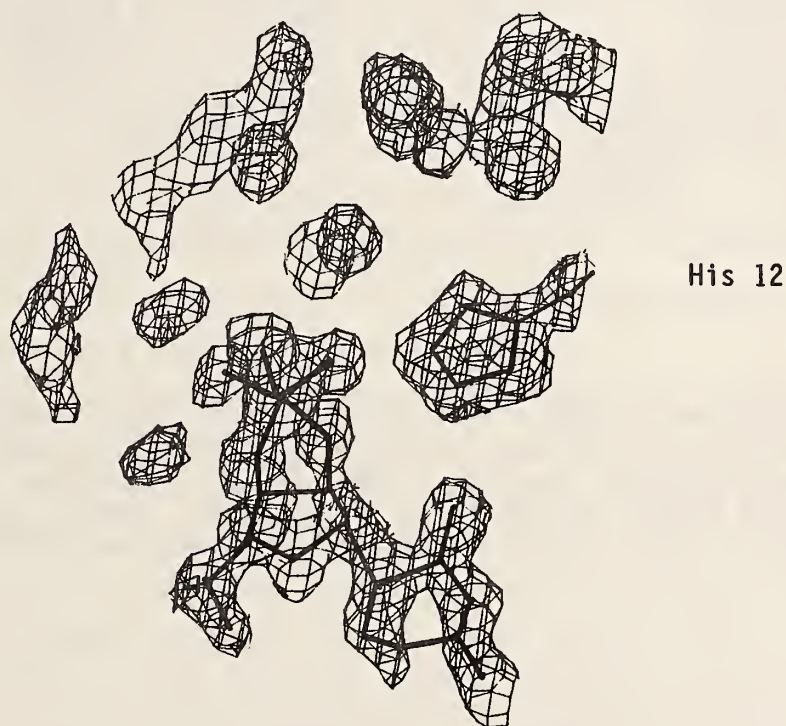
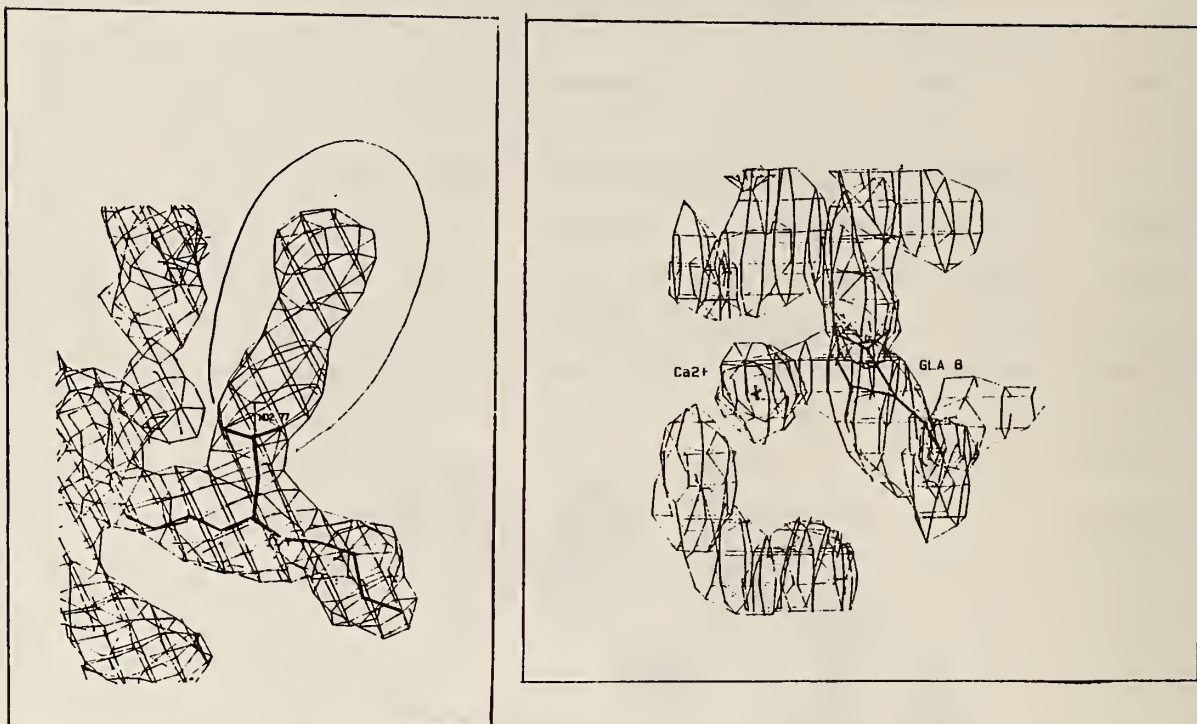


Figure 1. The electron density of the uridine vanadate complex in the active site of ribonuclease A, as calculated by maximum entropy methods. A histidine ring (His 12) from the protein molecule is also shown.



2a

2b

Figure 2. Electron density maps from calcium containing fragment 1 of bovine prothrombin, calculated using maximum entropy methods. Figure 2a shows extended density attached to a nitrogen atom of asparagine 77 that binds the protein to carbohydrate. Figure 2b shows the calcium site, near the rare amino acid residue γ -carboxy glutamic acid.

References

- [1] Prince, E. Acta Cryst. A45, 200-203 (1989).
- [2] Brunger, A. T. J. Mol. Biol. 203, 803-816 (1988).

**BACKGROUND CONTRIBUTIONS AND QUANTITATIVE PHASE DETERMINATION
IN RIETVELD STRUCTURE REFINEMENT**

J. K. Stalick and E. Prince

Accurate treatment of background contributions is important in the Rietveld method of structure refinement, particularly when one is attempting to determine small structural features such as occupancies of crystallographic sites or the amount of site substitution by different elements. For partial site substitution or site occupancy, the average scattering length, b , for a given site is actually determined. In the case of 10% substitution of Zn for Cu, for example, one is looking for a very small difference: $b = 0.772 \times 10^{-12}$ cm for Cu, and 0.752×10^{-12} cm for 90% Cu, 10% Zn. It is important to treat the pattern background scattering as carefully as possible to augment the significance level of the resulting atomic site occupancies. To this effect, two strategies have been employed: (1) inclusion of higher-order polynomial terms in the background function to enable the use of low-angle peaks in the refinement, and (2) inclusion of the scattering due to impurity phases as a contribution to background.

In order to determine adequately the amount of substituent on a given crystallographic site, it is important that the data cover as large an angular range as possible to decouple the occupancy parameters from the thermal parameters in the refinement. Since a linear approximation to background is not adequate for materials with relatively large unit cells, additional background parameters were added to the NIST version of the Rietveld refinement program in the form of Chebychev polynomial coefficients [1]. The use of the orthogonal Chebychev polynomials instead of a power series eliminates any problems with correlations in the refinement, as adding additional terms to improve the approximation does not affect the values of the coefficients of the preceding terms. Figure 1 shows the agreement of calculated and observed data, along with a residual plot, for $\text{YBa}_2\text{Cu}_3\text{O}_7$ in the low-angle region. A six-parameter Chebychev polynomial function provided an adequate fit of the background.

The Rietveld refinement program has also been modified to include scattering from up to five impurity phases as contributions to background. In order to include impurity phases, the impurities must first be identified from peak positions and intensities. The known structure of the impurity phase is used to obtain a calculated pattern, assuming the same zero point

and range of data as the main phase, and a scale factor k_j is refined for each impurity phase according to the equation

$$(1/c) Y_i(\text{calc}) + B_i + \sum_{j=1}^n k_j Y_{ij} = Y_i(\text{obs})$$

where B_i is the background intensity defined by the Chebychev polynomial coefficients and Y_{ij} is the calculated intensity of impurity phase j at point i . The ratio $1/c:k_j$ gives the main phase : impurity phase ratio.

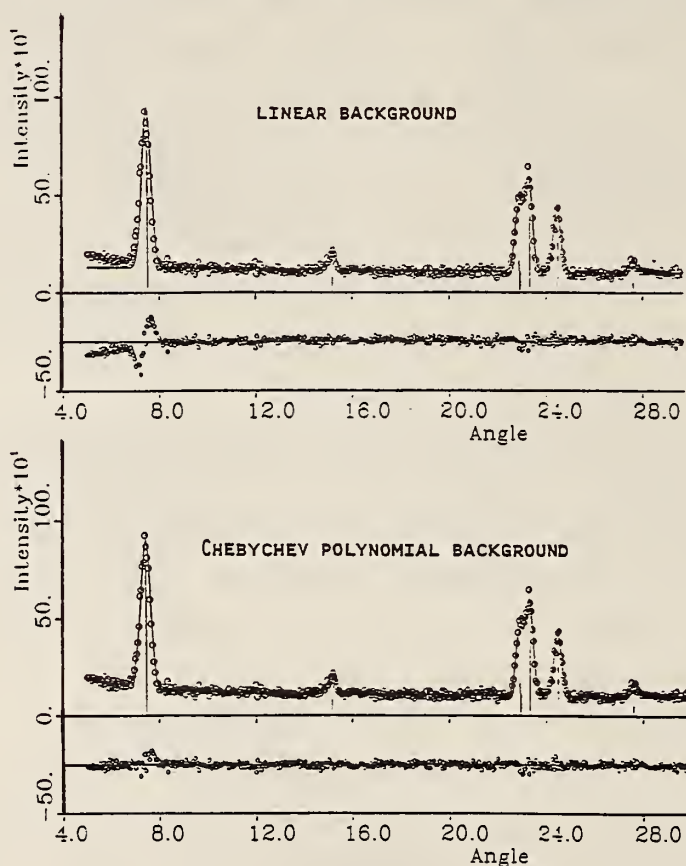


Figure 1. Agreement between calculated and observed intensities for $\text{YBa}_2\text{Cu}_3\text{O}_{6.98}$.

Reference

- [1] Prince, E. Mathematical techniques in crystallography and materials science. Springer-Verlag, New York, 1982.

**NEUTRON RIETVELD ANALYSIS OF ANION AND CATION DISORDER
IN THE FAST-ION CONDUCTING PYROCHLORE SYSTEM $Y_2(Zr_xTi_{1-x})_2O_7$**

S. M. Haile and B. J. Wuensch
(Massachusetts Institute of Technology, Cambridge, MA)

and

E. Prince

The cubic pyrochlore structure type, $A_2B_2O_7$, space group $Fd3m$, is a superstructure with lattice constant double that of a fluorite-like array of ions. Cations A and B order in positions $16c\ 000$ and $16d\ 1/2\ 1/2\ 1/2$; oxygen ions are ordered in $48f\ x\ 1/8\ 1/8\ 1/8$ and $8a\ 1/8\ 1/8\ 1/8$, leaving an anion vacancy (relative to a fluorite array) at $8b\ 3/8\ 3/8\ 3/8$. $Y_2Ti_2O_7$ is a fully-ordered pyrochlore, whereas $Y_2Zr_2O_7$ is fully disordered and statistically has the fluorite structure. Intermediate solid solutions have partial order. A progressive increase in ionic conductivity by two and one-half orders of magnitude ($1.6\ 10^{-5}$ to $5.0\ 10^{-3}\ \text{ohm}^{-1}\text{cm}^{-1}$ at $1000\ ^\circ\text{C}$) accompanies the disorder [1].

High quality powders have been synthesized for compositions $Y_2(Zr_xTi_{1-x})_2O_7$ having $x = 0, 0.3, 0.45, 0.60$, and 0.90 to permit correlation of structure with oxygen ion conductivity with the aid of Rietveld powder profile analysis. Data have been recorded with $1.5530\ \text{\AA}$ thermal neutrons for the samples with $x = 0$ and 0.90 . Refinement has been successfully completed for the former composition providing as residuals $R_{\text{Bragg}} = 2.17\%$, $R_{\text{WP}} = 9.96\%$ and $R_E = 7.36\%$.

Most of the information on ordering is contained in the superstructure intensities. Identically zero in the disordered fluorite state, the magnitudes of the superstructure intensities are determined by the amount of displacement of the $48f$ oxygen ion from the ideal value of $x = 3/8$ (relaxation toward the oxygen vacancy occurs) and, secondly, by the difference between the scattering length of the cation species which order in the A or B site, and the average cation scattering length for a given composition. The scattering length of Ti is negative (-0.3438) relative to values 0.775 and 0.716 for Y and Zr, respectively. The average cation scattering length is small, therefore, and the difference between individual and average cation scattering lengths is unusually large. The superstructure maxima are thus as much as three times more intense than the fluorite-type

substructure intensities that appear in the powder diffraction pattern. Neutron scattering is, accordingly, an especially sensitive measure of order in the present system.

Reference

- [1] Moon, P. K.; Tuller, H. L. Solid State Ionics 28-30, 470 (1988).

CRYSTAL STRUCTURE OF 11,23-DI-TERT-BUTYL-1,9,11,13,21,23-HEXA-AZAPENTACYCLO[19.3.1^{3,7}.1^{9,13}.1^{15,19}]OCTACOSA-3,5,7(28),15,17,19(26)-HEXAENE-25,27-DIONE, (C₃₀H₄₂N₆O₂)

H. L. Ammon
(University of Maryland, College Park, MD)

and

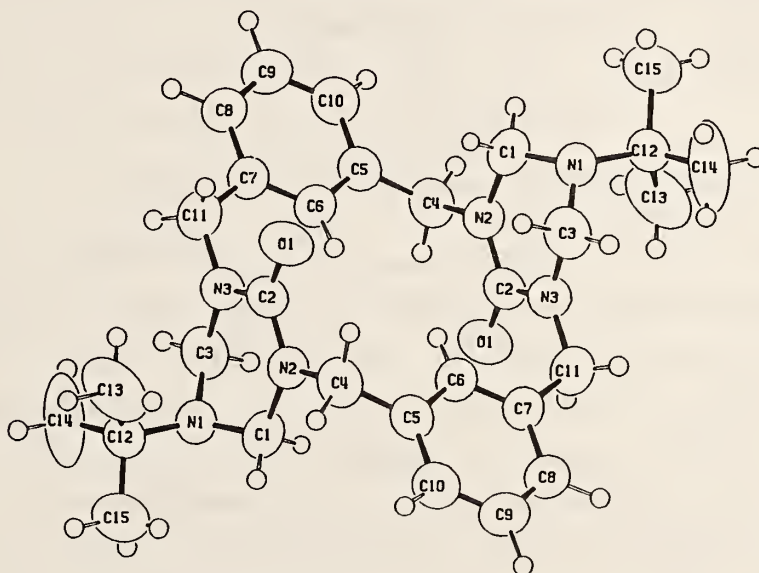
C. S. Choi
(ARDEC, Picatinny Arsenal, NJ and Reactor Radiation Division)

The crystal structure of the titled compound was determined by x-ray diffraction, using the ENRAF-NONIUS CAD4 diffractometer at the x-ray laboratory of the Department of Chemistry, University of Maryland. The crystals were synthesized and grown by P. R. Dave of Geo-Centers, Inc., Hopatcong, NJ. The compound crystallizes in the triclinic $P\bar{1}$ space group with unit cell dimensions of $a = 11.2931(9)$, $b = 12.4655(8)$, $c = 13.0891(8)$, $\alpha = 68.820(7)$, $\beta = 71.056(6)$, $\gamma = 74.530(6)$, containing two formula units of the titled compound and an acetonitrile molecule per unit cell. The structure was solved with the MITHRIL direct methods link, and was refined to the final R-factors of $R = 0.065$ and $R_w = 0.092$.

There are two independent centrosymmetric molecules in the crystal, namely molecule A and molecule B, as shown in figure 1. The two molecules have virtually identical molecular conformations. The benzene ring and their methylene substituents are planar within experimental error. The heterocyclic six-membered rings are bent into two planar parts, along the C1...N3 line in molecule A and C21...N23 in molecule B. The intramolecular distances across the center of the molecular rings are 5 Å or longer in both molecules. Hydrogen atoms H6 and H6' (molecule A) and H26' and H26' (molecule B) point into the 5 Å cavity.

A three atom moiety, which we have interpreted as acetonitrile (crystallization solvent), is rather poorly defined because of the large thermal motions and, subsequently, the methyl hydrogens were not modeled. The shortest intermolecular distances are C43...O1 = 3.147(9) and C43...O2 = 3.29(1) Å. There are no other contacts within 5 Å distances.

A.



B.

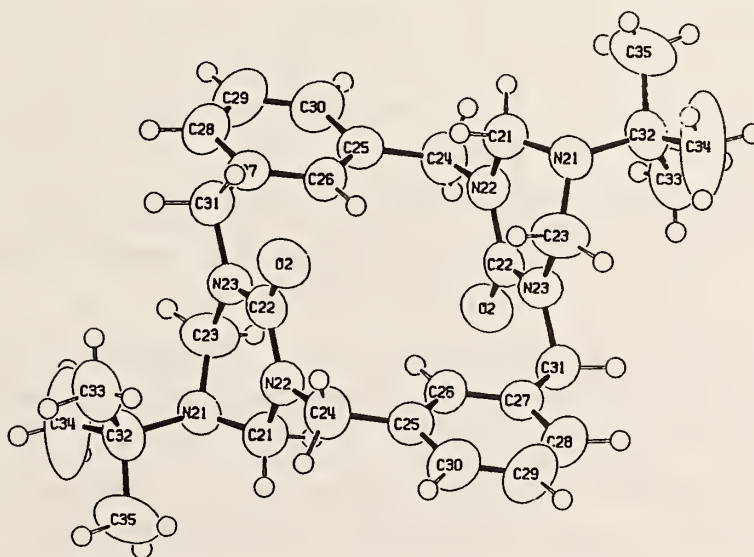


Figure 1. ORTEP drawings of molecules A and B.

**NEUTRON DIFFRACTION STUDIES OF THE MARTENSITIC
TRANSFORMATION IN SODIUM METAL**

R. Berliner
(University of Missouri, Columbia, MO)

H. G. Smith
(Oak Ridge National Laboratory, Oak Ridge, TN)

J. R. D. Copley

and

J. Trivisonno
(John Carroll University, Cleveland, OH)

Recent neutron diffraction experiments on single crystals of sodium, using the BT-9 spectrometer, have improved our understanding of the structure of this metal at low temperatures [1]. We now have ample evidence that sodium, after passing through the martensitic transformation, adopts a structure similar to that of the low temperature form of lithium, i.e., the 9R (Sm-type) trigonal structure [2]. The transformation in sodium is observed to occur abruptly at about 35 K, where about 40% of the specimen transforms to the trigonal form, with the c-axis of the 9R structure aligned to within a few degrees of the original bcc [110] direction. Each bcc [110] direction is associated with four variants of the 9R structure, located symmetrically about the bcc [110] at $(1.018, 0.92, \pm\delta)$ and $(0.92, 1.018, \pm\delta)$, δ being of the order of 0.06. The low-temperature diffraction pattern is considerably complicated by the presence of these 24 variants. Elastic diffraction scans along the trigonal $[10\bar{l}]$ and $[20\bar{l}]$ directions show that the diffraction peaks are both shifted and broadened in a manner characteristic of layer defects (typically stacking faults) [3]. The shifting and broadening are consistent with the presence of a "double-twin" layer defect, a defect which is created whenever the 9R stacking order, ..ABCBCACAB.., is altered at a layer such that the stacking sequence reverses for a single layer and then proceeds forward again, e.g., ..ABCBCBCACAB... The correspondence between the model diffraction calculations and the $(10\bar{l})$ elastic scans is shown in figure 1. This type of defect is similar to the defect predicted by Gooding and Krumhansl [4] in their analysis of the martensitic transformation in lithium.

In addition to the broadened and shifted 9R diffraction peaks, the diffraction pattern shows evidence of another phase, tentatively identified as hcp. The extra peaks appear near the $(\pm 1, 0, \pm 4.5)$ and $(\pm 1, 0, 0)$ reciprocal lattice points. The intensities of the hcp and 9R peaks were monitored as the temperature of the specimen was changed, as shown in figure 2. We find that the 9R phase reverts to the bcc near 55 K whereas the hcp phase remains, transforming to bcc at a somewhat higher temperature. The shifts in position of the hcp diffraction peaks, from their ideal (9R index) positions of $(\pm 1, 0, \pm 4.5)$ and $(\pm 1, 0, 0)$, are not yet understood.

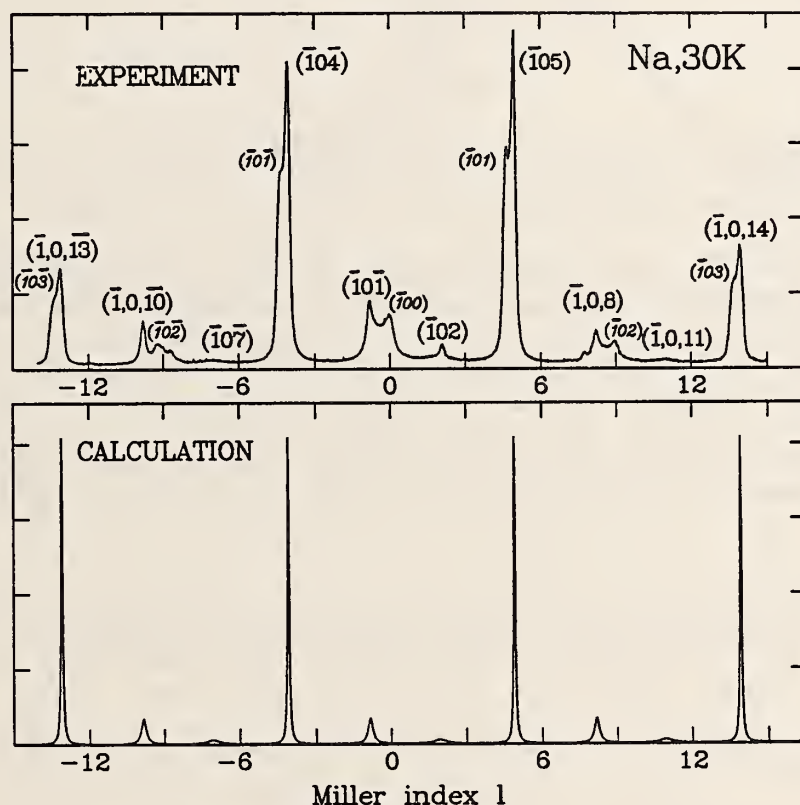


Figure 1. Upper figure: the measured $(\bar{1}0\bar{l})$ diffraction pattern for sodium at 30 K. Both 9R and hcp peaks are shown: the hcp peak labels are indicated in italics. Measured peak shifts range from -0.11, for the $(-1, 0, -13)$ 9R peak, to +0.17 for the $(-1, 0, -1)$ and $(-1, 0, 3)$ hcp peaks. Unassigned peaks are believed to be associated with additional variants in the sample.

Lower figure: the calculated diffraction pattern for a 9R sodium lattice with 10% single layer "double-twin" stacking faults. The theoretical diffraction pattern repeats every nine units in l . The calculated peak shifts are in reasonable agreement with experiment.

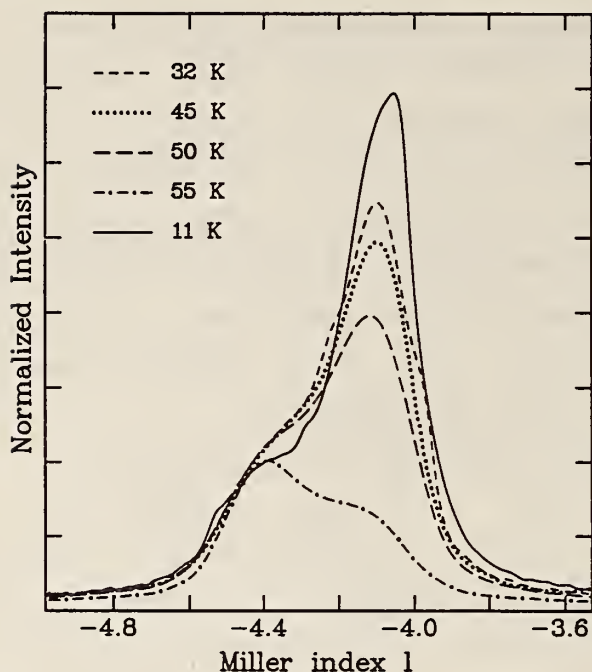


Figure 2. A series of $(\bar{1}0\ell)$ scans from $\ell = -5$ to -3.5 , normalized to the same neutron monitor count, which demonstrate the existence of a second low temperature phase in sodium. The shifted $(\bar{1}0\bar{4})$ peak, which is associated with the 9R phase, was observed to disappear rapidly (though not completely) as the temperature was increased from 32 to 55 K, whereas the $(\bar{1}0\bar{1})$ hcp peak, at $(-1,0,-4.5)$ in the 9R notation, remained. The shifted 9R $(\bar{1}0\bar{4})$ peak reappeared, with increased intensity, when the sample was cooled to 11 K.

References

- [1] Berliner, R.; Smith, H. G.; Copley, J. R. D.; Trivisonno, J. NIST Tech. Note 1257, C. O'Connor, ed. p. 69 (1989); Bull. Am. Phys. Soc. 34, 769 (1989).
- [2] Berliner, R.; Fajen, O.; Smith, H. G.; Hitterman, R. J. Phys. Rev. (in press).
- [3] Berliner, R.; Werner, S. A. Phys. Rev. B34, 3586 (1986).
- [4] Gooding, R. J.; Krumhansl, J. A. Bull. Am. Phys. Soc. 33, 615 (1988).

STRUCTURE OF AlCuFe ALLOYS EXHIBITING THE ICOSAHEDRAL PHASE

Y. Calvayrac, M. Cornier-Quiquandon, D. Gratias, and A. Quivy
(C.E.C.M./C.N.R.S.)

R. Bellissent
(C.E.N.-Saclay)

F. Biancaniello, F. W. Gayle, and R. Schaefer
(Metallurgy Division)

J. W. Cahn
(Institute for Materials Science and Engineering)

and

B. Mozer

AlCuFe alloys have been shown to form a stable icosahedral phase [1]. Particular alloys of this phase have been produced which form very perfect singly oriented specimens exhibiting very narrow line widths in their x-ray diffraction patterns [2]. Some of these singly oriented specimens are of sufficient size to yield precise neutron diffraction patterns [3].

We have obtained both x-ray and powder neutron diffraction patterns on several specimens of $\text{Al}_{63}\text{Cu}_{25}\text{Fe}_{12}$ prepared according to the procedure determined by some of us [2] which produced the pure icosahedral phase. Figure 1 shows the x-ray diffraction patterns taken of our specimens. One observes the narrowness of the peaks of the pattern where many of the peak widths are essentially determined by the instrumental resolution. The lines are very well indexed by the procedure for powders given by Cahn, Gratias, and Shechtman for a 6-d fcc reciprocal lattice [4] and show that this alloy belongs to the face centered icosahedral lattice, different from the primitive icosahedral lattice of our other alloy systems. Neutron diffraction data were taken on only the alloy prepared as an ingot. Figure 2 shows both the x-ray and neutron diffraction pattern for this alloy. Here again, one observes the very narrow line shapes in the neutron diffraction pattern that has not been obtained in any other icosahedral system. The x-ray and neutron diffraction patterns are very similar for this alloy in contrast with the patterns observed for AlMnSi alloys which have the primitive icosahedral lattice and where the manganese has a negative scattering length which produces large differences in the relative intensities of the peaks.

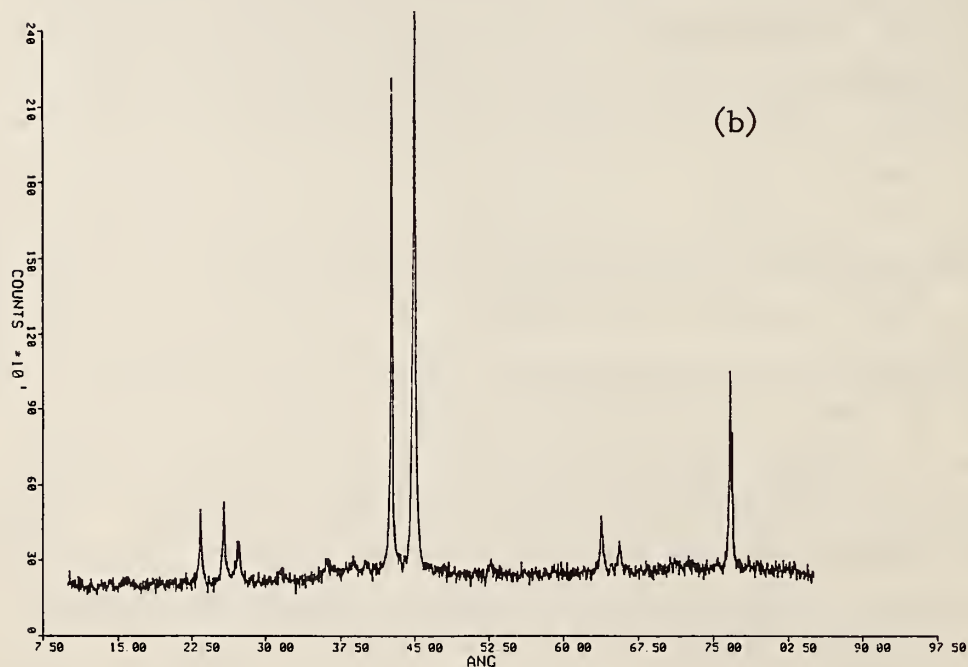
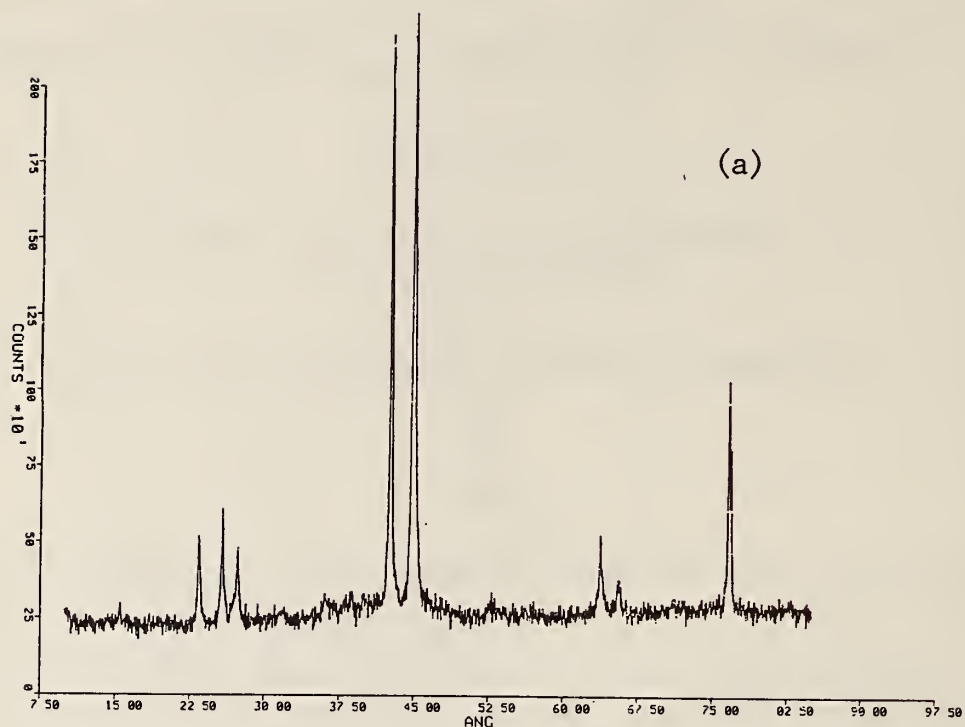


Figure 1. X-ray diffraction patterns of $\text{Al}_{63}\text{Cu}_{25}\text{Fe}_{12}$ prepared by (a) rapid solidification, powdering, and annealing; and (b) melting an ingot in the arc furnace, powdering a small piece cut from the ingot, and then annealing.

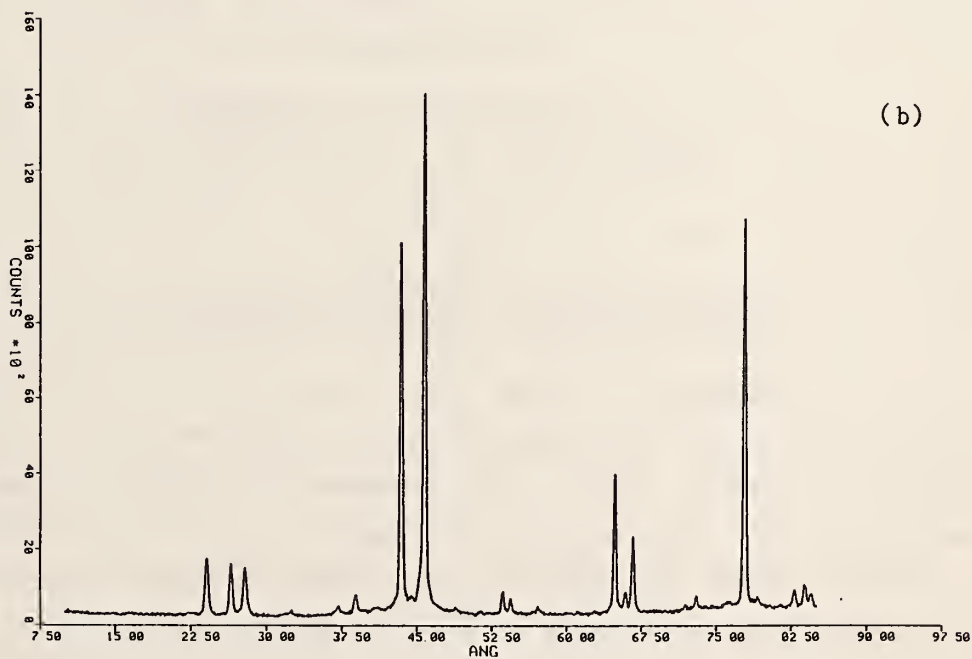
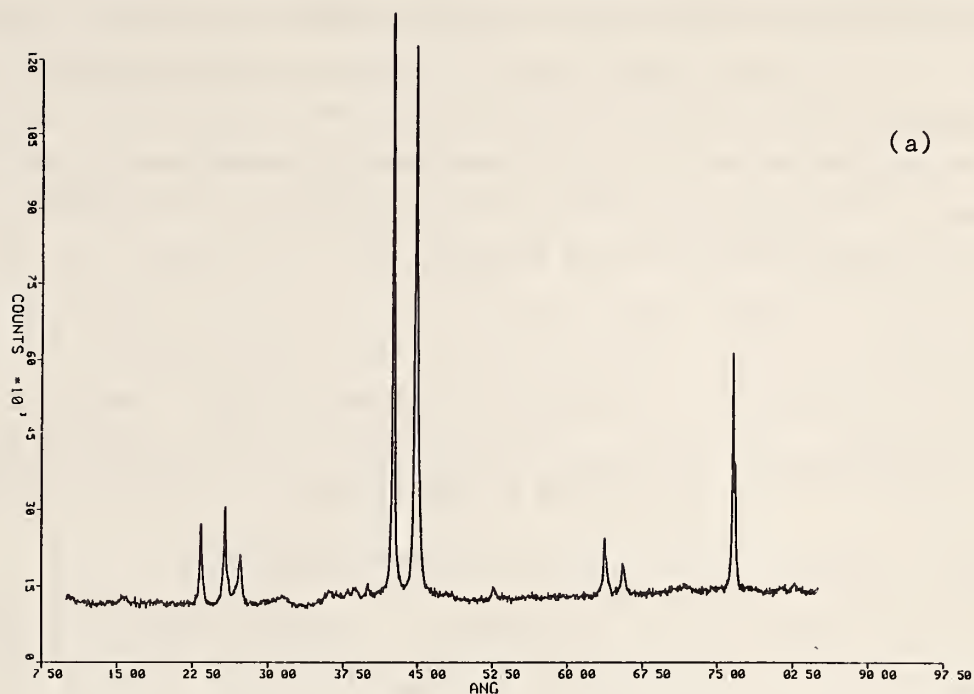


Figure 2. A comparison of the x-ray and neutron diffraction patterns of the alloy prepared as in figure 1b. (a) X-ray pattern with good statistics, and (b) neutron diffraction of the annealed ingot not powdered.

These preliminary studies are part of an international cooperation between the three laboratories to determine the boundaries of the icosahedral phase of the ternary phase diagram, to determine the procedure for producing a unique phase of isotopically substituted alloys, and to use these alloys in x-ray and neutron diffraction to determine the structure of each constituent element of these alloys so that a precise model for the atomic distribution of an icosahedral alloy can be determined.

References

- [1] Tsai, A.; Inoue, A.; Masumoto, T. J. Appl. Phys. (Japan), L1505 (1987).
- [2] Devaud-Rzepski, J.; Quivy, A.; Calvayrac, Y.; Cornier-Quiquandon, M.; Gratias, D. Phil. Mag. (to be published).
- [3] Bellissent, R. et al.; private communication.
- [4] Cahn, J.; Gratias, D.; Shechtman, D. J. Mater. Res. 1, 13 (1986).

EVOLUTION OF THE MAGNETIC STRUCTURE IN $\text{Tb}_x\text{Y}_{1-x}\text{Ag}$

J. A. Gotaas

M. R. Said and J. S. Kouvel
(University of Illinois, Chicago, IL)

and

T. O. Brun
(Argonne National Laboratory, Argonne, IL)

As the nonmagnetic yttrium ion is substituted for terbium, the cubic intermetallic compound TbAg changes from a conventional antiferromagnet into a complex magnetic system with components of both commensurate and incommensurate spin structures and bulk magnetic properties typical of spin glass behavior for Tb concentrations less than 50%. We have carried out neutron diffraction experiments on polycrystalline samples of $\text{Tb}_x\text{Y}_{1-x}\text{Ag}$ with $x = 0.15, 0.5$, and 1.0 to complement our earlier studies for $x = 0.3$ [1].

For $x = 1.0$, the magnetic structure is the $(\pi\pi 0)$ antiferromagnetic structure observed in many of the CsCl-type RAg (R = rare earth) compounds, with ferromagnetically aligned [110]-type planes of rare-earth magnetic moments which are antiferromagnetically coupled. T_N is found to be

approximately 106 K, and there is no evidence for a change in magnetic structure on cooling as has been suggested recently on the basis of crystal field considerations [2].

For $x = 0.5$, the system orders at $T_N \approx 58$ K into the mixed structure observed for $x = 0.3$, with a peak corresponding to the commensurate $(\pi\pi 0)$ magnetic structure at the $(1/2, 1/2, 0)$ position and asymmetric satellites arising from an incommensurate modulation of the basic $(\pi\pi 0)$ structure. In this case, however, the $(1/2, 1/2, 0)$ peak is much sharper, and on cooling below 40 K the incommensurate peaks almost disappear, remaining only as low-intensity shoulders of the commensurate peak at the lowest temperature measured ($T = 4$ K). Hysteresis is observed in the relative intensity of the two components of the structure between 45 and 55 K.

For $x = 0.15$, the system orders at $T_N \approx 18$ K into the two component structure, but with the $(1/2, 1/2, 0)$ peak much broader than the incommensurate satellite peaks, indicating that the commensurate spin correlations are an order of magnitude shorter than that of the modulated structure. The two components have an approximately constant intensity ratio and show no evidence of hysteresis, similar to the behavior found for $x = 0.3$. Thus, as the Tb concentration decreases, the relative stability of the commensurate and incommensurate structures appears to change. In the case of $x = 0.5$, the balance is so close that the structure changes from mixed commensurate/incommensurate to primarily commensurate as the magnetic moment develops. For $x = 0.3$ and 0.15 , on the other hand, the incommensurate component exists over larger distances, but the commensurate component remains in coexistence down to the lowest temperatures measured.

References

- [1] Gotaas, J. A.; Said, M. R.; Kouvel, J. S.; Brun, T. O. J. Phys. 49, C8-1103 (1988).
- [2] Aleonard, R.; Morin, P.; Rouchy, J. J. Phys. 49, C8-395 (1988).

MAGNETIC ORDER IN A $\text{Tb}_{0.5}\text{Dy}_{0.5}$ SINGLE CRYSTAL

M. L. Spano
(Naval Surface Warfare Center, Silver Spring, MD)

and

J. A. Gotaas and J. J. Rhyne

The rare-earth elements Tb and Dy both order magnetically with decreasing temperature into a basal-plane helical state, followed at lower temperatures by a transition to a basal-plane ferromagnetic state. In the low-temperature ferromagnetic phase, the b-axis is the magnetic easy axis for Tb, while the a-axis is the easy axis in the case of Dy. In the mixed alloy system, the competition of the different basal-plane anisotropies leads to temperature-dependent changes in the easy-axis direction, as indicated by magnetostriction results [1]. We have utilized neutron diffraction to study the nature of the magnetic ordering in a single crystal of $\text{Tb}_{0.5}\text{Dy}_{0.5}$ at the NIST reactor.

Measurements were performed on the crystal with the b-axis oriented perpendicular to the scattering plane, primarily on the (0002) peak and the satellites observed along the c-axis in the helical phase. On cooling from the high-temperature paramagnetic phase, the crystal orders into the helical phase with magnetic peaks observed at $(0002 \pm \delta)$ at $T_N \approx 206$ K. In the vicinity of 170 K, second harmonics begin to appear at $(0002 \pm 2\delta)$, arising from bunching of the moments prior to the ferromagnetic ordering which appears at $T_C \approx 152$ K. At this temperature, there is an abrupt reduction in the intensity of the satellite peaks at δ , while the harmonics at 2δ effectively vanish, as the ferromagnetic intensity increases sharply at the (0002) position. Some intensity remains at the satellite positions down to approximately 130-135 K.

We also observe a Lorentzian peak underlying the (0002) which appears as the moments order into the helical phase. As the temperature decreases, the width of this Lorentzian decreases and the intensity grows, showing a peak in the vicinity of 152 K before decreasing again. This may indicate the presence of critical scattering in the helical-ferromagnetic phase transition, which would be quite unusual. Further experimental work may be able to clarify this situation.

In the ferromagnetic phase, the magnetostriction measurements indicate that the easy magnetic axis changes from the b to the a direction in the basal plane at about 100 K. In principle, this leads to a rotation of the ferromagnetically aligned moments from the b to the a axis in the vicinity of this temperature, which can be observed via neutron diffraction by looking at the $(10\bar{1}0)$ or $(11\bar{2}0)$ reflections. However, in the absence of an applied magnetic field, there will be domain formation such that the domain-averaged intensity would be the same whether the moments lie along the a- or b-axis, making a zero-field measurement insensitive to this transition. It may be possible to apply a field sufficient to form a single domain, yet weak enough to allow the moments to rotate when the sample cools enough. This experiment will be attempted in the future.

Reference

- [1] Spano, M. L.; Clark, A. E.; Teter, J. P.; Cullen, J. R. J. Phys. 49, C8-347 (1988).

ORIENTATION DEPENDENCE OF THE MAGNETIC STRUCTURE IN Dy/Y SUPERLATTICES

F. Tsui, C.P. Flynn, and M. B. Salamon
(University of Illinois at Urbana-Champaign, Urbana, IL)

and

R. W. Erwin and J. J. Rhyne

The dependence of the magnetic structure on growth direction has been investigated in superlattices made from alternating layers of Dy and Y metals. Using new molecular beam epitaxy techniques we have succeeded in growing high quality single crystal materials with structural coherence lengths $> 500 \text{ \AA}$ and with the growth direction oriented along the a, b, or c crystallographic axes. In earlier work we showed that, in c-axis samples, Dy layers order coherently via RKKY-like interactions propagated through Y layers up to about 150 \AA thick [1].

In figure 1 we show neutron diffraction data for a b-axis superlattice $[\text{Dy}_{26}|\text{Y}_9]$. The nuclear superlattice satellites, here enhanced by inducing a ferromagnetic state in the sample, are clearly visible. However, the magnetic scattering is not resolvable into separate superlattice peaks, and

furthermore the width of the magnetic peak suggests that the magnetic coherence is confined to a single Dy layer.

One possible explanation is due to the anisotropy of the interaction length in yttrium as related to the structure of the conduction electron susceptibility $\chi(\mathbf{q})$. Alternatively, the lack of long-range order might be related to frustration effects which could be observed in a compositionally modulated b-axis sample.

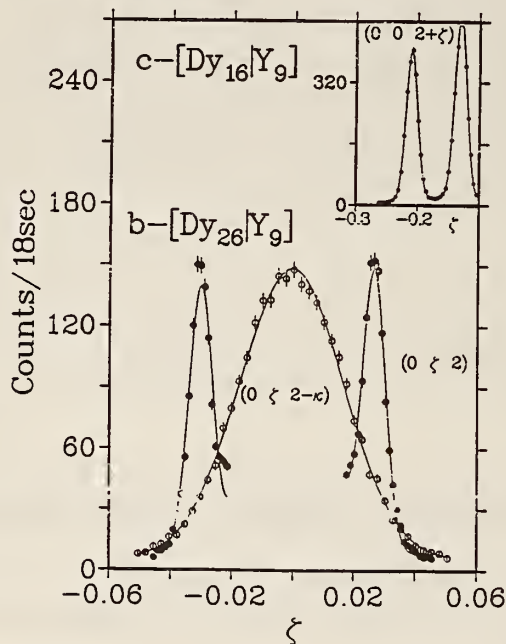


Figure 1. Magnetic and structural peaks of the b-axis superlattice $[Dy_{26}|Y_9]$. The open circles are an $(\xi 0 0 2-\kappa)$ scan across one of the magnetic peaks and the closed circles are an $(\xi 0 0 2)$ scan in a field of 2.5 Tesla to show the structural satellites of $(0 0 0 2)$. The inset shows a comparable scan through a magnetic group of the c-axis superlattice $[Dy_{14}|Y_9]$ having long-range order.

Reference

- [1] Rhyne, J. J.; Erwin, R. W.; Borchers, J.; Sinha, S.; Salamon, M. B.; Du, R.; Flynn, C. P. J. Appl. Phys. 61, 4043 (1987).

REACTOR RADIATION DIVISION AND COLLABORATIVE PROGRAMS
MAGNETOELASTICITY IN RARE-EARTH SUPERLATTICES AND FILMS

R. W. Erwin and J. J. Rhyne

and

J. Borchers, R. Du, M. B. Salamon, and C. P. Flynn
(University of Illinois at Urbana-Champaign, Urbana, IL)

Recently developed techniques for growing epitaxial rare-earth superlattices and thin films have afforded a unique opportunity to study the interactions responsible for the complex magnetic orderings in these materials. In particular, it has been possible to measure the range, strength, and nature of rare-earth exchange interactions by interleaving dissimilar layers of rare earths with and without local magnetic moments [1], thereby fine-tuning the already well developed and successful theoretical framework for rare-earth magnetism [2].

We have been focusing on investigations of the role of magneto-elastic energetics in determining the magnetic structure. These energetics are modified by the constraints imposed by epitaxy of the magnetic lattice to nonmagnetic interlayers and the substrate. Because magnetostriction is large in magnetic rare earths, approaching one percent, we can expect that the role of magnetoelastic energetics in determining the magnetic structure will be emphasized in these highly strained materials.

Neutron diffraction data from a Dy thin film and a [Dy|Y] superlattice are shown in figure 1. These data were collected at the NIST reactor using a beam of 13.5 meV neutrons and wave vector resolution of 0.02 \AA^{-1} at wave vector transfers near 2 \AA^{-1} . The magnetic structure of Dy [3] is a basal-plane helix modulated along the c-axis of the hcp structure. This structure is also found in the films and superlattices. This magnetic order is thus described by the single parameter ω , the precession angle of the basal-plane moments from one atomic plane to the next.

The data for a 4000 Å Dy film shown in figure 1a, are quite similar to those obtained for the bulk material. The helimagnetic structure collapses in a first-order phase transition to a ferromagnetic state just below $T_C = 80 \text{ K}$ (compared to 85 K for the bulk). However, the temperature hysteresis for this transition is about 15 K (compared to 5 K for bulk Dy), and on cooling the transition may require as long as one hour for completion.

The diffraction from a superlattice consisting of bilayers of 16 atomic planes of Dy alternated with 9 atomic planes of Y is compared to the film in figure 1b. Although the initial ordering temperature, T_N , is within 7 K of the bulk and film values (185 K), there is evidently no collapse to the ferromagnetic state down to 5 K. The temperature dependence of ω obtained for the Dy layers is shown in figure 2b for three different superlattices, while the result for bulk Dy is shown in figure 2a for comparison.

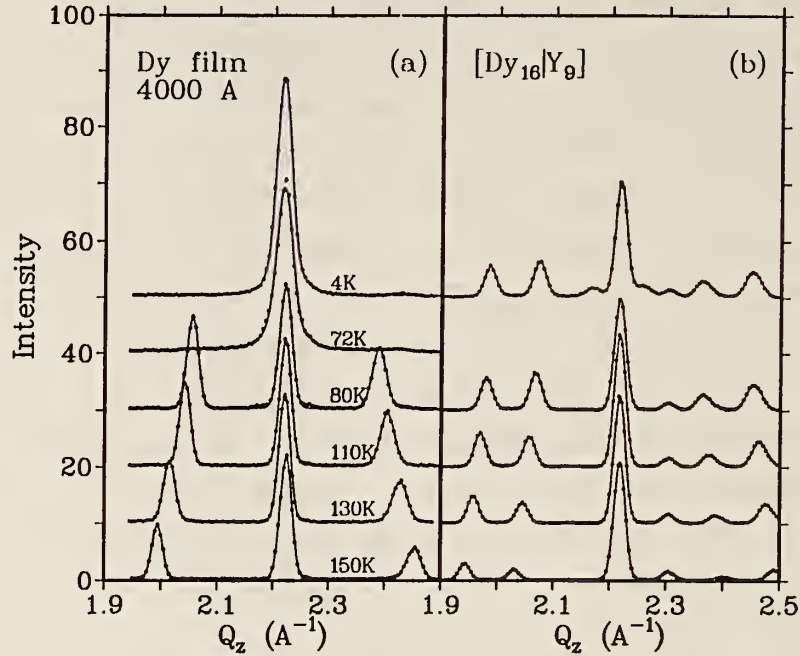


Figure 1. (a) The neutron diffraction scan along the (000ξ) direction determines the magnetic structure in a 4000 Å film as a function of temperature. The intensity associated with the helimagnetic state collapses onto the (0002) Bragg peak below about 80K, but the width of this magnetic scattering is not resolution limited. This zero field ferromagnetic correlation length is about 200 Å. In (b) the same scans at the same temperatures for a $[Dy_{16}|Y_9]$ superlattice show that the ferromagnetic transition is suppressed, although weak magnetic satellites appear about the (0002) position.

As a first step towards understanding the magnetic structure in the Dy films and superlattices, we apply the theories developed to explain the ordering in bulk Dy [2]. The elastic energy is quadratic in the strains and the magnetoelastic energy is linear,

$$f_{me} = \frac{1}{2} (c_{11}^{\alpha} \epsilon_1^2 + c_{22}^{\alpha} \epsilon_2^2 + c_{\gamma}^{\gamma} \epsilon_{\gamma}^2) - K_1 \epsilon_1 - K_2 \epsilon_2 - K_{\gamma} \epsilon_{\gamma} . \quad (1)$$

The c 's are the elastic constants and the K 's are the magnetoelastic coupling parameters in a hexagonal symmetry basis. The magnetoelastic energy obtained experimentally from the elastic constants and the anomalous strains as obtained by Rosen et al. [4], is reproduced in figure 2c. The discontinuous decrease of the magnetoelastic energy at T_c drives the transition by overcoming the exchange energy difference between the ferromagnetic and helimagnetic states. The γ -mode associated with an orthorhombic distortion is the part of the magnetoelastic energy which is primarily responsible for the ferromagnetic transition, and this magnetoelastic energy can only be gained when $\omega = 0$ (the clamping effect).

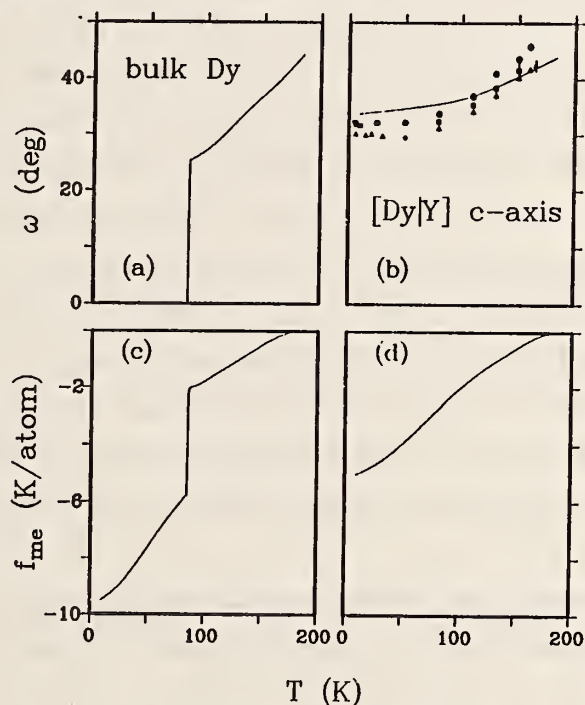


Figure 2. The turn angles, ω , are compared as a function of temperature for bulk Dy (a) and the c-axis superlattices (b). The superlattice values are greater than in the bulk, remaining at or above 30° down to the lowest temperatures. The solid curve in (b) is the calculation for the completely "clamped" film or superlattice. The measured magnetoelastic energy for bulk Dy, obtained from the elastic constants and anomalous strains is shown in (c), while the calculation for the "clamped" material is shown in (d).

Two mechanisms [2] have been proposed to explain the decrease of ω as the temperature is lowered. Either the position of the minimum of the exchange energy shifts, possibly due to the creation of magnetic super-zone gaps, or the temperature and ω dependence of the magnetoelastic energy produces a shift in the minimum of the total energy. The ω dependence of the

magnetoelastic energy arises from the strain derivative of the exchange energy and produces a $\cos\omega$ term. To model the effect of the α -modes on the temperature dependence of ω above T_C we use a parabolic approximation for the exchange energy near ω_0 so the turn angle which minimizes the energy satisfies

$$S^2 J''(\omega_0) (\cos\omega - \cos\omega_0) = K_\omega. \quad (2)$$

The more rapid temperature dependence of the magnetoelastic coefficient K_ω compared to S^2 drives the turn angle towards zero in this model.

At this point we can transfer the analytic result for the exchange of bulk Dy directly to the superlattices. The epitaxial constraints can be built into the equilibrium magnetoelastic energy expression for the c-axis growth direction materials to show that the strains in the growth plane are reduced by the factor $1/(1+r)$, where r is the ratio of nonmagnetic to magnetic material, and the contribution of those strains to the magnetoelastic energy is also reduced by this same factor. The nonmagnetic strain along the z-axis is determined solely by Poisson's ratio, while the magnetic z-axis strain includes the z-axis magnetoelastic contribution K_z/c_{33} .

A calculation of the temperature dependence of ω based on this model is shown in figure 2b, showing a reasonable agreement with the observed values in the superlattices.

The energy difference between the helimagnetic and ferromagnetic states in the superlattice is calculated to be roughly 2 K/atom at 10 K, compared to the 4 K/atom jump at T_C in the bulk. This difference corresponds to a critical field of $2 \text{ K/atom} \approx 3.5 \text{ kOe}$ on $10 \mu_B$. Magnetization measurements in fact show the low temperature critical fields are 3 kOe or less.

The above predictions are in sharp disagreement with the observation for the Dy film where T_C was only suppressed by 5 K. In the ferromagnetic state we have applied a saturating field of 25 kOe along the easy a-axis direction to insure that we are not measuring a domain averaged lattice parameter. The application of the magnetic field was observed to sharpen the (0002) Bragg peak to a resolution limited width, consistent with the formation of a single domain. We then measured the change in the b-axis lattice parameter from just above T_C in zero field to below T_C with the field applied. The resulting anomalous strain was found to be only about 1/3 of the

discontinuity at T_C in bulk Dy. This is a peculiar result since it suggests that the γ -mode driving energy is also reduced by 1/3, yet the ferromagnetic transition still occurs. Furthermore, we found that the Nb buffer layer undergoes no anomalous strains at all. This indicates that anelastic processes are involved, probably at the interface between the rare earths and the Nb.

As the magnetic structures in Er are more complicated than in Dy, so are the theories which attempt to explain them. This makes the transfer of these theoretical ideas to the superlattices and films a more difficult and less certain procedure. For example, the magnetoelastic energy can be treated with the same formalism outlined for Dy. Using the measured elastic constants and anomalous strains in bulk Er, we estimate the magnetoelastic driving energy for the ferromagnetic transition to be 2.2 K/atom in agreement with the original calculation of Rosen et al. [4]. Assuming complete clamping in the growth (basal) plane as before, we find that the magnetoelastic driving energy should be reduced to about 1.4 K/atom. While this might explain qualitatively the suppression of the ferromagnetic transition, it fails to explain quantitatively the magnitude of the critical field measured in the superlattices and films by Borchers et al. [5]. It also doesn't explain the dependence of the critical field on sample thickness observed in these materials [5]. It requires a 1 micron thick film before the energy associated with the critical field becomes roughly equivalent to the calculated magnetoelastic energy for the completely "clamped" material.

In summary, the magnetic structure of Dy films and superlattices when compared to that of bulk Dy suggests that magnetoelastic interactions predominantly control the temperature dependence of the turn angle. Quantitative calculations of the magnetoelastic energies are also in agreement with the observed critical fields in these materials. The energetics determining the magnetic structure in the Er films and superlattices cannot be explained by magnetoelasticity alone, and additional work is in progress on these materials.

References

- [1] Rhyne, J. J.; Erwin, R. W.; Shantanu Sinha; Borchers, J.; Salamon, M. B.; Du, R.; Flynn, C. P. J. Appl. Phys. 61, 4043 (1987); Salamon, M. B.; Shantanu Sinha; Rhyne, J. J.; Cunningham, J. E.; Erwin, R. W.; Borchers, J.; Flynn, C. P. Phys. Rev. Lett. 56, 259 (1986); Erwin, R. W.; Rhyne, J. J.; Salamon, M. B.; Borchers, J.; Shantanu Sinha; Du, R.;

- Cunningham, J. E.; Flynn, C. P. Phys. Rev. B35, 6808 (1987); Majkrzak, C. F.; Gibbs, D.; Boni, P.; Goldman, A. I.; Kwo, J.; Hong, M.; Hsieh, T. C.; Fleming, R. M.; McWhan, D. B.; Yafet, Y.; Cable, J. W.; Bohr, J.; Grimm, H.; Chien, C. L. J. Appl. Phys. 63, 3447 (1988).
- [2] Cooper, B. R. Phys. Rev. Lett. 19, 900 (1967); Phys. Rev. 169, 281 (1968); Evenson, W. E.; Liu, S. H. Phys. Rev. 178, 783 (1969); Elliot, R. J.; Wedgwood, F. A. Proc. Phys. Soc. (London) 81, 846 (1963).
- [3] Wilkinson, M. K.; Koehler, W. C.; Wollan, E. O.; Cable, J. W. J. Appl. Phys. 32, 48S (1961).
- [4] Rosen, M.; Klimer, H. Phys. Rev. B1, 3748 (1970); Rosen, M.; Kalir, D.; Klimer, H. Phys. Rev. B8, 4399 (1973).
- [5] Borchers, J.; Salamon, M. B.; Du, R.; Flynn, C. P.; Erwin, R. W.; Rhyne, J. J. J. de Physique (to be published); Borchers, J.; Salamon, M. B.; Du, R.; Flynn, C. P.; Erwin, R. W.; Rhyne, J. J. J. Appl. Phys. 61, 4050 (1987); J. Appl. Phys. 63, 3458 (1988).

NEUTRON DIFFRACTION STUDIES OF $\text{Cd}_{1-x}\text{Mn}_x\text{Se}$ FILMS AND ZnSe/MnSe MULTILAYERS

T. M. Giebultowicz, P. Klosowski, N. Samarth, H. Luo, and J. K. Furdyna
(University of Notre Dame, Notre Dame, IN)

and

J. J. Rhyne

We have begun neutron diffraction studies of new diluted magnetic semiconductor (DMS) films and superlattices grown by molecular beam epitaxy (MBE). This technique makes possible the preparation of entirely new DMS systems that do not form in the bulk. One of the latest achievements in this field [1] has been the growth of zinc-blende (ZB) type $\text{Cd}_{1-x}\text{Mn}_x\text{Se}$ epilayers on (100) GaAs substrates with Mn concentrations up to $x = 0.75$ and thicknesses up to $2\text{ }\mu\text{m}$. In the bulk form, $\text{Cd}_{1-x}\text{Mn}_x\text{Se}$ can be obtained only in the wurtzite structure with $x \leq 0.50$. In samples with $x = 0.70$ and 0.75 we have observed additional diffraction maxima at low temperatures clearly indicating the Type III antiferromagnetic structure (AF III). This type of order, which is associated with doubling of the crystallographic unit cell along one of the cubic axes, also occurs in two other alloys from the $\text{A}_{1-x}^{\text{II}}\text{Mn}_x\text{B}_{1-x}^{\text{VI}}$ DMS series, $\text{Cd}_{1-x}\text{Mn}_x\text{Te}$ and $\text{Zn}_{1-x}\text{Mn}_x\text{Te}$, which form bulk ZB-type crystals. However, in striking contrast with the short-range nature of the

spin correlations seen in those materials, our data from $\text{Cd}_{1-x}\text{Mn}_x\text{Se}$ epilayers indicate a formation of long-range ordered AF III domains. Such domains have the doubling direction parallel to the epilayer surface, whereas for the third domain orientation the order remains of a short range (see fig. 1). The reasons for such an anisotropic behavior are not yet clear, considering that the epilayers exhibit no significant tetragonal distortion.

Another example of new MBE-grown DMS systems are ZnSe/MnSe multilayers [2]. The Mnse and ZnSe layers grow both in the ZB structure, although bulk MnSe forms only NaCl-type crystals. We have investigated superlattices containing 100-200 ZnSe/MnSe bilayers with thicknesses 60-105 Å, and the MnSe layer thicknesses 22-50 Å. Nuclear diffraction patterns from the multilayers exhibit a number of satellite lines well resolved from the GaAs substrate reflections, in good agreement with theoretical calculations. At low T we have observed additional peaks, clearly indicating an AF III spin structure in the MnSe layers. However, in contrast to the behavior observed in the $\text{Cd}_{1-x}\text{Mn}_x\text{Se}$ epilayers, the tetragonal axes of the domains are oriented in the direction perpendicular to the layers. The magnetic reflections were strongly broadened in the growth directions, showing that the AF III order does not propagate through the non-magnetic ZnSe layers, which is consistent with the short-range nature of the exchange interactions in a semiconducting crystal. The data obtained from supperlattices with MnSe thickness 22 Å (i.e., corresponding to about 7 nanomolecular layers) exhibit no indication of antiferromagnetic order breakdown which is expected in the 2D limit, confirming previous conclusions that films with such thicknesses can be still treated as three-dimensional systems.

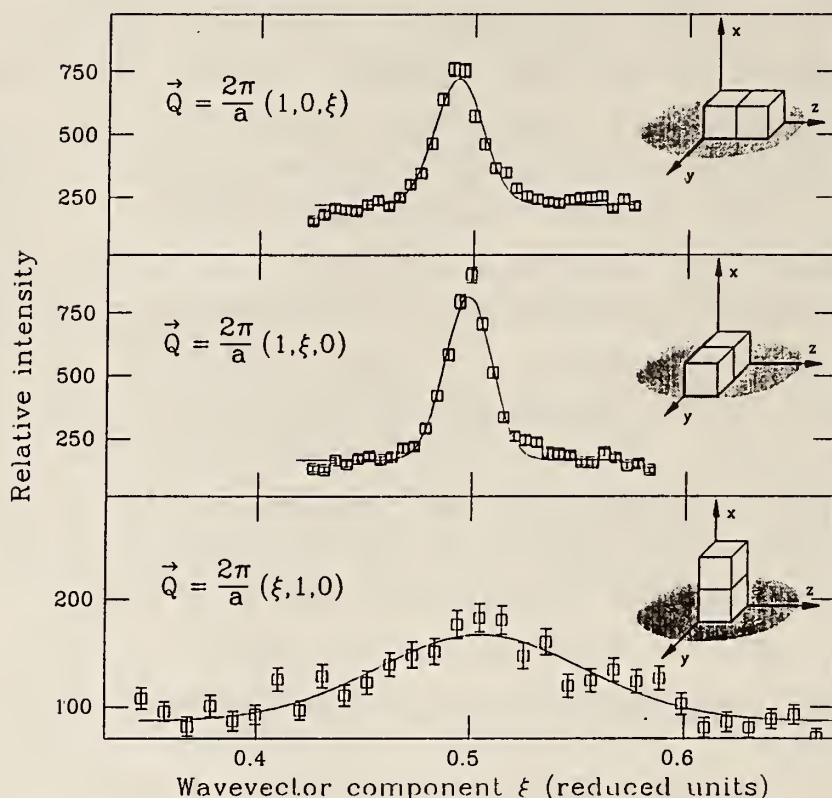


Figure 1. Diffraction scans through AF III reflection points $(10\frac{1}{2})$, $(1\frac{1}{2}0)$, and $(\frac{1}{2}10)$ for a $\text{Cd}_{0.3}\text{Mn}_{0.7}\text{Se}$ epilayer at 4.2 K. The three points correspond to AF III domains with the doubling directions oriented, respectively, along the z, y, and x crystallographic axes, as shown in the insets. Note the striking difference between the the peak widths and intensities for the in-plane and normal-to-the-plane domain orientations.

References

- [1] Samarth, N.; Luo, H.; Furdyna, J. K. Appl. Phys. Lett. (in press).
- [2] Kolodziejwski, L. A.; Gunshor, L. A.; Otsuka, N.; Gu, B. P.; Hefetz, Y.; Nurmikko, A. V. *ibidem*, 47, 1482 (1986).

EXCHANGE INTERACTIONS IN Co-BASED II-VI DILUTED MAGNETIC SEMICONDUCTORS

T. M. Giebultowicz, P. Klosowski, and J. K. Furdyna
(University of Notre Dame, Notre Dame, IN)

and

J. J. Rhyne and T. J. Udovic

The nature of the basic magnetic exchange interactions between substitutional magnetic ions in host semiconducting lattices (such systems are referred to as Diluted Magnetic Semiconductors (DMS)) continues to receive strong attention from both experimentalists and theorists. Significant progress has been recently made [1,2] in understanding the Mn-Mn interaction in DMS materials belonging to the $A_{1-x}^{II}Mn_xB^{VI}$ class (where $A^{II} = \text{Zn, Cd, or Hg}$, and $B^{VI} = \text{S, Se, or Te}$; e.g., $\text{Cd}_{1-x}\text{Mn}_x\text{Te}$, or $\text{Zn}_{1-x}\text{Mn}_x\text{Se}$). In contrast, very little is still known about the exchange interactions in II-VI DMS alloys containing transition metal atoms other than Mn. Progress in experimental studies of such systems has been limited due to the lack of high quality crystals. However, new opportunities have opened up in this field thanks to recent developments in sample preparation techniques. For instance, the use of high-pressure inert gas furnaces, as well as the adaptation of ceramic techniques, have made it possible to prepare an entirely new line of Co-based II-VI DMS compounds.

We have carried out the first direct measurements of the nearest-neighbor (NN) antiferromagnetic exchange constant J_{NN} in three of the new alloys ($\text{Zn}_{1-x}\text{Co}_x\text{S}$, $\text{Zn}_{1-x}\text{Co}_x\text{Se}$, and $\text{Zn}_{1-x}\text{Co}_x\text{Te}$) using neutron scattering methods. Measurements performed on samples with $x = 0.01 - 0.06$ at low T revealed distinct inelastic scattering maxima corresponding to transitions between the excited states of isolated NN Co-Co pairs. In II-VI lattices the orbital momentum of the Co^{2+} ion ($L = 3$) is quenched by the tetrahedral crystal field, and the Co-Co interaction can be treated, to a very good approximation, as a Heisenberg-type exchange between two $S = 3/2$ spins. Such a pair, normally possessing a ground state with total spin $S_T = 0$, has three excited levels with $S_T = 1, 2$, or 3 , and with energies $2J_{\text{NN}}$, $6J_{\text{NN}}$, and $12J_{\text{NN}}$, respectively. The selection rules for neutron scattering allow transitions between adjacent levels only ($\Delta S_T = \pm 1$), so that the inelastic maxima occur at $E = 2J_{\text{NN}}$, $4J_{\text{NN}}$, and $6J_{\text{NN}}$. One of the clear signatures of this process is the temperature behavior of the maxima. At low T the excited levels are not

populated, and one observes only a single maximum at $E = 2J_{NN}$ corresponding to a transition from the ground state to the first excited state ($|0\rangle \rightarrow |1\rangle$). As T is raised, the population of the $S_T = 1$ level gradually increases, giving rise to a $|1\rangle \rightarrow |2\rangle$ peak at $E = 4J_{NN}$. At the same time, the first maximum decreases in intensity. An example of the $Zn_{1-x}Co_xS$ data illustrating such behavior is displayed in figure 1. From the positions of the $|0\rangle \rightarrow |1\rangle$ maxima we have established that the J_{NN} values for the three systems investigated are 4.1 ± 0.05 , 4.2 ± 0.1 , and 3.3 ± 0.1 meV, respectively. The exchange interaction in all three systems is decidedly stronger, and exhibits a different chemical trend than the interactions in their Mn-based counterparts. This latter fact cannot be understood in light of the presently existing theory of II-VI DMS systems [1].

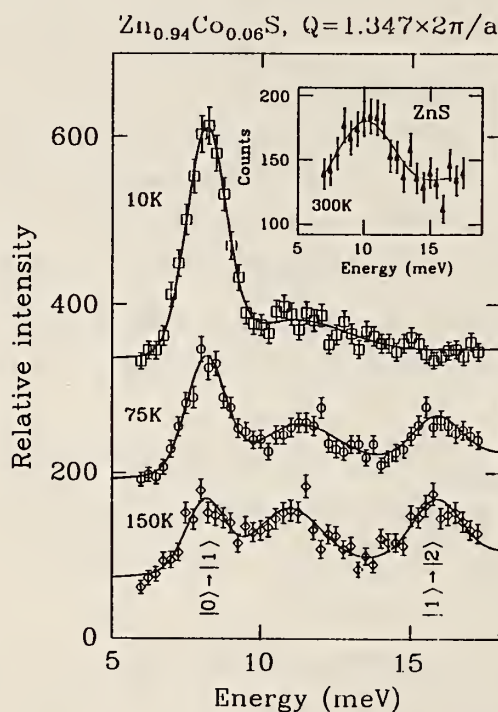


Figure 1. Inelastic scattering spectra from polycrystalline $Zn_{0.94}Co_{0.06}S$ at three different temperatures, showing the $|0\rangle \rightarrow |1\rangle$ and $|1\rangle \rightarrow |2\rangle$ transition peaks from NN Co-Co pairs. The broad feature at $E \approx 11$ meV, which is seen also in pure ZnS (see the inset), can be attributed to phonon scattering.

References

- [1] Larson, B. E.; Hass, K. C.; Ehrenreich, H.; Carlsson, A. E. Rev. B37, 4137 (1988).
- [2] For review of experimental studies of Mn-based II-VI DMS, see, eg., Fudyna, J. K. J. App. Phys. 64, R29 (1988).

CHARACTERIZATION OF THE QUASICRYSTALLINE STATE OF $\text{Al}_{73}\text{Mn}_{21}\text{Si}_6$
FROM NEUTRON SCATTERING EXPERIMENTS

A. Goldman
(Iowa State University, Ames, IA)

M. Bessiere, Y. Calvayrac, D. Gratias, S. Lefebvre, and A. Quivy
(C.E.C.M./C.N.R.S. Vitry, France)

and

B. Mozer

Neutron scattering experiments were used to help characterize the magnetic state observed at low temperatures in the icosahedral phase of the alloy $\text{Al}_{73}\text{Mn}_{21}\text{Si}_6$ which was prepared at C.E.C.M./C.N.R.S., Vitry. Measurements were performed at the NIST research reactor on the powder diffraction instrument, BT-1, at room temperature and at low temperature below the magnetic transition to observe if there were any changes in the relative intensities of the diffraction peaks. The diffraction peaks observed for this alloy show narrow peaks but they still exhibit evidence of disorder. Preliminary analysis of the data indicates no significant changes in the peak intensities associated with the magnetic ordering and do not show any evidence of new peaks which might indicate a possible ferro- or antiferromagnetic transition. Polarized neutron scattering experiments were then performed on the triple-axis spectrometer H8 at Brookhaven National Laboratory using polarized neutrons and polarization analysis. The spectrometer was used in the spin-flip mode of operation so as to observe only the magnetic contribution to the scattering from our powder sample. The collimation of the instrument and the incoming energy were chosen so as to insure that all energies of the scattered neutrons were included in the acceptance angles of the analyzer-detector when used in the elastic scattering mode.

Spin-flip measurements were taken on the sample at temperatures of 9 K and 150 K as a function of the wave vector difference (q) for values of q from 0.40 to 2.84 \AA^{-1} . A spin-flip measurement at constant q , 0.40, as a function of the temperature was taken for temperatures from 9 K to 280 K. Figure 1 shows the form factor for the magnetic scattering of our icosahedral alloy at the two different temperatures. The form factor at the lowest temperature is the same as that measured by one of us [1] on the icosahedral

alloy Al_4Mn . This form factor is very different from that observed for manganese in metal alloys or compounds. The higher temperature form factor is much different than would be expected for a paramagnetic scatterer as observed by K. R. A. Ziebeck and P. J. Brown [2] and still seems to show some magnetic ordering.

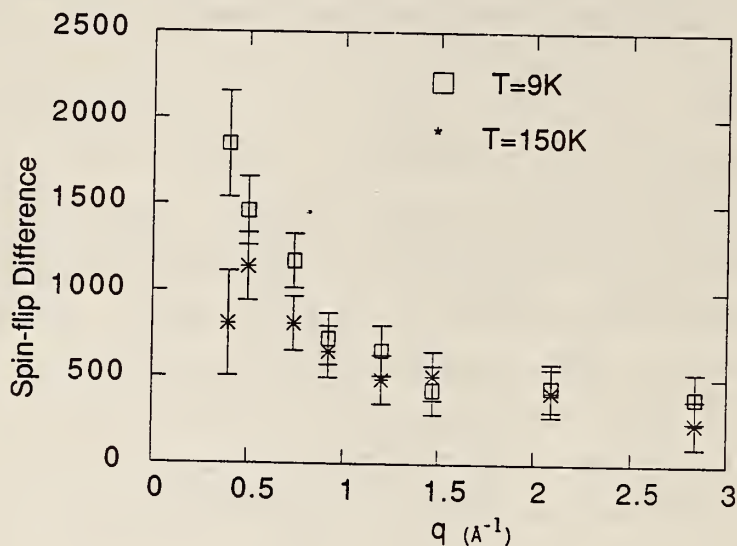


Figure 1. The spin-flip differential scattering from the icosahedral phase of $\text{Al}_{73}\text{Mn}_{21}\text{Si}_6$ as a function of $q = 4\pi\sin\theta/\lambda$ at 9 K and 150 K.

References

- [1] Goldman, A.; Zabel, H. private communication.
- [2] Ziebeck, K. R. A.; Brown, P. J. J. Phys: Metal Phys. 10, 2015 (1980).

ANTIFERROMAGNETIC ORDER IN $\text{YBa}_2\text{Cu}_{3-x}\text{Co}_x\text{O}_{6+y}$

P. F. Miceli, J. M. Tarascon, L. H. Greene, P. Barboux, and M. Giroud
(Bell Communications Research, Red Bank, NJ)

and

D. A. Neumann and J. J. Rhyne

and

L. F. Schneemeyer and J. V. Waszczak
(AT&T Bell Laboratories, Murray Hill, NJ)

While the mechanism responsible for superconductivity in the high temperature superconducting oxides is still not understood, current theories suggest that electron pairing may arise from antiferromagnetic correlations. This viewpoint is supported by the discovery of long-range antiferromagnetic order in the nonsuperconducting parent compounds, $\text{La}_2\text{CuO}_{4-y}$ and YBaCu_3O_6 , which suggests that antiferromagnetic correlations may indeed exist in the superconducting phases. It is therefore of interest to understand how substitutions for Cu, particularly by other magnetic ions such as Co, affect the magnetic properties of the parent compounds. Thus we have undertaken a neutron diffraction study of magnetic order in oxygen deficient $\text{YBa}_2\text{Cu}_{3-x}\text{Co}_x\text{O}_{6+y}$ for two powder samples, one with $x = 0.2$ and $y = 0.45$, and the other having $x = 0.8$ and $y = 0.91$.

The results show that the $x = 0.2$ sample orders antiferromagnetically in a two step process. Below $T_l \approx 211$ K, $(\frac{1}{2}\frac{1}{2}\ell)$ reflections exist for both integral and half-integral values of ℓ (fig. 1a). For temperatures between T_l and a second transition at $T_u \approx 415$ K, only peaks corresponding to integral ℓ remain (fig. 1b). Above T_u long-range magnetic order disappears. The appearance of $(\frac{1}{2}\frac{1}{2}\ell)$ reflections is characteristic of a structure consisting of antiferromagnetic sheets ordered with spins alternately along $[110]$ and $[\bar{1}\bar{1}0]$, while the absence of a $(\frac{1}{2}\frac{1}{2}0)$ peak indicates that the net spin is zero when summed along the c-axis. In order to further determine the stacking of the antiferromagnetic sheets, structure factor calculations have been performed for the 5 K data. For integral ℓ , the best fit to the observed intensities was obtained using a model in which the moment on the single "chain" site is zero, while the moments on the two "plane" sites are $0.41 \mu_B$. The stacking sequence can then be represented as $+0 - +0 -$ where

the + and - refer to the moments on the "plane" sites. For half-integral ℓ it was necessary to also include a nonzero moment on the "chain" site and an angle of $\approx 111^\circ$ between the spins on the different types of sites in order to obtain an acceptable fit to the observed intensities. The stacking sequence can then be represented as $+r + -r'$ - where the + and - again refer to the spins on the "plane" sites and r refers to the moment on the "chain" site which has been rotated in the basal plane (r' denotes a spin which is antiparallel to that denoted by r). The best fit moments were $0.18 \mu_B$ and $0.62 \mu_B$ for the "plane" and "chain" sites respectively. The total magnetic structure for the $x = 0.2$ sample is then simply the vector sum of the structures determined for the above two cases.

A substantially different magnetic structure is found for the $x = 0.8$ sample. Here only half-integral ℓ peaks are observed between 5 K and a single magnetic transition at $T_1 \approx 435$ K (fig. 2). This immediately implies that the moments on the two types of sites are equal. An excellent fit to the intensities measured at 5 K was obtained for a moment of $0.68 \mu_B$ and a simple stacking of $+--+--$.

Thus the presence of Co substantially alters the antiferromagnetic structure of oxygen deficient $\text{YBa}_2\text{Cu}_{3-x}\text{Co}_x\text{O}_{6+y}$ by enhancing the half-integral ℓ type of ordering. This implies an increased magnetic coupling between the "plane" and "chain" sites upon the substitution of Co, which resides principally on the "chain" sites. However, it is not possible to decouple the effects of O concentration from those due to differing Co concentrations with the present data. Further studies are planned to clarify the effects of O concentration on the magnetic properties of these materials.

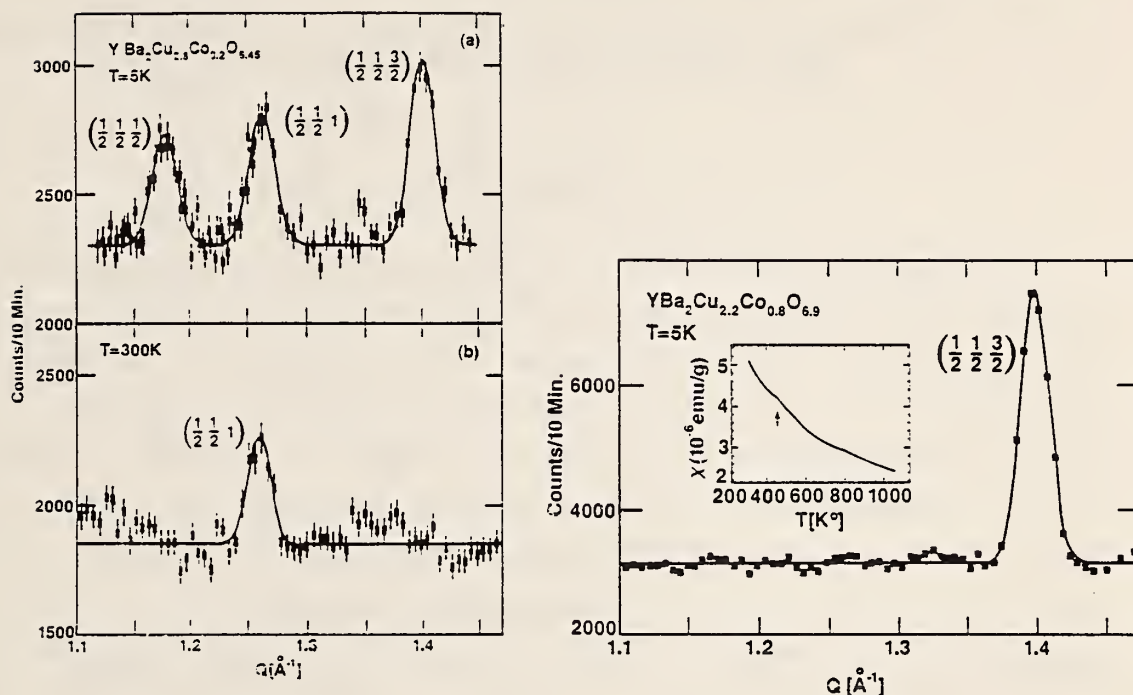


Figure 1. (left) Antiferromagnetic diffraction peaks for $\text{YBa}_2\text{Cu}_{2.8}\text{Co}_{0.2}\text{O}_{6.45}$. (a) The occurrence of peaks of the form $(1/2, 1/2, l')$ where l' is half integral indicates the occurrence of antiferromagnetic spin ordering on the chain Cu,Co-O sites below $T_1 \approx 211 \text{ K}$ in addition to order on the Cu-O plane sites manifested by the integral l $(1/2, 1/2, l)$ peaks. (b) At temperatures above T_1 , but below the upper Néel temperature $T_u \approx 415 \text{ K}$, only integral l peaks occur indicating that the chain site moments have become disordered. Within each Cu-O layer (chain or plane) spins are oriented antiparallel with a propagation vector along $[110]$.

Figure 2. (right) In the more full Co substituted compound $\text{YBa}_2\text{Cu}_{2.2}\text{Co}_{0.8}\text{O}_{6.9}$ only half-integral l' peaks are observed over the full temperature range below $T_N \approx 435 \text{ K}$. This indicates that the additional Co has enhanced the exchange coupling and produces essentially similar moments on both chain and plane sites.

OXYGEN DEPENDENCE OF THE MAGNETIC PHASE TRANSITIONS IN $\text{YBa}_2\text{Cu}_{2.8}\text{Co}_{0.2}\text{O}_{6+y}$

P. F. Miceli, J. M. Tarascon, P. Barboux, L. H. Greene, and M. Giroud
(Bell Communications Research, Red Bank, NJ)

and

D. A. Neumann and J. J. Rhyne

A complete understanding of high-temperature superconductivity must include the interesting magnetic properties of the Cu oxide based superconductors, which are either superconducting or antiferromagnetic depending on the composition. An important tool for probing the basic physical properties, in particular the magnetic properties, of these systems is the isomorphous substitution of magnetic ions such as Co for Cu. Previous work has shown that Co preferentially occupies the "chain" site in these materials [1] and that two antiferromagnetic transitions exist for $y = 0.45$ corresponding to magnetic ordering first on the "plane" sites (AF1) followed by ordering on the "chain" sites as well as the "planes" (AF2) [2]. At higher oxygen concentrations the samples become superconducting. Thus, this system exhibits all of the essential magnetic and superconducting features which are present in the parent compound $\text{YBa}_2\text{Cu}_3\text{O}_{6+y}$. We have therefore performed neutron scattering studies in order to determine the oxygen dependence of these transitions in $\text{YBa}_2\text{Cu}_{2.8}\text{Co}_{0.2}\text{O}_{6+y}$.

These experiments were performed on six powder samples, each weighing about 10 grams, prepared by standard solid-state reaction techniques. Powder diffraction measurements were performed using the BT-1 spectrometer which allowed the determination of the O content to ± 0.02 using Rietveld analysis. The magnetic structures were then determined as a function of temperature using the triple-axis spectrometers at BT-2 and BT-9. AC susceptibility showed that only the sample with $y = 1.0$ was superconducting with a $T_c = 60$ K.

The oxygen dependence of the two magnetic phase transitions determined from the temperature dependence of the whole and half integer ℓ is shown in figure 1. Here T_{N_1} and T_{N_2} refer to the transition to the antiferromagnetic phase which displays "plane" site ordering only (integer ℓ) and to the phase which displays ordered moments on both "chain" and "plane" sites (half-integer ℓ), respectively. The solid and dashed lines serve as guides to the eye; however, the dashed lines are not intended to be used for interpolation.

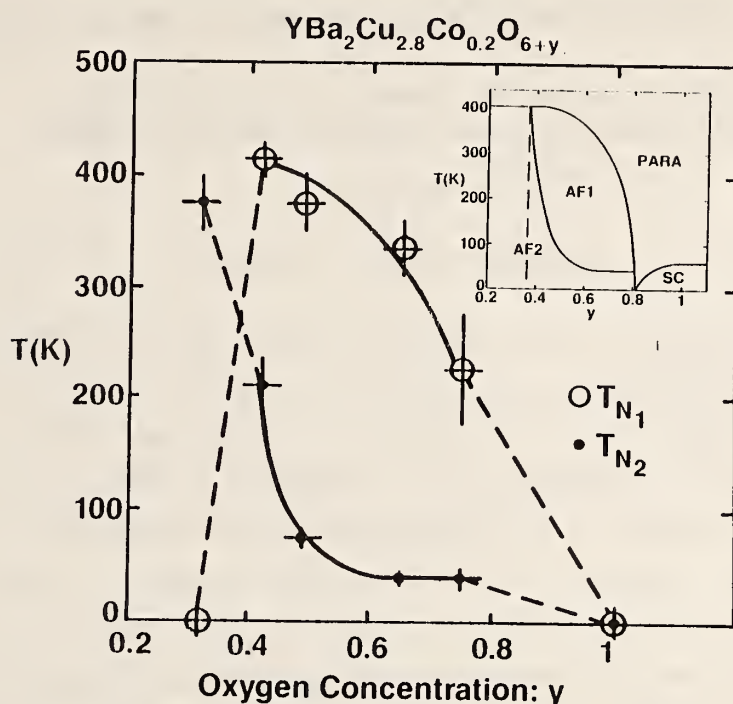


Figure 1. Oxygen dependence of the two magnetic phase transition temperatures in $\text{YBa}_2\text{Cu}_{2.8}\text{Co}_{0.2}\text{O}_{6+y}$. The results are presented schematically in the inset.

It is seen that both transition temperatures increase with decreasing oxygen content until $y = 0.32$ where both "chains" and "planes" order at a single temperature. No magnetic ordering has been found at $y = 1$. The inset is a schematic diagram showing the regions of paramagnetic (PARA), superconducting (SC), and antiferromagnetic behavior. We have also performed a similar experiment on a sample with a Co concentration of 0.8 which displayed only half-integer ℓ peaks for all O concentrations [2]. Thus the effect of adding Co is to raise the "chain" site ordering temperature T_{N1} until $T_{N1} = T_{N2}$. These results provide a direct test for theoretical models which make predictions concerning the electronic and magnetic interactions in these materials.

References

- [1] Miceli, P. F.; Tarascon, J. M.; Greene, L. H.; Barboux, P.; Rotella, F. J.; and Jorgensen, J. D.; Phys. Rev. **B37**, 5932 (1988).
- [2] Miceli, P. F.; Tarascon, J. M.; Greene, L. H.; Barboux, P.; Giroud, M.; Neumann, D. A.; Rhyne, J. J.; Schneemeyer, L. F.; and Waszczak, J. V.; Phys. Rev. **B38**, 9209 (1988).

MAGNETIC PROPERTIES OF $\text{Bi}_2\text{A}_2\text{T}_2\text{O}_6$: A = MSr,Ca AND T = Co,Mn

P. F. Miceli, J. M. Tarascon, P. Barboux, G. W. Hull, and L. H. Greene
(Bell Communications Research, Red Bank, NJ)

and

J. J. Rhyne and D. A. Neumann

$\text{Bi}_2\text{Sr}_2\text{CuO}_6$ belongs to the general class of high-temperature superconductors of the form $\text{Bi}_2\text{Sr}_2\text{Ca}_{n-1}\text{Cu}_n\text{O}_y$ with $n = 1, 2, 3$ where n is the number of CuO_2 layers. Antiferromagnetic interactions are believed to be important to all Cu oxide superconductors; however, unlike $\text{La}_{2-x}\text{Sr}_x\text{CuO}_{4-y}$ and $\text{YBa}_2\text{Cu}_3\text{O}_{6+y}$, there has been no clear experimental verification of a crossover from antiferromagnetic order to superconductivity in the Bi based Cu oxide systems due to the difficulties in varying the composition of these materials. Therefore we have begun neutron scattering studies of $\text{Bi}_2\text{Sr}_2\text{CoO}_6$, $\text{Bi}_2\text{Sr}_2\text{MnO}_6$, and $\text{Bi}_2\text{Ca}_2\text{MnO}_6$ to investigate the magnetic properties, which directly reflect the electronic structure, of this general class of compounds. These materials also exhibit a structural modulation and it is of considerable fundamental interest to understand how the modulation impacts the magnetic properties. Recent magnetic susceptibility studies have suggested the presence of weak ferromagnetic and/or spin canting behavior.

The magnetic neutron diffraction results obtained by subtracting high temperature data from that at 6 K are shown in figures 1-3. The intensities of the peaks can be reproduced with simple spin structures. For $\text{Bi}_2\text{Sr}_2\text{CoO}_6$, the spins are antiferromagnetically ordered in the a-b plane, while in both of the Mn compounds, the spins are antiferromagnetically ordered along the c-axis. These powder diffraction results suggest that there is an average spin structure in these compounds which is unaffected by the modulation. In contrast, very recent measurements performed on single crystals of $\text{Bi}_2\text{Sr}_2\text{MnO}_6$ have shown an interesting field dependence as well as very weak magnetic satellite peaks which indicates that the average spin structure is indeed perturbed by the modulation.

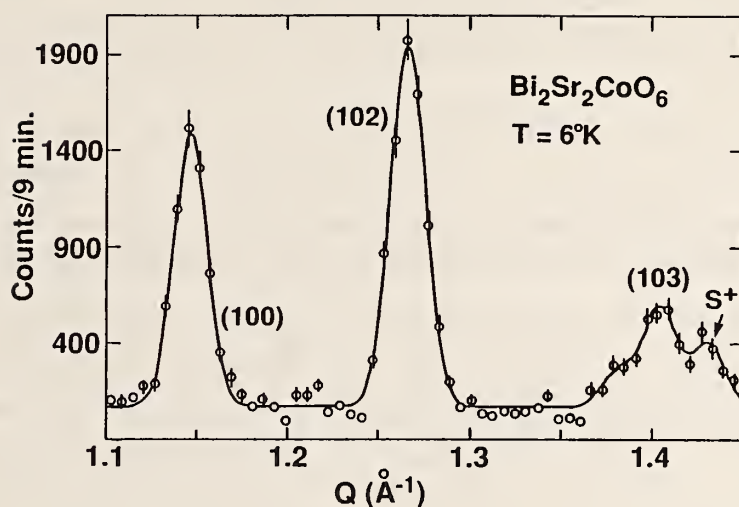


Figure 1. Magnetic neutron diffraction scan for $\text{Bi}_2\text{Sr}_2\text{CoO}_6$ at 6 K.

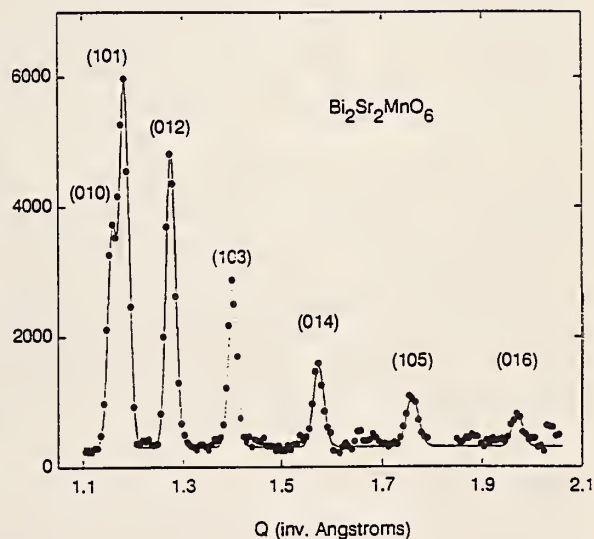
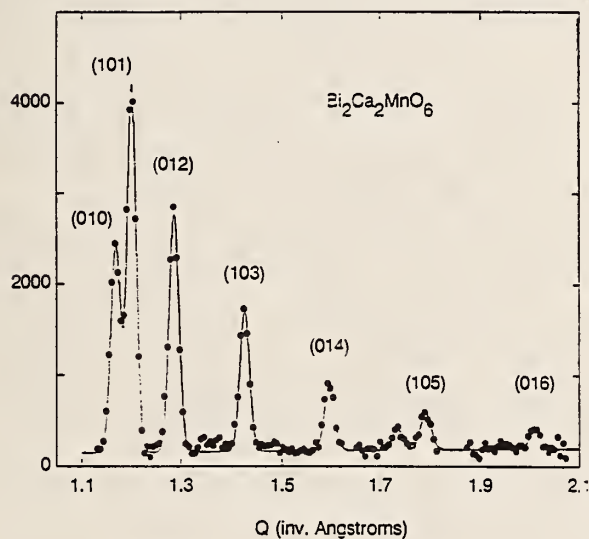


Figure 2. (left) Magnetic neutron diffraction scan for $\text{Bi}_2\text{Ca}_2\text{MnO}_6$ at 6 K.

Figure 3. (right) Magnetic neutron diffraction scan for $\text{Bi}_2\text{Sr}_2\text{MnO}_6$.

THE DEFECTIVE STRUCTURES OF $\text{Ba}_2\text{YCu}_3\text{O}_{6+x}$ AND $\text{Ba}_2\text{YCu}_{3-y}\text{M}_y\text{O}_{6+z}$ (M = Fe, Co, Al, Ga)

A. Santoro

A knowledge of the oxygen distribution in the basal planes of $\text{Ba}_2\text{YCu}_3\text{O}_{6+x}$ and $\text{Ba}_2\text{YCu}_{3-y}\text{M}_y\text{O}_{6+z}$ is a prerequisite to an understanding of the superconducting properties of these materials. Models for the oxygen ordering and the defect structure in $\text{Ba}_2\text{YCu}_3\text{O}_{6+x}$ and $\text{Ba}_2\text{YCu}_{3-y}\text{M}_y\text{O}_{6+z}$ may be derived from a study of the twinning present in the orthorhombic phase of these compounds, from an analysis of the possible structures at the twin boundaries, from the coordinations available to the copper and M ions for various models, etc. It has been shown [1] that the twin laws operating in this system are $(110)_m$, $(1\bar{1}0)_m$, and $[001]_{90^\circ}$ and that there is a strong relationship between twin boundaries and the oxygen stoichiometry. In addition, it seems that the most probable structure of the twin walls is one in which the copper ions at the boundary have a distorted tetrahedral coordination. By eliminating from this model the oxygen atoms so that small chains with different crystallographic orientations are formed, it is possible to derive configurations for the defect oxygen compositions in which the number of copper ions in three-fold coordination is minimized, or reduced to zero. Similar considerations, and essentially the same oxygen configurations, are used to build models of the defect structures of the M substituted compounds, $\text{Ba}_2\text{YCu}_{3-y}\text{M}_y\text{O}_{6+z}$. In these cases, the type and the degree of the substitution depend very strongly on the size and the coordination of the M cations replacing the copper ions on the basal plane.

Reference

- [1] Hodeau et al. Solid State Commun. 64, 1349-1352 (1987).

MAGNETIC ORDER OF Nd IN $\text{NdBa}_2\text{Cu}_3\text{O}_{6+x}$

W.-H. Li and J. W. Lynn
(University of Maryland, College Park, MD and Reactor Radiation Division)

R. W. Erwin

and

K. N. Yang, J. M. Ferreira, B. W. Lee, and M. B. Maple
(University of California San Diego, La Jolla, CA)

The nature of the magnetic ordering of the rare earth ions R in the $\text{RBa}_2\text{Cu}_3\text{O}_{6+x}$ system and the identity of the dominant interaction, exchange or dipolar, has become somewhat controversial. Specific heat measurements [1] on the Nd system show that at full oxygen stoichiometry ($x = 1$) the anomaly associated with magnetic ordering at $T_N \approx 0.5$ K can be analyzed quantitatively on the basis of the 2-d anisotropic Ising model, indicating that the interactions are highly anisotropic, while at $x \sim 0$ the anomaly is much broader, and occurs at a temperature which is three times higher. In the related Er system we have recently shown [2] that the magnetic interactions are indeed 2-d in nature, even though 3-d Bragg peaks are observed below the Néel temperature.

To determine the spin configuration of the Nd ordering in this system, neutron powder diffraction measurements were taken on a standard triple-axis spectrometer, with the conventional experimental setup of employing a pyrolytic graphite PG(002) monochromator and PG filter, and a wavelength of 2.355 Å. The sample was mounted in a top-loading dilution refrigerator with a low temperature capability of ~ 25 mK. A complete magnetic diffraction pattern was obtained by using the subtraction technique, in which data taken at high temperatures are subtracted from data taken well below T_N : only the magnetic contribution to the scattering will survive the subtraction procedure.

The data obtained are quite similar to other systems we have studied recently, and hence we will only summarize the results. The observed widths of the magnetic peaks are consistent with the instrumental resolution, thus indicating that the system exhibits 3-d long-range magnetic order, with the magnetic unit cell just double the chemical unit cell along all three crystallographic directions. This is a simple magnetic structure in which nearest neighbor spins in all three directions are aligned antiparallel, and

is the same type of structure which has been found for the Dy [3], Gd [4], and Pr[5] systems. The low-temperature ordered moment we obtain from our data is $\langle \mu_z \rangle = (1.07 \pm 0.07) \mu_B$, with the direction along the c-axis. This value is substantially smaller than the free-ion moment of $2.14 \mu_B$ for Nd^{3+} .

The antiferromagnetic transition temperature is also very sensitive to the value of the oxygen concentration, as shown in figure 1. The shape of the intensity versus temperature curves are very similar for the two samples, and yields an estimate for the critical exponent $\beta \sim 1/3$, typical for a 3-d transition, but the ordering temperature varies by a factor of three between the two samples. Crystal field effects could no doubt be important in causing this behavior, and inelastic neutron scattering measurements as a function of x are planned to determine the crystal field splittings in this system.

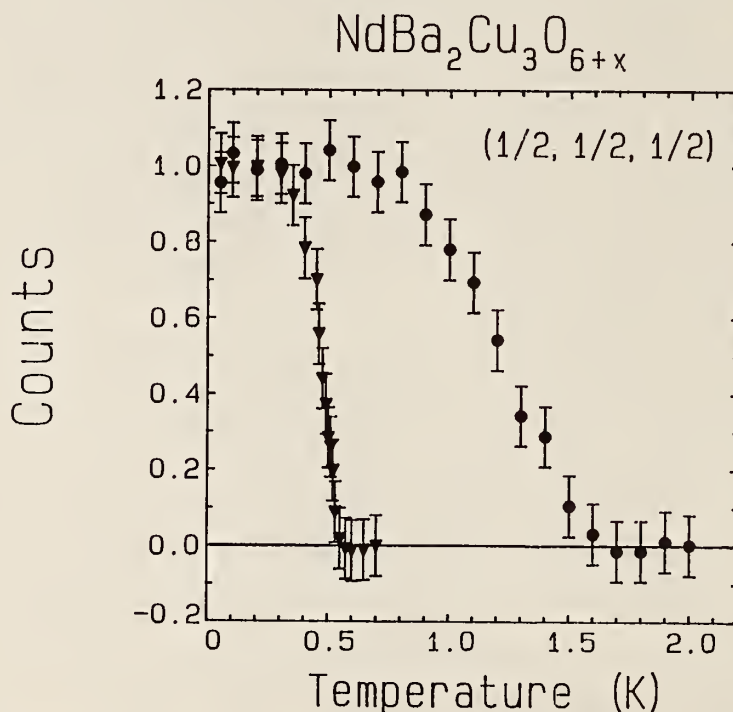


Figure 1. Temperature dependence of the $\{1/2 \ 1/2 \ 1/2\}$ peak intensity, showing the variation of the square of the staggered magnetization with temperature. The Néel temperature for the system with $x = 0.9$ (triangles) is $\sim 1/2$ K, while T_N for $x = 0.3$ (solid circles) is 1.5 K.

References

- [1] Yang, K. N.; Ferreira, J. M.; Lee, B. W.; Maple, M. B.; Li, W.-H.; Lynn, J. W.; Erwin, R. W. (submitted for publication).

- [2] Lynn, J. W.; Clinton, T. W.; Li, W.-H.; Erwin, R. W.; Liu, J. Z.; Shelton, R. N.; Klavins, P. (to be published); Lynn, J. W.; Li, W.-H.; Li, Q.; Ku, H. C.; Yang, H. D.; Shelton, R. N. Phys. Rev. B36, 2374 (1987).
- [3] Goldman, A. I.; Yang, B. X.; Tranquada, J.; Crow, J. E.; Jee, C.-S. Phys. Rev. B36, 7234 (1987).
- [4] Paul, D. McK.; Mook, H. A.; Hewat, A. W.; Sales, B. C.; Boatner, L. A.; Thompson, J. R.; Mostoller, M. Phys. Rev. B37, 2341 (1987). Chattopadhyay, T.; Maletta, H.; Wirgen, W.; Fischer, K.; Brown, P. J. Phys. Rev. B38, 838 (1988). Mook, H. A.; Paul, D. McK.; Sales, B. C.; Boatner, L. A.; Cussen, L. Phys. Rev. B38, 12008 (1988).
- [5] Li, W.-H.; Lynn, J. W.; Skanthakumar, S.; Clinton, T. W.; Kebede, A.; Crow, J. E.; Mihalisin, T. Phys. Rev. B: (*Rapid Communications*), (to be published).

TWO- AND THREE-DIMENSIONAL MAGNETIC BEHAVIOR OF Er IN $\text{ErBa}_2\text{Cu}_3\text{O}_7$

J. W. Lynn, T. W. Clinton, and W.-H. Li
(University of Maryland, College Park, MD and Reactor Radiation Division)

R. W. Erwin

J. Z. Liu and K. Vandervoort
(Argonne National Laboratory, Argonne, IL)

and

R. N. Shelton
(University of California, Davis, CA)

The magnetic properties of the rare earth ions R in the $\text{RBa}_2\text{Cu}_3\text{O}_7$ superconductors are of interest because of experiments which have shown that the superconductivity is not significantly affected by the substitution of several rare earth ions [1-2]. The $\text{RBa}_2\text{Cu}_3\text{O}_7$ materials order antiferromagnetically, where the system is orthorhombic and superconducting. The magnetic interactions are very weak, yielding ordering temperatures ($T_N \sim 1$ K) well below the superconducting transition temperature ($T_C \sim 92$ K), making these materials good examples for investigating the competing interactions of superconductivity and magnetism. The first neutron experiments on $\text{ErBa}_2\text{Cu}_3\text{O}_7$ [3] powder showed a magnetic phase transition at $T_N \sim 0.6$ K, which agreed with the specific heat data [4-5]. The Er moments exhibited a two-dimensional character in the a-b plane, while there were no significant

magnetic correlations detected along the c-axis down to the lowest temperatures achieved (0.33 K). This anisotropic behavior was expected since the interactions are primarily dipolar in origin, and the spacing between Er ions along the c-axis is three times longer than along the a-b directions. Additional powder measurements found that the system ordered three dimensionally at lower temperatures (140 mK).

Recently we have made measurements on a high quality single crystal. Above the 3-d ordering temperature ($T_N = 0.618$ K) we observe a rod of scattering along $(1/2, 0, \ell)$ which demonstrates the expected strong anisotropy of the magnetic interactions and the concomitant 2-d character of the system. Figure 1 shows three scans through the rod and one scan along the rod just above the 3-d ordering temperature. The scans through the rod have a width which is limited by the instrument resolution, while the scan along the rod shows that there are no significant spin correlations between adjacent a-b layers.

Below the 3-d Néel temperature we find that two magnetic structures can occur at low T, one characterized by a wave vector $(1/2, 0, 0)$ and the other by $(1/2, 0, 1/2)$. The spin structure for the $(1/2, 0, 1/2)$ configuration consists of ferromagnetic chains of spins along the b direction, with adjacent chains in the a-b plane coupled antiferromagnetically. Along the c-axis the spins are antiparallel. The spin structure for the $(1/2, 0, 0)$ configuration corresponds to parallel spins along the c-axis. Both of these structures are observed in our powder samples, while only the $(1/2, 0, 1/2)$ structure is found in our single crystal sample. We thus believe that the $(1/2, 0, 1/2)$ structure represents the true ground state configuration. The two structures probably occur because the dipolar energies of these configurations are almost identical, as calculated by Felsteiner [7] for the Gd system, and the energetics may be influenced by the detailed metallurgical properties of the crystallites such as strains, grain and twin boundaries, etc.

The temperature dependence of the $(1/2, 0, 1/2)$ peak is shown in figure 2. Both specific heat [4-5] and inelastic neutron scattering [8] reveal that the ground state is a doublet, so that $S = 1/2$ is appropriate. In addition, in an orthorhombic structure with such a low Néel temperature we might expect the anisotropy to be large compared to the magnetic interactions, thus defining a unique spin direction. This corresponds to a 2-d Ising model,

which is the only one exhibits long-range magnetic order in 2-d. The solid curve is a fit to the Onsager's exact solution for $S = 1/2$ 2-d Ising model [9] which is seen to provide an excellent description of the data. In addition, if we analyze the data in the reduced temperature range $1 \times 10^{-3} < (T_N - T)/T_N < 0.11$, we obtain $\beta = 0.122 \pm 0.004$, in good agreement with the theoretical result $\beta = 1/8$. It should be noted that our data are very similar to the prototypical $S = 1/2$ 2-d Ising system K_2CoF_4 [10]. Thus, we believe that the physics of the rare earth ordering in these materials is controlled by the 2-d like character, with the 3-d ordering being induced as a necessary consequence of the onset of long range order within the a-b planes.

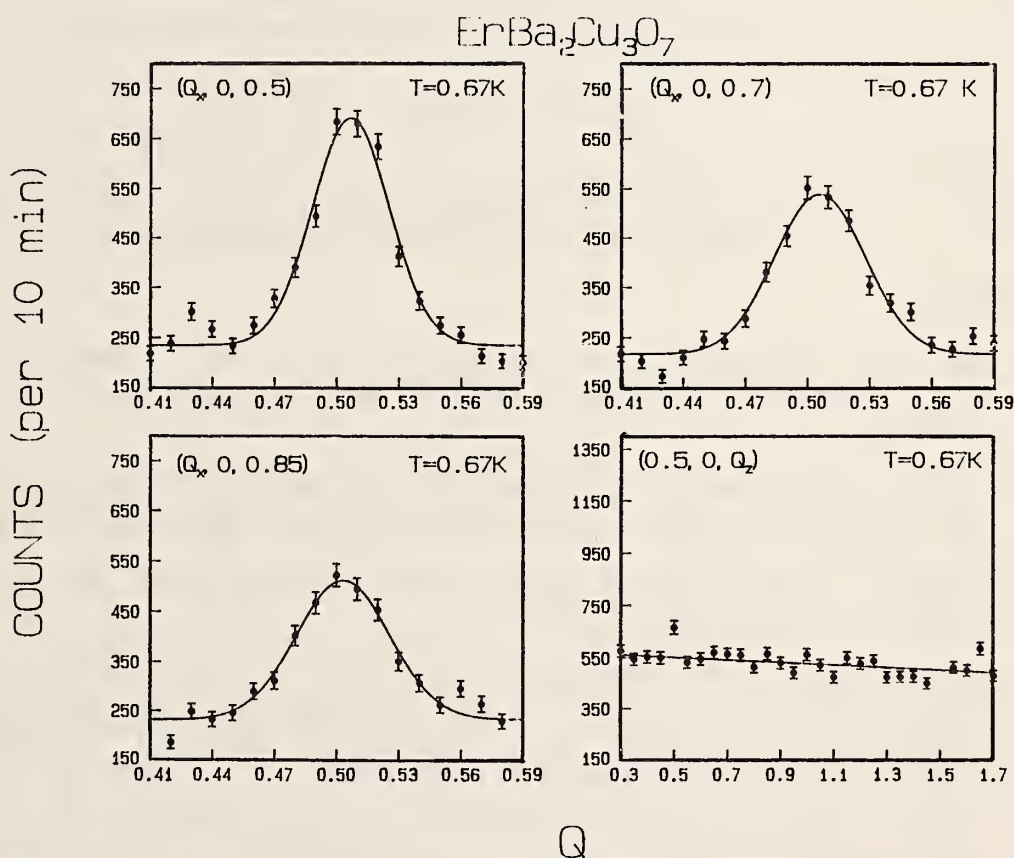


Figure 1. Three scans across the rod of scattering in reciprocal space, showing the 2-d character just above $T_N = 0.618$ K. The fourth scan shows that the scattering intensity does not vary significantly along the rod, indicating that there are no significant spin correlations between planes.

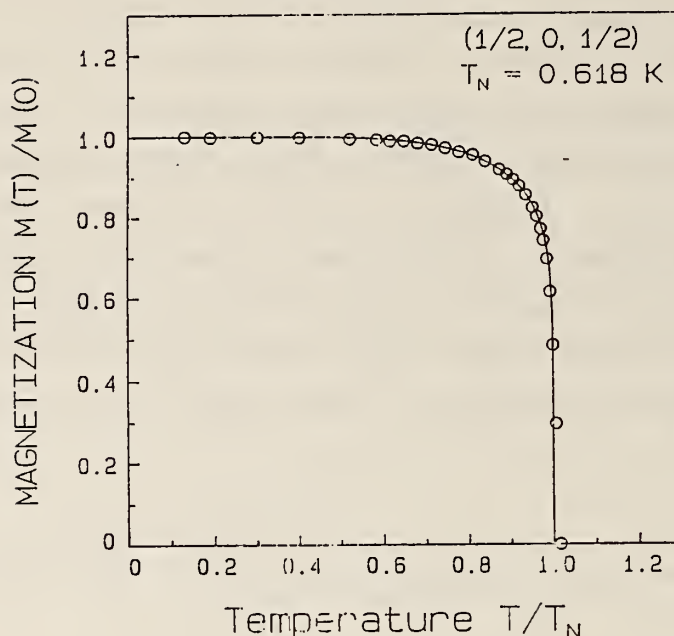
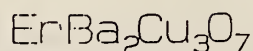


Figure 2. Sublattice magnetization versus temperature. The solid curve is a fit to the Onsager exact solution for the $S = 1/2$ 2-d Ising model.

References

- [1] Wu, M. K.; Ashburn, J. R.; Torng, C. J.; Hor, P. H.; Meng, R. L.; Gao, L.; Huang, Z. J.; Wang, Y. Q.; Chu, C. W. *Phys. Rev. Lett.* **58**, 908 (1987).
- [2] Hor, P. H.; Meng, R. L.; Wang, Y. Q.; Gao, L.; Huang, Z. J.; Bechtold, J.; Forster, K.; Chu, C. W. *Phys. Rev. Lett.* **58**, 1891 (1987).
- [3] Lynn, J. W.; Li, W.-H.; Li, Q.; Ku, H. C.; Yang, H. D.; Shelton, R. N. *Phys. Rev.* **B36**, 2374, (1987).
- [4] See Brown, S. E.; Thompson, J. D.; Willis, J. O.; Aikin, R. M.; Zirgib, E.; Smith, J. L.; Fisk, Z.; Schwarz, R. B. *Phys. Rev.* **B36**, 2298 (1987). Dunlap, B. D.; Slaski, M.; Hinks, D. G.; Soderholm, L.; Beno, M.; Zhang, K.; Segre, C.; Crabtree, G. W.; Kwok, W. K.; Malik, S. K.; Schuller, I. K.; Jorgensen, J. D.; Sungaila, Z. *J. Mag. Mag. Matl.* **68**, 1139 (1987). Lee, B. W.; Ferreira, J. M.; Dalichaouch, Y.; Torikachvili, M. S.; Yang, K. N.; Maple, M. B. *Phys. Rev.* **B37**, 2368 (1988). Van Der Muelen, H. P.; Franse, J. J. M.; Tarnawski, Z.; Kawdowaki, K.; Klaasse, J. C. P.; Menovsky, A. A. *Physica C* **152**, 65 (1988).
- [5] van den Berg, J.; van der Beek, C. J.; Kes, P. H.; Mydosh, J. A.; Nieuwenhuys, G. J.; de Jongh, L. J. *Solid State Commun.* **64**, 699 (1987). Simizu, S.; Friedberg, S. A.; Hayri, E. A.; Greenblatt, M. *Phys. Rev.* **B36**, 7129 (1987). Dirken, M. W.; de Jongh, L. J. *Solid State Commun.* **64**, 1201 (1987).

- [6] Chattopadhyay, T.; Brown, P. J.; Bonnenberg, D.; Ewert, S.; Maletta, H. *Europhys. Lett.* 6, 363 (1988).
- [7] Felsteiner, F. *Phys. Rev.* B39, 7248 (1989).
- [8] Walter, U.; Fahyl, S.; Zettl, A.; Louie, S. G.; Cohen, M. L.; Tejedor, P.; Stacy, A. M. *Phys. Rev.* B36, 8899 (1987). Furrer, A.; Bruesch, P.; Unternahreh, T. *Phys. Rev.* B38, 4616 (1988). Goldman, A. I.; Gao, Y.; Ting, S. T.; Crow, J. E.; Li, W.-H.; Lynn, J. W. *J. Mag. Mag. Matl.* 76-77, 607 (1988) (to be published).
- [9] Onsager, L. *Phys. Rev.* 65, 117 (1944).
- [10] Ikeda, H.; Hirakawa, K. *Solid State Commun.* 14, 529 (1974).

**EFFECT OF SUPERCONDUCTIVITY
ON THE SMALL ANGLE NEUTRON SCATTERING IN $\text{ErBa}_2\text{Cu}_3\text{O}_7$**

J. W. Lynn, H. Zhang, and W.-H. Li
(University of Maryland, College Park, MD and Reactor Radiation Division)

M. Yethiraj
(Los Alamos National Laboratory, Los Alamos, NM)

and

J. Z. Liu
(Argonne National Laboratory, Argonne, IL)

The central issue for the oxide superconductors is to understand the origin of the superconducting state. One aspect concerns the basic character and symmetry of the superconducting state itself; that is, whether it develops in the usual BCS way as a result of an instability of the Fermi liquid, or perhaps entails a different mechanism such as RVB. The second basic question involves the identification of the interaction responsible for the electron pairing. Since the discovery that the Cu ions carry a magnetic moment, some of the leading contenders have been theories in which the spin degree of freedom plays a fundamental role, thus making the magnetic properties of these systems of special interest [1].

In the "parent" insulating phases such as La_2CuO_4 , Nd_2CuO_4 , and $\text{RBa}_2\text{Cu}_3\text{O}_6$ (R = rare earth), long-range antiferromagnetic order has been observed, and considerable information has been obtained about the spin dynamics both by neutron [2-4] and Raman [5] scattering. For the La_2CuO_4 and $\text{YBa}_2\text{Cu}_3\text{O}_6$ ordered antiferromagnets, the measurements reveal that the exchange

interactions within the Cu-O planes are very much larger than between the layers, which gives rise to 2-d magnetic behavior above the ordering temperatures, and an overall energy scale which is much larger than the ordering temperatures would suggest. The essential question then is whether the Cu magnetic moments, and the very strong spin energetics, survive into the superconducting state. A number of experiments have been performed which provide evidence that the spin fluctuations do indeed exist in the superconducting state, in particular in the $\text{La}_{2-x}\text{Sr}_x\text{CuO}_4$, $\text{YBa}_2\text{Cu}_3\text{O}_7$, and $\text{Bi}_2\text{Sr}_2\text{CaCu}_3\text{O}_8$ superconducting phases. The correlation range is found to be quite short in the superconducting state, but the amplitude of the magnetic moment appears not to be diminished substantially. In addition, the magnetic fluctuations which are observed in the superconducting region of the phase diagram have been found by Raman scattering [5] and our own small angle neutron scattering (SANS) measurements [4] to be suppressed by superconductivity. One expected suppression effect [6] in SANS is the screening of the magnetic fluctuations by the superconducting electrons, at wavelengths $\geq \lambda_L$, where λ_L is the London penetration depth. This suppression comes from the electromagnetic interactions: there is a magnetic field $\mathbf{B}(\mathbf{q})$ associated with the magnetic fluctuations, and the supercurrents will screen these fluctuations at small wave vectors. However, the length scale which was obtained from the data is only 22 Å, which is much too short to be interpreted as a London penetration depth. A second effect is expected from the reduction of the spin susceptibility of the superconducting electrons themselves [6], which is caused by the formation of Cooper pairs. The length scale associated with this effect is the coherence length ξ . In the traditional "magnetic superconductors" the superconducting electrons do not have a spin component, and hence the conduction electron spin susceptibility is too small to be observed. But in the oxide superconductors the Cu ions carry a spin in the superconducting phase.

Our early SANS results on polycrystalline samples showed [4] that the intensity at small wave vectors q did in fact decrease when the sample became superconducting, with a characteristic length scale ~ 20 Å. Thus we could interpret this as a reduction of the paramagnetic spin susceptibility of the Cu ions, with a length scale $\sim \xi$. However, the signal-to-noise ratio for these powder data was not very good. To improve the experimental data we have redone this experiment with single crystal specimens. Approximately 15

single crystals ($T_c \approx 93$ K) were mounted on a perfect single crystal of Si, to minimize SANS from the sample holder. Each crystal was aligned with its c-axis parallel to the beam, and the data were taken at 10.5 \AA to minimize multiple Bragg scattering. The total volume of the sample was ~ 0.08 gm. This is more than an order of magnitude smaller than our powder sample, but the signal-to-noise was dramatically improved since the metallurgical SANS was drastically reduced. The sample was put in physical contact with the cold finger of the cryostat and allowed to equilibrate in temperature. Hence no exchange gas was used in order that we might eliminate any possible concern about the exchange gas condensing [7] on the sample and changing the SANS signal.

Some data, shown in figure 1, were taken with the SANS instrument in the "coarse" resolution mode. Data obtained at 120 K were used as "background," and subtracted from the data taken at lower temperatures. The intensity has been summed over the region of Q from 0.023 \AA^{-1} to 0.038 \AA^{-1} to improve statistics, as we had done previously [5]. We see that the scattering clearly decreases with decreasing temperature below T_c , quite similar to our previous data on the polycrystalline sample. Hence we have demonstrated that the SANS scattering does in fact decrease below the superconducting transition.

Although these preliminary results on single crystals are suggestive, much more work needs to be done. Since these are not polarized SANS experiments, experimentally we can only say that there is a decrease in overall scattering, which we assume is magnetic in origin. We also have assumed that since the length scale is short ($\sim 20 \text{ \AA}$) that the Cu ions are involved. One obvious experiment to do is to repeat these SANS studies on a sample of $\text{YBa}_2\text{Cu}_3\text{O}_7$. Hopefully we can obtain a much larger sample volume, so that the shape of the curve and the temperature dependence can be obtained much more accurately, and without the complication of having Er in the sample. Further work is in progress.

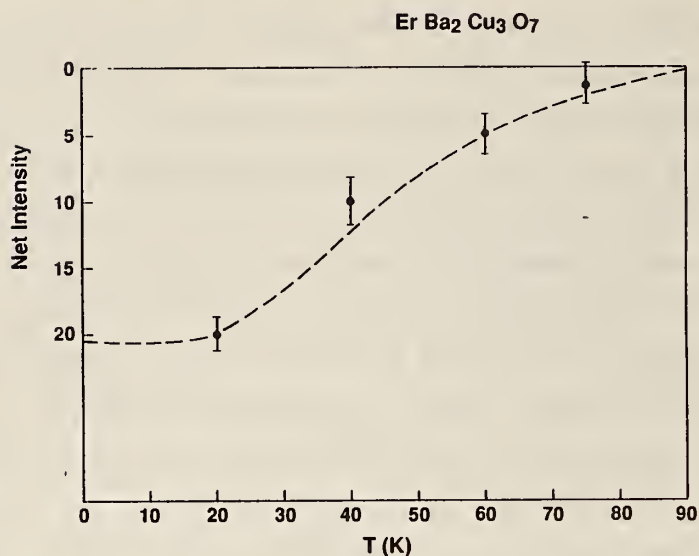


Figure 1. Temperature dependence of the net small angle neutron scattering, integrated over the Q range from 0.023 \AA^{-1} to 0.038 \AA^{-1} . The "background" data at 120 K have been subtracted from the data at lower temperatures. The scattering is seen to decrease below the superconducting transition temperature. The dashed curve is a guide to the eye.

References

- [1] For a recent review, see chapter 8 of High temperature superconductivity. J. W. Lynn, ed. Springer-Verlag, New York, 1989.
- [2] Endoh, Y. et al. Phys. Rev. B37, 7443 (1988). Birgeneau, R. J. et al. Phys. Rev. B38, 6614 (1988).
- [3] Sato, M. et al. Phys. Rev. Lett. 61, 1317 (1988). Mezei, F. et al. Physica C153-155, 1669 (1988).
- [4] Lynn, J. W. et al. Phys. Rev. B36, 2374 (1987).
- [5] Lyons, K. B.; Fleury, P. A. J. Appl. Phys. 64, 6075 (1988).
- [6] See, for example, Fulde, P.; Keller, J. in Topics in Current Physics 34, Chapter 9, Fisher, Ø.; Maple, M. B.; eds. Springer-Verlag, New York, 1983.
- [7] Lynn, J. W. Physica B 136, 117 (1986).

MAGNETIC ORDER OF Pr IN $\text{PrBa}_2\text{Cu}_3\text{O}_7$

W.-H. Li, J. W. Lynn, S. Skanthakumar, and T. W. Clinton
(University of Maryland, College Park, MD and Reactor Radiation Division)

and

A. Kebede, C.-S. Jee, J. E. Crow, and T. Mihalisin
(Temple University, Philadelphia, PA).

The superconducting transition temperature of the $\text{Y}_{1-x}\text{R}_x\text{Ba}_2\text{Cu}_3\text{O}_7$ (R = rare earth) compounds does not depend significantly on the concentration x of trivalent rare earths in the material. An important exception to this behavior is Pr, which forms the same orthorhombic structure but is thought to be strongly mixed valency, and close to the tetravalent ionic state. The superconductivity is found to be strongly suppressed as a function of Pr concentration [1,2] with a behavior which is consistent with the classical Abrikosov-Gorkov depairing theory [7], and superconductivity is lost for Pr concentration $x \geq 0.6$. On the Pr-rich end, on the other hand, there is evidence in specific heat and susceptibility of a magnetic phase transition, with a Néel temperature which is strongly x dependent and maximizes at 17 K for $x = 1$. The purpose of our measurements was to determine if indeed these anomalies originated from magnetic ordering, and if so, to determine the nature of the ordering.

The samples were made by the usual solid state reaction technique. Both x-ray diffraction and high resolution neutron profile refinement measurements were used to characterize the samples prepared for these measurements. From the neutron measurements, the nominal oxygen concentration was determined to be 7.00 ± 0.08 , and any impurity phases were found to be less than 1% of the sample.

Two magnetic Bragg reflections have been identified, and may be indexed as $\{1/2, 1/2, 1/2\}$ and $\{1/2, 1/2, 3/2\}$ reflections, on the orthorhombic chemical unit cell. Since all three Miller indices are half-integer, the magnetic unit cell is just double the chemical unit cell along all three crystallographic directions as shown in the insert in figure 1. Hence the underlying magnetic structure consists of nearest neighbor spins in all three directions which are aligned antiparallel, and is the same type of structure as has been found for the Dy, Gd, and Nd systems. The observed intensity for the $\{1/2, 1/2, 2/3\}$ peak is considerably weaker than that for the $\{1/2, 1/2,$

1/2} peak which then suggests that the moment direction in the system is predominantly along the c-axis direction. However, in the present case there are only two observable peaks due to the small value of the magnetic moment (as discussed below), and hence we should only consider this spin direction as tentative.

The low-temperature ordered moment we obtain from our data is $\langle \mu_z \rangle = (0.74 \pm 0.08) \mu_B$. This value is much smaller than the free-ion moment of $2.14 \mu_B$ for Pr^{4+} ($J = 5/2$) or $3.18 \mu_B$ for Pr^{3+} ($J = 4$). Crystal field (CF) effects may be important in reducing the value of $\langle \mu_z \rangle$ below the free-ion result. An ordered moment of $0.71 \mu_B$ would be expected for the most likely CF ground state ($| \pm 1/2 \rangle$ doublet) of Pr^{4+} . For Pr^{3+} , on the other hand, the orthorhombic distortion would totally remove the nine-fold degeneracy [3], concomitantly reducing T_N , the ordered moment, and the entropy removal at T_N , which is inconsistent with our data.

Figure 1 shows the temperature dependence of the {1/2, 1/2, 1/2} peak intensity, and reveals a typical order parameter with a Néel temperature of $T_N \approx 17$ K. The temperature dependence of the specific heat $C(T)$ for this compound is shown in figure 2, where a clear anomaly in the vicinity of 17 K is evident. The magnetic entropy associated with this transition is ~ 5.0 J/mole-K [2], and is somewhat smaller than the expected entropy change due to the ordering of a CF doublet ground state; i.e., 5.7 J/mole-K.

The essential difference in the magnetic ordering between the present nonsuperconducting $\text{PrBa}_2\text{Cu}_3\text{O}_7$ system and the trivalent superconducting $\text{RBa}_2\text{Cu}_3\text{O}_7$ systems is their Néel temperatures T_N , and the values of the ordered moment. If we scale these temperatures with respect to either the size of the (free ion) magnetic moment of Pr, or the spin of the Pr via a possible Ruderman-Kittel-Kasuya-Yosida (RKKY) exchange interaction, then we would expect a transition temperature for $\text{PrBa}_2\text{Cu}_3\text{O}_7$ which is an order of magnitude smaller than for $\text{GdBa}_2\text{Cu}_3\text{O}_7$. The observed transition is of course about an order of magnitude larger than these trivalent rare earths. In addition, the ordered moments for the heavy rare earth materials Er, Dy, and Gd were found to be 4.9, 7.2, and $7.4 \mu_B$, respectively, while the Pr moment is only $0.74 \mu_B$. Thus the higher ionic state for the Pr affects not only the electronic and superconducting properties of the Cu-O layers (e.g., the suppression of T_c), but also the electronic and magnetic properties of the Pr sublattice. The present specific heat and neutron data taken together

indicate that the $4f$ level for the Pr ions hybridize strongly with the electrons at the Fermi level.

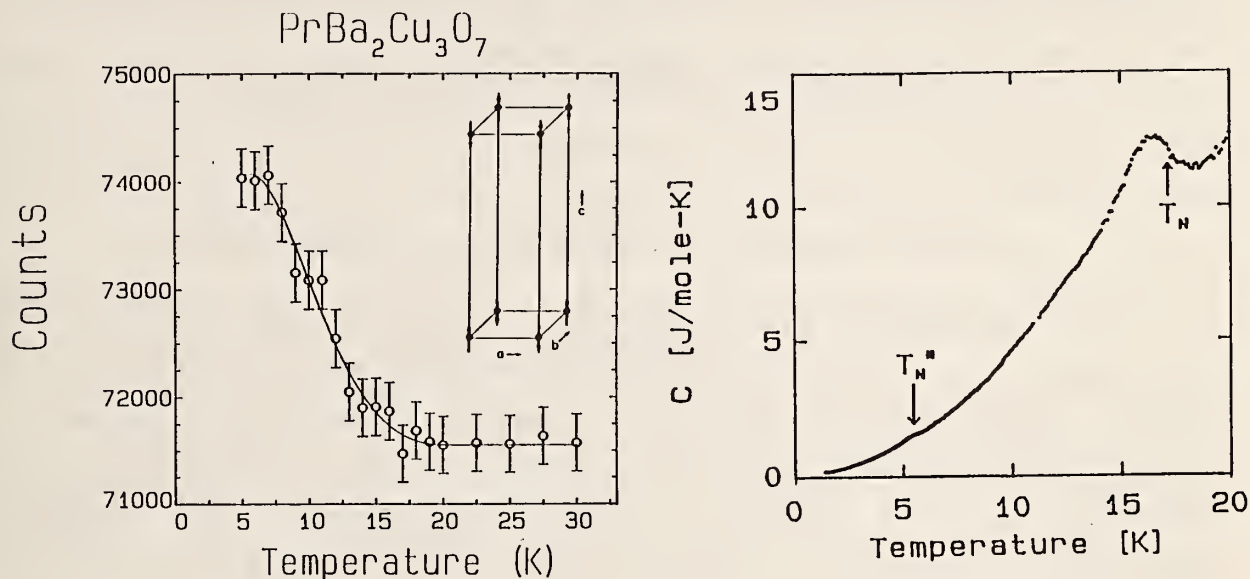


Figure 1. (left) Temperature dependence of the $\{1/2, 1/2, 1/2\}$ peak intensity, showing the variation of the square of the staggered magnetization with temperature. The Néel temperature for this system is ~ 17 K based on these data as well as on the specific heat data. The solid curve is a guide to the eye. The insert shows the magnetic configuration of the Pr spins.

Figure 2. (right) Measurements of the specific heat at low temperatures for $\text{PrBa}_2\text{Cu}_3\text{O}_7$, showing the magnetic transition at $T_N = 17$ K.

References

- [1] Dalichaouch, Y.; Torikackvili, M. S.; Early, E. A.; Lee, B. W.; Seaman, C. L.; Yang, K. N.; Zhou, H.; Maple, M. B. *Solid State Commun.* **65**, 1001 (1988).
- [2] Jee, C.-S.; Kebede, A.; Nichols, D.; Crow, J. E.; Mihalisin, T.; Myer, G. H.; Perez, I.; Salomon, R. E.; Schlottmann, P. *Solid State Commun.* (in press).
- [3] A recent theoretical calculation predicts a T_1 singlet as ground state, and an overall energy splitting of ~ 110 meV for Pr ions: Nekvasil, V.; Stehno, J.; Sebek, J.; Havela, L.; Sechovsky, V.; Svoboda, P. *J. de Physique* (in press).
- [4] See, for example, Stewart, G. R. *Rev. Mod. Phys.* **56**, 755 (1984). Fisk, Z.; Hess, D. W.; Pethick, C. J.; Pines, D.; Smith, J. L.; Thompson, J. D.; Willis, J. O. *Science* **239**, 33 (1988).

PRESSURE DEPENDENCE OF THE Cu MAGNETIC ORDER IN $R\text{Ba}_2\text{Cu}_3\text{O}_{6+x}$

J. W. Lynn and W.-H. Li,
(University of Maryland, College Park, MD and Reactor Radiation Division)

S. F. Trevino
(EWD, ARDEC, and Reactor Radiation Division)

and

Z. Fisk
(Los Alamos National Laboratory, Los Alamos, NM)

The paramagnetic-antiferromagnetic ordering temperature of the $R\text{Ba}_2\text{Cu}_3\text{O}_{6+x}$ (R = rare earth) compounds was found to be very sensitive to the oxygen concentration x in the chain layers. We have studied the magnetic order of the Cu spins in two single crystals of composition $\text{NdBa}_2\text{Cu}_3\text{O}_{6.35}$ and $\text{NdBa}_2\text{Cu}_3\text{O}_{6.1}$ as a function of hydrostatic pressure. The temperature dependence of the magnetic intensity of the $(1/2, 1/2, 2)$ Bragg peak for the $\text{NdBa}_2\text{Cu}_3\text{O}_{6.35}$ crystal is shown in figure 1 at a series of pressures. At zero pressure the ordering temperature is 230 K [1]. With increasing pressure the curves are seen to shift rapidly to higher temperatures, indicating that the ordering temperature T_{N1} is increasing.

In this temperature regime the intensity is approximately linearly dependent on temperature [1], and to obtain an estimate of T_{N1} we have simply least squares fit a straight line (solid curves) to the data (symbols). The transition temperatures which have been obtained from these fits increase approximately linearly with pressure at the rate of (23 ± 3) K/kbar up to an applied pressure of 4 kbars. This rate of increase is more than two orders-of-magnitude higher than the rate of 0.05 K/kbar observed for the superconducting transition temperature T_c for $\text{YBa}_2\text{Cu}_3\text{O}_7$, and is also two orders-of-magnitude larger than the calculated shift in T_N .

The pressure dependence of the Bragg scattering associated with the lower transition temperature T_{N2} , which is where the Cu chain spins order, is shown in figure 2. There is a small increase in the maximum value of the intensity, but only a very little shift in T_{N2} . We believe that this weak pressure dependence is representative of the fact that when the chain ions order, then the spacing between the Cu ions in the a , b , and c directions is about equal and we have a fully 3-d magnetic structure with simple antiferromagnetic nearest neighbor interactions, in contrast to the situation

at T_{N1} as discussed below. At T_{N2} the magnitude of the pressure effect is typical of 3-d phase transitions.

The Néel temperature T_{N1} is known to be quite sensitive to the oxygen concentration, so that the pressure effect we see might be explained by the removal of oxygen from the sample. However, below room temperature the oxygen will not reenter the sample, and we find no evidence for any irreversible effects in our data. We therefore discard this as a possibility. We have also measured the pressure dependence of the lattice parameters, and find a smooth decrease of $\sim 0.03\%/kbar$, which translates into a compressibility of $7.5 \cdot 10^{-13} \text{ Pa}^{-1}$. We detect no anomalies or abrupt changes in the lattice over the pressure range explored.

The most likely explanation for the strong pressure sensitivity of T_{N1} is in terms of the large magnetic anisotropy and competing exchange interactions which are present when the Cu chain spins are disordered in the $R\text{Ba}_2\text{Cu}_3\text{O}_{6+x}$ system. The magnetic exchange interaction J within the Cu-O_2 layers is very large, and thus in the vicinity of T_{N1} there are very strong magnetic correlations within the Cu-O_2 planes. Hence we have 2-d like magnetic behavior, with the preferred spin direction in the tetragonal plane, and since there is no 2-d long range order [2] above T_{N1} an x-y model should be appropriate. The 3-d phase transition is then driven by the weak effective interaction J' between layers. Since the in-plane exchange J is already very large, it is likely that J is near a maximum versus ionic separation and thus will not be particularly sensitive to pressure. On the other hand, the effective interaction J' , which is mediated through the spin-disordered Cu chain layer, results from an overlap of wavefunctions on ions which are well separated. The overlap integral should then depend exponentially on separation, and a substantial increase in J' with pressure can be expected. A calculation [3] based on spin wave fluctuations gives $T_{N1} \sim J \ln^{-1}(J/J')$ for large J/J' , which would yield a linear dependence of T_{N1} on P as observed. However, T_{N1} would be a weak function of J/J' and hence this scenario would then require a large change in J' to explain the data. Such a large change could be the result of a significant pressure-induced change in the electronic structure, similar to the change in T_{N1} caused by oxygen variation, or it could be due to some competing interactions caused by the disordered spins on the chain layers.

A second possibility is that the anisotropy within the plane increases with pressure, which would increase the in-plane correlations and eventually produce a phase transition with long-range order in 2-d [4]. Indeed, if there were a tendency for pressure to cause an orthorhombic distortion, for example, then the magnetic behavior of the layers would crossover to a 2-d Ising system (with long range order), and T_{N1} could increase dramatically. However, so far we have found no indication experimentally of an orthorhombic distortion.

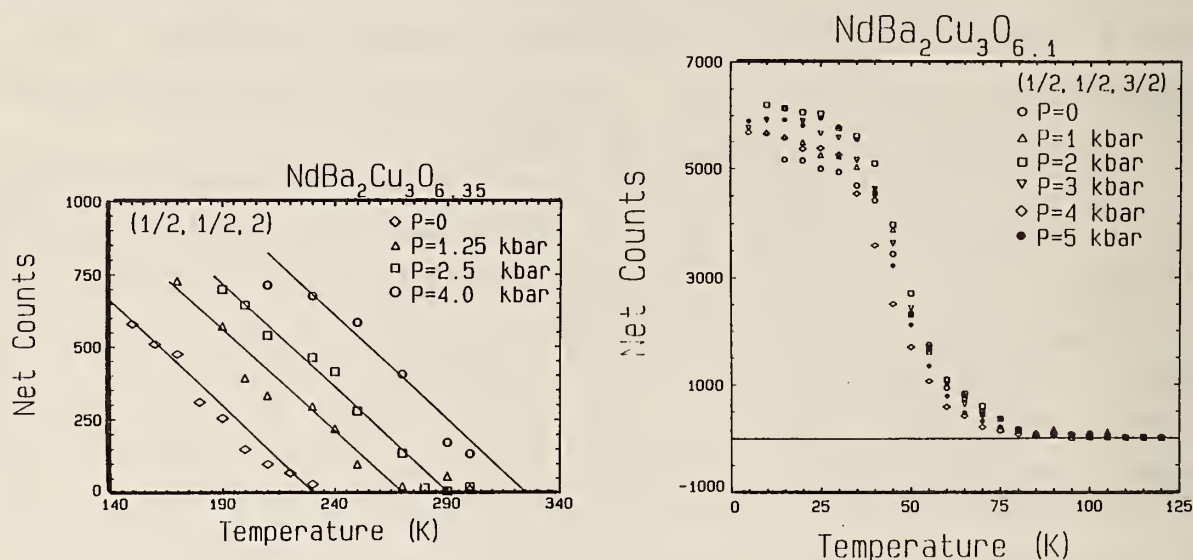


Figure 1. (left) Temperature dependence of the $(1/2, 1/2, 2)$ Bragg peak intensity in the vicinity of T_{N1} for the $\text{NdBa}_2\text{Cu}_3\text{O}_{6.35}$ crystal at a series of pressures. The solid lines are fits to the data to obtain T_{N1} .

Figure 2. Intensity of the $(1/2, 1/2, 3/2)$ Bragg peak from the $\text{NdBa}_2\text{Cu}_3\text{O}_{6.1}$ crystal at a series of pressures.

References

- [1] Li, W.-H.; Lynn, J. W.; Mook, H. A.; Sales, B. C.; Fisk, Z. Phys. Rev. B37, 9844 (1988). Lynn, J. W.; Li, W.-H.; Mook, H. A.; Sales, B. C.; Fisk, Z. Phys. Rev. Lett. 60, 2781 (1988) (to be published). Lynn, J. W.; Li, W.-H. J. Appl. Phys. 64, 6065 (1988). Lynn, J. W.; Li, W.-H.; Trevino, S. F.; Fisk, Z. Phys. Rev. B. (to be published).
- [2] Shirane, G.; Endoh, Y.; Birgeneau, R. J.; Kastner, M. A.; Hidaka, Y.; Oda, M.; Suzuki, M.; Murakami, T. Phys. Rev. Lett. 59, 1613 (1987). Lyons, K. B.; Fleury, P. A.; Remeika, J. P.; Cooper, A. S.; Negran, T. J. Phys. Rev. B37, 7443 (1988).
- [3] Ferrel, R. A. (private communication).

- [4] See, for example, Kosterlitz, J. M.; Thouless, D. J. J. Phys. C 6, 1181 (1973). Jose, J. V.; Kadanoff, L. P.; Kirkpatrick, S.; Nelson, D. R. Phys. Rev. B 16, 1217 (1977).

TWO- AND THREE-DIMENSIONAL MAGNETIC ORDER IN $R\text{Ba}_2\text{Cu}_4\text{O}_8$

H. Zhang, J. W. Lynn, W.-H. Li, and T. W. Clinton
(University of Maryland, College Park, MD and Reactor Radiation Division)

and

D. E. Morris and R. Sid
(Lawrence Berkeley Laboratory, Berkeley, CA)

The magnetic properties of the oxide superconductors have been of particular interest for two reasons. One is that the Cu magnetism may be related in a fundamental way to the pairing mechanism in these materials, and the second is that these are ideal systems in which to investigate the electromagnetic coupling between the rare earth magnetic and superconducting order parameters. In this latter regard we have been systematically investigating the nature of the rare earth ordering in the $R\text{Ba}_2\text{Cu}_3\text{O}_{6+x}$ systems, and have found [1,2] that they are prototypical two-dimensional magnetic systems. We are now extending these measurements to the $R\text{Ba}_2\text{Cu}_4\text{O}_8$ class of materials, which is similar to the 1-2-3 system except that the (orthorhombic) c-axis is approximately twice as long, with two rare earth ions in the chemical unit cell [3].

The diffraction data were collected with the BT-2 triple-axis spectrometer using the standard subtraction technique, in which the scattering well above the ordering temperature is subtracted from the scattering at low T, to isolate the magnetic response of the system. A dilution refrigerator was employed to cool the powder samples down as low as 0.05 K. Two polycrystalline samples were investigated, with compositions $\text{ErBa}_2\text{Cu}_4\text{O}_8$ and $\text{DyBa}_2\text{Cu}_4\text{O}_8$.

For the $\text{ErBa}_2\text{Cu}_4\text{O}_8$ system, the data reveal three dimensional Bragg peaks at low temperatures, which may be easily indexed on the chemical unit cell. The magnetic spin configuration is shown in figure 1, and the system has a Néel temperature of 0.43 K. Just above T_N , we also found evidence of two-dimensional behavior similar to the behavior found [1,2] in the $\text{ErBa}_2\text{Cu}_3\text{O}_7$ system.

The data for the $\text{DyBa}_2\text{Cu}_4\text{O}_8$ system was quite different. Figure 2a shows the diffraction profile observed at low temperatures. The skewed lineshape is characteristic of a system with two-dimensional behavior, and in fact the solid curve is the theoretical calculation assuming long-range order in the a-b planes, with no correlations between the spins along the c-axis [4]. The theory is seen to provide a good description of the data. In the bottom part of the figure is a plot of the observed intensity at the peak position as a function of temperature, and is quite typical of an order parameter, with a Néel temperature of ~ 0.74 K.

The lack of any 3-d order in the $\text{DyBa}_2\text{Cu}_4\text{O}_8$ material is quite surprising. In the conventional two-dimensional systems such as K_2CoF_4 [5], K_2NiF_4 [6] and more recently $\text{ErBa}_2\text{Cu}_3\text{O}_7$ [2], the 2-d ordering and the 3-d ordering occur at (essentially) the same temperature. The reason for the close proximity of the two transitions is that when the system develops a static moment in the layers, then there is an energy $\pm JA^2$ between the layers, where J is the exchange interaction between planes and A is the average size of a domain in the layer. The - sign is for layers that are properly matched (e.g., antiferromagnet if $J < 0$) and + is for layers that are out of phase. Thus even if the interlayer coupling is very weak, there is an energy difference $2JA^2$ between the "correct" and the "wrong" spin configurations, which can be quite large since A is large: Hence the layers will order along the c-axis producing 3-d Bragg peaks. In the present $\text{DyBa}_2\text{Cu}_4\text{O}_8$ system these interplanar correlations appear to be disrupted, leaving only 2-d order. Further work will be needed to isolate the origin of this unusual behavior.

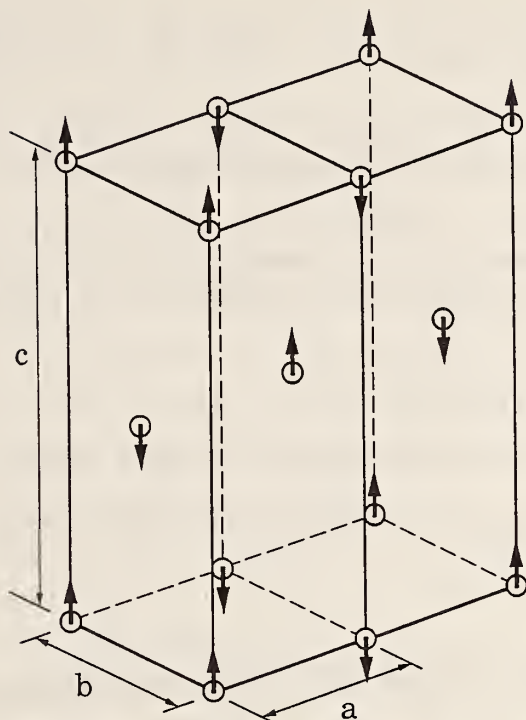
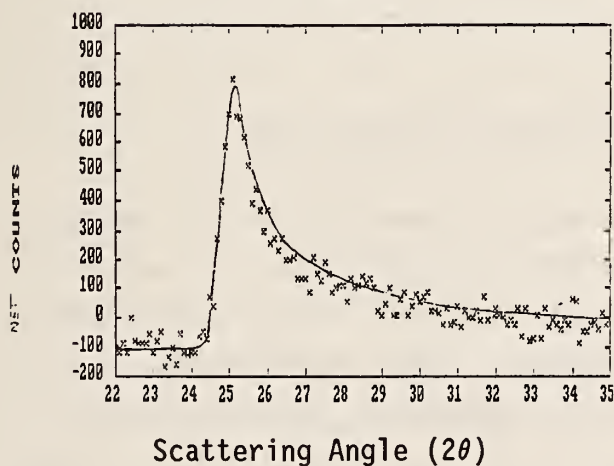
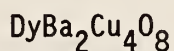
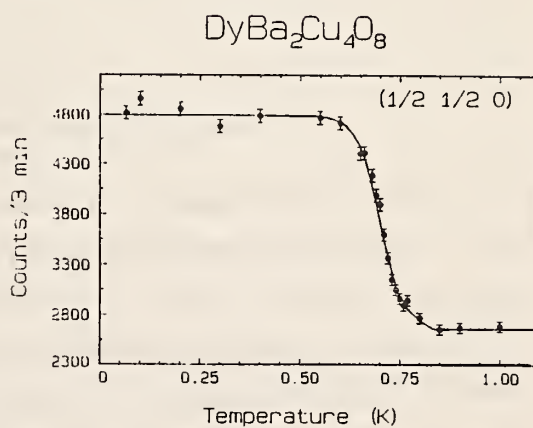


Figure 1. Ground state magnetic spin configuration of the Er spins in $\text{ErBa}_2\text{Cu}_4\text{O}_8$.



2 a)



2 b)

Figure 2. a) Magnetic scattering profile of $\text{DyBa}_2\text{Cu}_4\text{O}_8$ at $T=0.05$ K. The solid curve is a theoretical fit to a two-dimensionally ordered system. b) Intensity versus temperature for the $(1/2, 1/2, 0)$ peak, revealing a Neel temperature $T_N \approx 0.74$ K.

References

- [1] Lynn, J. W.; Li, W.-H.; Li, Q.; Ku, H. C.; Yang, H. D.; Shelton, R. N. Phys. Rev. B36, 2374 (1987).
- [2] Lynn, J. W.; Clinton, T. W.; Li, W.-H.; Erwin, R. W.; Liu, J. Z.; Vandervoort, K.; Shelton, R. N. (to be published).
- [3] See, for example, Morris, D. E.; Nickel, J. H.; Wei, J. Y. T.; Asmar, N. G.; Scott, J. S.; Scheven, U. M.; Hultgren, C. T.; Markelz, A. G.; Post, J. E.; Heaney, P. J.; Veblen, D. R.; Hazen, R. M. Phys. Rev. B39, 7347 (1989)
- [4] Warren, B. E. Phys. Rev. 59, 693 (1941).
- [5] Ikeda, H.; Hirakawa, K. Solid State Commun. 14, 529 (1974).
- [6] Birgeneau, R. J.; Guggenheim, H. J.; Shirane, G. Phys. Rev. B1, 2211 (1970).

MAGNETIC ORDER OF THE Cu PLANES AND CHAINS IN $R\text{Ba}_2\text{Cu}_3\text{O}_{6+x}$

W.-H. Li and J. W. Lynn
(University of Maryland, College Park, MD and Reactor Radiation Division)

Z. Fisk
(Los Alamos National Laboratory, Los Alamos, NM)

and

H. A. Mook and B. C. Sales
(Oak Ridge National Laboratory, Oak Ridge, TN)

Both the magnetic and superconducting properties of the $R\text{Ba}_2\text{Cu}_3\text{O}_{6+x}$ (R = rare earth) compounds are very sensitive to the oxygen concentration x in the "chain" layers. In the small x regime, where the materials are tetragonal and semiconducting, the Cu "plane" layers were found [1,2] to order antiferromagnetically with a Néel temperature T_N as high as 500 K. At lower temperatures the spins on the Cu "chain" sites have also been observed [3,4] to order antiferromagnetically. This additional ordering causes an interplanar competition between the "plane" and the "chain" layers, and results in a rich behavior of the magnetic structure as a function of temperature.

The spins in all three layers turn out to be coupled antiferromagnetically within the tetragonal layers. For the unit cell along the c-axis, there are two types of ordering that have been observed. At low temperatures both the "chain" layers and the "plane" layers can be ordered, with an antiferromagnetic sequence along the c-axis like (+ - + - + - ...) as shown in figure 1(a). This yields a magnetic unit cell double the chemical one along all three crystallographic directions. Magnetic Bragg reflections with all three Miller indices half integral are then expected. We refer to these peaks as "half-integral peaks."

In the high-T phase, the "chain" moments disorder while the "plane" moments reorient themselves into a new antiferromagnetic configuration, and we have an ordering sequence like (+ 0 - + 0 - ...) along the c-axis as shown in figure 1(b). In this case the magnetic and chemical unit cells are the same in this direction and ℓ will be integral. We refer to these peaks as "whole-integral peaks."

Measurements were made on four different samples with different oxygen concentrations. Two samples were polycrystalline, with compositions $\text{YBa}_2\text{Cu}_3\text{O}_{6.13}$ and $\text{NdBa}_2\text{Cu}_3\text{O}_{6.03}$, and weighing ~9 g each. The other two samples were single crystals, one with composition $\text{NdBa}_2\text{Cu}_3\text{O}_{6.35}$ and weighing ~9.5 mg, and a second one with composition $\text{NdBa}_2\text{Cu}_3\text{O}_{6.1}$ and weighing ~45 mg. The Rutherford backscattering measurements on the single crystals revealed a ratio of Nd:Ba:Cu = 1:2:3, indicating that there is no significant substitution of the rare earth onto the Ba site.

The temperature dependence of the strongest of the two types of peaks is shown in figure 2 for the $x = 0.1$ crystals. The data obtained from the $x = 0.35$ crystal show identical behavior, except that the magnetic transition temperatures T_{N1} and T_{N2} are of course different due to the different oxygen content. The decrease in the intensity of the (1/2 1/2 2) peak at low T is accompanied by the development of intensity at the (1/2 1/2 3/2) peak position. Both changes mark the onset of the "low-T phase" at T_{N2} . Our measurements indicate that $T_{N1} \approx 430$ K and $T_{N2} \approx 80$ K for the $x = 0.1$ crystal, and $T_{N1} \approx 230$ K and $T_{N2} \approx 10$ K for the $x = 0.35$ crystal.

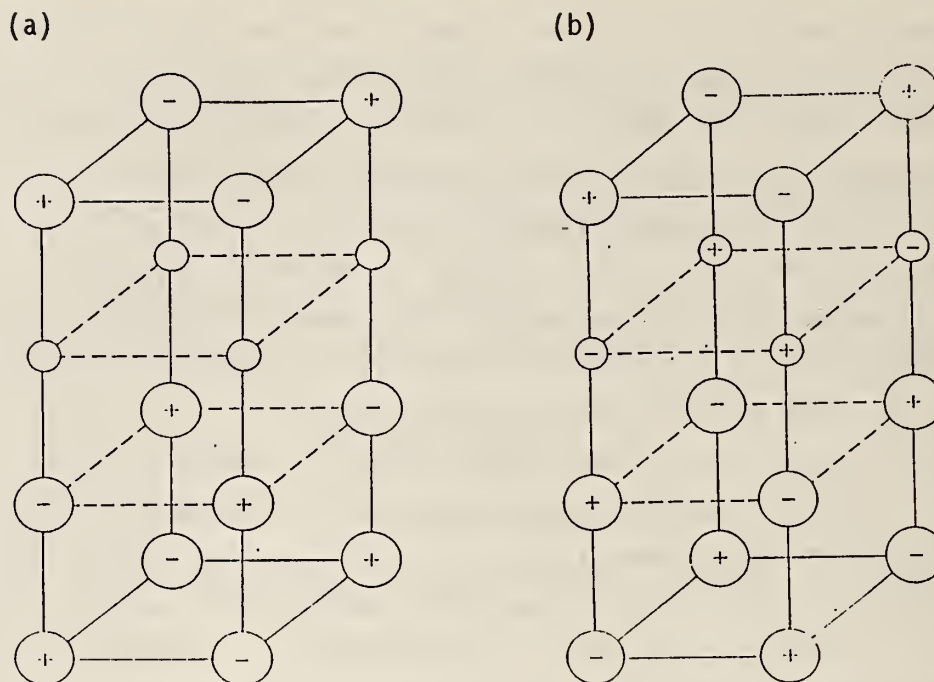


Figure 1. The basic spin structure for the Cu moments at (a) low T and (b) high T. There is a substantial moment on the Cu ions in the oxygen deficient planes (small circles) in the low-T phase. These Cu "chain" ions in the oxygen deficient planes become disordered at the high-T phase.

Since the half-integral and whole-integral Bragg reflections correspond to separate Fourier components, they can be treated separately, and if we make the physically reasonable assumption that the magnitude of the moments on the two "plane" layers are the same, then the angle between the two components of the spin structure must be 90° . There are, therefore, three adjustable spin parameters we have taken in our model: M_C , $M_{p\parallel}$, and $M_{p\perp}$, where \vec{M}_C and \vec{M}_p are the moments on the "chain" and the "plane" layers, respectively. The \parallel and \perp represent moment directions parallel and perpendicular, respectively, to the moment direction on the "chain" layers, so that $\vec{M}_p = \vec{M}_{p\parallel} + \vec{M}_{p\perp}$. A qualitative survey of the observed intensities shows that the spin direction must lie in the tetragonal plane.

At high temperatures for $T < T_{N1}$, only whole-integral reflections were observed. Upon cooling from the paramagnetic state, as T reaches T_{N1} the Cu spins on the "plane" layers start to align, and the value of $M_{p\perp}$ starts to develop. We note that the "flattening" of the order parameter at lower temperatures has been observed in a number of crystals. The maximum

intensity occurs at about 100 K for the $x = 0.1$ crystal. We use the value of the moment obtained from our powder results (where extinction is not a problem), and that is determined to be $0.64 \pm 0.06 \mu_B$ for the saturated $M_{P\perp}$.

Upon further cooling, the system undergoes a change in its spin structure which is characterized by the coexistence of the whole-integral and half-integral peaks. For the $x = 0.1$ crystal, at $T = 100$ K the whole-integral reflections dominate the scattering. As the temperature is decreased, the half-integral reflections become more intense while the intensities for the whole-integral reflections decrease. At $T = 20$ K, the half-integral reflections are much stronger than the whole-integral reflections.

As the temperature is decreased, $M_{P\perp}$ decreases together with a development of both M_C and $M_{P\parallel}$. The spin structure along the c-axis is a superposition of two orthogonal collinear sequences of $+\vec{M}_{P\perp}, 0, -\vec{M}_{P\perp}, +\vec{M}_{P\perp}, 0, -\vec{M}_{P\perp}$, and $-\vec{M}_{P\parallel}, +\vec{M}_C, -\vec{M}_{P\parallel}, +\vec{M}_{P\parallel}, -\vec{M}_C, +\vec{M}_{P\parallel}$, which results in a noncollinear structure along this axis. Along both directions in the tetragonal planes, the structure remains a collinear arrangements of $+\vec{M}_P, -\vec{M}_P$, and $+\vec{M}_C, -\vec{M}_C$ in the "plane" and "chain" layers, respectively.

A relative moment of $M_C/M_{P\parallel} \approx 0.43$ is deduced from our data taken on the $x = 0.1$ crystal at $T = 10$ K. The values of the ordered moments that we obtained at low temperatures are $M_P = 0.81 \pm 0.08 \mu_B$ for the "plane" layers and $M_C = 0.35 \pm 0.06 \mu_B$ for the "chain" layers. The temperature dependence of the moments on the Cu ions for the $x = 0.1$ crystal is shown in figure 3. The relatively large moment observed in the "chain" layers is somewhat surprising. As the temperature is raised, the thermal agitation randomizes the spins and results in a reduction of the (average) moments: both M_C and M_P decrease with increasing temperature, with M_C decreasing faster than M_P does. As the temperature reaches T_{N2} , M_C drops to zero and the Cu spins in the "chain" layers become completely disordered, while a moment of as high as $\sim 0.65 \mu_B$ still remains on the Cu ions in the "plane" layers.

The 43 independent magnetic reflections that we observed on the single crystals of $\text{NdBa}_2\text{Cu}_3\text{O}_{6.1}$ and $\text{NdBa}_2\text{Cu}_3\text{O}_{6.35}$ are well explained by the assumption of a 3-d magnetic form factor on the Cu ions with no need for a significant moment on any of the oxygen ions. The essential difference between the low- and high-T spin structures is of course the moment M_C on the

"chain" layers which develops below T_{N2} . The unexpectedly large value of M_C which we have observed on the Cu "chain" layers demonstrates that the Cu^{1+} state is not an appropriate description of the electronic configuration of the "chain" layers in these materials. There must be strong hybridization of the (band) electronic wave functions within all three Cu layers. It is quite clear that the "plane" layers are intimately involved in both the magnetism and superconductivity, and the oxygen plays a determinative role in the system.

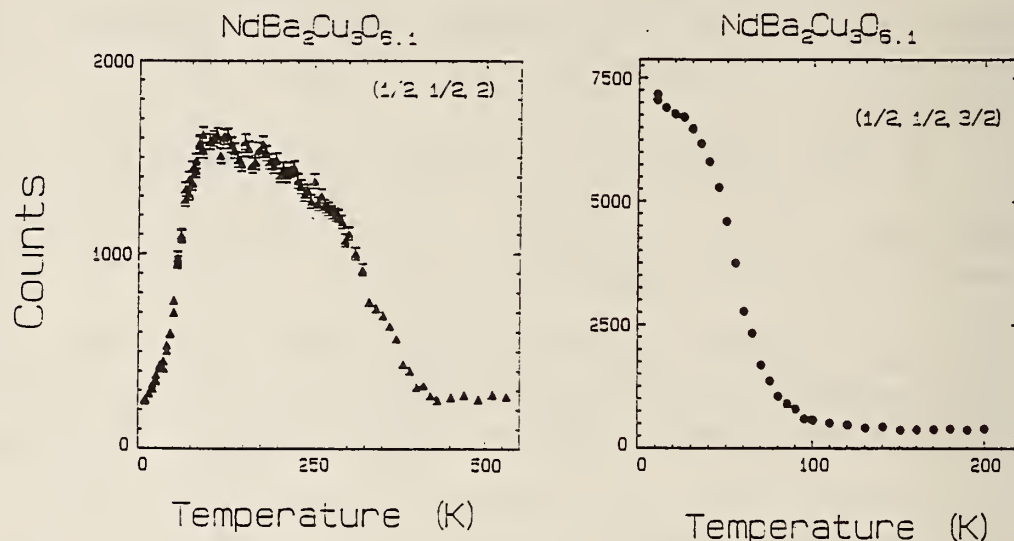


Figure 2. (left) Temperature dependence of the magnetic intensities for the $NdBa_2Cu_3O_{6.1}$ crystal. The onset of magnetic order for this oxygen concentration is $T_{N1} \approx 430$ K as revealed by the intensity of the $(1/2, 1/2, 2)$ peak shown in (a).

(right) The sharp downturn in the $(1/2, 1/2, 2)$ intensity at low temperatures is accompanied by new Bragg peaks at positions such as $(1/2, 1/2, 3/2)$ as shown in (b), indicating that the spins are undergoing a change in structure. T_{N1} for this oxygen concentration is ≈ 80 K.

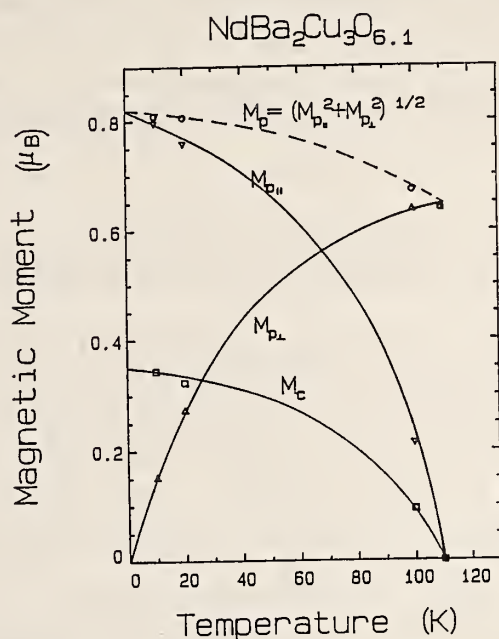


Figure 3. Temperature dependence of the ordered moment on the Cu ions for the $x = 0.1$ crystal. M_C is the moment on the "chain" layers, $M_{p\parallel}$ and $M_{p\perp}$ are the components of the moments on the "plane" layers

that are \parallel and \perp , respectively, to \vec{M}_C . At low temperatures, the moment on the "chain" layers is about 40% of that on the "plane" layers. At $T = T_{N2}$, M_C drops to zero, and only the spins of the Cu in the "plane" layers remain ordered. The solid curves are guides to the eye.

References

- [1] Tranquada, J. M.; Cox, D. E.; Kunnmann, W.; Moudden, A. H.; Shirane, G.; Suenaga, M.; Zolliker, P.; Vaknin, D.; Sinha, S. K.; Alvarez, M. S.; Jacobson, A. J.; Johnston, D. C. Phys. Rev. Lett. 60, 156 (1988).
- [2] Li, W.-H.; Lynn, J. W.; Mook, H. A.; Sales, B. C.; Bull. Am. Phys. Soc. 33, (1988); Li, W.-H.; Lynn, J. W.; Mook, H. A.; Sales, B. C.; Fisk, Z. Phys. Rev. B37, 9844 (1988).
- [3] Kadowaki, H.; Nishi, M.; Yamada, Y.; Takeya, H.; Takei, H.; Shapiro, S.; Shirane, G. Phys. Rev. B37, 7932 (1988).
- [4] Lynn, J. W.; Li, W.-H.; Mook, H. A.; Sales, B. C.; Fisk, Z. Phys. Rev. Lett. 60, 2781 (1988); Lynn, J. W.; Li, W.-H. J. Appl. Phys. 64, 6065 (1988).

ANTIFERROMAGNETIC ORDER OF THE Cu IN Nd_2CuO_4

S. Skanthakumar, H. Zhang, T. W. Clinton, W.-H. Li, and J. W. Lynn
(University of Maryland, College Park, MD and Reactor Radiation Division)

and

Z. Fisk and S.-W. Cheong
(Los Alamos National Laboratory, Los Alamos, NM)

The magnetic properties of the oxide superconductors are of particular interest because of the intimate relationship between the magnetic and superconducting properties, which raises the possibility that the copper magnetism may play an important role in Cooper pairing. The structures of the La_2CuO_4 and $\text{YBa}_2\text{Cu}_3\text{O}_7$ classes of materials consist of strongly bound planes of CuO_2 ions, which results in highly anisotropic magnetic and superconducting properties [1]. Recently, electron superconductors have been discovered [2], typified by the parent material Nd_2CuO_4 , where charge carriers are electrons rather than holes. Their existence places important constraints on any theory which is successful in describing the overall behavior of these systems. It is interesting in this regard to establish the nature of the magnetic ordering in the parent material. In the present work we report neutron and x-ray scattering experiments, in which we find a relatively simple magnetic spin arrangement.

Unpolarized diffraction data were taken with a wavelength of 2.359 Å and a pyrolytic graphite monochromator and filter, at the BT-2 triple-axis spectrometer. Polarized neutron measurements were taken at approximately the same wavelength, with a Heusler alloy monochromator, and a multilayer polarizing analyzer. The polarization analysis measurements were essential in establishing that the spin structures are noncollinear.

The magnetic behavior of this system turns out to be rather complicated; we have in fact already found five magnetic transitions. The magnetic peaks can be indexed as $(h/2, k/2, \ell)$, with h, k odd integers, which is the same indexing as found for La_2CuO_4 [3,4] and related compounds [5]. The half-integral values for the first two Miller's indices signify that the unit cell is doubled in size in the (pseudo)tetragonal a and b directions, while in the c direction the unit cell above and below T_N is the same size. The temperature dependence of some reflections is shown in figure 1. All the $(1/2 \ 1/2 \ \ell)$ type reflections increase in intensity with decreasing

temperature, and reveal a Néel temperature $T_N = 245$ K. Peaks with ℓ even are observed to have quite different intensities compared to those with ℓ odd. The $(1/2 \ 1/2 \ 0)$ peak is found to have negligible intensity except in the temperature region between 30 K and 75 K. In the high temperature phase ($75 \text{ K} < T < 245 \text{ K}$) we found that the ratios of the spin-flip scattering of polarized neutrons for the even-integral peaks were quite large (~ 6), while the odd-integral peaks we measured had ratios near unity. These data lead us to the spin structure proposed in figure 1c. Note that the spins within each Cu-O layer are antiferromagnetically coupled. At 78 K essentially the full Cu moment has ordered, and we obtain a saturated moment of $\sim 0.4 \mu_B$.

The data in figure 1a and 1b also show that at 75 K the intensity of the odd-integral peaks suddenly drops, while the even integral peaks increase abruptly in intensity. We interpret this as a spin reorientation transition, in which the sense of the spin direction changes from $[110]$ to $[1\bar{1}0]$. This then reverses the character of the spin-flip ratios observed in the polarized beam data. A similar type of transition has been observed recently for La_2CoO_4 [5], but the structure is different in that case. At 30 K another abrupt spin reorientation takes place, where the spins rotate back to the original spin sense as indicated by the negligible intensity for $T < 30$ K of the $(1/2 \ 1/2 \ 0)$ peak. At low temperatures (1.5 K), the Nd ions also order antiferromagnetically and we find a fifth transition of a continuous nature at 0.15 K [6].

Our neutron (above T_N) and x-ray scattering data gave evidence for a small distortion in this material from the tetragonal crystal structure [7]. The x-ray intensities were found to be essentially independent of temperature over the range from 100 K to 300 K and we conclude that the structural and magnetic peaks behave independently over this temperature range.

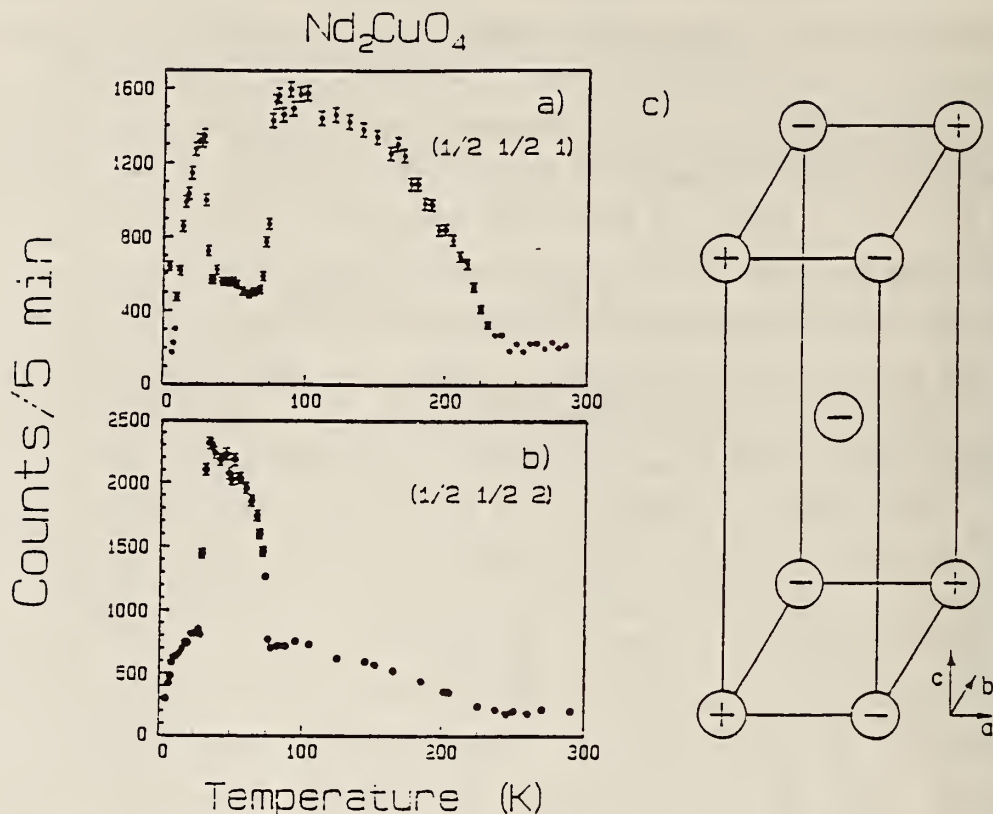


Figure 1. (a),(b) The intensity of the $(1/2 \ 1/2 \ 1)$ and $(1/2 \ 1/2 \ 2)$ peaks as a function of temperature. Below the Néel temperature of 245 K the intensity of all the peaks increase with decreasing T. At 75 K there is a sudden spin reorientation, in which the even-integral peaks $[(h/2, k/2, 2n)]$ increase in intensity while the odd-integral peaks $[(h/2, k/2, 2n+1)]$ decrease in intensity. At 30 K a second spin reorientation takes place in which the spin directions return to their original directions. (c) Magnetic spin configuration of the Cu spins in Nd_2CuO_4 .

References

- [1] For a general review see High temperature superconductivity, Lynn, J.W, ed. Springer, New York, 1989.
- [2] Tokura, Y.; Takagi, H.; Uchida, S. *Nature* **337**, 345 (1989).
- [3] Vaknin, D.; Sinha, S. K.; Moncton, D. E.; Johnston, D. C.; Newsam, J. M.; Safinya, C. R.; King, Jr., H. E. *Phys. Rev. Lett.* **58**, 2802 (1987)
- [4] La_2CuO_4 is orthorhombic, and the crystallographic notation is different than in the present case. The $(1/2 \ 1/2 \ 0)$ peak in the present notation corresponds to the (100) magnetic peak in La_2CuO_4 .
- [5] Yamada, K.; Matsuda, M.; Endoh, Y.; Keimer, B.; Birgeneau, R. J.; Onodera, S.; Mizuaski, J.; Matsuura, T.; Shirane, G. *Phys. Rev.* **B39**, 2336 (1989).

- [6] Li, W.-H.; Skanthakumar, S.; Sumarlin, I. W.; Lynn, J. W.; Shelton, R. N.; Peng, J. L.; Cheong, S.-W.; Fisk, Z. (private communication).
- [7] Skanthakumar, S.; Zhang, H.; Clinton, T. W.; Li, W.-H.; Lynn, J. W.; Fisk, Z.; Cheong, S.-W. Physica C (to be published).

**SUPERCONDUCTING $\text{Tl}_{2.0}\text{Ba}_{2.0}\text{CuO}_{6+\delta}$:
A HIGH RESOLUTION NEUTRON POWDER INVESTIGATION**

J. B. Parise and M. A. Subramanian
(E. I. du Pont de Nemours & Company, Wilmington, DE)

and

E. Prince

Preliminary reports of the new family of thallium based superconductors [1-3] have led to a windfall of investigations designed to reveal the structural features unique to this new class of materials.

Perhaps the most enigmatic of this family is $\text{Tl}_2\text{Ba}_2\text{CuO}_6$ (fig. 1). It has been variously described as a nonsuperconductor [4], low- T_c superconductor [5], moderate- T_c (<70 K) superconductor [5,6], and high- T_c (>90 K) superconductor [3,7]. The composition as written implies a formal oxidation state for Cu of 2+ (or of 2- for the single CuO_2 -sheet, and this composition, containing no excess of holes or electrons, would not be expected to superconduct on the basis of comparison with other Cu-O based superconductors [8]. Several suggestions have been advanced as possible mechanisms for the production of the holes in the CuO_2 sheets [3,8]. These include internal redox mechanisms, metal nonstoichiometry, and oxygen nonstoichiometry; recently the presence of oxygen defects has been revealed in a study of the related bismuth system [9]. Gross metal vacancies have also been proposed in $\text{Tl}_2\text{Ba}_2\text{CuO}_6$ [6] as a means of introducing holes in the CuO_2 sheets. This suggestion, in particular, requires investigation since it proposes that as many as 12% of the available thallium sites are vacant; a precise single crystal x-ray investigation [3] found no evidence for such vacancies.

Our results on this system provide evidence that neither Tl-vacancies nor tetragonal symmetry are necessary conditions for superconductivity in $\text{Tl}_2\text{Ba}_2\text{CuO}_6$. The structure of the orthorhombic form of $\text{Tl}_2\text{Ba}_2\text{CuO}_{6+\delta}$ (T_c = 90 K), synthesized in sealed gold tubes using BaO_2 , has been refined using high resolution neutron powder diffraction data collected at 4 K. No

significant deficiency in metal stoichiometry could be inferred from the crystal structure analysis. The space group (Fmmm) used in this study gives essentially the same results as the alternatives (Abma, Amaa) proposed in earlier work. The large amount of disorder that exists in the Tl_2O_2 -slab is mirrored in the large thermal parameters for this structural unit compared to those for the CuO_2 sheet (tables 1 and 2). A site at $(1/4 \ 1/4 \ 1/4)$ is occupied by an amount of oxygen to give overall stoichiometry $\text{Tl}_2\text{Ba}_2\text{CuO}_{6.10}$, suggesting that oxygen nonstoichiometry plays an important role in producing high T_c superconductivity in this system as has recently been reported [10] in the cadmium doped system $\text{Tl}_{2-x}\text{Cd}_x\text{Ba}_2\text{CuO}_{6+8}$.

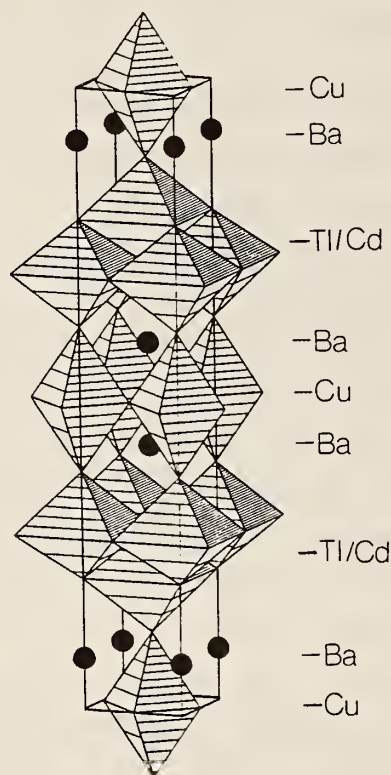


Figure 1. A view of the structure of $\text{Tl}_2\text{Ba}_2\text{CuO}_6$. Oxygen atoms are at the corners of corner sharing or edge sharing octahedra. Copper and thallium atoms are in the octahedral holes in the planes indicated.

Table 1. Refined parameters^a for $\text{Tl}_2\text{Ba}_2\text{CuO}_{6.10}$ at 4 K. The usual discrepancy indexes [11] are reported

Atom	Site	x	y	z	B(Å ²)
Tl ^b	16m	0	-0.025(1)	0.2024(1)	0.43(5)
Ba	8i	1/2	0	0.0828(1)	0.48(6)
Cu	4a	0	0	0	0.41(5)
O(1)	8e	1/4	3/4	0	0.45(5)
O(2)	8i	0	0	0.1163(1)	0.59(5)
O(3) ^{b,c}	16m	0	-0.059(1)	0.2895(2)	3.6(2) ^d
O(4) ^e	8f	1/4	1/4	1/4	7(2)

Cell parameters (Å)^f

$$a = 5.4604 (2)$$

$$R_N = 0.049$$

$$b = 5.4848 (2)$$

$$S_p^2 = 2.26$$

$$c = 23.2038 (6)$$

$$R_{wp} = 0.076$$

(a) Space group Fmmm (no. 69).

(b) Close to ideal site (8i; 0,0,z); half occupancy of site 16m.

(c) Refined occupancy: 0.98(1) atom/site.

(d) Equivalent isotropic B. This atom refined with anisotropic thermal parameters:

$$B_{11} = 7.2(3), B_{22} = 3.3(5), B_{33} = 0.2(1), B_{23} = -0.2(2);$$

$$\exp [-0.25(B_{11}h^2a^2 + \dots + 2(B_{12}hka \cdot b \cdot \dots))]$$

(e) Refined occupation: 0.07(1) atom/site.

(f) a and b reversed from reference [10].

Table 2. Selected interatomic distances^a for $\text{Tl}_2\text{Ba}_2\text{CuO}_{6.10}$

Cu	-O(1)	(x4)	1.9349(1)
	-O(2)	(x2)	2.698(3)
Ba	-O(1)	(x4)	2.723(2)
	-O(2)	(x2)	2.838(1)
	-O(2)	(x2)	2.850(1)
	-O(3)	(x1)	2.981(6)
Tl	-O(2)	(x1)	2.004(3)
	-O(3)	(x1)	2.028-2.073(4)
	-O(3)	(x2)	2.284-2.932(9)
	-O(3)	(x2)	2.213-2.566(9)
	-O(3)	(x4)	2.776-2.743(9)
	-O(4)		2.144-2.317(5)
O(4) - O(3)			1.949(4)-2.361(4)

^a Those distances involving O(3) and Tl have been calculated for both partially occupied sites (at Oyz and O-yz). When these are not equivalent, a range is shown.

References

- [1] Sheng, Z. Z.; Hermann, A. M. *Nature* **332**, 138 (1988).
- [2] Hazen, R. M. et al. *Phys. Rev. Lett.* **60**, 1657 (1988).
- [3] Torardi, C. C. et al. *Phys. Rev.* **B38**, 225 (1988).
- [4] Parkin, S. S. P. et al. *Phys. Rev.* **B38**, 6531 (1988).
- [5] Shimakawa, Y. et al. *Physica C* (in press).
- [6] Hewat, A. W. et al. *Physica C* **156**, 369 (1988).
- [7] Parise, J. B. et al. *J. Solid State Chem.* **76**, 432 (1988).
- [8] Sleight, A. W. *Science* **242**, 1519 (1988).
- [9] Torardi, C. C. et al. *Physica C* **157**, 115 (1989).
- [10] Parise, J. B. et al. *Physica C* **159**, 255 (1989).
- [11] Young, P. A. et al. *J. Appl. Cryst.* **15**, 357 (1982).

NEUTRON POWDER DIFFRACTION STUDY OF $\text{Pb}_2\text{Sr}_2\text{YCu}_3\text{O}_8$, THE PROTOTYPE OF A NEW FAMILY OF SUPERCONDUCTORS

R. J. Cava, M. Marezio, J. J. Krajewski, and W. F. Peck, Jr.
(AT&T Bell Laboratories, Murray Hill, NJ)

and

A. Santoro and F. Beech

The structure of $\text{Pb}_2\text{Sr}_2\text{YCu}_3\text{O}_8$ has been analyzed with powder neutron diffraction techniques and profile analysis. The results of this study confirm the general structural features determined by x-ray single-crystal methods. The material has pseudo tetragonal symmetry, but is orthorhombic, space group Cmmm with lattice parameters $a = 5.3933(2)$, $b = 5.4311(2)$, and $c = 15.7334(6)$ Å. The orthorhombic distortion is caused by the disordering in the ab plane of the oxygen atoms of the PbO layers over the general position of the space group, with $x = 0.275(5)$ and $y = 0.402(5)$ Å. The structure of this compound can be derived from that of $\text{YBa}_2\text{Cu}_3\text{O}_6$ by substituting the Cu layers with blocks of ...PbO.Cu.PbO.... Of the two Cu atoms in the asymmetric unit, one has twofold coordination while the other has fivefold pyramidal coordination with the apex elongated along the c -axis.

SANS STUDY OF $\text{YBa}_2\text{Cu}_3\text{O}_{7-x}$ SOL-GEL PROCESSING

G. Moore, G. Kordas, and M. B. Salamon
(University of Illinois, Urbana, IL)

J. Hayter
(Oak Ridge National Laboratory, Oak Ridge, TN)

and

C. J. Glinka

Sol-gel methods offer a novel route to the fabrication of high-temperature superconducting materials. They offer the advantage of mixing at the atomic level, synthesis at ordinary temperatures, and possible routes to thin films and wires without high temperature processing. The chemistry of this process has been studied at the University of Illinois (G. Kordas) who has found that alkoxides of Cu, Ba, and Y can be dissolved in suitable

solvents (e.g., methylethylketone), dried, and converted to the superconducting phase after processing in oxygen. The purpose of these SANS experiments was to monitor the development of the gel by determining the fractal dimensionality of the structure.

A preliminary experiment was performed in February, while the cold source was not in operation. Evidence for the development of fractal structures was seen in this work, but the range of accessible q -values was too small to give definitive results. We were able, however, to determine the optimal solvent conditions and to assure that the component materials were in the sol phase.

A second 2-day run was carried out in May. Very good evidence for fractal structure formation was observed and complements SAXS results taken on similar gels. The data are presently being analyzed for inclusion in the dissertation of G. Moore, and will be prepared for publication in the near future. The effects of differing solvents (mixtures of MEK with toluene, for example) were also studied, and show that solvent conditions can strongly affect the microstructure of the resultant gel.

INTERPLANAR-BOSON-EXCHANGE MODELS OF HIGH-TEMPERATURE SUPERCONDUCTIVITY-- THEORETICAL COMPARISONS AND POSSIBLE EXPERIMENTAL TESTS

R. C. Casella

I have generalized my earlier attempts to understand high- T_c superconductivity in the layered CuO_2 compounds in terms of the exchange of (unspecified) high-energy ($\omega \gg \omega_{\text{phonon}}$) intermediate bosons (IB) between different CuO_2 planes [1]. The earlier work was limited to IB exchange between only two CuO_2 layers. In order to include systems such as the Tl and Bi compounds, the analysis has been extended to include IB exchange between a number n of closely spaced CuO_2 layers in a cluster, as well as between members of different nearby clusters [2]. While limited to IB exchange between only two layers, the earlier analysis involved IB exchange between pairs of carriers, which pairs lie in two distinct types of quasi-two-dimensional bands, leading to various two-gap scenarios [1]. In the extension to n -clusters the analysis is simplified by considering only a single band type, whence, under appropriate averaging procedures, a single-gap parameter $\Delta(n)$ emerges [2]. $\Delta(n)$ and the critical temperature $T_c(n)$

depend upon the number n of CuO_2 layers per cluster for a given compound. In the coupled-gap equations employed in the formalism, IB penetration of several layers is allowed under the assumption that the IB couples weakly to the paired carriers in the CuO_2 layers [1,2]. (The predicted values of $T_C(n)$ for $n > 3$, given experimental values for smaller n , do not depend upon the absolute scale of the effective coupling parameters g_n within the formalism, but only on the ratios $\zeta_n = g_n/g_1$.) In common with other theoretical models [3], I find a rapid saturation of $T_C(n)$ with increasing n for the Tl_2 and Bi compounds. I also obtain the possibility of a diminution of $T_C(n)$ for $n > 3$ in the Tl_2 systems, as illustrated in table 1. Results are presented for two models. In model #1 the coupled equations in reference [2] lead to an effective coupling parameter of the form

$$g_n = (n - 1) \Lambda_N + (2n)\Lambda_F. \quad (1)$$

Here Λ_N is the average effective four-fermion coupling resulting from IB exchange between pairs residing in distinct layers of the same cluster and Λ_F , that between a CuO_2 layer in a given cluster with each of the n layers in either of the two immediately adjacent clusters. The factor $(n - 1)$ in the intracluster term is a consequence of the basic assumption [1,2] that IB exchange between pairs in the same CuO_2 layer (if occurring) does not contribute to g_n . In model #2 assumed fixed ranges delineate IB exchange leading to near (N) and far (F) components V_N and V_F of the otherwise averaged four-fermion interaction potential V . As shown in table 1, both models lead to rapid saturation of $T_C(n)$ with increasing n . The possibility of a diminution of $T_C(n)$ for $n > 3$ in the Tl_2 systems exists in model #2 when one assumes a high value for $T_C(n = 1)$ within the range $0 \lesssim T_C(1) \lesssim 85$ K reported by various experimental groups [6,7]. However, this case leads to technical difficulties in matching the two models at small values of n where physically one expects them to coalesce. Whether the difficulty encountered for this case is due to the crude cut-off and averaging procedures employed or is endemic to IB exchange models if the ratio $T_C(1)/T_C(2)$ is not sufficiently small, is presently unclear.

I have recently considered the possibility that, even under optimal doping, $T_C(1) \lesssim 10$ K for the Tl_1 and Tl_2 systems, a possibility which one might reconcile with the higher values reported if the latter were due to,

say, otherwise undetected small inclusions of materials with clusters having $n > 1$. A value of T_c in this low range need not be considered as requiring a special mechanism such as high-energy interlayer IB exchange. Therefore, within the context of these models, I have replaced the possible condition $T_c(1) \lesssim 10$ K by the formal assumption $T_c(1) = 0$ [4,5]. This has led to modifications of models #1 and #2. These are, respectively, models #1' and #2' in which $g_1 = \Lambda_F = 0$, whence the predicted values of $T_c(n)$ for $n > 3$ depend only upon the ratios $\zeta_n' = g_n/g_2$ of the couplings. In model #1' only intracluster IB exchange coupling occurs, and in model #2' IB exchange occurs only between CuO_2 layers separated by distances $\lesssim 0.9$ nm for the Tl_1 and Tl_2 systems. Results obtained for these systems are presented in table 2 and table 3, respectively. These tables include results for yet another model (#3) in which only nearest-layer intracluster exchange is allowed despite the assumed weakness of the IB coupling. Comparison of the results for models #1' and #3 given in the tables shows that they are equal. This equality is demonstrated analytically in reference [5] and complicates the task of separating the two experimentally.

The assumption that the effective range for IB exchange along the c axis is approximately the same in the Tl_1 and Tl_2 series (≈ 0.9 nm, with comparable values in the LaSr, LaBa, Bi, and the 1-2-3 yttrium compounds), allows an understanding of the relatively low values for $T_c(1)$ reported for the Tl_1 and Bi systems, while allowing $T_c \approx 92$ K in the 1-2-3 compound (where $n = 2$) and the somewhat reduced but still high values for T_c in the LaSr and LaBa systems (where $n = 1$, but $c/2 < 0.9$ nm). Hence, resolving the experimental situation with good single crystals of the Tl_1 , Tl_2 and Bi layered CuO_2 compounds with only one CuO_2 layer per cluster is of considerable importance.

Table 1. Values of $T_c(n)$ for $n = 4, 5, 6$ for $Tl_2Ca_{n-1}Ba_2(CuO_2)_nO_{4+x}$ as predicted by models #1 and #2

n	$T_c(n)$ [K]			
1	83 ^a		10 ^b	
2	109 ^a		102 ^b	
3	122 ^a		122 ^b	
	model #1	model #2	model #1	model #2
4	130	121	130	130
5	135	118	135	132
6	139	112	138	134

^aInput from reference [6].

^bAverages over ranges quoted in reference [7].

 Table 2. Values of $T_c(n)$ for $n = 4, 5, 6$ for $Tl_1Ca_{n-1}Ba_2(CuO_2)_nO_{3+x}$ as predicted by models #1', #2', and #3 when $T_c(1) \lesssim 10$ K

n	$T_c(n)$ [K]		
1	0 ^a		
2	75 ^b		
3	105 ^b		
	model #1'	model #2'	model #3
4	117	112	117
5	124	116	124
6	128	117	128

^aFormal assumption when $T_c(1) \lesssim 10$ K, the latter implied by the data of reference [7].

^bAverages over ranges quoted in reference [7].

Table 3. Values of $T_c(n)$ for $n = 4, 5, 6$ for $Tl_2Ca_{n-1}Ba_2(CuO_2)_nO_{4+x}$ as predicted by models #1', #2', and #3 when $T_c(1) \lesssim 10$ K.

n	$T_c(n)$ [K]		
1	0 ^a		
2	102 ^b		
3	122 ^b		
	model #1'	model #2'	model #3
4	130	126	130
5	133	128	133
6	136	130	136

^aFormal assumption when $T_c(1) \lesssim 10$ K, the latter compatible with the data of reference [7].

^bAverages over ranges quoted in reference [7].

References

- [1] Casella, R. C. Nuovo Cimento D 10, 1439 (1988).
- [2] Casella, R. C. Solid State Commun. 70, 75 (1989).
- [3] Wheatley, J. M.; Hsu, T. C.; Anderson, P. W. Nature 333, 121 (1988); Birman, J. L.; Lu, J. P. Phys. Rev. B39, 2238 (1989).
- [4] Casella, R. C. Post-deadline poster presented at the March meeting of the American Physical Society, St. Louis, MO (1989).
- [5] Casella, R. C. Appl. Phys. Lett. (in press).
- [6] Torardi, C. et al. Science 240, 631 (1988).
- [7] Parkin, S. et al. Phys. Rev. Lett. 61, 750 (1988).

TEXTURE STUDY OF MAGNETICALLY ALIGNED $\text{YBa}_2\text{Cu}_3\text{O}_{7-x}$ BY NEUTRON DIFFRACTION

C. S. Choi
(ARDEC, Picatinny Arsenal, NJ and Reactor Radiation Division)

H. J. Prask

and

C. P. Ostertag
(Ceramic Division)

Crystals of $\text{YBa}_2\text{Cu}_3\text{O}_{6+x}$ high- T_c superconducting materials have a layer type structure, consisting of sheets of CuO_x , BaO , and CuO_2 , oriented perpendicular to the c-axis, and hence, their superconducting properties are extremely anisotropic. The critical current density along the direction parallel to the basal plane (i.e., 001 plane) is more than 10 times larger than that in the direction perpendicular to the plane (or c-axis direction) in a single crystal sample, with approximately $3 \times 10^6 \text{ A/cm}^2$ at 45 K in the favorable directions of the crystal. However, the current densities of polycrystalline materials are about two orders of magnitude less, which is attributed to random orientation and grain boundary effects. Therefore, a higher degree of alignment of the crystallites along the c-axis is an important factor for a polycrystalline material to achieve higher current density.

The crystallite orientation distributions of two magnetically aligned samples: $\text{YBa}_2\text{Cu}_3\text{O}_6$ aligned in the tetragonal phase followed by oxidation for orthorhombic conversion (YBaCuO-153), and orthorhombic $\text{YBa}_2\text{Cu}_3\text{O}_7$ (YBaCuO-151), were studied by neutron pole figure measurements. The intensity distributions of (004) over the entire orientation hemisphere, with the ϕ -angle ranging from -180 to 180 and χ -angle from 90 to 0 in 5° intervals, were measured using the single-crystal neutron diffractometer. The observed pole figures of the two samples, which are shown in figure 1, show a fiber texture with the c-axis parallel to the applied magnetic field direction. The orientation distributions of the fiber axes could be described quite satisfactorily with Lorentzian or March distribution functions, as shown in table 1. The sample aligned in the tetragonal phase had distinctly better alignment than that aligned in the orthorhombic phase, with FWHMs of $19.3(3)^\circ$ and $37.8(7)^\circ$ respectively. The contour lines of the pole figures showed

irregularities which could be attributed to the presence of coarse grains in the samples.

Table 1. Results of the nonlinear least squares fits of the χ -angular distributions of the fiber axes to Lorentzian (L) and March (M) function. The functions used are in the form:

$$L = A\{1+4(C-\chi)^2/W^2\}^{-1}, \text{ and}$$

$$M = S(r^2 \cos^2(C-\chi) + r^{-1} \sin^2(C-\chi))^{-3/2} \text{ with } r < 1.$$

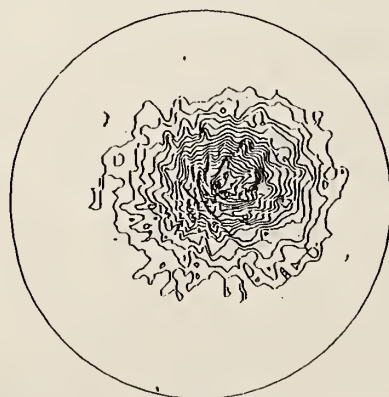
The peak height (A) and FWHM (W) of M function were calculated by,

$$A = S(r^{-3}) \text{ and FWHM} = 2\arcsin\{(4^{1/3}-1)/(1-r^3)\}^{1/2}.$$

The GL function is a linear combination of Gaussian and Lorentzian with the same FWHM, and with the best-fitted scale ratio of Gaussian/Lorentzian = 1.3(4).

<u>Sample/function type</u>	<u>Amplitude(A)</u>	<u>FWHM(W)</u>	<u>Position(C)</u>	<u>RSD</u>
YBaCuO-151/L	681(9)	37.8(7)	76.1(2)	0.053
YBaCuO-151/M	673(15)	38.7(4)	76.1(3)	0.059
YBaCuO-153/L	1720(18)	19.3(3)	83.5(1)	0.045
YBaCuO-153/M	1667(49)	21.0(2)	83.5(9)	0.061

YBACUO-151 (004)



YBACUO-153 (004)

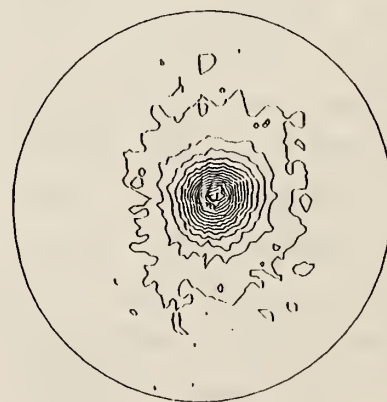


Figure 1. Observed 004 pole figures of YBaCuO-151 and YBaCuO-153. The contour lines below 1 m.r.d. levels are deleted. The step intervals are 0.3 m.r.d. for the 151 samples and 1 m.r.d. for 153.

GRAZING-ANGLE NEUTRON DIFFRACTION STUDY OF Cr/Nb/Al₂O₃ FILM

J. F. Ankner, H. Zabel, J. A. Dura, and C. P. Flynn
(University of Illinois, Urbana, IL)

and

D. A. Neumann and C. F. Majkrzak

Grazing-angle diffraction is a powerful tool in the study of surfaces and interfaces. The development of synchrotron sources in the decade since the first demonstration of grazing-angle diffraction has led to a broad application of the method as an x-ray structural probe. The comparatively low flux of conventional neutron sources had, until recently, prevented a similar use of the technique in neutron experiments. We first demonstrated the feasibility of grazing-angle neutron diffraction using a large perfect silicon crystal [1] and have now extended the technique to the study of ideally imperfect crystals, using Cr/Nb/Al₂O₃ as a test case [2]. These experiments pave the way for the use of grazing-angle neutron diffraction in studies of those materials to which neutrons are uniquely sensitive (e.g., magnetic and hydrogen-rich interfaces, surfaces, and films).

The essence of the grazing-angle diffraction technique is the excitation of a diffracted beam under conditions of total external reflection of the incident beam. Figure 1 shows the wave-vectors external to the crystal in the grazing-angle geometry. A neutron beam (\vec{k}) strikes the sample at an angle ϕ with respect to the surface and is specularly reflected (\vec{k}_s, ϕ); the sample is oriented such that an in-plane reflection (\vec{k}_G) is excited at glancing angle ϕ_G . The total reflection occurring simultaneously with the diffraction process ensures that the diffracted intensity originates in that portion of the sample which lies close to the surface.

To demonstrate grazing-angle neutron diffraction in the kinematical regime, we studied an molecular-beam epitaxy (MBE)-grown film consisting of 3200 Å Cr(110) on a 400 Å Nb(110) buffer layer atop an Al₂O₃(11 $\bar{2}$ 0) substrate. The Cr and Nb layers were crystalline with mosaic spreads of 0.3°. Figure 2 shows the intensity distributions of the specularly reflected (solid curve) and the grazing-angle diffracted beams for two different in-plane Bragg reflections: Cr(11 $\bar{2}$) (dashed) and Nb(2 $\bar{2}$ 0) (dotted). The diffracted curves were recorded with collimations ϕ_G and θ relaxed (see fig. 1) to maximize intensity. The incident beam (ϕ) had 0.017° angular divergence and was

scanned ($Q \approx 4\pi\phi/\lambda$) up through the critical angles for total external reflection of the layers; the intensity of the specularly reflected beam (solid) drops off as the critical Q of the sapphire substrate ($Q_c = 0.016 \text{ \AA}^{-1}$) is reached. The intensities of the grazing-angle diffracted beams increase with Q below Q_c as the neutron beam penetrates deeper into the sample; above Q_c (less than that of the substrate for both Cr and Nb) the intensity falls off as the in-crystal wave vector no longer satisfies the diffraction condition. This behavior occurs for both the Cr(1 $\bar{1}$ 2) and Nb(2 $\bar{2}$ 0) scans and is the signature of grazing-angle diffraction.

In summary, we have modified a triple-axis diffractometer so that it can be used for grazing-angle neutron diffraction and demonstrated the applicability of the method to imperfect crystals. The application of grazing-angle neutron diffraction to studies of magnetic and hydrogen-rich materials promises to enhance our understanding of surface and interfacial physics by utilizing the unique sensitivity of neutrons to these systems.

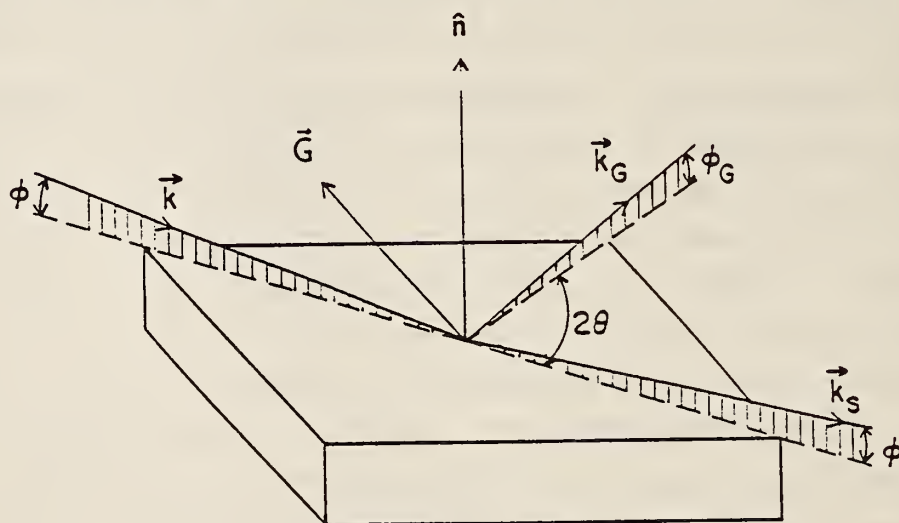


Figure 1. Grazing angle diffraction geometry. \vec{k} , \vec{k}_s , and \vec{k}_G are the incident, specularly reflected, and reflected-diffracted wave vectors.

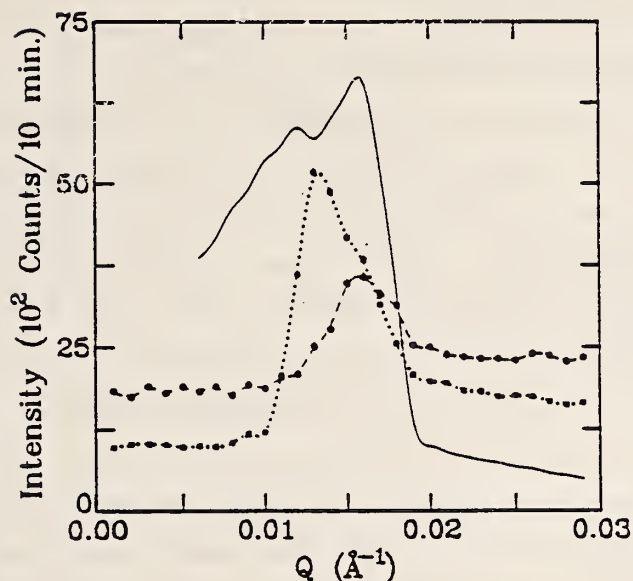


Figure 2. Grazing-angle reflectivity scans. Solid line is specularly reflected intensity (scaled down by a factor of 100), dashed Cr(112) reflected-diffracted, and dotted Nb(220) reflected-diffracted.

References

- [1] Ankner, J. F.; Zabel, H.; Neumann, D. A.; Majkrzak, C. F. Phys. Rev. B40, 792 (1989).
- [2] Ankner, J. F.; Zabel, H.; Neumann, D. A.; Majkrzak, C. F.; Dura, J. A.; Flynn, C. P. J. Phys. (submitted for publication).

NEUTRON REFLECTIVITY STUDY OF GD-Y INTERFACE

J. F. Ankner, H. Zabel, A. Matheny, J. A. Dura, and C. P. Flynn
(University of Illinois, Urbana, IL)

and

D. A. Neumann and C. F. Majkrzak

In recent years, there has been a great deal of interest in surface, interface, and thin-film magnetism. Using neutron reflectometry and grazing-angle diffraction, one can determine the magnetic structure of surface and subsurface layers in these types of systems. We have studied, using spin-polarized neutron reflectometry, the interface between Y(0001) and Gd(0001) films grown by molecular beam epitaxy (MBE).

Bulk gadolinium is a ferromagnet with $T_c = 293$ K. Recent measurements by Weller et al. [1], on the magnetism of Gd (Gd/vacuum interface) have indicated that a surface magnetic moment persists as much as 20 K above T_c . We have therefore been interested in the nature of the magnetism in other interfacial Gd systems, a first example of which is the interface with non-magnetic yttrium. Both Gd and Y are hcp metals, with approximately the same lattice constants at room temperature. The film we studied consists of a 100 Å Y(0001) cap layer on 1000 Å of Gd(0001) atop a 300 Å Y(0001) seed layer, which grows on a 1000 Å Nb(110) buffer layer and an $Al_2O_3(11\bar{2}0)$ substrate. The mosaics of the metal layers range from 0.1-0.4°. Figure 1 shows the neutron reflectivity of the film at $T = 151$ K with the incident neutron beam polarized parallel (closed circles) and antiparallel (open circles) to the magnetic moment in the Gd. At this temperature (well below T_c), the Gd layer is fully magnetized. By careful analysis of these reflectivity profiles and comparison with x-ray reflectivity data, we will be able to determine the depth-dependence of the magnetization at the topmost Gd-Y interface. We have also searched for an interfacial magnetic state above T_c (at $T = 295$ K) and find, within experimental uncertainty, no net moment at the Gd-Y interface. This result is in agreement with results obtained for Gd-Y superlattices studied by polarized neutron diffraction and suggests that the Gd-Y interface is indeed different from the surface of Gd in vacuum. We plan to study Gd interfaces with nonmetallic compounds and to use grazing-angle neutron diffraction to determine the spin orientation and crystal structure of these interfacial regions.

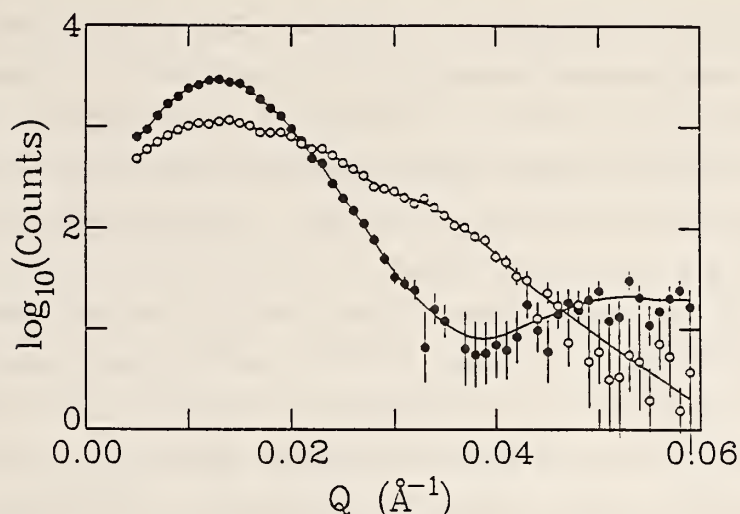


Figure 1. Neutron reflectivity of Y/Gd/Y/Nb/Al₂O₃ film at 151 K. Closed circles have neutron polarized parallel to sample moment, open antiparallel.

Reference

- [1] Weller, D.; Alvarado, S. F.; Gudat, W.; Schröder, K.; Campagna, M. Phys. Rev. Lett. 54, 1555 (1985).

DETERMINATION OF HYDROGEN DENSITY PROFILES IN THIN FILMS AND MULTILAYERS BY NEUTRON REFLECTION

C. F. Majkrzak, S. K. Satija, D. A. Neumann, and J. J. Rush

D. Lashmore and C. Johnson
(Metallurgy Division)

J. Bradshaw
(Optoline, Andover, MA)

and

L. Passell and R. DiNardo
(Brookhaven National Laboratory, Upton, NY)

The density of hydrogen in thin films or multilayers of metal hydrides can be inferred from an expansion of the host lattice as measured by conventional x-ray diffraction techniques. However, because hydrogen and deuterium have scattering lengths for neutrons that are comparable to those of most metal nuclei, unlike the corresponding case for x-ray atomic scattering amplitudes, the hydrogen density profile normal to the surface of

a flat, thin film can be determined directly from neutron reflectivity measurements. The hydrogen density modulation in an artificial superlattice along the growth direction can also be determined in this manner. Furthermore, the thin films or multilayers need be neither crystalline nor metallic; for example, the H composition profile in a H-Si superlattice created by chemical vapor deposition can be obtained by neutron reflection [1].

Often hydrogen can be loaded into a film or multilayer in either a gas cell or electrolytically, in situ, thereby making possible real-time measurements of hydrogen concentration profiles in active electrodes. The latter configuration can be realized in practice by using a single-crystal substrate (e.g., silicon), which is nearly transparent to neutrons, as the incident medium. Several thin-film metal hydride systems are currently being studied, including a Ni-Ti multilayer electrolytically charged with H and D.

Reference

- [1] Abeles, B.; Yang, L.; Leta, D.; Majkrzak, C. F. J. of Non-Crystalline Solids 97 and 98, 353 (1987).

THE MORPHOLOGY OF SYMMETRIC DIBLOCK COPOLYMERS AS REVEALED BY NEUTRON REFLECTIVITY

S. H. Anastasiadis and T. P. Russell
(IBM Research Division, San Jose, CA)

and

S. K. Satija and C. F. Majkrzak

Recently, it has been shown that symmetric diblock copolymers of polystyrene (PS) and polymethylmethacrylate (PMMA) when prepared as thin films (5000 Å or less) on silicon substrates, exhibit a strong orientation of the lamellar microdomains parallel to the surface of the substrate [1,2]. This orientation occurs when the copolymer films are annealed at temperatures above the glass transition temperatures of the PS and PMMA blocks and results from the interactions of the two blocks with the air and substrate interfaces. PMMA, the more polar species, preferentially resides at the silicon (silicon oxide)/copolymer interfaces, whereas PS, the lower surface energy component, preferentially segregates to the air/copolymer interface.

These interactions, coupled with the chemical connectivity of the PS and PMMA blocks, result in the observed multilayered structure.

In this report the details of the lamellar morphology for a series of PS and PMMA, symmetric diblock copolymers is reported where the molecular weight of the copolymer is varied. It is shown that neutron reflectivity provides the key means by which the exact nature of the interface between the copolymer microdomains can be investigated. It is also shown that the interface between homopolymers of PS and PMMA is identical to that seen in the copolymers.

Symmetric, diblock copolymers of PS and PMMA, denoted P(S-b-MMA), were purchased from Polymer Laboratories and were prepared by a successive anionic polymerization process. The complete characterization of the copolymers is shown in table 1. As can be seen, the copolymers have narrow molecular weight distributions and styrene contents close to the desired 50%. It should also be noted that either the PS or PMMA block in the copolymer was perdeuterated which provided the contrast necessary for the neutron reflectivity studies.

Samples of the copolymers were prepared on 10 cm diam, polished Si substrates. The substrates were ~ 5 mm in thickness to ensure that the substrate did not bow or bend when mounted in the sample holder. Solutions of the copolymer were prepared in toluene with the concentration being varied to produce the desired sample thickness. The substrates were fully coated with copolymer solutions and spun at 2000 rpm to produce a film with a uniform thickness. The spinning process also served to evaporate most of the solvent in the film. The substrates were then placed under vacuum at 80 °C for 24 h to remove the remaining solvent and then were heated to 170 °C for 72 h to produce the oriented lamellar morphology. The specimens were then cooled to room temperature and investigated without further heating.

Neutron reflectivity measurements were performed on the BT-4 triple-axis diffractometer at the NIST reactor. Details of the experimental geometry can be found elsewhere [7]. Experiments were performed with neutrons of wavelength $\lambda = 2.35 \text{ \AA}$ over an angular range of $2\theta = 0^\circ$ to 1.7° . This translates into a neutron momentum, k_0 range from 0 to $\sim 0.1 \text{ \AA}^{-1}$ where $k_0 = (2\pi/\lambda) \sin \theta$. Under such condition reflectivities down to 10^{-6} could be measured which proved to be crucial to these studies [7,8].

The neutron reflectivity profile measured for the P(S-b-d-MMA) diblock copolymer, where the molecular weight of each block is $\sim 15,000$, after annealing at 170°C for 72 h is shown in figure 1. As can be seen at small values of the neutron momentum, total external reflection is seen below the critical angle. Above this the reflectivity drops by nearly two orders of magnitude whereupon a strong first-order Bragg-reflection at $k_0 = 0.0195 \text{ \AA}^{-1}$ is seen. This is followed by a further decrease in the reflectivity with the appearance of second- and third-order reflections at k_0 's of 0.0375 and 0.0540 \AA^{-1} , respectively. The Bragg reflections are directly attributable to the layering of the lamellar morphology parallel to the surface of the film and the positions of the Bragg reflections yield directly the period of the lamellar microdomain morphology. In this case the period is 175 \AA which is comprised of a PS microdomain with a size of 91 \AA and a PMMA microdomain of 84 \AA . More importantly, the interface between the PS and PMMA microdomains is found to be $50 \pm 3 \text{ \AA}$. Using this model for the variation in the neutron scattering length density normal to the film surface, the calculated reflectivity profile, indicated by the solid line in figure 1, is obtained. The agreement between the calculated and measured reflectivity profile is very good over the entire k_0 range and over 5.5 orders of the reflectivity. Variation of the parameters outside of the stated values produces reflectivity profiles that do not agree with the experimentally measured profile. It must be emphasized that such precision on the width of the interface between the two microdomains was, heretofore, impossible.

Increasing the molecular weight of the blocks to $\sim 50,000$ per block produces dramatic changes in the neutron reflectivity profiles. Shown in figure 2 is the measured reflectivity profile of the P(d-S-b-MMA) diblock copolymer after annealing at 170°C for 72 h under vacuum. As with the lower molecular weight specimen, at small values of k_0 total external reflection. However, at higher k_0 at least five orders of Bragg reflections are evident which yield a period of 398 \AA which is comprised of PS and PMMA microdomain sizes of 210 \AA and 188 \AA , respectively. As expected, the period of the lamellar morphology has increased with the increase in the molecular weight of the copolymer. The large number of Bragg reflections also provides a high sensitivity to the interface between the copolymer microdomains. Shown in figure 2 by the solid line is the calculated reflectivity profile where the interface is described by a hyperbolic tangent function where the effective

width of the interface is 50 ± 3 Å. This describes the observed reflectivity quite well over the entire measured k_0 range. Using this functional form for the interface, variation of the interface width outside of these limits produces an unacceptable description of the measured reflectivity profile. Also shown in figure 2 as the dashed line, is the calculated reflectivity profile where a simple linear gradient of the neutron scattering length density was used to describe the concentration variation across the interface between the PS and PMMA microdomains. As can be seen, this model describes the data reasonably well over the entire k_0 range, but does not produce as good a fit to the data as the hyperbolic tangent function. Consequently, the neutron reflectivity results clearly show that whatever the functional form of the concentration gradient across the interface is, it must closely follow the hyperbolic tangent functional form. Such details on the morphology of block copolymers were previously unattainable by other techniques.

Similar studies have been performed on the P(S-b-d-MMA) diblock copolymer where the molecular weight of each block is $\sim 50,000$. In this case the neutron reflectivity profile yields a period of 512 Å comprised of a PS and PMMA microdomains with sizes of 268 Å and 244 Å. As with the P(d-S-b-MMA) copolymer the interface was well described by a hyperbolic tangent function with an effective width of 47 ± 4 Å. Thus, with the exception of the variation in the length of the period due to the increase in the molecular weight, these results are identical to the other cases.

Finally, a P(d-S-b-MMA) diblock copolymer where the molecular weight of each block was $\sim 150,000$ was investigated. It has been found that the rate at which the copolymer microdomains orient parallel to the film surface depends strongly upon the molecular weight of the copolymer. For such high molecular weights the time required for the lamellar orientation is quite long. Therefore, a copolymer film was prepared where the total thickness of the specimen corresponded to one-half of the period size. This specimen was annealed for 240 h at 170 °C. The neutron reflectivity profile obtained from this specimen is shown in figure 3. As can be seen, periodic oscillations are seen in the data with at least two different characteristic frequencies. The frequencies correspond to the total thickness of the specimen and the thickness of the deuterated PS microdomain. The reflectivity results could be well described by the scattering length density profile shown in the inset of the figure. This model is comprised of a 225 Å layer of deuterated PS on

top of a 156 Å layer of PMMA. The two layers are separated by an interface with a composition variation across the interface that is given by a hyperbolic tangent function with an effective width of 50 ± 4 Å.

Therefore, the clear picture that emerges from the combined results of these studies is that the period of the lamellar microdomain morphology increase with the molecular weight of the copolymer. If N is the total number of segments in the copolymer, then these results indicate that L , the period, varies with $N^{0.65}$ which agrees with theories describing copolymers in the strong segregation limit. The width of the interface is found to be independent of the copolymer molecular weight, and, for the P(S-b-MMA) copolymers, is found to be 50 Å. Independent studies on bilayers of PS and PMMA homopolymers [7,9] have shown that the interface between the homopolymers is well described by a hyperbolic tangent function (or other functions that closely follow this form) with an effective width of 50 Å in precise agreement with the copolymer results. From the measured values of the interaction parameter between PS and PMMA [10] and the values of the statistical segment lengths of PS and PMMA, the width of the interface can be calculated theoretically. These calculations yield a value of the interface of 21 Å. Unfortunately, this value is more than a factor of two smaller than the measured value. This discrepancy is well outside of any experimental errors in the reflectivity results or errors associated with the interaction parameter or the statistical segment lengths and, in our opinion, points to a significant shortcoming of current theoretical treatments of the interface between homopolymers and copolymer microdomains.

Table 1. Temperature dependence of PS/PMMA parameters

Copolymer	M_{ps}	M_{PMMA}	M_w/M_n	χ
P(S-b-d-MMA)	14,670	15,107	1.10	0.50
P(d-S-b-MMA)	52,900	48,000	1.07	0.50
P(S-b-d-MMA)	56,300	65,000	1.12	0.47
P(d-S-b-MMA)	169,500	131,900	1.08	0.53

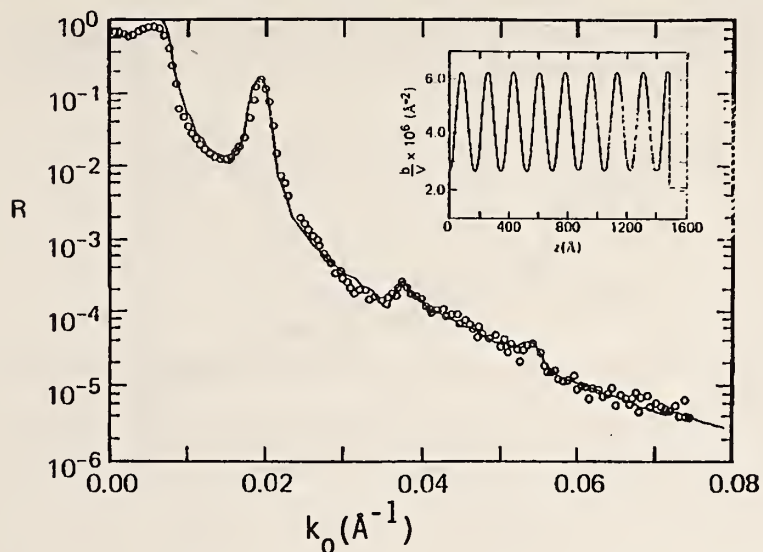


Figure 1. Neutron reflectivity profile of a P(S-b-d-MMA) diblock copolymer film annealed on a Si substrate for 72 h at 170 °C where the total copolymer molecular weight is $\sim 30,000$. The points are the measured reflectivity profile whereas the solid line is the calculated reflectivity profile using the scattering length density profile shown in the inset.

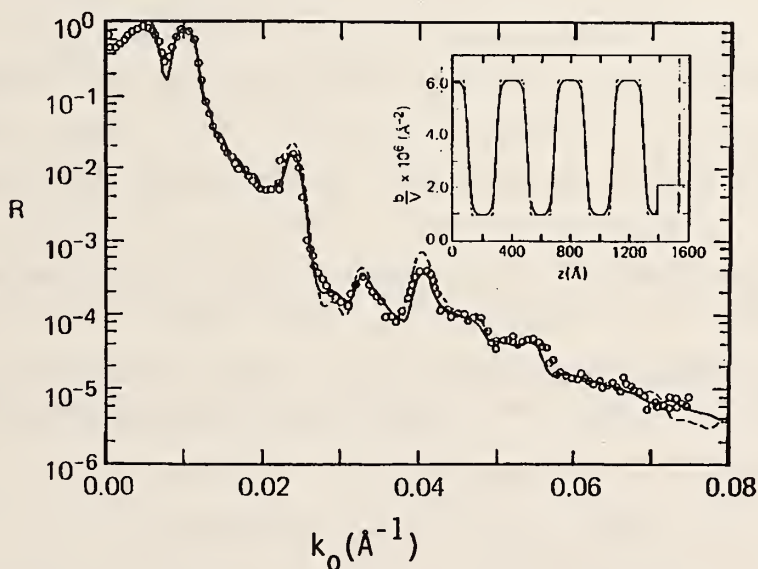


Figure 2. Neutron reflectivity profile of a P(d-S-b-MMA) diblock copolymer film on a Si substrate annealed for 72 h at 170 °C where the total copolymer molecular weight is $\sim 100,000$. The points are the measured reflectivity profile the line is the calculated reflectivity profile using the hyperbolic tangent function to describe the interface between the copolymer microdomains and the dashed line is that calculated assuming a linear gradient between the microdomains. The models used to calculate the reflectivity profiles are shown in the inset.

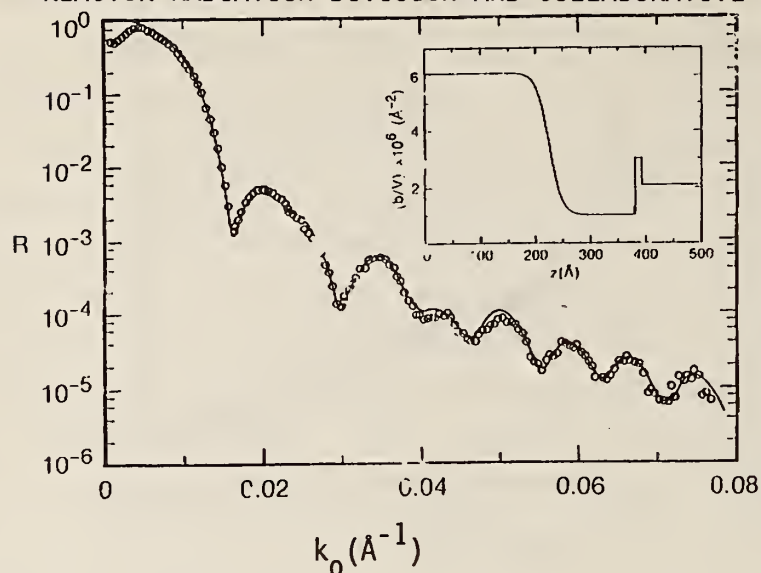


Figure 3. Neutron reflectivity profile for a P(d-S-b-MMA) diblock copolymer annealed for 240 h at 170 °C where the total molecular weight of the copolymer is ~ 300,000. The solid line is the calculated reflectivity profile using the scattering length density profile shown in the inset.

References

- [1] Coulon, G.; Russell, T. P.; Deline V. R.; Green P. F. *Macromol.* **22**, 2581 (1989).
- [2] Russell, T. P.; Coulon, G.; Deline, V. R.; Miller, D. C. *Macromol.* (in press).
- [3] Helfand, E.; Wasserman, Z. R. *Developments in block copolymers - 1*. I. Goodman, ed. Appl. Sci. Pub., New York (1982).
- [4] Meier, D. J. *Thermoplastic elastomers--research and development*. N. Legge, G. Holden, H. Schroeder, eds. Hanser Pub., Germany (1988).
- [5] Ohta, T.; Kawasaki, K. *Macromol.* **19**, 2621 (1986).
- [6] Semenov, A. N. *Zh. Eksp. Teor. Fiz.* **88**, 1242 (1985).
- [7] Anastasiadis, S. H.; Russell, T. P.; Satija, S. K.; Majkrzak, C. F. *J. Chem. Phys.* (submitted for publication).
- [8] Anastasiadis, S. H.; Russell, T. P.; Satija, S. K.; Majkrzak, C. F. *Phys. Rev. Lett.* **62**, 1852 (1989).
- [9] Fernandez, M. L.; Higgins, J. S.; Penfold, J.; Ward, R. C.; Shackleton, C.; Walsh, D. J. *Polymer* **29**, 1923 (1988).
- [10] Russell, T. P.; Hjelm, R. P.; Seeger, P. A. *Macromol.* (submitted for publication).

TEMPERATURE DEPENDENCE OF THE MORPHOLOGY OF THIN DIBLOCK
COPOLYMER FILMS AS REVEALED BY NEUTRON REFLECTIVITY

T. P. Russell and S. H. Anastasiadis
(IBM Research Division, San Jose, CA)

and

S. K. Satija and C. F. Majkrzak

Thin films of symmetric diblock copolymers on solid substrates have been shown to exhibit a strong orientation of the lamellar microdomains parallel to the surface of the substrate upon heating to temperatures above the glass temperature [1-4]. Specular neutron reflectivity measurements [3,4] clearly show that this orientation is parallel to the surface of the substrate over large lateral length scales. Consequently, the morphology produced by simply annealing the films above the glass transition temperature is that of a perfect multilayer. This behavior is found provided the annealing temperature is below the microphase separation transition temperature (MST) where a transition from an ordered to a disordered morphology occurs. For perfectly symmetric diblock copolymers the MST occurs when $\chi N = 10.5$ where χ is the Flory-Huggins interaction parameter and N is the total number of segments in the copolymer chain. For thin films of symmetric diblock copolymers annealed at temperatures above the MST, recent neutron reflectivity studies [3] have shown that there is a preferential segregation of one of the components to the air/copolymer and the copolymer/substrate interfaces. Due to the connectivity of the blocks this excess surface concentration induces an oscillatory variation in the composition of the two components normal to the interface that is exponentially damped. This behavior has been shown to be in agreement with recent theoretical arguments [5].

In this report neutron reflectivity studies on the temperature dependence of the morphology of diblock copolymers in the vicinity of the MST are discussed. At temperatures below the MST the ordered multilayered lamellar morphology is found to penetrate through the entire specimen. At temperatures above the MST the periodic variation in the composition of the components is maintained but a clear dissipation of the order is found with increasing distance from either the air/copolymer or copolymer/substrate interfaces. An exponentially damped squared cosine function from both interfaces is found to well describe the reflectivity results. The

characteristic decay length is found to decrease with increasing temperature in accordance with mean field arguments. Results from two different copolymers with two different molecular weights and, consequently, two different MST's are found to be identical on a reduced temperature scale.

Symmetric, diblock copolymers of PS and PMMA, denoted P(S-b-MMA), were purchased from Polymer Laboratories and were prepared by a successive anionic polymerization process. The P(S-b-d-MMA) copolymer, where the methacrylate block is perdeuterated, had a PS block molecular weight of 14,670 and a PMMA block molecular weight of 15,107. The total copolymer had an M_w/M_n of 1.1 and the fraction of PS in the copolymer was 0.5. The P(d-S-b-MMA) copolymer had a total molecular weight of 27,600 with $M_w/M_n = 1.08$ and a PS fraction of 0.43.

Samples of the copolymers were prepared on 10 cm diam, polished Si substrates. The substrates were ~ 5 mm in thickness to ensure that the substrate did not bow or bend when being mounted in the sample holder. Solutions of the copolymer were prepared in toluene with the concentration being varied to produce the desired sample thickness. The substrates were fully coated with the copolymer solutions and spun at 2000 rpm to produce a film with a uniform thickness. The spinning process also served to evaporate most of the solvent in the film. The substrates were then placed under vacuum at 80 °C for 24 hours to remove the remaining solvent.

Neutron reflectivity measurements were performed on the BT-4 triple-axis diffractometer at the NIST reactor experimental hall. Details of the experimental geometry can be found elsewhere [4]. Experiments were performed with neutrons of wavelength $\lambda = 2.35$ Å over an angular range of $2\theta = 0$ to 1.7° . This translates into a neutron momentum k_0 range from 0 to ~ 0.1 Å⁻¹ where $k_0 = (2\pi/\lambda) \sin \theta$.

Experiments were performed at temperature by heating the cast, dried specimen under vacuum in a heated sample stage on the spectrometer. It is important to note that experiments were performed initially at temperatures above the MST of the copolymers to prevent a complete ordering of the copolymer films. It was found that heating the samples to temperatures below the MST initially, followed by heating to temperatures above the MST was not successful. It appeared as if the specimens required a substantial amount of time to reach equilibrium; i.e., to lose completely the ordering induced at the lower temperature.

The neutron reflectivity profile measured for the P(S-b-d-MMA) diblock copolymer, where the molecular weight of each block is $\sim 15,000$, at 155°C is shown in figure 1. As can be seen at small values of the neutron momentum total external reflection is seen below the critical angle. Above this the reflectivity is seen to drop by nearly two orders of magnitude where upon a strong first-order Bragg reflection at $k_0 = 0.0195 \text{ \AA}^{-1}$ is seen. At higher values of k_0 a second-order reflection and a diffuse third-order reflection are evident. The solid line in the figure is the calculated reflectivity profile using the scattering length density profile shown in the inset where the period is 175 \AA and the effective width of the interface between the PS rich and PMMA rich microdomains is 50 \AA . For the P(S-b-d-MMA) copolymer investigated here the MST, calculated from the molecular weight of the copolymer and the temperature dependent interaction parameter [6], is 179°C .

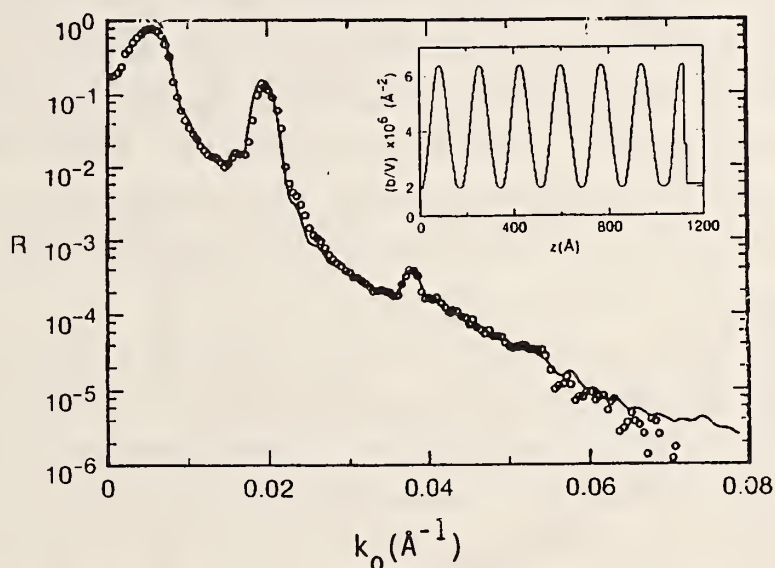


Figure 1. Neutron reflectivity profile of a P(S-b-d-MMA) diblock copolymer film on a Si substrate at 155°C . The points are the measured reflectivity profile, the line is the calculated reflectivity profile using scattering length density profile shown in the inset.

Thus, at 155°C the copolymer is below, but near, the MST. In keeping with this, the two microphases in the lamellar morphology are not pure PS or PMMA but are only rich in either component and the total fraction of the specimen that is occupied by the interface is ~ 0.65 . Consequently, while the oriented lamellar morphology propagates through the entire specimen, it is very diffuse due to the proximity of the MST.

Experiments were performed at several temperatures above the MST. As an example of a typical reflectivity result, the data for the experiment performed at 200 °C is shown in figure 2. In general, at temperatures not too far above the MST, the first order Bragg reflection persists but is broader and less intense than that seen at temperatures below the MST. In addition, the higher order reflections become much more diffuse. The solid line in this figure represents the reflectivity profile calculated using the scattering length density profile shown in the inset. Here the scattering length density as a function of the distance z from either interface is given by $b + b_E \exp(-z/\zeta) \cos^2(\pi z/L)$, where b is the average scattering length density of the specimen, b_E is the excess scattering length density at the interface, ζ is the correlation length characterizing the damping of the oscillatory composition profile and L is the period. For this measurement at 200 °C, ζ is 600 ± 50 Å and L is 162 Å. The results for the other measurement temperatures above the MST are given in table 1. Also shown in table 1 are the results for the P(d-S-b-MMA) specimen which was annealed at 170 °C and quenched to room temperature. Detailed discussions of these data can be found elsewhere [3]. It is important to note that the MST for this copolymer is 40 °C which results from the difference in the molecular weight.

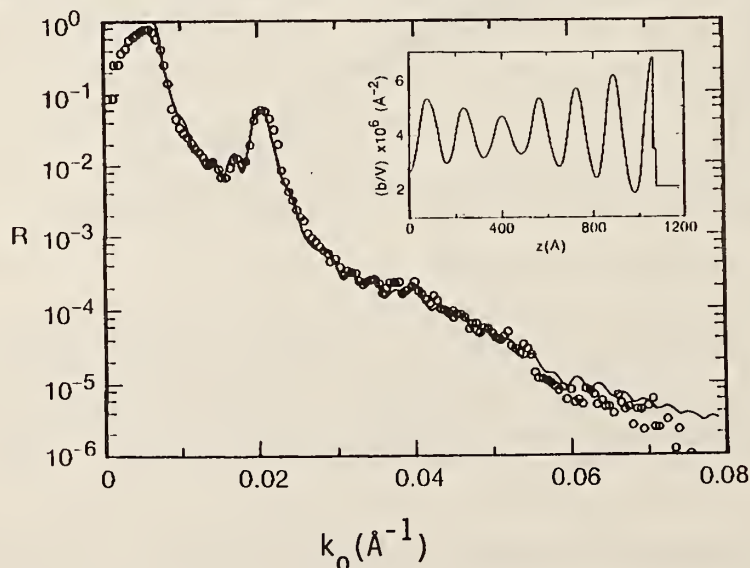


Figure 2. Neutron reflectivity profile for a P(S-b-d-MMA) diblock copolymer at 200 °C. The solid line is the calculated reflectivity profile using the scattering length density profile shown in the inset.

Table 1. Temperature dependence of PS/PMMA parameters

Copolymer	T°C	ζ (Å)	I(Å)
P(d-S-b-MMA)	170	95 ± 7	150
P(S-b-d-MMA)	185	1100 ± 100	166
P(S-b-d-MMA)	195	800 ± 75	161
P(S-b-d-MMA)	200	600 ± 50	162

The results in table 1 clearly show that the period above the MST is lower than that found for the copolymers at temperature below the MT and is not a strong function of the temperature. Secondly, as the temperature is increased above the MST, the correlation length is seen to decrease dramatically.

These results can be understood in terms of the recent mean field arguments of Fredrickson [5]. In his treatment the surface induced ordering can be described by an exponentially damped cosine function which is identical in form to the function used here to describe the scattering length density profile from the interface. According to Fredrickson [5] the correlation length ζ is given by

$$\frac{1}{\zeta} = \frac{(6f(1-f) [(\chi N)_s - (\chi N)])^{1/2}}{Nb^2} \quad (1)$$

where f is the fraction of one component in the copolymer, N is the total number of segments in the copolymer, b is the average statistical segment length of the copolymer, $(\chi N)_s$ is the value of (χN) at the MST and (χN) is the value of (χN) at the measurement temperature. These parameters are available from previous studies for the copolymers of interest here [3,6].

As shown previously, χ is of the form $A + B/T$ where T is the absolute temperature. Therefore, eq (1) can be rewritten as

$$\frac{1}{f(1-f)B\zeta^2} = \frac{6}{b^2} (1/T_s - 1/T) \quad (2)$$

From this equation it is seen that, at temperatures above the MST, as the measurement temperature approaches the MST, ζ gets larger and at the MST ζ becomes infinite. This merely states that as the MST is approached, the ordering induced by the surface propagates further into the specimen and at the MST and below the ordering completely saturates the specimen.

This behavior is precisely what is seen in the experiments reported here. However, direct application of eq (2), taking into account the differences in the molecular weights and fractions of PS in the copolymers, does not yield the expected linear behavior. This results from the precision to which χ must be known for this copolymer since χ has a very weak temperature dependence. Adjusting χ by only 2% brings the data into align with the theoretical arguments. It is not possible, at this time, to measure χ with better precision. However, variation of χ by this small amount brings the data for both the P(S-b-d-MMA) and the P(d-S-b-MMA), which have different molecular weights, fraction of PS, and MST's, into very good agreement with each other. It is clear from this that the mean field theoretical arguments describe the behavior seen for these copolymers well, within the experimental limitations.

References

- [1] Coulon, G.; Russell, T. P.; Deline, V. R.; Green, P. F. *Macromol.* 22, 2581 (1989).
- [2] Russell, T. P.; Coulon, G.; Deline V. R.; Miller, D. C. *Macromol.* (accepted for publication).
- [3] Anastasiadis, S. I.; Russell, T. P.; Satija, S. K.; Majkrzak, C. F. *Phys. Rev. Lett.* 62, 1852 (1989).
- [4] Anastasiadis, S. H.; Russell, T. P.; Satija, S. K.; Majkrzak, C. F. *J. Chem. Phys.* (submitted for publication).
- [5] Fredrickson, G. H. *Macromol.* 20, 2535 (1987).
- [6] Russell, T. P.; Hjelm, R. P.; Seeger, P. A. *Macromol.* (submitted for publication).

**NEUTRON REFLECTIVITY STUDY OF THE DENSITY PROFILE OF AN ADSORBED
DIBLOCK COPOLYMER AT THE SOLUTION-QUARTZ INTERFACE**

S. K. Satija and C. F. Majkrzak

S. K. Sinha, E. B. Sirota, and J. Hughes
(Exxon Research and Engineering Co., Annandale, NJ)

and

T. P. Russell
(IBM Almaden Research Center, San Jose, CA)

Adsorption of polymers at a solid-liquid interface is of considerable practical importance. There has been a considerable amount of work done to gain understanding of the conformations of adsorbed polymers from a solution near a solid surface. This work has involved various different techniques including, ellipsometry [1], surface force measurement [2,3], and x-ray fluorescence [4]. A large body of theoretical work [5,6] has also been carried out to understand the equilibrium concentration profiles for a polymer solution near a solid wall. Despite this work a detailed understanding of the problem is still lacking.

We present results of neutron reflectivity measurement on solutions of Poly (styrene-*b*-methymethacrylate), PS-PMMA, diblock copolymers near a quartz wall. By utilizing all four combinations of hydrogenated and deuterated blocks, we are able to determine the density profile of the PMMA blocks adsorbed on to the quartz wall. The concentration of polystyrene segments beyond this initial layer of PMMA block seems to be too small to be seen by our experiments.

The cell used for the experiment is shown in figure 1 and is similar in design to a cell used by Kitchens et al. [7] for their quartz/liquid-helium interface experiment. It consists of a large single crystal of quartz (B) (200 x 75 x 25 mm³) which was optically polished on one face (C). The quartz crystal was clamped with brass bolts between a pair of rigid stainless steel plates (A). An 0.5 mm teflon gasket was used as a seal between the quartz crystal and top steel plate. The gap provided by the teflon gasket was used as the cell volume for the polymer solutions. The cell was filled through two small openings (G) in the top steel plate. The neutron beam was transmitted through the quartz and reflected internally at the liquid interface with the reflected beam coming out through the quartz on the other side.

Figures 2 and 3 show neutron reflectivity profiles from all four combinations of block copolymers used for the present experiments. In each case the reflection cell was allowed to adsorb the polymer for 1 hour before taking reflectivity data. Each profile took 12 hours to complete and no time-dependent effects were seen. This was confirmed by rerunning the entire profile in two cases and rerunning selected portions of the profile in the other cases. For three of the copolymer solutions reruns were also done starting with fresh cleaned cell and polymer solutions. No difference was noted between the two runs. The profiles shown in figures 2 and 3 are thus reproducible.

The first thing to be noticed from figures 2 and 3 is that deuteration of the PS block does not change the reflectivity profile in any significant way. For example, profiles of hPS-hPMMA and dPS-hPMMA are similar in figure 2 and profiles of hPS-dPMMA and dPS-dPMMA are similar in figure 3. Deuteration of PMMA block, however, changes the reflectivity profile significantly at wavevectors higher than $.02 \text{ \AA}^{-1}$ as shown in figure 4 for hPS-hPMMA and hPS-dPMMA.

Analysis of the data was done by only varying the concentration of PMMA segments near the quartz surface assuming the concentration of PS to be zero. Many different scattering density profiles were tried in order to fit the reflectivity data for all four samples simultaneously. The density profile of PMMA that best seems to fit the data is as follows. According to this profile, near the quartz surface the density is given by

$$\phi = \phi_s \rho_{\text{PMMA}} + (1 - \phi_s) \rho_{\text{CCl}_4}$$

with the volume fraction of PMMA, $\phi_s = 0.42$. The volume fraction of PMMA then goes down in a parabolic manner with a functional form.

$$\phi_s * (D^2 - z^2)/D^2$$

with $D = 45 \text{ \AA}$. This is equivalent to a collapsed PMMA film of $\sim 30 \text{ \AA}$ thickness. Similar fits to the data could be obtained with a PMMA film of 30 \AA thickness with a 15 \AA Gaussian smearing at the polymer solvent interface.

The thickness of 30 Å means that quartz surface is covered by flattened disks of PMMA blocks whose thickness is roughly equal to $R_{g, \text{PMMA}}$, the radius of gyration of the PMMA block in CCl_4 . Thus the PS-PMMA copolymer adsorbs rather strongly to the quartz surface by virtue of the affinity of PMMA block to the quartz surface and the PS blocks extend from the PMMA blocks in a stretched configuration. This picture is similar to the one obtained by Hadziioannou et al. [3] from their experiment of forces between surfaces of PS-PV2P block copolymers adsorbed on mica. Hadziioannou et al., however, had to postulate the existence of a PV2P layer near the mica surface, whereas the reflectivity measurements do indeed show that there is an initial compacted layer of PMMA near the quartz surface.

In summary, we have shown that neutron reflectivity is a useful technique for the study of polymer-solution interfacial density profiles. In particular, the results of neutron reflectivity measurements, when combined with other techniques such as force measurements, x-ray reflectivity, etc., should lead to a good understanding of this long standing problem.

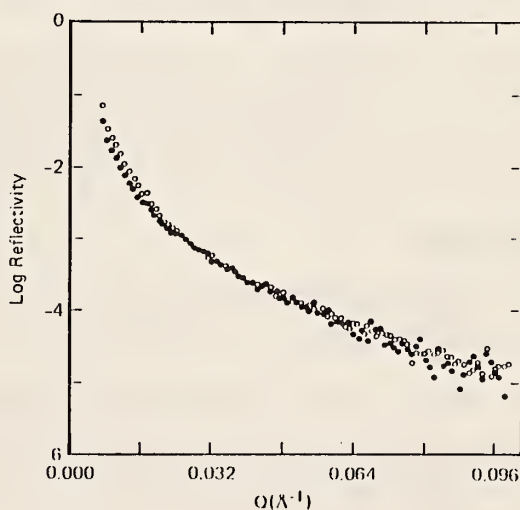
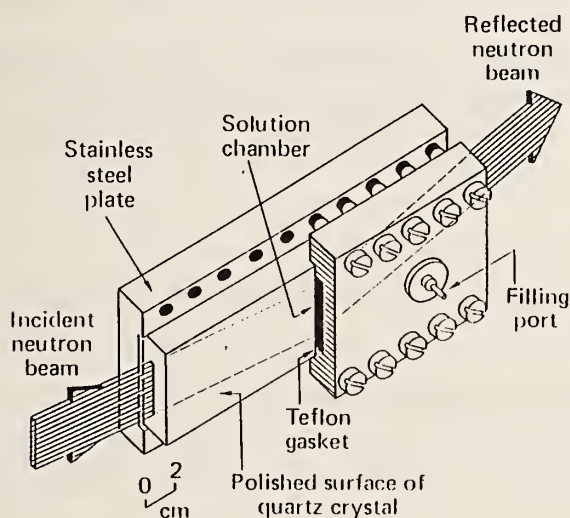


Figure 1. (left) Schematic diagram of the solution scattering cell used in these experiments. Details of the cell are discussed in the text.

Figure 2. (right) Neutron reflectivity profiles for P(S-b-MMA) [o] and P(d-S-b-MMA) [o] copolymers dissolved in CCl_4 at a concentration of $0.4\text{g}/100\text{ cm}^3$.

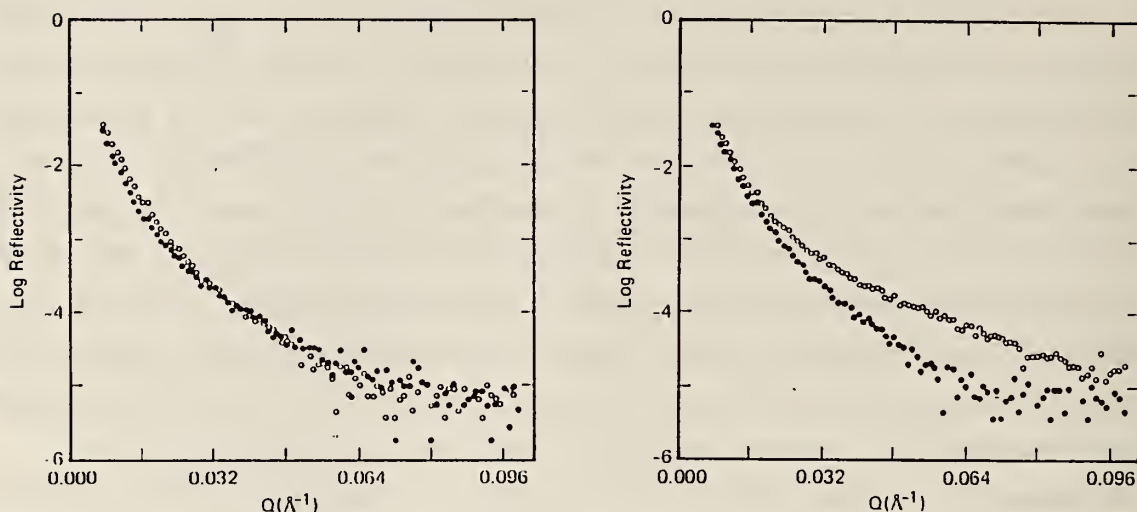


Figure 3. (left) Neutron reflectivity profiles for P(S-b-MMA) [o] and P(d-S-b-d-MMA) [o] copolymers dissolved in CCl_4 at a concentration of $0.4\text{g}/100\text{ cm}^3$.

Figure 4. (right) Comparison of the neutron reflectivity profiles obtained for P(S-b-MMA) [o] and P(S-b-d-MMA) [o] where only the labeling of the MMA block was varied and the concentrations of both copolymers in solution is $0.4\text{g}/100\text{ cm}^3$.

References

- [1] Kawaguchi, M.; Takahashi, A. J. J. Polym. Sci. Polym. Phys. Ed 18, 2069 (1980).
- [2] Klein, J. J. Chem. Soc., Faraday Trans. 79, 99 (1983).
- [3] Hadziioannou, G.; Patel, S.; Granick S.; Tirrell, M. J. Am. Chem. Soc. 108, 2869 (1986).
- [4] Bloch, J. M.; Sansone, M.; Rondelez, F.; Peiffer, B. G.; Pincus, P.; Kim M. W.; Eisenberger, P. Phys. Rev. Lett 54, 1039 (1985).
- [5] deGennes, P. G. Macromol. 14, 1637 (1981) and references therein.
- [6] Milner, S. T.; Witten, T. A.; Cates, M. E. Macromol. 21, 2160 (1988).
- [7] Kitchens, T. A.; Overshizen, T.; Passell, L.; Schermer, R. I. Phys. Rev. Lett. 32, 791 (1974).

SANS STUDIES OF BLENDS OF CROSSLINKED PSD WITH LINEAR PSH

R. M. Briber and B. J. Bauer
(Polymers Division)

Small angle neutron scattering (SANS) has been used to study the scattering function and thermodynamics of blends of linear protonated polystyrene (PSH) and crosslinked deuterated polystyrene (PSD). Two series of samples were synthesized. In both cases the linear PSH was dissolved in deuterated (d_8) styrene monomer containing a small amount of divinyl benzene as a crosslinker. The styrene/divinyl benzene mixture was then polymerized using a free radical initiator to form the PSD network around the linear PSH chains. The samples were all made at a concentration of 50/50 by weight PSD/PSH. Series 1 is a set of samples with the same network ($N_c = 387$, where N_c is the average number of monomer units between crosslinks) varying the length of the linear chain ($N_b = 91, 308, 422, 981, 1711$, and 3413 , where N_b is the number of monomer units in the linear chain). Series 2 is a set of samples containing the same length linear chain ($N_b = 422$) varying the network density systematically ($N_c = \infty, 960, 475, 345, 260$, and 158).

In the series 1 samples as the length of the linear chain is increased the SANS scattering increases as the sample approaches phase separation. The data were plotted in the form $S(q)^{-1}$ versus q^2 which yields a linear relation and allows extrapolation to $q = 0$ and hence gives $S(0)$. $S(0)$ is related to the second derivative of the free energy of the system, $\partial^2 \Delta f / \partial \phi^2$, which is composed of terms relating to the entropy and enthalpy of mixing of the linear chains in the network and the elasticity of the network. For H/D blends the enthalpy of mixing (i.e., the Flory-Huggins interaction parameter) is small ($\chi \sim 1.5 \times 10^{-4}$). As the length of the linear chain increases the entropy of mixing decreases until it can no longer balance the unfavorable elastic contribution from the network and phase separation occurs. Indeed it was found that the sample with the longest linear chain length ($N_b = 3413$) has a negative intercept when plotted as $S(q)^{-1}$ versus q^2 indicating that the sample was phase separated.

In the series 2 samples the scattering increases as the network density increases (N_c decreases). The elastic contribution to the free energy increases as N_c decreases until it overwhelms the mixing portion of the free energy and phase separation occurs. Again a plot of $S(q)^{-1}$ versus q^2 gave a straight line which allowed extrapolation to $q = 0$ to obtain $S(0)$. At the

highest crosslink density ($N_c = 158$) the intercept was negative indicating that phase separation had occurred. Assuming additivity of the elastic and mixing terms in the free energy, the second derivative of the elastic contribution to the free energy can be calculated from $S(0)$. The values of $\partial^2 \Delta f_{\text{elas}} / \partial \phi^2$ obtained for the series 2 samples are given in table 1. A plot of $S(0)^{-1}$ versus N_c^{-1} should allow the extrapolation to the value of N_c where $S(0)^{-1} = 0$ corresponding the value of N_c where the system phase separates. Such a plot is show in figure 1. The extrapolated value of N_c where phase separation occurs is $N_c = 160$, agreeing closely with the value of $N_c = 158$ for the sample which was found to be phase separated.

In conclusion, it has been found that linear chains can be incorporated into networks formed by sequential polymerization of the network around the linear component (i.e., single phase blend of linear and crosslinked polymers) if the network density is kept low ($N_c > 150$). This result helps to explain why similar systems studied in the past at higher crosslink densities have almost always phase separated at some point during the synthesis. SANS can be used as a tool to study the thermodynamics of these systems and values for the elastic contribution to the free energy can be calculated from the extrapolated zero angle scattering.

Table 1. Number of monomers between crosslinks, zero angle scattering, correlation length, $k_n/S(0)$ ($= \partial^2 \Delta f_{\text{total}} / \partial \phi^2$), and the elastic contribution to the second derivative to the free energy ($\partial^2 (\Delta f/kT) / \partial \phi^2$ elastic) for the series 2 samples.

Series 2 ($N_b = 422$)				
N_c	$S(0) \text{ cm}^{-1}$	$\xi \text{ \AA}^{-1}$	$k_n/S(0)$	$\partial^2 (\Delta f/kT) / \partial \phi^2$ elastic
			<u>mole/cm³ molecule x10⁶</u>	<u>mole/cm³ molecule x10⁷</u>
∞	79.0	51.9	5.2	----
960	65.9	60.0	4.3	4.4
475	113	66.3	3.6	- 61
345	127	93.6	3.2	-101
260	227	111	1.8	-243
158†	***	***	***	***

†The sample with $N_c = 158$ was phase separated.

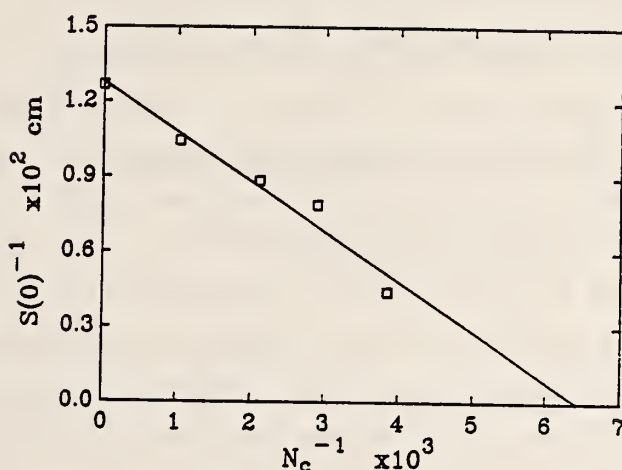


Figure 1. Plot of $S(0)^{-1}$ versus N_c for the series 2 samples.

THE EFFECT OF RADIATION CROSSLINKING ON THE SCATTERING FUNCTION IN WEAKLY INTERACTING MISCIBLE POLYMER BLENDS

R. M. Briber and B. J. Bauer
(Polymers Division)

Using small angle neutron scattering (SANS) the scattering function in the single phase region of the phase diagram was measured for the weakly interacting polymer blend system of protonated polystyrene (PSH) and deuterated polystyrene (PSD) which had been crosslinked by gamma rays from a cobalt 60 source. A theory presented by de Gennes [1] for the critical scattering from crosslinked blends and the effect of crosslinking on the phase diagram had been tested previously using SANS with the strongly interacting blend system poly(vinylmethylether)/PSD [2]. In the PVME/PSD system the theory was found to describe the behavior of the observed scattering function qualitatively (the scattering function for a crosslinked polymer blend develops a peak at a nonzero q vector, q^*). The measured behavior of q^* was found to agree with theory with q^* scaling with the average radius of gyration between crosslinks. The divergence of the scattering intensity at q^* , $S(q^*)$, was found to be mean field within experimental error with $S(q^*)^{-1} \sim (\chi_s - \chi)^\gamma$ where $\gamma = 1.0$ (χ is the Flory-Huggins interaction parameter and χ_s is the value of χ at the spinodal). The

peak observed in the scattering function at q^* was not present at the temperature of crosslinking but only became apparent upon raising the temperature (changing χ).

A blend of high molecular weight PSD and PSH (each with $M_n = 10^6$) was crosslinked using gamma rays from a Co^{60} source. Samples with doses of 0 (control), 55, 125, and 200 MRad were prepared. The corresponding number of monomers between crosslinks, N_c , calculated for these samples are ∞ , 1800, 700, and 500, respectively. In the crosslinked PSH/PSD system the measured scattering function was found to be essentially unchanged from the scattering function measured for the uncrosslinked system (see fig. 1). The predictions for the uncrosslinked and crosslinked system $N_c = 700$ is shown in figure 2. Other values of N_c gave similar results. Clearly the data shown in figure 1 does not agree with the prediction from the theory as shown in figure 2. There is no peak present as predicted by the theory, although there is a small decrease in $S(0)$ after crosslinking. The same results were observed initially with the PVME/PSD system though a peak did subsequently appear upon changing the temperature (changing χ). In the PSD/PSH system there is almost no temperature dependence of χ . Combining these observations with the results from the PVME/PSD system the conclusion can be drawn that the theory does not predict the scattering observed after crosslinking if χ remains roughly constant but does predict the observed behavior qualitatively when χ is subsequently changed.

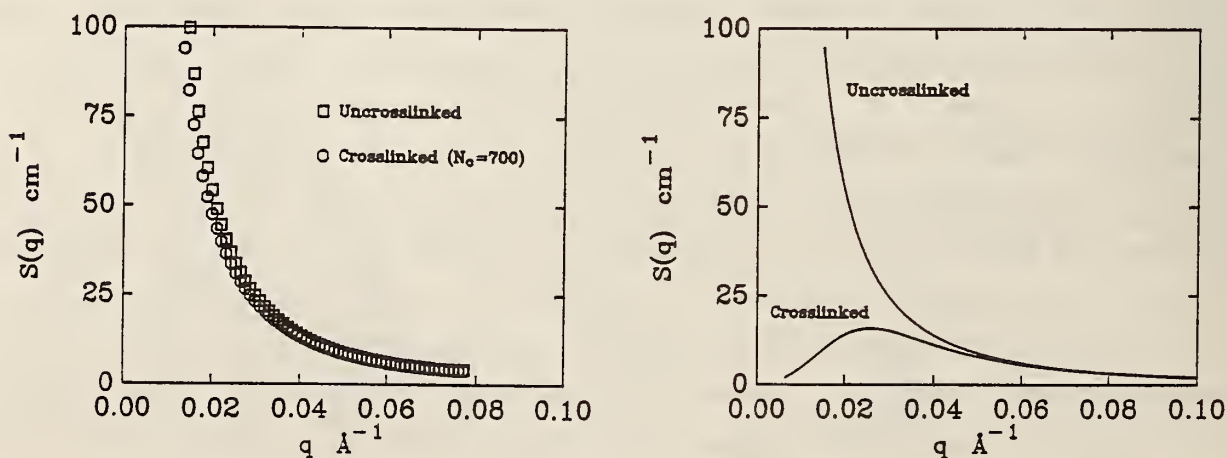


Figure 1. (left) SANS scattering for the crosslinked PSD/PSH blends (circles: 125 MRad, $N_c = 700$, squares: 0 MRad, $N_c = \infty$, (uncrosslinked)).

Figure 2. (right) Calculated scattering curves for the samples shown in figure 1.

References

- [1] de Gennes, P. G. J. Phys. (Les Ulis, Fr.) 40, L-49 (1979)
- [2] Briber, R. M.; Bauer, B. J. Macromol. 21, 3296 (1988)

GRAFTED INTERPENETRATING POLYMER NETWORKS

B. J. Bauer and R. M. Briber
(Polymers Division)

Interpenetrating polymer networks (IPN) are two component polymeric systems in which one polymer is swollen with monomer of a different type and polymerization of the monomer forms the second polymer. One or both of the polymers is crosslinked to itself, but crosslinks between the two different polymers are not present. Previous work at NIST [1] has shown that IPNs promote phase separation; i.e., mixtures of polymers that would form a single phase blend can be made to phase separate in a crosslinked IPN. When compatible blends are radiation crosslinked, forming crosslinks between the two different polymers, the single phase region is greatly enhanced, and a peak appears in the scattering, indicating that microphase separation would occur, forming domains of approximately 100 Å [2].

We have explored an alternate method of introducing bonds between the two polymers by use of macromonomers. Macromonomers are polymers with one end containing a functionality such as a methacrylate group that can copolymerize with the monomer that forms the second polymer, thereby grafting it to the crosslinked network. Figure 1 gives the scattering intensity from standard semi-II IPNs of 13,000 dalton polystyrene and crosslinked polystyrene-d with 0.2 and 0.5% divinylbenzene (DVB). As has been previously seen, added DVB increases the scattering intensity, pushing it towards phase separation. The three lower curves are for samples with 0.2, 0.5, and 1.0% DVB for the system of grafted polystyrene. The symbol at $q = 0$ is the calculated intensity for a blend of equivalent molecular weight. While a standard IPN structure promotes phase separation, the grafted IPN inhibits phase separation.

Figure 2 shows the results from a similar system except polymethylmethacrylate is grafted onto a network containing 0.5 and 1.0% DVB. In this polymer combination there is a small positive interaction parameter which

promotes phase separation. Prominent peaks can be seen in both scattering curves similar to the radiation crosslinked blends [2]. This type of grafted IPN would microphase separate into a system of domains. Therefore, by controlling the crosslinking reaction, the resulting morphology of crosslinked polymers can be easily controlled.

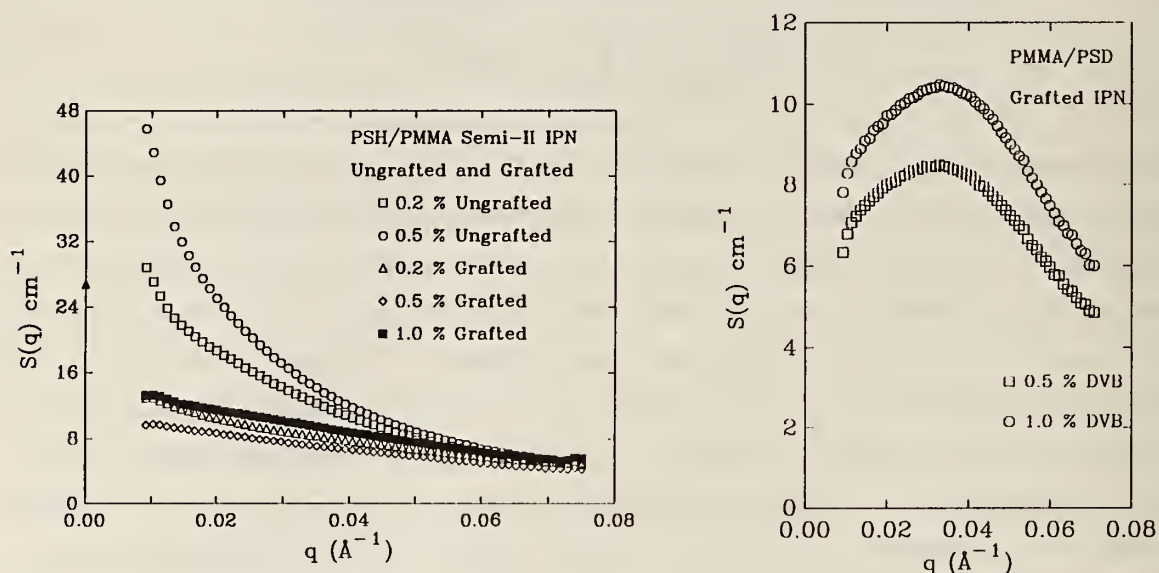


Figure 1. (left) SANS results for PSH/PSD grafted and ungrafted semi-II IPNs.

Figure 2. (right) SANS results for PMMA/PSD grafted semi-II IPNs.

References

- [1] Bauer, B. J.; Briber, R. M.; Han, C. C. *Macromol.* 22, 940 (1989).
- [2] Briber, R. M.; Bauer, B. J. *Macromol.* 21, 3296 (1988).

**MICROSTRUCTURE AND ISOTOPIC LABELING EFFECTS ON THE MISCIBILITY OF
POLYBUTADIENE BLENDS STUDIED BY THE SMALL ANGLE NEUTRON SCATTERING TECHNIQUE**

S. Sakurai, H. Hasegawa, and T. Hashimoto
(Kyoto University, Kyoto, Japan)

I. G. Hargis and S. L. Aggarwal
(Gen Corp, Akron, OH)

and

C. C. Han
(Polymers Division)

Polybutadiene blends of various microstructures are widely used in the rubber industry to tailor properties to applications. Such blends offer an ideal system to study the fundamentals of binary interaction parameters of butadiene monomers with different microstructures.

Small angle neutron scattering (SANS) should be the tool to use to study this microstructure effect. Unfortunately, the deuterium labeling of one of the components which is needed for SANS introduces a repulsive interaction [1] between the two components. This has prevented a straightforward measurement of the binary interaction parameter, χ , between a 1,2-unit and a 1,4-unit.

In this work, an attempt has been made to separate the isotope effect from the microstructure effect through a systematic SANS study of blends of deuterated polybutadiene (PBD) and protonated polybutadiene (PBH) with various vinyl contents. Random copolymer theory was used to carry out this separation.

All SANS data are analyzed with a nonlinear regression fitting routine according to the random phase approximation calculation of deGennes which can be written as follows:

$$S(q) = K_N / \frac{1}{\phi_A \langle Z_A \rangle_n v_A \langle g_D(q) \rangle_{A_w}} + \frac{1}{\phi_B \langle Z_B \rangle_n v_B \langle g_D(q) \rangle_{B_w}} - \frac{2\chi}{v_o} \quad (1a)$$

$$\text{with } S(q)_{\text{EXP}} = S(q) + \text{baseline.} \quad (1b)$$

In figure 1, typical SANS data from a miscible blend, in this case the VBRD6/VBRH6 (deuterated polybutadiene with 63% 1,2-content and $M_n = 134$ K, $M_w/M_n = 2.0$, hydrogenated polybutadiene with 68% 1,2-content and $M_n = 135$ K, $M_w/M_n = 1.8$) with volume fraction of $\phi_{VBRD6} = 0.278$ and at room temperature, is displayed together with the best fitted line according to eq (1). A normalized deviation plot is also displayed in the lower half of figure 1. The static structure factors for VBRD6/VBRH6 with $\phi_{VBRD6} = 0.375$ at various temperatures are shown in figure 2. It is clear from figure 2 that $S(q)$ decreases with increasing temperature. This implies the existence of an UCST below room temperature. SANS results for various compositions of VBRD6/VBRH6 series and VBRD6/CisBR7k (deuterated polybutadiene as defined above/hydrogenated polybutadiene with 7% 1,2-content and $M_n = 6.9$ K, $M_w/M_n = 1.5$) series at different temperature have also been analyzed. The interaction parameter, χ , zero wave number structure factor, $S(q = 0)$ and the correlation length, ξ , have been extracted for all experimental conditions. Since polymer/polymer blends can be described by the mean-field theory, spinodal or the critical temperature can be obtained through the extrapolation of χ , $S(q = 0)^{-1}$ or ξ^{-2} vs $1/T$ to $\chi = \chi_s$, $S(0)^{-1} \rightarrow 0$ or $\xi^{-2} \rightarrow 0$, respectively. Where χ_s is the χ at the spinodal temperature T_s . In figure 3, χ , $S(q = 0)^{-1}$ and ξ^{-2} are plotted vs $1/T$ for the VBRD6/VBRH6 ($\phi_{VBRD6} = 0.474$) blend. T_s of -37.2 °C is obtained consistently from the extrapolations of all three sets of results. A similar procedure has been carried out for all data sets of both the VBRD6/VBRH6 and the VBRD6/CisBR7k series of blends.

Besides the isotope effect which could cause incompatibility [1], the microstructure effect has to be properly accounted for in order to understand the phase behavior of rubber/rubber blends. If we define deuterated 1,2-butadiene, deuterated 1,4-butadiene, protonated 1,2-butadiene and protonated 1,4-butadiene monomers as A, B, C, and D, respectively, then for a blend of A-B copolymer with C-D copolymer, the free energy of mixing can be written as:

$$\frac{\Delta F}{RT} = (\phi_1/N_1) \ln \phi_1 + (\phi_2/N_2) \ln \phi_2 + \phi_1 \phi_2 \chi_{blend} \quad (2)$$

$$\text{with } \chi_{blend} = xy \chi_{AC} + (1-x)y \chi_{BC} + x(1-y) \chi_{AD}$$

$$+ (1-x)(1-y) \chi_{BD} - x(1-x) \chi_{AB} - y(1-y) \chi_{CD} \quad (3)$$

where x is the number fraction of A in A-B copolymer and y is the number fraction of C in C-D copolymer. x and y refer to the number fraction of repeat units in the lattice theory of blends. We equated number fractions to volume fraction for this work.

By neglecting the difference between trans and cis-1,4 polybutadiene and assuming polybutadiene is a simple random copolymer, we should be able to obtain all six χ -parameters if we have six sets of data for blends with different microstructure variations. We do not have six sets of data. Nonetheless, using the data from Bates et al. [1] and making a few assumptions about the interaction parameters, we shall demonstrate a scheme of separating various interaction parameters.

First, let us assume $\chi_{AC} = \chi_{BD} = \chi_3$. This assumption implies identical isotope effect between 1,2-pairs and between 1,4-pairs of different isotopes. Without knowledge of the exact intermolecular potential energy function between two isotopically labeled microstructure pairs the severity of this assumption cannot be assessed. Once we have made the above assumption, we can then assume $\chi_{AB} = \chi_{CD} = \chi_1$ and $\chi_{AD} = \chi_{BC} = \chi_2$. These two assumptions imply that pure microstructure effect (interaction between either protonated or deuterated 1,2- and 1,4-butadiene pairs) is independent of the isotope used and consequently that the cross (isotope labeled) microstructure effect is independent of which one of the two monomers is labeled. Actually, these two assumptions are implied from the previous assumption that identical isotope effects prevail between 1,2-pairs and 1,4-pairs.

We are now in a position to calculate the three interaction parameters χ_1 , χ_2 , and χ_3 for three sets of PBD/PBH blends. As noted before, we have two sets of χ data from this study, and we will also employ the literature

value of Bates et al. [1], which was reported for a PBD/PBH system with 11% of 1,2-unit for both components and with $\phi_{\text{PBD}} = 0.31$.

Thus, three simultaneous equations can be obtained from equation 3 as

$$\chi (\text{VBRD6/VBRH6}) = - 0.451\chi_1 + 0.454\chi_2 + 0.546\chi_3 \quad (4a)$$

$$\chi (\text{VBRD6/CisBR7k}) = - 0.307\chi_1 + 0.610\chi_2 + 0.390\chi_3 \quad (4b)$$

$$\chi (\text{Bates et al.}) = - 0.196\chi_1 + 0.196\chi_2 + 0.804\chi_3 \quad (4c)$$

Values of χ_1 , χ_2 , and χ_3 obtained are displayed in figure 4 as a function of $1/T$.

In figure 5, χ values obtained from SANS measurements of a separate set of blends, H-19/H-16 (H-19 with $M_n = 71$ k and 28% of 1,2-unit; H-16 with $M_n = 281$ k and 40% of 1,2-units are displayed as a function of $1/T$, together with the predicted values (solid line) which were calculated according to equation 3 and χ_1 , χ_2 , and χ_3 values obtained before. Although the predicted numbers are slightly lower than the experimental values, considering the assumptions and errors involved in the calculation, in this analysis, in sample preparation, and in SANS experiments, this agreement may be considered to be excellent.

We should point out that the main contribution for miscibility in a blend of a A-B copolymer with a C-D copolymer is due to the interaction between the intramolecular pairs of A/B and C/D which has a negative coefficient as indicated in equation 3. Actually, in order to maximize this negative contribution (in magnitude) to the total interaction, χ_{blend} , copolymers of equal constituents ($x_A = x_B = 0.5$, $y_C = y_D = 0.5$) should be used. If we examine figure 3 again with these intramolecular interactions in mind, then it becomes clear why negative χ 's have been obtained for deuterated polybutadiene/protonated polybutadiene blends, which lack any specific attractive interaction.

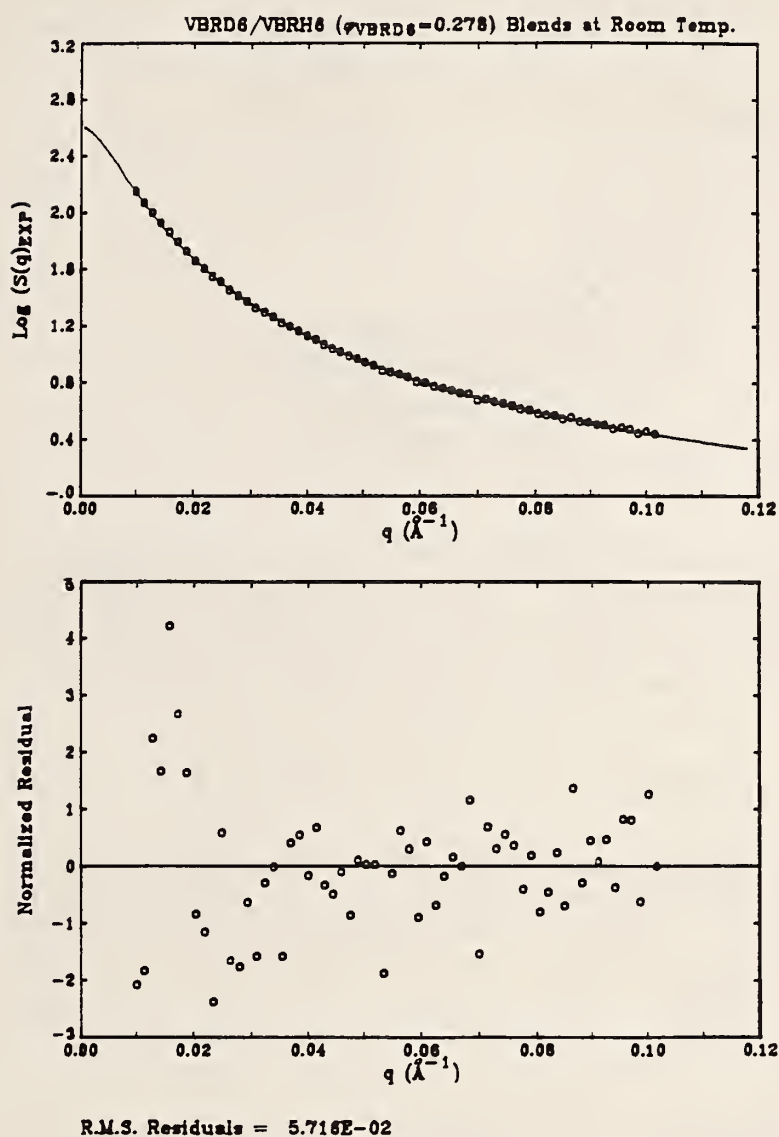


Figure 1. Normalized SANS intensity $S(q)$ of VBRD6/VBRH6 with volume fraction $\phi_{\text{VBRD6}} = 0.278$ at room temperature is displayed in logarithmic scale as a function of scattering vector q together with the best fitted line according to eq (1). Normalized deviation is plotted in the lower half of the graph.

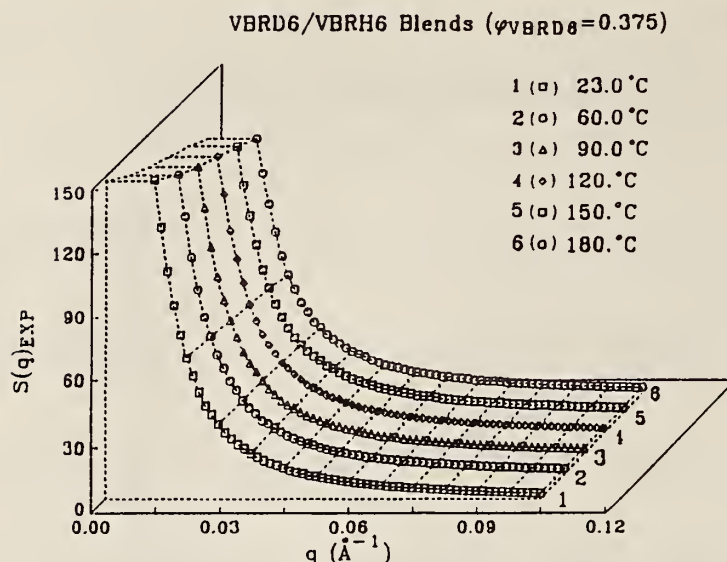


Figure 2. SANS data from the VBRD6/VBRH6 series with $\phi_{\text{VBRD6}} = 0.375$ at various temperatures (shown in the graph) is plotted as $S(q)$ vs. q . Data are shifted along the 45 ° line for clarity.

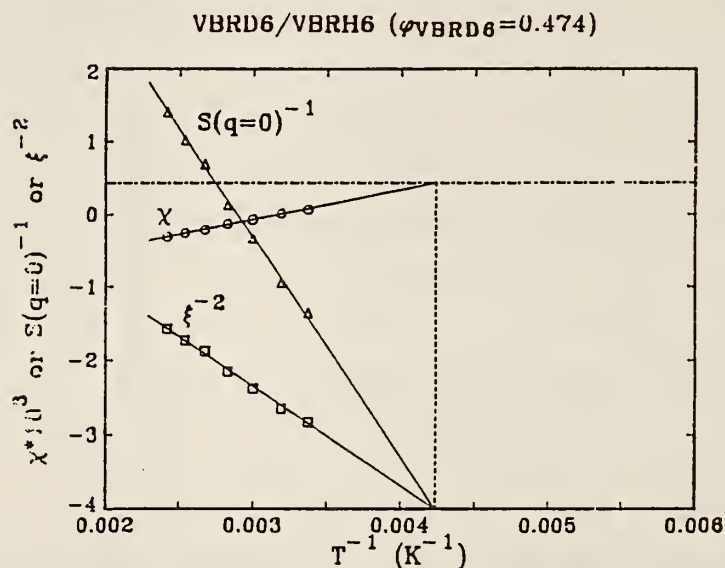


Figure 3. SANS results of χ [○], $S(q = 0)^{-1}$ [Δ] and ξ^{-2} [□] from non-linear regression analysis for the VBRD6/VBRH6 ($\phi_{\text{VBRD6}} = 0.474$) are plotted against $1/T$. A dotted-and-broken (—•—) horizontal line displays χ_s value for this system. Linear extrapolation are performed simultaneously for all three plots to obtain the spinodal temperature, T_s , in a consistent manner. In this case $T_s = -37.2$ °C. The scales labeled on the ordinate is for χ values. The scales for $S(q = 0)^{-1}$ is from 0.0 to 0.006 with interval of 0.001 and for ξ^{-2} is from 0.0 to 0.00024 with interval of $4 \times 10^{-5} \text{ Å}^{-2}$.

REACTOR RADIATION DIVISION AND COLLABORATIVE PROGRAMS

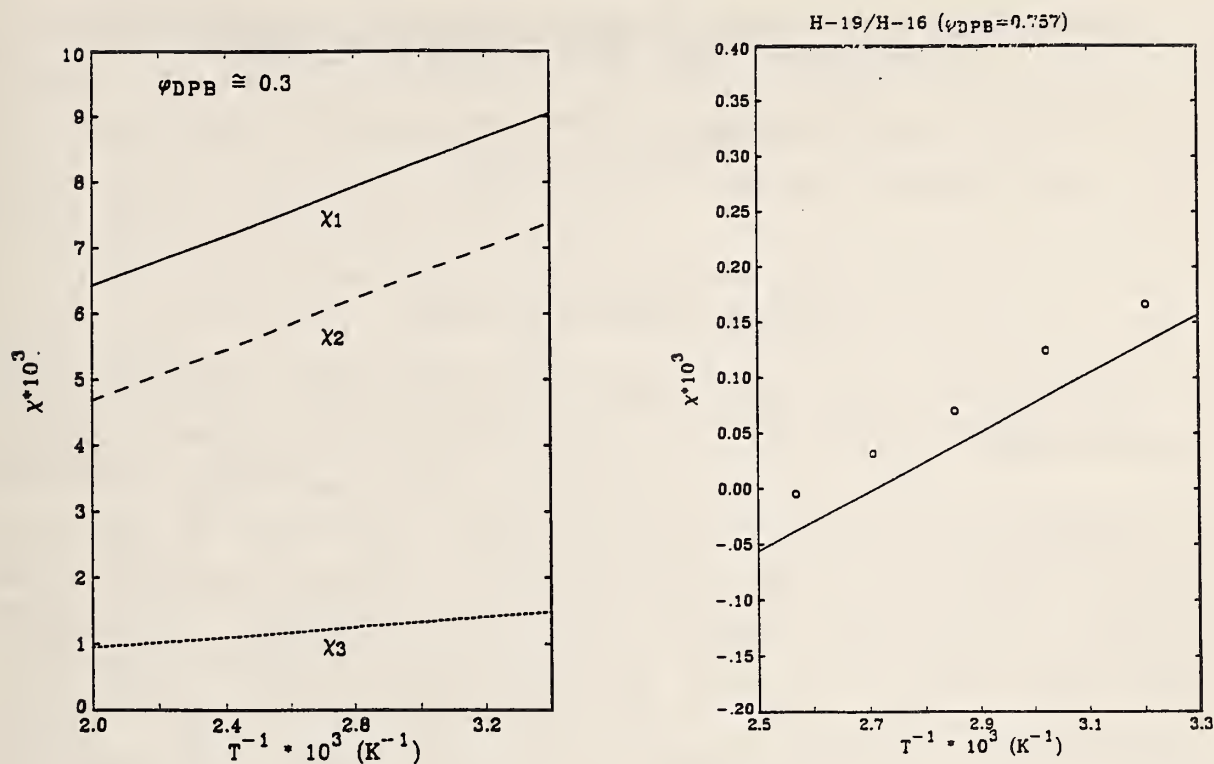


Figure 4. (left) χ_1 , χ_2 and χ_3 presented as a function of $1/T$.

Figure 5. (right) Measured χ values [o] for series H-19/H-16 (PBD/PBH) at volume fraction of 0.757 of H-19 (PBD) is plotted against $1/T$ together with the predicted χ values in solid line which was calculated by using eq (4) and the χ_1 , χ_2 and χ_3 values from table 3.

Reference

- [1] Bates, F. S.; Dierker, S. B.; Wignall, G. D. *Macromol.* **19**, 1938 (1986).

**SHEAR EFFECTS ON THE PHASE SEPARATION BEHAVIOR OF A POLYMER BLEND
IN SOLUTION BY SMALL ANGLE NEUTRON SCATTERING**

A. I. Nakatani, H. Kim, and C. C. Han
(Polymers Division)

and

Y. Takahashi
(Nagoya University, Japan)

The effect of shear on the phase separation of polymer blends has been examined extensively [1-5] and is of dual importance for polymer mixtures. First, a basic understanding of the behavior of polymer blends is required for optimization of process parameters. Second, the study of the phase behavior of quiescent polymer blends has been of paramount importance in the development and testing of theories of critical phenomena. Experimental studies have primarily utilized light scattering techniques to examine the size and shape of concentration fluctuations of the order of 1000 Å. Further studies using shorter wavelength radiation such as neutrons to understand the influence of flow fields on smaller critical fluctuations as the system approaches instability from the one-phase state have not been performed. In this communication we report preliminary results on the small angle neutron scattering (SANS) behavior of a solution of two homopolymers under shear. Observations were made at various combinations of temperature and shear rate for two samples representing compositions close to and far from the critical composition.

For miscible polymer blends, the structure factor, $S(q)$, can be analyzed according to the random phase approximation calculated by deGennes [6]. For small q ($q = (4\pi/\lambda)\sin(\theta/2)$), the structure factor is identical to the Ornstein-Zernike form of a Lorentzian function as follows:

$$S(q) = [S(q = 0)/(1 + \xi^2 q^2)] \quad (1)$$

The concentration correlation length is given by the variable, ξ . The correlation length is related to the spinodal temperature by the following relation:

$$\xi \propto (1/T_{sp} - 1/T)^{-\nu} \quad (2)$$

where ν is predicted to be $1/2$ for a mean field system and $2/3$ for an Ising system. Therefore by fitting the structure factor to equation 1, the correlation length, ξ , and $S(q = 0)$ can be obtained. By plotting ξ^{-2} versus the reciprocal of the temperature, the spinodal temperature may also be estimated for a mean field system.

The system chosen for study in these experiments was a solution of linear polystyrene- d_8 (PSD) and linear polybutadiene (PB) in dioctyl phthalate (DOP). Two different PSD samples were used: 1) $M_w = 27,000$, $M_w/M_n = 1.06$, and 2) $M_w = 85,000$, $M_w/M_n = 1.02$. The polybutadiene sample had a M_w of 24,000, with $M_w/M_n = 1.07$.

Two different samples were prepared. The first sample contained 8% total polymer by weight with a composition of 35% of the 85,000 molecular weight PSD and 65% of the PB in DOP (sample designation = 088535). The second solution contained 12% total polymer by weight and had a composition of 50% of the 27,000 molecular weight PSD and 50% of the PB (sample designation = 122750). The first sample has a composition close to the critical composition while the second sample is off-critical. Total polymer concentration was selected to give transitions from the two phase to one phase region around 40 °C.

A couette-geometry shear cell was designed and constructed to fit within the constraints of the SANS instrument at the NIST reactor. The geometry of the cell is similar to that described by Lindner and Oberthur [7]. An incident wavelength of 9 Å was used and sector averages of the data parallel (horizontal) and perpendicular (vertical) to the flow directions were obtained in 10° arcs.

Both 088535 and 122750 were tested at 0 and 600 s^{-1} between 30 and 60 °C. Both solutions exhibit UCST behavior and optical cloud points of the solutions were 40.6 °C for 088535 and 34.8 °C for 122750.

For both samples at 0 s^{-1} , the scattering intensity increased as temperature decreased in the one-phase region. In the two-phase region, the scattering intensity then decreased with decreasing temperature as expected for a phase separated system. The maximum scattering intensity was observed at between the horizontal and vertical sector averages. An example of the temperature dependence of the scattering intensity at zero shear in the horizontal direction is shown in figure 1 for 088535.

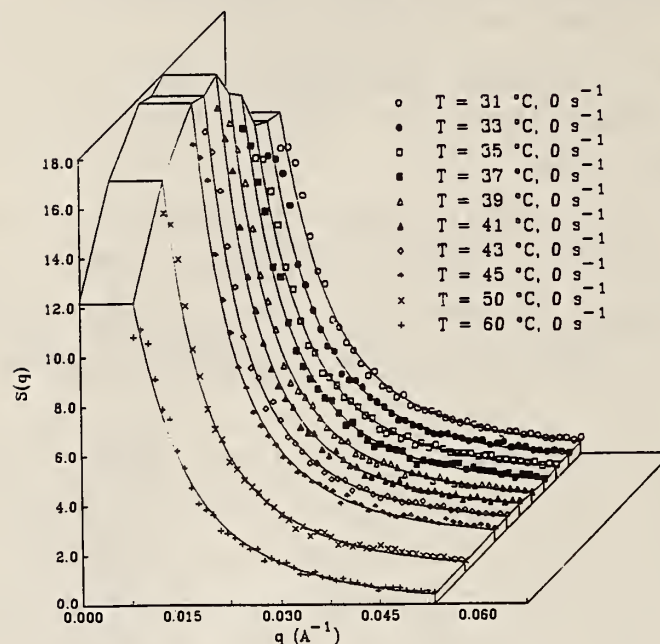


Figure 1. $S(q)$ versus q at 0 s^{-1} as a function of temperature for 088535. Curves represent nonlinear regression fits to data. Data points are the horizontal sector averages.

The temperature dependence of the scattering at 600 s^{-1} for 088535 in the direction parallel to the flow is shown in figure 2. As observed in the static case, the scattering intensity increased as temperature decreased in the one-phase region and continues to increase in the two-phase region. Similar behavior is observed in the direction perpendicular to the flow.

The increase in $S(q)$ with shear at temperatures which are below the static cloud point is taken to be evidence for the disruption of large droplets due to shear. This effect will cause increased scattering intensity in the wavelength range of our SANS experiments due to smaller droplet structures and increased sample transmission.

Correlation lengths were obtained by fitting the experimental SANS data to eq (1) using a nonlinear regression routine. For points of ξ^{-2} versus $1/T$, extrapolation to $\xi^{-2} = 0$ was performed using a linear regression routine utilizing the points in the one-phase region only (43 to 60 °C for 088535). Examples of these plots for 088535 are shown in figures 3 and 4. The extrapolated spinodal temperatures in the sheared and unsheared case for the

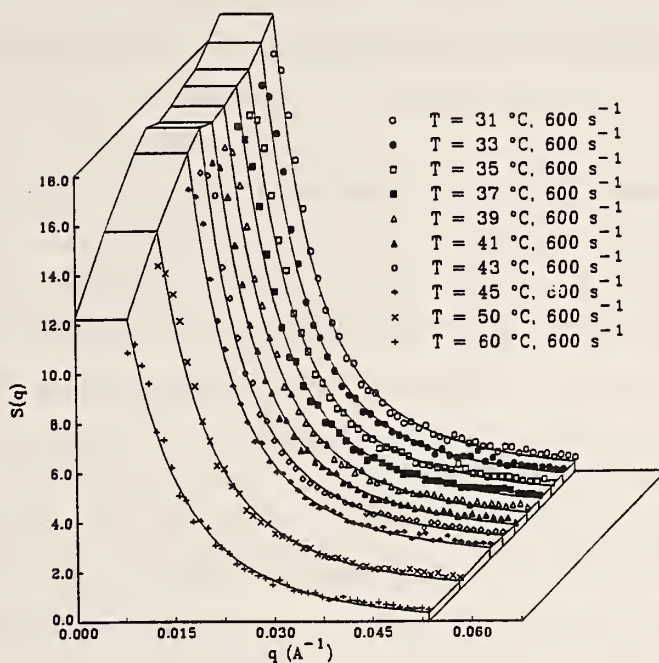


Figure 2. $S(q)$ versus q at 600 s^{-1} as a function of temperature for 088535. Curves represent nonlinear regression fits to the data. Data points are the horizontal sector averages.

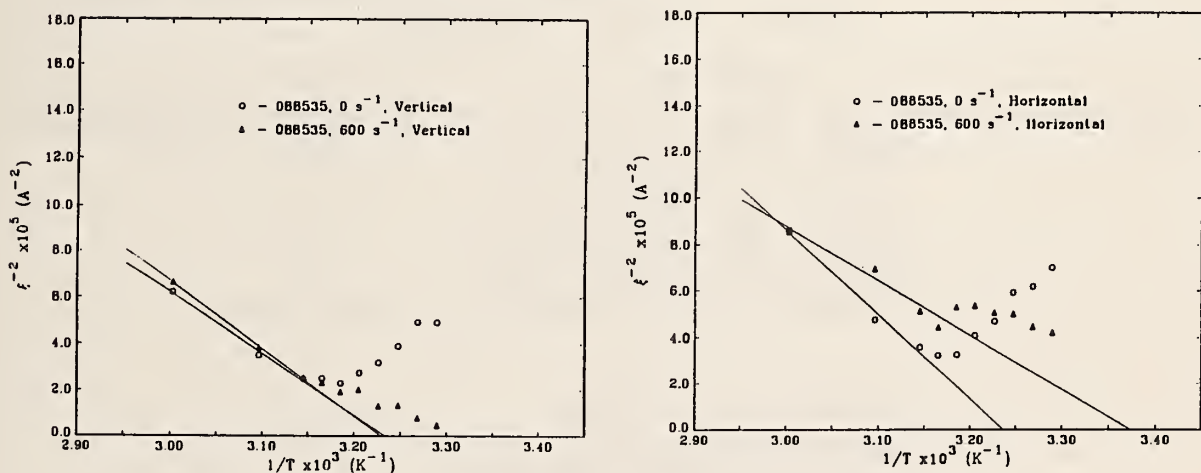


Figure 3. (left) ξ^{-2} versus temperature at 0 and 600 s^{-1} in the direction perpendicular (vertical) to the flow. Solid lines represent linear regression fits extrapolated to $\xi^{-2} = 0$.

Figure 4. (right) ξ^{-2} versus temperature at 0 and 600 s^{-1} in the direction parallel (horizontal) to the flow. Solid lines represent linear regression fits extrapolated to $\xi^{-2} = 0$.

horizontal and vertical sector averages are given in table 1. For both samples, the spinodal temperature determined from the vertical and horizontal sector averages at rest and the spinodal temperature in the direction perpendicular to the flow direction are equal within experimental error. The spinodal temperature determined from the horizontal sector averages during shear are much lower. At this time, we do not have enough data to determine the shear rate dependence of the spinodal temperature. However, the limited existing data seem to indicate that the magnitude of the depression of the spinodal temperature increases with increasing shear rate. Additional experiments are being planned to confirm this effect.

The above observations are qualitatively consistent with the notion of shear stabilization and decoupling of the flow field to its orthogonal directions proposed by Onuki [8-10]. As the shear field is applied to the system, very large concentration fluctuations are suppressed in the one-phase region along the shear direction causing a decrease in the scattering intensity as well as the correlation length. This effect is more pronounced as the system is brought closer to the phase boundary; consequently, the

Table 1. Spinodal temperatures

Condition	T (°C)
088535, 0 s ⁻¹ , Vertical	36.2
088535, 0 s ⁻¹ , Horizontal	35.9
088535, 600 s ⁻¹ , Vertical	36.6
088535, 600 s ⁻¹ , Horizontal	23.4
122750, 0 s ⁻¹ , Vertical	39.2
122750, 0s ⁻¹ , Horizontal	37.5
122750, 600 s ⁻¹ , Vertical	35.2
122750, 600 s ⁻¹ , Horizontal	13.3

phase transition temperature is depressed by the shear field. The question of whether the concentration fluctuations in a shear field will still follow the conventional scattering of eq (2) has yet to be determined. In the analysis of this work, we have assumed the system follows mean-field behavior although both samples are in the semi-dilute regime. While the mean-field

assumption is not quantitatively justified, the qualitative features of the phenomena and conclusions we present here will not change.

References

- [1] Hashimoto, T.; Takebe, T; Suehiro, S. J. Chem. Phys. 88, 5874 (1988).
- [2] Takebe, T.; Hashimoto, T. Polym. Commun. 29, 227 (1988).
- [3] Lyngaae-Jorgensen, J.; Sondergaard, K. Polym. Eng. Sci. 27, 344 (1987).
- [4] Wolf, B. A. Macromol. 17, 615 (1984).
- [5] Rangel-Nafaile, C.; Metzner, A. B.; Wissbrun, K. F. Macromol. 17, 1187 (1984).
- [6] deGennes, P. G. Scaling concepts in polymer physics. Cornell University Press, Ithaca, New York (1979).
- [7] Lindner, P.; Oberthur, R. C. Revue Appl. Phys. 19, 759 (1984).
- [8] Onuki, A. Physica 140A, 204 (1986).
- [9] Onuki, A. Phys. Rev. A34, 3528 (1986).
- [10] Onuki, A. Phys. Rev. A35, 5149 (1987).

CONCENTRATION FLUCTUATIONS IN MIXTURES OF LINEAR AND STAR SHAPED POLYMERS

T. P. Russell
(IBM, San Jose, CA)

L. J. Fetters
(Exxon Research and Engineering Co., Annandale, NJ)

and

J. C. Clark, B. J. Bauer, and C. C. Han
(Polymers Division)

Mixtures of linear polyvinylmethylether (PVME) with four armed star polystyrene (PS) were studied to evaluate the effect of chain topology on the critical fluctuations in homogeneous polymer mixtures. It was found that the cloud-point curve of the PS/PVME mixtures was elevated by about 10 °C over that of the corresponding linear mixtures. The use of deuterated PS (PSD) elevated the cloud point about 10 °C beyond that of hydrogen containing PS (PSH). SANS studies of blends of PSH and PSD stars were used to measure the

single chain structure factor of the stars, and were found to be in excellent agreement with the theories of Benoit [1] and Burchard [2]. This structure factor was then used to analyze the concentration fluctuations of PSD/PVME blends over a range of compositions and temperatures.

The inverse of the zero-angle scattering vector, $S(0)^{-1}$, extrapolated linearly with inverse temperature to yield the spinodal temperature, T_s . The correlation length, ξ , was found to depend upon $[(T - T_s)/T_s]^{-\nu}$ where $\nu = 0.5$. ξ^{-2} was also linearly dependent on inverse temperature yielding values of T_s in close agreement with the $S(0)^{-1}$ results. ξ_0 , the bare correlation length, was found to depend upon composition in a manner similar to a previous study. The Flory-Huggins interaction parameter was also measured and found to vary linearly with inverse temperature and to be a function of concentration.

References

- [1] Benoit, H. J. Polym. Sci. 11, 561 (1953).
- [2] Burchard, W. Macromol. 10, 919 (1977).

CHAIN CONFORMATION OF A BLOCK POLYMER IN A MICROPHASE-SEPARATED STRUCTURE

Y. Matsushita, K. Mori, Y. Mogi, R. Saguchi, I. Noda, and M. Nagasawa
(Nagoya University, Nagoya, Japan)

T. Chang and C. C. Han
(Polymers Division)

and

C. J. Glinka

It is important to study the single-chain conformation of polymers in order to understand their physical properties at the molecular level. In dilute solutions it is well established that the chain conformation is Gaussian in θ -solvents; i. e., $\nu = 0.5$ in the molecular weight dependence of mean square radius of gyration, $\langle s^2 \rangle$; that is, $\langle s^2 \rangle \propto M^{2\nu}$, while it is non-Gaussian; i. e., $\nu \sim 0.6$ in good solvents [1]. In condensed polymer systems, such as concentrated solutions and melts, it was found by small angle neutron scattering (SANS) that the chain conformation is Gaussian as predicted by Flory [1,2,11]. In microphase-separated structures, where the block polymers

are confined anisotropically, however, their conformations should be distorted, as suggested by the molecular weight dependence of domain spacing, D ; i.e., $D \propto M^{2/3}$ [3-5]. Therefore, it will be very interesting to study the conformation of a block polymer chain not merely because it could lead to the understanding of the microphase-separated structure at the molecular level but because it could clarify the difference between conformations of polymer chains in free space and in anisotropic domains.

Typical microdomain structures of block copolymers are lamellar, cylindrical, and spherical structures of which the first one is the most suitable microdomain for the study of a single-chain conformation because this structure can be assumed to be in an equilibrium state but not the other two structures [5,6]. If the lamellar structure is oriented along the direction parallel to the surface of a film specimen, moreover, we can measure dimensions of a polymer chain along the orthogonal axes as we will mention later. Two experimental works have been published so far on conformations of block polymers in lamellar structures using styrene-isoprene block copolymers [7,8]. They reported that the dimension of a block polymer extends along the direction perpendicular to the lamellae, while it shrinks along the direction parallel to the lamellae. The extension of a block polymer along the perpendicular direction can be understood by the theories of Meier and Helfand for microphase-separated structures [3,4]. However, the reason for the shrinkage of block polymer along the parallel direction remains unknown. As usually carried out in the study of chain conformation in dilute solutions, the molecular weight dependence of polymer dimensions in microphase-separated structures should be studied in order to have a definite and quantitative conclusion on this problem. In this work, therefore, we prepared diblock copolymers of deuterated styrene-2-vinylpyridine with different molecular weights and studied molecular weight dependences of radii of gyration of the polystyrene block along the orthogonal axes in lamellar structures by SANS. These samples are considered particularly suitable for the SANS study, because the scattering length of poly(2-vinylpyridine) is between those of labeled and unlabeled polystyrenes. Therefore, we could make a contrast matching between two domains to extract a single chain scattering if the labeled and unlabeled polystyrene blocks would be randomly mixed. Moreover, it is noted that the statistical segment lengths of both block polymers are almost the same.

As reported in a previous paper [9], a contrast matching between two domains is required to extract a single-chain scattering of a block polymer along the perpendicular direction, though it is not required along the parallel direction since the lamellae are predominantly oriented along the direction parallel to a film surface. However, we could not achieve a contrast matching except for a low molecular weight sample. Hence, we measured the radius of gyration along the perpendicular direction only for the low molecular weight sample and assumed that the radii of gyration along the perpendicular direction for the higher molecular weight samples are proportional to their domain spacings determined by small angle x-ray scattering (SAXS) [10].

Since the lamellae are predominantly oriented along the direction parallel to the film surface, only single chain scattering was observed at the through view, while the strong diffractions from the lamellae were observed together with a single chain scattering at the edge view. Therefore, the contrast matching is necessary to extract the single chain scattering at the edge view. Figure 1 shows the single chain scattering of a typical sample pair at the through view after the incoherent scattering intensity was subtracted. The corresponding Guinier plot is displayed in figure 2. For other sample pairs similar figures are obtained. Radii of gyration for different molecular weight pairs in the X and Z directions (parallel to the lamella surface) have been evaluated from these Guinier plots.

As mentioned before, we could achieve a contrast matching only for the low molecular weight sample pair, (II), therefore, this is the only sample pair with radii of gyration measured in all three X, Y (perpendicular to lamella surface) and Z directions.

Figure 3 shows molecular weight dependences of radii of gyration of block polymer along x-axis, that is, along the direction perpendicular to lamellae. Here, we assumed that the radius of gyration along y-axis increases with increasing molecular weight according to the same power law as the molecular weight dependence of the domain spacing, D

$$D = 0.33_2 M_n^{0.64} \text{ (Å)}. \quad (1)$$

From figure 3, we have the molecular weight dependences of radii of gyration of a block polymer along x-, y- and z- axis as

$$R_{g,x} = R_{g,z} = 0.289 M^{0.43} (\text{\AA}). \quad (2)$$

$$R_{g,y} = 0.0453 M^{0.64} (\text{\AA}). \quad (3)$$

On the other hand, since deuterium-labeled polystyrene chains in bulk were determined to have the conformation of the ideal chain as [11]

$$R_{g,0} = 0.275 M^{0.5} (\text{\AA}). \quad (4a)$$

so that we can obtain the following relationship between unperturbed dimension along an axis, $R_{g,k0}$, and the molecular weight using the condition $R_{g,0}^2 = 3R_{g,k0}^2$:

$$R_{g,k0} = 0.159 M^{1/2}. \quad (4b)$$

This relationship is also shown in figure 3. Comparing equations 2, 3 and 4b, we find that the shrinking ratio along the direction parallel to lamellae is lower than the extending ratio along the direction perpendicular to the lamellae.

If we assume that the shapes of deformed polymer chain in lamellar structures and undeformed polymer chain in melts are an ellipsoid of revolution and a sphere, respectively, and their radii are proportional to the corresponding radii of gyration, the volumes of the ellipsoid of revolution V_e and the sphere V_s can be written as:

$$V_e \propto (4\pi/3)R_{g,x}R_{g,y}R_{g,z} = 0.16 M^{1.5} \quad (5)$$

$$V_s \propto (4\pi/3)R_{g,k0}^3 = 0.017 M^{1.5}. \quad (6)$$

The comparison between eqs (5) and (6) reveals that not only the molecular weight dependences but also the pre-factors of the volumes occupied by a single chain are almost the same in melts and in lamellar structures. That is, there is no change in the volume occupied by a block polymer; i.e., no change of degree of coil-overlapping, when a block polymer is brought into lamellar structures. This implies that block polymers shrink along the direction parallel to the lamellae to preserve the same intermolecular interactions in lamellar structures as in disordered states.

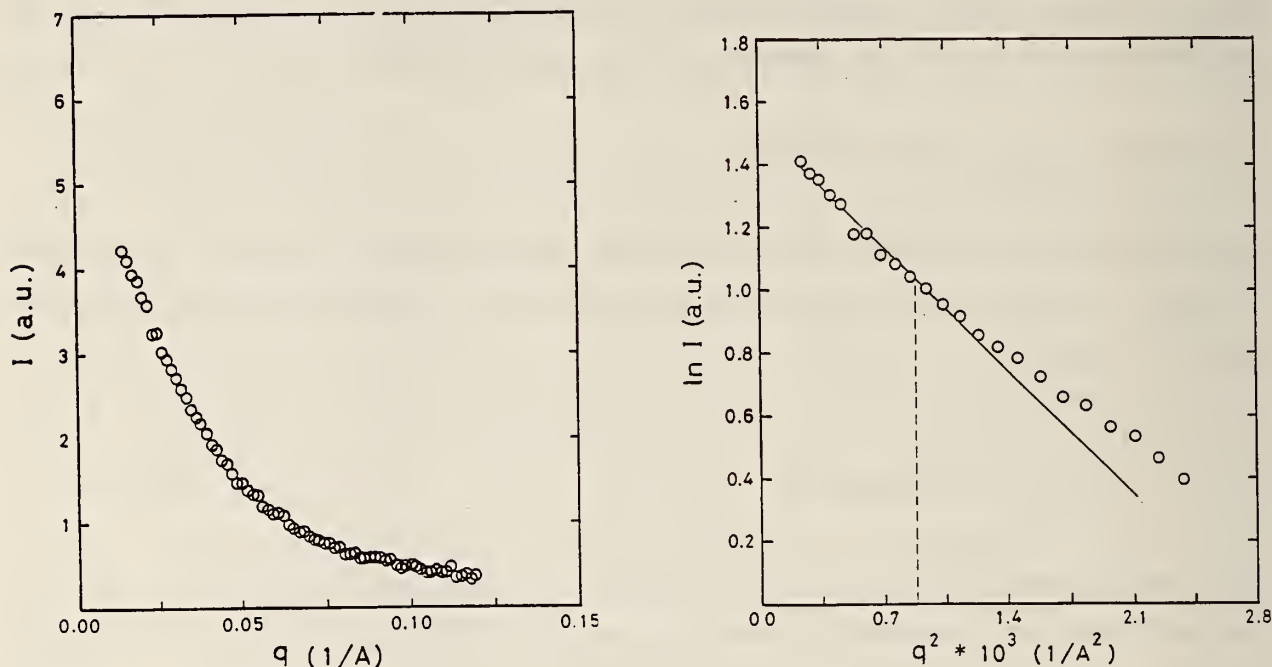


Figure 1. (left) Typical plots of coherent scattering intensity versus the magnitude of the scattering vector for a blend of labeled and unlabeled block copolymers with a highly oriented lamellar structure at the through-view. Intensities were obtained by a circular average of the two-dimensional data. Sample; DP-33/SP-33, mixing ratio; 12/88 by weight.

Figure 2. (right) Guinier plot of the data in figure 2. Dotted vertical line indicates the limit of Guinier's region described in the text.

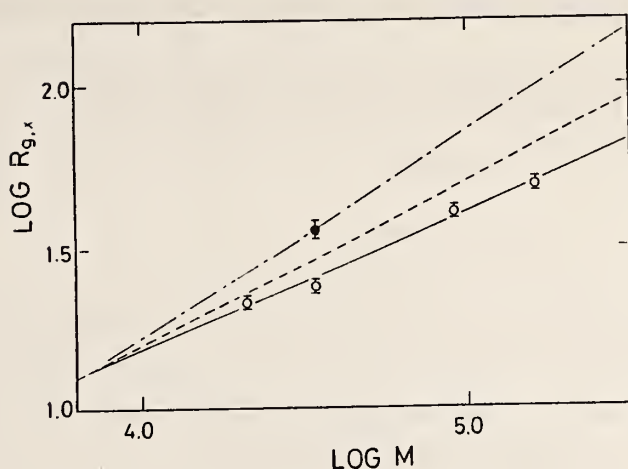


Figure 3. Double logarithmic plots of the radii of gyration along x-axis (O) and y-axis (O) against the molecular weight of labeled polystyrenes in block copolymers. The solid, chain and dotted lines denote eqs (3), (4), and (4b), respectively.

References:

- [1] Flory, P. J. Principle of polymer chemistry. Cornell University Press, Ithaca, NY (1953).
- [2] Higgins, J. S.; Stein, R. S. J. of Appl. Cryst. 11, 346 (1978).
- [3] Meier, D. J. J. Polym. Sci., Part C, 26, 81 (1969). Meier, D. J. Block and graft copolymers. J. J. Burke and V. Weiss, eds. Syracuse University, NY (1973).
- [4] Helfand, E.; Wasserman, Z. R. Macromol. 9, 879 (1976).
- [5] Hashimoto, T.; Shibayama, J.; Kawai, H. Macromol. 13, 1237 (1980).
- [6] Hashimoto, T.; Fujimura, M.; Kawai, H. Macromol. 13, 116 (1980).
- [7] Hadziioannou, G.; Picot, C.; Skoulios, A.; Ionescu, M.-L.; Mathis, A.; Duplessix, R.; Gallot, Y.; Lingelser, J.-P. Macromol. 15, 263 (1982).
- [8] Hasegawa, H.; Hashimoto, T.; Kawai, H.; Lodge, T. P.; Amis, E. J.; Glinka, C. J.; Han, C. C. Macromol. 18, 67 (1985).
- [9] Matsushita, Y.; Nakao, Y.; Saguchi, R.; Mori, K.; Choshi, H.; Murogoa, Y.; Noda, I.; Nagasawa, M.; Chang, T.; Glinka, C. J.; Han, C. C. Macromol. 21, 1802 (1988).
- [10] Matsushita, Y. (to be published).
- [11] Cotton, J. P.; Decker, D.; Benoit, H.; Farnoux, B.; Higgins, J.; Jannink, G.; Ober, R.; Picot, C.; des Cloizeaux, J. Macromol. 6, 863 (1974).

SANS STUDY OF ORDER AND DISORDER IN A MODEL DIBLOCK COPOLYMER

F. S. Bates, J. H. Rosedale, and G. H. Fredrickson
(AT&T Bell Laboratories, Murray Hill, NJ)

and

C. J. Glinka

A partially deuterated poly(ethylenepropylene)-poly(ethylethylene) (PEP-PEE) diblock copolymer containing 55% by volume PEP was studied by small angle neutron scattering (SANS). Two series of measurements were conducted, separately addressing the disordered and ordered states of this material. As described in a recent publication [1], the order-disorder transition (also referred to as the microphase-separation transition (MST)) for this diblock copolymer occurs at $T_{MST} = 125 \pm 1^\circ\text{C}$

The first set of SANS experiments on this sample was designed to examine the significance of fluctuations above T_{MST} . Recent theory [2] predicts non-mean-field behavior for disordered block copolymers well above the MST. By precisely measuring the SANS peak intensity between 126 and 181 $^\circ\text{C}$, we were able to conclusively demonstrate that fluctuation effects play a dominant role in determining the location of the MST. In addition, these measurements provide the first quantitative test of the fluctuation-induced first-order transition theory of Braovskii [3], which finds application in various areas of physics.

The second set of SANS measurements addressed the ordered state. For the nearly symmetric composition characterizing our sample, a lamellar phase is anticipated [2] at temperatures below T_{MST} . However, simply cooling the sample produces a macroscopically isotropic (i.e., "powdered") material, and accordingly a Debye-Scherrer scattering pattern. We have found that shearing this material on a dynamic mechanical spectrometer produces dramatic changes in the rheological properties which we attributed to the development of long range order, i.e., orientation. In order to test this hypothesis, specimens were sheared, and subsequently studied on the SANS instrument. As illustrated in figure 1, this shearing in fact results in the spectacular alignment of lamellae, which is preserved over long times at room temperature (fig. 1A). As this sample is heated towards T_{MST} the initial anisotropy begins to decrease (fig. 1B) due to the influence of the fluctuations already demonstrated to be significant above T_{MST} [1] (see above). The residual

anisotropy evident at 123 °C (fig. 1C) clearly disappears with heating through T_{MST} to 127 °C (fig. 1D).

Through these SANS studies we are developing a qualitatively new understanding of the behavior of block copolymers near the order-disorder transition.

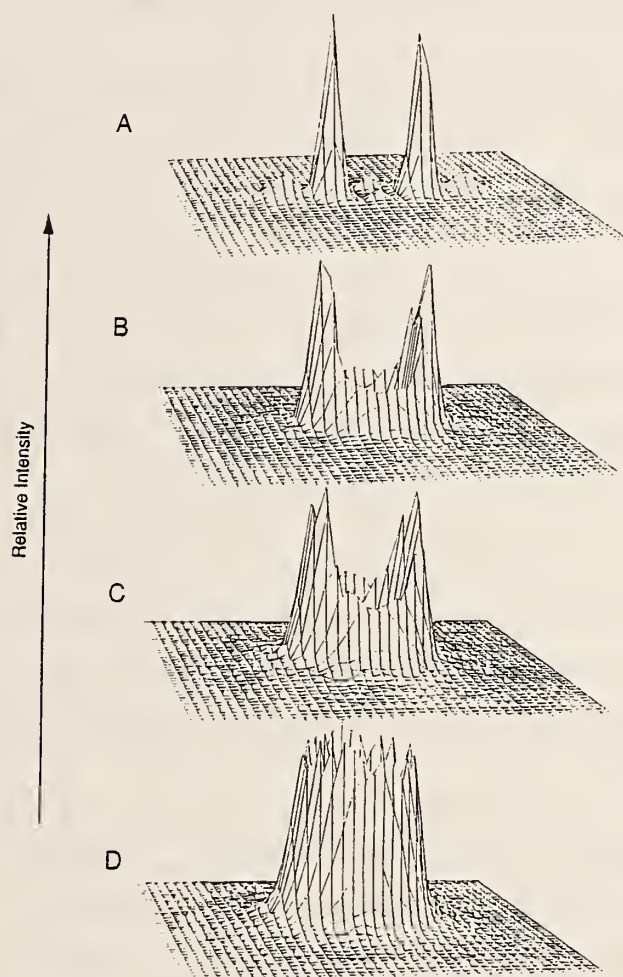


Figure 1. Relative SANS intensity (all scaled to equal magnitude) recorded on a two-dimensional detector for a shear-oriented PEP-PEE diblock copolymer: A) as prepared, 22 °C heating to B) 99 °C, C) 123 °C, and D) 127 °C. The loss of anisotropy between 123 and 127 °C results from passing through the microphase separation transition.

References

- [1] Bates, F. S.; Rosedale, J. H.; Fredrickson, G. H.; Glinka, C. J. Phys. Rev. Lett. 61, 2229 (1988).
- [2] Fredrickson, G. H.; Helfand, E. J. Chem. Phys. 87, 697 (1987).
- [3] Brazovskii, S. A. Sov. Phys. JETP 41, 85 (1975).

MOLECULAR STRUCTURE OF BIMODAL POLYMER NETWORK

W.-L. Wu and L. D. Coyne
(Polymers Division)

and

L. Jong, A. Hanyu, and R. S. Stein
(University of Massachusetts, Amherst, MA)

Model polymer networks have been prepared by reacting polymer chains exclusively at their ends. The chain length distribution of the resultant network is thus identical to that before crosslinking. It was observed that for polydimethylsiloxane (PDMS) the networks prepared with a bimodal molecular weight distribution exhibited some unique features compared to the unimodal networks [1]. The most noticeable difference is the ultimate strength before break; the bimodal networks are much stronger or tougher than the unimodal ones. Progress has been made toward the understanding of the molecular origins of this difference in network properties. Stress-strain, stress-birefringence and stress-temperature measurements were conducted to elucidate the cause of this unusual feature in bimodal networks [2]. However, experiments which can provide a direct characterization of the molecular structure in these networks have not been carried out.

In this report, a set of preliminary results from small angle neutron scattering (SANS) of bimodal polytetrahydrofuran (PTHF) network will be presented. The question to be addressed is whether the short and the long chains are deposited randomly in the bimodal network. A random disposition of the long and the short chains within an average network is the obvious choice, and is also assumed in all the previous work, at least implicitly. However, in an early work with an epoxide-amine reaction as the crosslinking mechanism, SANS results indicated that the short and the long chains were segregated [3]. The definition of segregation needs to be clarified; it does not necessarily imply the existence of long-chain and short-chain domain structure as for the cases of segregated block copolymer. Such segregation will be called as phase segregation. The other segregation to be emphasized in this work is defined as follows: the makeup of the chemical neighbors of a short chain (or a long one) is not statistically random. In an early work, the chemical neighbors of a short chain were found to be a long one and vice versa [3]. Such segregation will be called the molecular segregation. The

linear chain analog of a molecular segregated network is a block copolymer; the short chain (S) and long chain (L) after crosslinking forms $(S-L)_n$ or other block-like structures with certain regularity.

For all the SANS specimens, every short chain is deuterated while the long one is hydrogenated. The synthesis of the difunctional PTHF with narrow molecular weight distribution was carried out according to the method of Smith and Hubin. The GPC results of the prepolymers used in this work is given in table 1; two pairs of prepolymers were used and they were denoted by the subscripts 1 and 2, respectively. The polydispersity of these prepolymers is in the range of 1.1 to 1.3. The details of the synthesis can be found elsewhere [4].

Pentaerithritol tetrakis (3-mercaptopropionate) was used as the crosslinking agent and a stoichiometric amount of it was used for all the samples. The reaction was initiated with benzopinacole which was stable at ambient temperature, by heating to 80 °C or above this compound would be activated to start the crosslink process. Two sets of samples were prepared using prepolymer pair 1; one contained 0.19% wt. initiator and the other with 0.16% wt. For both sets of the samples the molar ratio of the long to short chain was kept at 1.1. The third set of samples was prepared with prepolymer pair 2 with a molar ratio of long to short chain at 3:7. The initiator concentration used was 0.6% wt. The specifications of the samples are given in table 2.

For each of the three sets of samples, SANS measurements were conducted on the uncured, the completely cured and a few intermediately cured samples. The SANS facility at the NIST reactor was used. The sample temperature was kept at 50 °C, a few degrees above the melting point of PTHF, throughout the SANS measurements. The wavelength of the incident neutrons was set at 12 Å and the q range covered was from 0.005 to 0.08 Å⁻¹. After subtracting the incoherent component and the empty cell background, the scattered neutron intensity was reduced to its absolute scale with a silica gel sample as a secondary scattering standard.

The SANS results of sample set A are given in figure 1. For the uncured sample (curve a), the $I(q \rightarrow 0)$ is estimated to be 0.7 cm⁻¹ which is very close to the theoretical value of 0.74 for the prepolymer pair assuming an ideal mixing. This result strongly suggests that the mixing of the long and the short chains in the uncured state approaches that of an ideal solution.

REACTOR RADIATION DIVISION AND COLLABORATIVE PROGRAMS

If cure or crosslink does not induce either molecular or phase segregation between the hydrogenated long chains and the deuterated short chains, the scattering intensity will stay unchanged. However, as illustrated in curve b, a dramatic increase in intensity occurred in the small q range. This provides an unequivocal evidence for segregation. However, from curve b alone one can not yet determine that the type of segregation is of the phase type or the molecular one.

As cure proceeds to its completion, the scattering intensity, especially in the low q region, exhibits a remarkable decrease. In addition, a weak maximum appeared around q of 0.04 \AA^{-1} in the scattering intensity for the cured sample (curves c and d).

This trend was also observed in sample sets B and C. The weak maximum resembles that observed for regular block copolymer. The intensity at the maximum is only a few times greater than that of the uncured sample. This tends to suggest that the segregation is of the molecular type instead of the phase type.

At the present time we cannot rationalize all the findings and more work is apparently needed. Nevertheless, the SANS results covered in this note strongly suggests that crosslink can induce segregation in bimodal network. This result is consistent with the early finding of the epoxy-amine system. In light of this new discovery, some of the earlier observations made on bimodal network needs to be re-examined.

Table 1. Molecular weight of PTHF prepolymers

	<u>Mn</u>
L_1	8286
S_1	995
L_2	10034
S_2	1018

Table 2. Specifications of SANS samples

<u>Designation</u>	<u>Prepolymers</u>	<u>Initiator Concentration % wt.</u>	<u>Molar Ratio L:S</u>
A	L_1, S_1	0.19	1:1
B	L_1, S_1	0.14	1:1
C	L_2, S_2	0.6	3:7

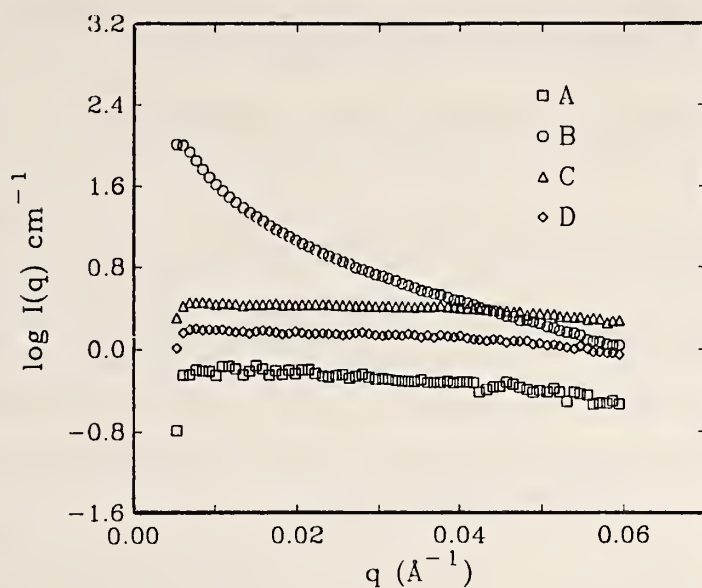


Figure 1. SANS results of PTHF at different levels of Crosslinking--
A, uncrosslink; B, C, intermediate; D, completely crosslinked.

References

- [1] Mark, J. E. *Advances in Polym. Sci.* **44**, 1 (1982).
- [2] Mark, J. E.; Andrady, A. L. *Rubber Chem. Tch.* **54**, 366 (1981).
- [3] Wu, W.; Bauer, B. J. *Macromol.* **19(6)** 1613 (1986).
- [4] Jong, L. Doctor Dissertation, University of Massachusetts (1989).

REACTOR RADIATION DIVISION AND COLLABORATIVE PROGRAMS

**SMALL ANGLE NEUTRON SCATTERING STUDIES ON CHAIN ASYMMETRY
OF COEXTRUDED POLY(VINYLALCOHOL) FILM**

M. Shibayama, H. Kurokawa, and S. Nomura
(Kyoto Institute of Technology, Kyoto, Japan)

S. Roy
(Polaroid Corporation, Norwood, MA)

R. S. Stein
(University of Massachusetts, Amherst, MA)

and

W.-L. Wu
(Polymers Division)

Poly(vinylalcohol) (PVA) is a crystalline polymer for which the local conformation is not well understood. Fringed-micelle type structure has been accepted for a long time for PVA film prepared from aqueous solution. On the other hand, folded chain crystals are observed if it is solidified from an organic solvent [1]. It is natural to expect that intra- and inter-chain hydrogen bonding play an important role in local chain organization. On deformation, these hydrogen bonds may work as crosslinking points or entanglements. Since PVA is a polymer widely used in industry [2]; e.g., fibers, staples, asbestos alternatives, sheet, high oxygen barrier film, and so on, it is worthwhile to explore chain asymmetry of deformed PVA fibers and/or films.

In this work, we examine the radii of gyration of solid state co-extruded PVA film cast from aqueous solution in both the extension and the perpendicular directions by small angle neutron scattering. Deutereous and hydrogenous poly(vinylalcohol)s were supplied by Kuraray Co., Ltd. Those are coded as d-PVA and h-PVA followed by the viscosity-average degree of polymerization, respectively. A 50/50 (by weight) mixture of d-PVA and h-PVA powder was dissolved in boiling distilled water. The solution of ~ 10 wt.% was stirred for a few hours at 90 °C then cooled gradually to room temperature. Films of the PVA mixture were prepared by solution casting onto a glass plate at 60 °C. The thickness of the films was around several hundred microns.

The films were coextruded with a polyoxymethylene billet at 165-170 °C at a crosshead speed of 1 mm/s. The extension draw ratio (EDR) was varied by

changing aspect ratio of the conical die. Coextrusion with EDR larger than 5 was difficult because of the extruded film becoming inhomogeneous.

The SANS results can be summarized as follows: the statistical segment length for PVA is found to be 5.76 Å. Chain asymmetry of solid-state coextruded PVA was examined by both small-angle neutron scattering and birefringence measurements. It was found that PVA chains were affinely deformed for extension up to $EDR = \sim 5$. Birefringence measurements also show the affine nature of the deformation of PVA chains. Birefringence measurements show that PVA is more effectively deformed than polystyrene, which is explained by a positive effect of hydrogen bonding on extension.

References

- [1] Tuboi, K.; Mochizuki, T. *Kobunshi Kagaku* 23, 636 (1966); 24, 433 (1967).
- [2] For example, Sakurada, I. *Polyvinylalcohol fibers*. Marcel Dekker, NY (1985).

IN-SITU NEUTRON DIFFRACTION ON DEUTERIUM LOADED PALLADIUM IN AN ELECTROCHEMICAL CELL

S. K. Satija, D. A. Neumann, C. F. Majkrzak, and J. J. Rush

D. Lashmore and C. Johnson
(Metallurgy Division)

and

R. M. Lindstrom
(Inorganic Analytical Research Division)

The phase diagram of the palladium/hydrogen system is well known. At room temperature and low concentration of hydrogen (or deuterium) the system exists in the α -phase with a lattice constant very similar to that of pure palladium. At higher concentrations of H(D) there exists a β phase with a considerably expanded lattice where the H(D) atoms are located in the octahedral interstitial sites [1].

We report here in-situ neutron diffraction measurements on palladium in an electrochemical cell. This was done in order to investigate whether tetrahedral interstitial sites could be filled with D by the electrolysis process. The electrolysis cell was made out of thin walled teflon sheet.

The electrolyte used was 0.1 M LiOH in D₂O (99.5%). The palladium electrode was in the form of a sheet .4 mm thick. The other electrode was a thin sheet of platinum. During the diffraction data collection the cell was rotated by 180° in order to average out the effect of any preferred orientation of crystallites in the original palladium sample.

Figure 1 shows the neutron diffraction pattern (taken with 1.53 Å neutrons) from Pd before electrolysis. All the Pd peaks are labeled in the figure. The other peaks are from the teflon cell. The Pd peak intensities (after correction for the Lorentz factors) are in good agreement with what is expected from pure FCC palladium. The palladium was first loaded with D by applying a current of 1 A for 12 h before taking the diffraction data. The same current of 1 A was kept on while collecting the diffraction data. The lower part of figure 1 shows the diffraction pattern from D loaded Pd under the conditions described above. All of the peaks shift to lower angles due to expansion of the lattice. The even hkl peaks increased in intensity and all the odd hkl peaks decreased in intensity. For clarity, two of the diffraction peaks (311) and (222) before and after electrolysis are shown in figure 2.

The lattice constant of the cell after electrolysis was found to be 4.035 Å. This is similar to what is reported for β-phase Pd-D(H) in the literature [1]. Our attempts to fit the data to a β-phase Pd-D cell, in which D atoms are located in octahedral sites, resulted in an octahedral site occupancy of only 0.32 as opposed to the known value of ~0.7. The results of such a fit are shown in table 1. The rms displacement of D atoms was found to be 0.21 Å in very good agreement with earlier results [1]. Any attempts to fit the data by partially or fully filling the tetrahedral sites was unsuccessful.

An occupancy factor of only 0.32 for D loaded sample points to the fact that there is a considerable amount of H along with D in the electrolysed palladium. Assuming a filling factor of 0.7 for octahedral sites, one can calculate the amount of H present in the D loaded Pd sample. This turns out to be H(0.35) and D(0.65). Even though the electrolytes used contained at most 1-1.5% H, the final loaded Pd contains nearly 35% H. Higher solubility of H (as compared to D) in Pd under electrolysis is quite well known [2]. However the separation factor

$$S_{\text{metal/liq}} = (H/D)_{\text{metal}} / (H/D)_{\text{liq}} \approx 35$$

REACTOR RADIATION DIVISION AND COLLABORATIVE PROGRAMS

that we obtain seems to be much higher than the highest values reported in literature (of the order of 10-13). A neutron activation analysis of the electrolysed Pd sample also confirmed our estimate of about 30% H in the sample.

Table 1. Measured and calculated ratios of the integrated intensities of the observed peaks after the sample was loaded to those of the pristine sample. The calculated values were obtained using an octahedral site occupancy of 0.32 D/Pd and an rms displacement of 0.21 Å for the octahedral atoms

Peak	Measured Ratio	Calculated Ratio
(111)	0.40 ± 0.03	0.48
(200)	1.68 ± 0.08	1.67
(220)	1.49 ± 0.07	1.52
(311)	0.47 ± 0.03	0.64
(222)	1.14 ± 0.17	1.41
(400)	1.44 ± 0.12	1.33
(331)	0.51 ± 0.07	0.76
(420)	1.11 ± 0.08	1.26

The electrolysis of Pd in nearly 99% deuterated electrolysis solution leads to substantial amounts of H isotope being incorporated in the Pd sample. No evidence for incorporation of D (or H) into the tetrahedral sites was seen. It seems, therefore, that in the recent experiments on cold fusion done by many groups a large amount of H along with D was present in the Pd electrodes.

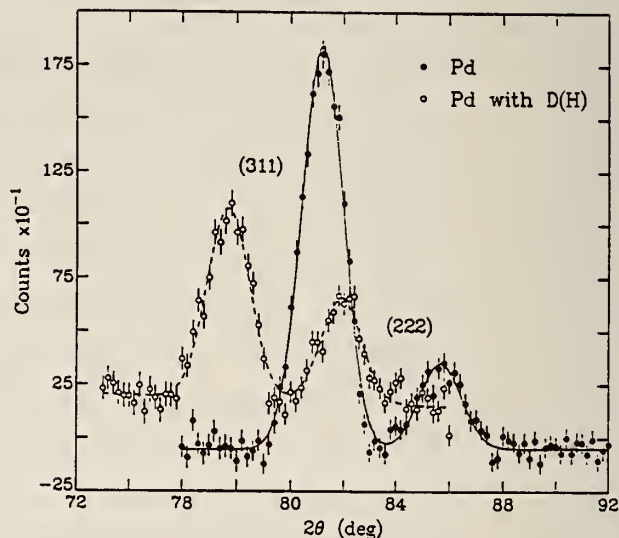
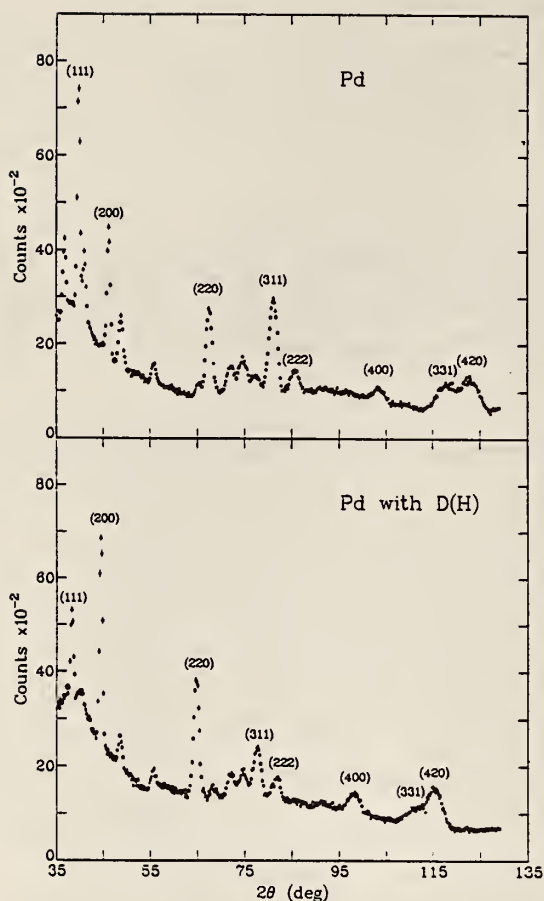


Figure 1. (left) In-situ neutron diffraction patterns of Pd before and after electrolysis. The neutron wavelength used was 1.53 Å. Both Pd and Pd D(H) peaks are marked in the figure. The other peaks are from the teflon cell.

Figure 2. (right) A selected section of in-situ neutron diffraction pattern of Pd before and after electrolysis. The lines are fit to the data with gaussian line shapes.

References

- [1] Worsham, J. E.; Wilkinson, M. K.; Shull, C. G. J. Phys. Chem. Solids **3**, 303 (1957).
- [2] See e.g., Lewis, F. A. The Palladium-Hydrogen System, Academic Press (1967).

COMMENTS ON COLD FUSION IN METALS

R. C. Casella

I spent some time thinking about (and discussing with other NIST scientists [1]) possible low-temperature fusion of deuterons in Pd and Ti metals [2]. Two qualitative conclusions were drawn. (i) The idea that a condensed-matter quasiparticle of large effective mass m^* in metallic Pd or Ti could play a role analogous to that of the muon in the known muon-induced fusion process by drawing the deuterons very close together in a solid (a theoretical motivation discussed by Jones et al. [2]) is incorrect. The concept of effective mass applies when reckoning the response of a quasiparticle in a solid to potentials which vary slowly over distances of the order of a lattice constant--not rapidly on the scale of tenths of angstroms. For example, one uses the free-electron mass to compute the core levels of heavy atoms in the solid state, not the effective mass of some band-like or quasi-localized electron contributing to the conduction process. (ii) A three-body DDPd process (suggested by M. Danos [3]) involving a recoiling Pd nucleus, which allows direct production of a fast-moving (23 MeV) α particle in its internal ground state, should lead to the production of host-metal x-rays by the heavily ionizing α 's as they are stopped in the solid. (The Danos mechanism proceeds by exchange of off-shell γ 's and yields no final-state proton, neutron or on-shell γ , unlike the two-body DD fusion process.) The x-rays produced by the stopping α 's ought to be observed in experiments originally designed to look for host-metal x-rays generated by the stopping protons, which are produced with branching ratio $\sim 50\%$ in two-body DD fusion. To my knowledge, such x-rays have not been detected. The absence of a signal in the charged modes, coupled with the serious background problems associated with the minuscule neutron counting rates [2] implies that considerable effort will be required to place reliable quantitative bounds on (or to detect) cold fusion in metals, including the three-body amplitude in question.

References

- [1] Berger, M.; Berk, N.; Danos, M.; Fleming, R.; Gilliam, D.; Lamaze, G.; Lashmore, D.; Lindstrom, R.; Majkrzak, C.; Neumann, D.; O'Connell, J.; Rush, J.; Satija, S.; Schrack, R.; Stone, C.; Wasson, O. private communications (unpublished).

- [2] Jones, S.; Palmer, E.; Czirr, J.; Decker, D.; Jensen, G.; Thorne, J.; Taylor, S.; Rafelski, J. Nature 338, 737 (1989).
- [3] Danos, M. Post-deadline paper presented at the spring meeting of the American Physical Society, Baltimore, MD (1989) and private communication.

CAVITY GROWTH RATES IN FATIGUED COPPER

J. G. Barker and J. R. Weertman
(Northwestern University, Evanston, IL)

Materials stressed at high temperatures, $(0.4 - 0.7) T_m$, fail by the nucleation, growth, and coalescence of grain boundary cavities. Diffusional growth of cavities in materials under static stress has been adequately described [1], but predicts no net growth under fully reversed fatigue conditions. By including a second order stress dependence of grain boundary diffusivity, a small net growth rate is expected [2], but in practice, the cavity growth rate under fatigue matches or exceeds that under creep conditions. Other mechanisms involving plastic strain or gas stabilization have also been proposed [3-5].

The present study separates the stress and plastic strain effects by measuring cavity growth as a function of fatigue frequency. A weighted cavity size, $R_p = \langle R^3 \rangle / \langle R^2 \rangle$, is measured by combining precision density measurements to determine cavity volume fraction, V_v , with SANS measurements in the Porod region to determine cavity surface area, S_v . A characteristic cavity volume is defined as: $V_p = 4/3\pi R_p^3$; $R_p = 3V_v/S_v$; a characteristic cavity number as: $N_p = V_v/V_p$.

V_p and N_p will give estimates of cavity growth and nucleation, respectively. The cavity volume, V_p , measures a weighted cavity growth; due to the distribution of cavity sizes, N_p is also affected. The true cavity size and number are measured only with a monodisperse size distribution.

The 99.999% pure copper samples were tested at 405 °C temperature and 34.4 MPa stress amplitude. The cavity volume fraction varied from 10×10^{-5} to 600×10^{-5} and the cavity surface area varied from 8 to 250 cm^{-1} . A series of samples were tested at 17 Hz frequency with varied number of cycles. The cavity growth rate was found to be constant, $dV_p/dt = 7.5 \times 10^{-23} \text{ m}^3 \text{ s}^{-1}$ (see fig. 1a). The nucleation appears to be mostly completed within the first 10% of sample life, ($N_f = 810,000$). Snowden [6]

et al. also claim nucleation is completed within 20% of fatigue life, but during creep nucleation has been found to be continuous.

Another series of samples were tested with fixed number of cycles, (100,000), but with the frequency varied from 2 to 100 Hz. The growth rate was found to increase with increased frequency. Weertman's theory predicts growth should be independent of fatigue frequency. Since the plastic strain amplitude is constant over this frequency range, the growth rate should be linear with respect to frequency if plastic strain was controlling the growth process. The total number of cavities also increases with increased frequency (see fig. 2b).

In summary, by combining PDM and SANS measurements, a characteristic cavity size and number can be estimated. Measurements completed on fatigued copper samples indicate:

- o Most cavities are nucleated early in sample life.
- o The cavity growth rate is constant at fixed frequency.
- o Growth rate increases with increased frequency.
- o Number of cavities increases with increased frequency.

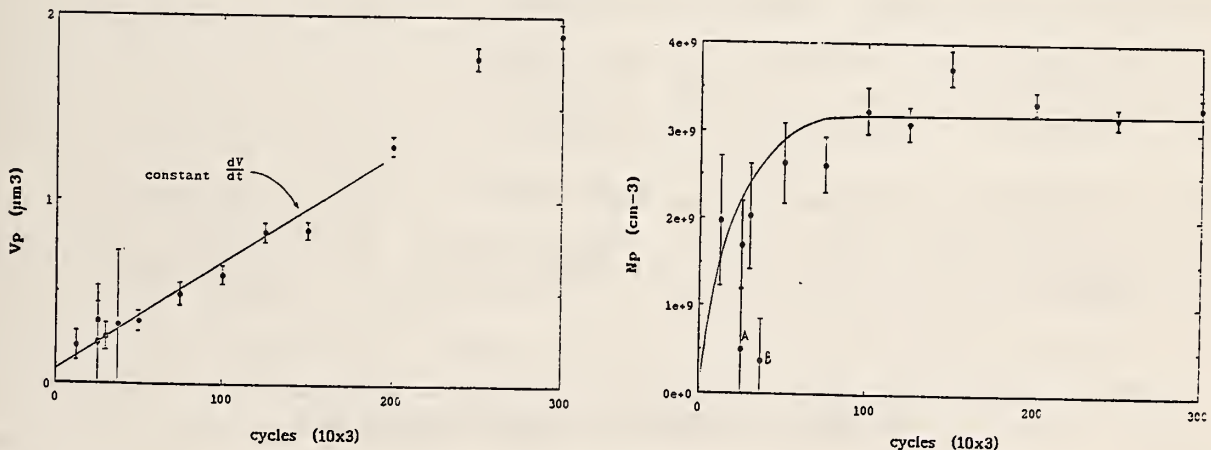


Figure 1. All samples in the figure were tested at 17 Hz, 405 C, and 34.4 MPa. Left figure plots cavity volume V_p as a function of number of fatigue samples. Right figure plots number of cavities N_p as a function of number of cycles. Points denoted as A and B correspond to samples with a 200 micron grain size, explaining the low N_p values, all other samples have a 50 micron grain size.

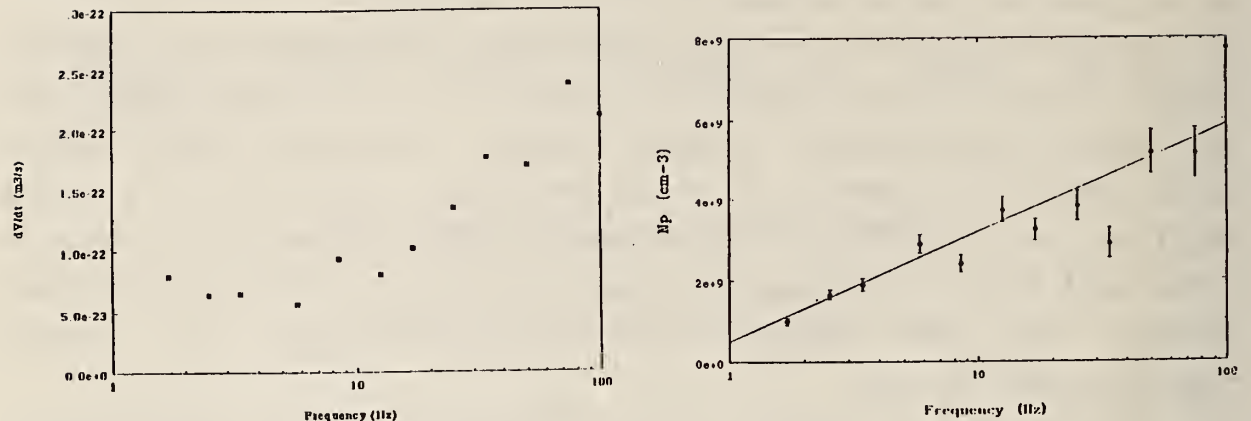


Figure 2. All samples in the figure were tested at 405 C, 34.4 MPa, and 100,000 cycles. Left figure plots cavity growth rate dV_p/dt , as a function of fatigue frequency. The right figure plot cavity number versus fatigue frequency.

References

- [1] Speight, M. V.; Beere, W. J. Met. Sci. 9, 190 (1975).
- [2] Weertman, J. Met. Trans. 5, 1743 (1974).
- [3] Skelton, R. P. Phil. Mag. 14, 563 (1966).
- [4] Gittins, A. J. Met. Sci. 2, 51 (1968).
- [5] Trinkaus, H. Scripta Met. 15, 825 (1981).
- [6] Snowden, K. U.; Stathers, P. A.; Hughes, D. S. Res. Mechanica 1, 129 (1980).

TEXTURES OF SPECIALLY FABRICATED METALS

C. S. Choi
(ARDEC, Picatinny Arsenal, NJ and Reactor Radiation Division)

and

H. J. Prask

During the reporting period, the textures of three specially fabricated metal samples were studied. They are a Ta sheet provided by the Naval Surface Warfare Center, a hemispherical Ti shell fabricated at Los Alamos National Laboratory, and DU tensile specimens with 7% and 20% tensile strains

provided by the Army Materials Technology Laboratory. The measurements of the Ti and DU tensile samples will be continued in FY 90 with new samples.

Ta Sheet. The samples were prepared from a cylindrical ingot by applying a series of thermomechanical treatments: upset forge, reforge to original cylinder, rolling to a plate form, and annealing at high temperature. The sample used was a large triangular piece with edge lengths of approximately $7.6 \times 10.2 \times 12.7 \text{ cm}^3$. Since the sample was much larger than the neutron beam cross section, the exposure volume was limited by covering the surface with a thin Cd sheet (0.25 mm thick), leaving a circular exposure hole (12.7 mm diam) at the center of the sample. The texture was measured over the partial orientation hemisphere ranging from $\chi = 90^\circ$ to 20° , $\phi = -180^\circ$ to 180° , using the reflection method. The 110, 200, 211, and 222 pole figures were measured. In this nondestructive method, the exposed volume varies as a function of scattering angles and of χ -angles. Therefore, the data were normalized to the calculated exposure volume, then were converted to the pole density in the units of multiples of a random distribution (m.r.d.). Among the four pole figures, 220 and 222 are shown in figure 1. The pole figures could be interpreted as having three preferential orientations, each with the slip plane (pole in the normal direction) of 111, 100, and 113, respectively. The corresponding pole-density peak positions based on the three-texture model are marked in the pole figures.

Ti Hemispherical Shell. The textures of two samples, labeled E and P, which were cut from a quarter-sphere sample, were measured by neutron diffraction. Sample E is approximately a rectangle cut from the equatorial region, with approximate dimensions of 10 mm x 8 mm x 2 mm. Sample P is approximately a rhombus cut from the pole region, with side edges approximately 8 mm long and the short diagonal, 7 mm long. The samples were mounted on the goniometer of the χ -circle cradle, with the sample rotation axis (ϕ -axis) perpendicular to the sample surface. Due to the scheduled shutdown of the reactor, only three pole figures (100, 101, and 110) were measured from sample P, and only two (100 and 101) from sample E. The diffraction intensities were measured over an entire hemisphere using 1.275 Å wavelength neutrons. The observed intensities were converted to the pole density in m.r.d. units, and are presented in equal-area type pole figures, using established procedures. The 101 pole figures are shown in figure 2. Comparing the pole figures of the two samples, some texture gradients are

evident in going from equator to pole of the hemispherical sample. At the pole, a fiber-texture distribution is clear in all patterns, which in the equator pole figures, becomes a sheet-texture type.

DU Tensile Samples. The textures of four uranium samples, labeled A, WR, A2, and WR2, were measured by neutron diffraction methods. Sample A was prepared by annealing at a high temperature to reduce the texture. Sample WR was prepared by a warm rolling of cast ingot. Sample A2 was prepared by applying 7% tensile deformation to the annealed sample, and WR2 by applying 20% tensile strain to the warm-rolled sample. Each sample was cut into two identical-sized pieces ($1.9 \times 1.9 \times 0.25 \text{ cm}^3$), which were stacked with the rolling directions aligned in the same direction to make a square plate.

Four pole figures, 020, 111, 112 and 131, were measured using the normal procedures, with 1.275 Å wavelength neutrons. The absorption corrections were calculated by assuming that the effect of the ϕ -angular orientation is negligibly small. The observed pole figures of the WR2 sample are given in figure 3. The 020 pole figure indicates clearly that the crystallites in the warm-rolled tensile sample are highly oriented with the 010 poles concentrated in the rolling direction, with the maximum pole densities of 11 m.r.d.. The pole figures of the WR samples are quite similar to those of WR2, which indicates that the two samples have essentially an identical texture. Since the 010 poles are concentrated in the rolling direction, the preferential poles in the normal direction must consist of one or more of h0l-type poles. An examination of the 111, 112, and 131 pole figures suggested that the preferential pole in the normal direction is the 103 pole. Based on the (103)[010] slip model, the peak positions in the four pole figures were calculated and marked on the corresponding pole figures to compare with the observed pole densities.

The four pole figures of the annealed blank showed no particular texture except the several well-defined isolated peaks in the 020 pole figure, which suggests the presence of several large grains in the annealed blank. The annealed tensile sample with 7% strain (A2) showed very weak texture. The general features of the pole figures showed some similarity with the corresponding pole figure of WR or WR2 samples.

TA-5590 (220)

TA-5590 (222)



Figure 1. The 220 and 222 pole figures of the Ta sheet. The center of the pole figures correspond to the normal direction ($\chi = 90^\circ$) and the periphery to $\chi = 20^\circ$. The calculated pole density peak positions based on the three preferential slips were indicated with, squares for 100 slip plane, triangles for the 111 slip plane and x's for the 113 slip plane model. The contour levels of 1 m.r.d. or higher are given in steps of 0.5 m.r.d.

P-101

E-101

ZSTEP = 10

ZSTEP = 10

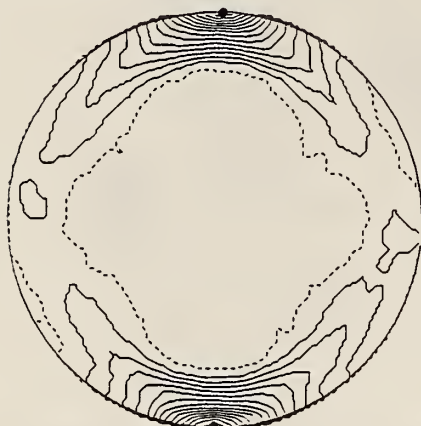


Figure 2. The 101 pole figures of the Ti samples S, P, and E. The center of each pole figure corresponds to the normal direction to the sample surface. The symbol LD in the pole figures of sample E indicates the longitudinal direction of the sample hemisphere, and in sample P it indicates the direction of the long diagonal of the rhombic shape. The densities lower than random intensity are shown by dotted contours, the lowest solid contour lines corresponding to "random." The contour intervals, in 0.1 m.r.d. units, are shown by the symbol ZSTEP in each pole figure.

REACTOR RADIATION DIVISION AND COLLABORATIVE PROGRAMS

WR 020

ZSTEP = 5.0



WR2 111

ZSTEP = 2.0

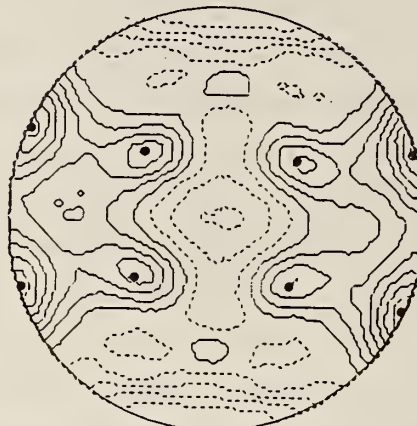


Figure 3. The 020 and 111 pole figures of the WR2 DU sample. The center of the pole figure corresponds to the normal direction of the sample. The calculated pole density peak positions based on a (103)[010] slip model are indicated with shaded circles.

RESIDUAL STRESS MEASUREMENTS IN METALLURGICAL SAMPLES

H. Prask

and

C. Choi

(ARDEC, Picatinny Arsenal, NJ and Reactor Radiation Division)

Energy-dispersive neutron diffraction was used to nondestructively determine subsurface residual stress distributions in three types of technologically important samples: plastically deformed U-0.75 wt% Ti rods, 7075-T6 aluminum nose cones ("ogives") for 155 mm shells, and an induction-hardened steel axle--a test specimen for the Society of Automotive Engineers. The first two represent new work in long-term programs which have been reported on previously; the last is a new effort.

In the U-0.75 Ti project, samples with different types of plastic deformation were provided to the Army by Battelle Pacifac Northwest Labs. The residual stress distribution in these samples is of interest because of their susceptibility to stress corrosion cracking and because of the effect of stresses on yield strength. Of particular interest in this case is the

separation of pseudo macrostresses produced by plastic deformation (i.e., microstresses which cause changes in d-spacings like long-range stresses) and the macrostresses of engineering interest. Initial measurements on small specimens cut from the samples of interest suggest that direction-dependent, measured effective d.-spacings may provide a means for removing the pseudo macrostress contribution from measured strains. This work is in progress.

Earlier residual stress measurements on two types of ogives suggested that a cold-sizing operation in the fabrication of one type induced tensile residual stresses which reduced the effective strength and led to documented failures. In the present effort pre- and post-sizing samples of the failure-prone type were examined by energy-dispersive neutron diffraction to determine changes in the residual stress distributions. A beam spot of $4 \times 4 \times 4 \text{ mm}^3$ was used to determine the stresses at four positions through the 18.2 mm thickness in the region where the failures occur. The results are summarized in the table 1.

Comparison of the hoop stress distributions for sized and unsized ogive blanks shows that sizing significantly affects the stresses. In the axial direction the final machining steps remove more than half of the starting material in the region of interest, and could necessitate a major redistribution of stresses to maintain balance over the equilibrium plane. However, the σ_{zz} distribution in the non-removal region (ID to ID + 8.6 mm) has the appearance of the finished ogive for both the sized and the unsized blanks. This suggests that the steps which produce the significant differences in the failing and nonfailing ogive axial stress distributions occur before the cold sizing.

In this reporting period a feasibility study was made for the SAE Fatigue Design and Evaluation (FD&E) Committee to determine the applicability of the neutron diffraction technique to residual stress determination in a multiaxial fatigue lifetime prediction project. Specifically, the project is part of an integrated engineering approach for design analysis and validation of components for vehicles in which test spindles, shown in figure 1, will be tested for fatigue life, characterized for materials properties--including residual stress, and modeled by finite element techniques. Depth-profiling of residual stresses had been done by x-ray diffraction with layer removal, about which the FD&E Committee felt some uncertainty.

REACTOR RADIATION DIVISION AND COLLABORATIVE PROGRAMS

Table 1. Residual stresses from neutron diffraction measurements

	<u>Unsize</u>		<u>Sized</u>	
	0°	180°	0°	180°
<u>OD - 2.25 mm</u> ^a				
σ_{rr}	-33(14)MPa	27(9) ^b	-70(14)	-82(11)
$\sigma_{\theta\theta}$	-21(26)	16(13)	-178(27)	-219(19)
σ_{zz}	-104(16)	-37(10)	-85(15)	-107(12)
<u>OD - 6.75 mm</u>				
σ_{rr}	-34(11)	-1(7)	9(10)	18(12)
$\sigma_{\theta\theta}$	54(22)	81(13)	-38(21)	-30(21)
σ_{zz}	36(14)	76(9)	23(13)	45(14)
<u>OD - 11.25 mm</u>				
σ_{rr}	-25(13)	-25(10)	49(10)	-13(14)
$\sigma_{\theta\theta}$	40(25)	138(19)	-30(19)	-126(27)
σ_{zz}	53(15)	90(12)	82(12)	5(16)
<u>OD - 15.75 mm</u>				
σ_{rr}	-23(12)	-72(11)	-1(10)	-4(9)
$\sigma_{\theta\theta}$	-21(24)	-2(22)	-96(19)	-81(17)
σ_{zz}	-50(14)	-49(13)	30(11)	29(11)

^aPosition of center of beam spot

^bStandard deviation due to counting statistics

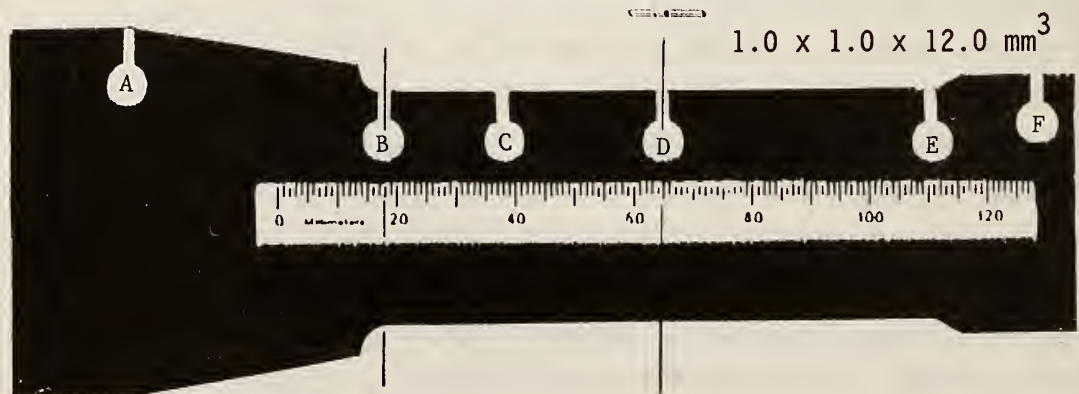


Figure 1. Schematic of SAE fatigue test specimen and neutron beam spot. The axle diameter at "D" is 40 mm.

For the initial neutron measurements, a simplified procedure was employed in which d-spacings were measured only for probe directions in the r - θ plane; i.e., with Q perpendicular to the cylinder axis. The beam-spot employed was 1 mm x 1 mm x 12 mm in size, oriented such that the long dimension was always parallel to the cylinder axis. Measurements were made with the center of the 1 mm x 1 mm cross section at 1.3, 3.3, and 6.3 mm below the 40 mm diam surface, which allows a relatively quick determination of $(\sigma_{rr}-\sigma_{\theta\theta})$, but not of the individual stress components. Several measurements were made at each of three depths along single radii with the center of the 12 mm length at positions "B" and "D" of figure 1, at which a finite element analysis (FEA) had been done.

From information provided and neglecting stress gradients in the axial direction, an FEA- $(\sigma_{rr}-\sigma_{\theta\theta})$ can be determined and compared to the neutron results (fig. 2). It is clear that the FEA- $(\sigma_{rr}-\sigma_{\theta\theta})$ changes much more sharply with depth than the measured values for both positions.

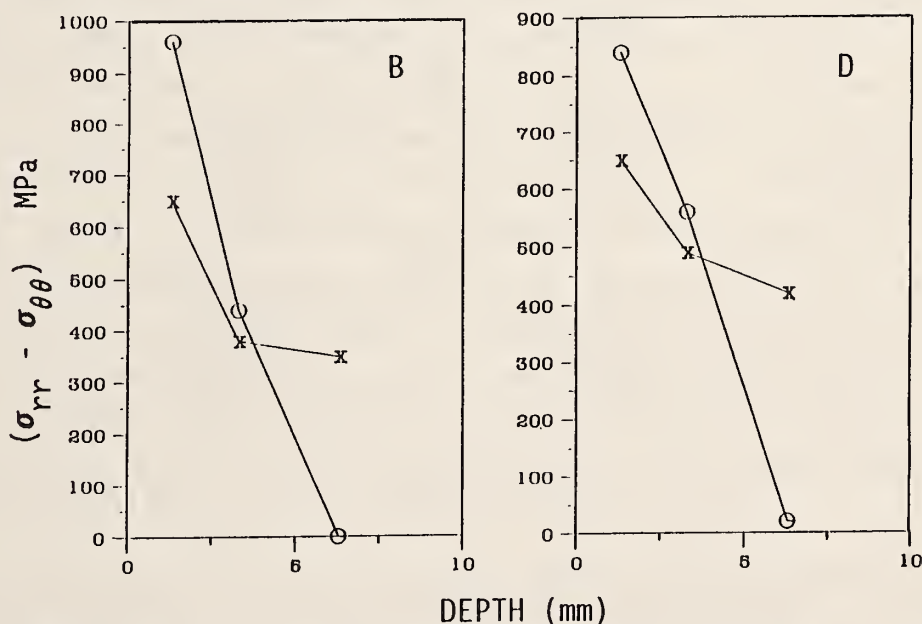


Figure 2. Comparison of $(\sigma_{rr}-\sigma_{\theta\theta})$ at points B and D of figure 1, as measured by neutron diffraction and as calculated; x = neutron, 0 = FEA.

With regard to the x-ray results, a direct comparison cannot be made since the x-ray measurements cannot determine σ_{rr} . However, it is worth noting that both the x-ray and the neutron results are in reasonably good agreement with the FEA calculations at a depth of ~3 mm, and in poor

agreement at ~6 mm. At ~1 mm the neutron results are in rather poor agreement with the FEA, whereas the x-ray/FEA agreement is variable. The FD&E Committee has requested continuation of the neutron measurements since a reliable determination of the triaxial stress distribution is not available to them and is essential for further refinement of FEA models.

MICROSTRESSES IN CERAMIC COMPOSITES

H. Prask

C. Choi

(ARDEC, Picatinny Arsenal, NJ and Reactor Radiation Division)

E. Fuller and R. Krause

(Ceramics Division)

Micro residual stresses occurring between constituents of a composite, e.g., between particles or fibers and matrix, are prime factors in determining the physical and mechanical properties (e.g., fracture toughness) of these materials. X-ray diffraction provides the best-established method for determination of residual stresses and has been used for the study of ceramic composites. In the x-ray case, however, surface macrostresses contribute to peak shifts and complicate the analysis. Neutron diffraction parallels x-ray diffraction for residual stress determination, but because neutrons in the diffraction-wavelength regime penetrate, typically, three orders of magnitude deeper than x-rays, either depth-profiling or total-sample averaging of stresses is possible. When a sample is totally immersed in the neutron beam, the macrostress contribution to peak shifts averages to zero.

In the present measurements, Al_2O_3 reinforced with 30 vol% SiC(whisker) was studied. To elucidate the effect of whisker size and mean spacing on the development of microstresses during processing, two different types of whiskers were used: Tokai TWS 100 (~0.4 μm diameter, ~10 μm long) and Tokai TWS 400 (~1.1 μm diameter, ~50 μm long). With each whisker type, processing into the composite was the same: hot-pressing into a disk 5 cm in diameter and 1.3 cm thick, at 42 MPa at 1700 °C for 30 min. The samples for neutron study were cut from the center of the pressed disks and ground to cubes 1 cm on a side.

The diffraction pattern of the pure SiC whiskers indicates that it is in the cubic form. In the composite, the most favorable SiC peak--based on intensity and overlap considerations--is the (311); Al_2O_3 peaks with similar d-spacings are the (300) and (125), of which the (300) is much more intense. The unstressed d-spacings were taken to be the values for the initial materials. Energy-dispersive neutron diffraction was used to determine the average d-spacings of each sample, totally immersed in the beam, for eight different orientations of each, from which strains were calculated using the assumed unstressed d-spacings. Stresses were calculated from the strains in the standard way, using an average of Reuss and Voigt diffraction elastic constants for SiC(311) and the elastic isotropic values for Al_2O_3 (300). The results are shown in the table 1, in which σ_{zz} corresponds to the pressing direction.

Table 1. Average microstresses in Al_2O_3 /30 vol% SiC(wh.)

	<u>TWS 100</u>	<u>TWS 400</u>
	Al_2O_3	
σ_{xx}	373(4) * MPa	301(4) MPa
σ_{yy}	336(6)	310(5)
σ_{zz}	273(5)	202(6)
	SiC	
σ_{xx}	-1018(6)	-1023(5)
σ_{yy}	-1055(9)	-1013(6)
σ_{zz}	-990(7)	-909(6)

* Standard deviations due to counting statistics only.

For both samples it is clear that the pressing direction is unique, with significantly less average stress than is observed in the orthogonal directions. As one would expect from the difference in thermal expansion coefficients and as has been observed elsewhere, the whiskers are in a state of high compression, the matrix in tension. Of particular interest is the fact that the TWS 400 composite, on the average, shows lower stress magnitudes than the TWS 100 material, which is possibly indicative of the different mean-spacing between fibers in the two samples.

REACTOR RADIATION DIVISION AND COLLABORATIVE PROGRAMS

**MULTIPLE SMALL ANGLE NEUTRON SCATTERING CHARACTERIZATION
OF THE DENSIFICATION OF ALUMINA**

G. G. Long
(Ceramics Division)

S. Krueger
(Polymers Division)

and

R. A. Page
(Southwest Research Institute, San Antonio, TX)

Over the past two decades, clear associations between microstructural character and performance capabilities have been identified for a number of ceramic systems. Progress toward achieving an improved process model and improved process control will be achieved when a better understanding of the relationships between processing variables and the resulting microstructure is obtained. Toward this end, we have been investigating the microstructure evolution as a function of thermal processing in well-characterized systems with precisely defined chemistries.

Until now, it has been very difficult to perform quantitative microstructure studies of ceramics in the early and intermediate stages of sintering because the relevant size range (0.08-10 μm) is beyond the resolution of standard techniques, and the density is between 55% and 90% of theoretical. The multiple scattering formalism developed by Berk and Hardman-Rhyne at NIST successfully addresses these issues [1]. Their formalism has been applied by us to the problem of microstructure evolution during the sintering of pure alumina and has led to the first detection of the transition from one sintering mechanism to another by small angle neutron scattering.

The samples were made by conventional sintering of Baikowski alumina powder (CR6, $6\text{m}^2/\text{g}$) that had been slipcast to an average green density of 53% theoretical density (TD). Samples were removed from the furnace at different times during the sintering process to yield examples of material between 56.5 and 98.9% TD.

Using the multiple scattering analysis formalism, the radius of curvature was determined as a function of neutron wavelength for each of eight samples. Figure 1 shows the radii of curvature measured (symbols) and the theoretical radii (solid lines). The densities measured volumetrically

and those determined by the neutron scattering are shown in the inset to the figure.

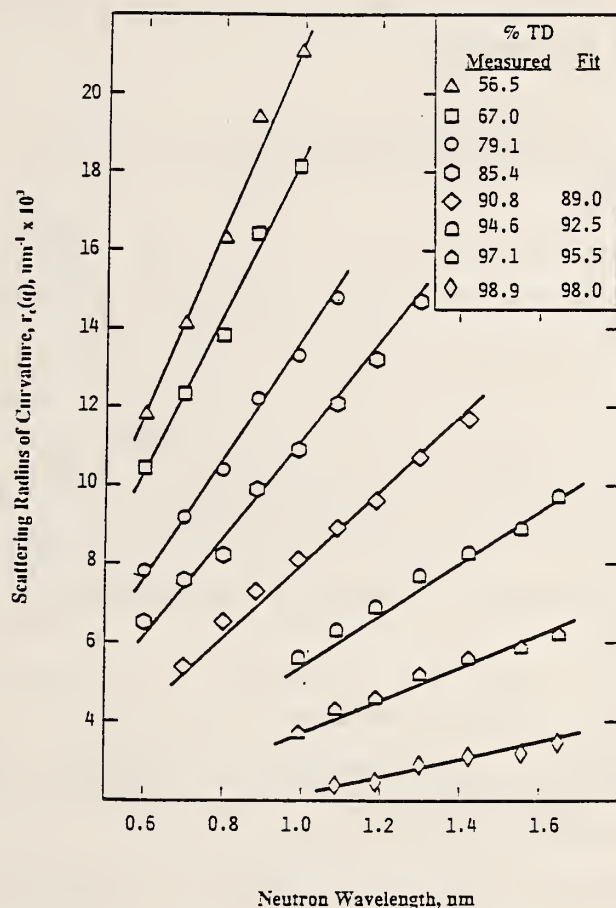


Figure 1. Measured radii of curvature (symbols) and the theoretical radii (solid lines) as a function of neutron wavelength. The inset identifies the sample symbols by their measured densities and shows the densities fitted by the theory, where different.

Figure 2 shows the effective average pore radius for the alumina samples as a function of percent theoretical density determined from the multiple scattering formalism ($R_{\text{eff}}(0)$) and from the single particle Porod measurement ($R_{\text{eff}}(\infty)$). The multiple scattering determinations, which are strongly weighted to the larger volume particles [2] indicate that the average effective pore radius for the distribution within the alumina decreases in the intermediate sintering stage and increases sharply in the final stage. The Porod determinations, which are made from the total surface scattering area, indicate an average effective pore radius that is slowly increasing during the intermediate stage of sintering and rapidly increasing during the final stage. Both methods show a break between the intermediate stage

processes, in which the pores are believed to be open, and the final stage processes, in which the pores become sealed off. The multiple scattering and the Porod analyses are combined to model the total pore size distribution during each step of thermal processing.

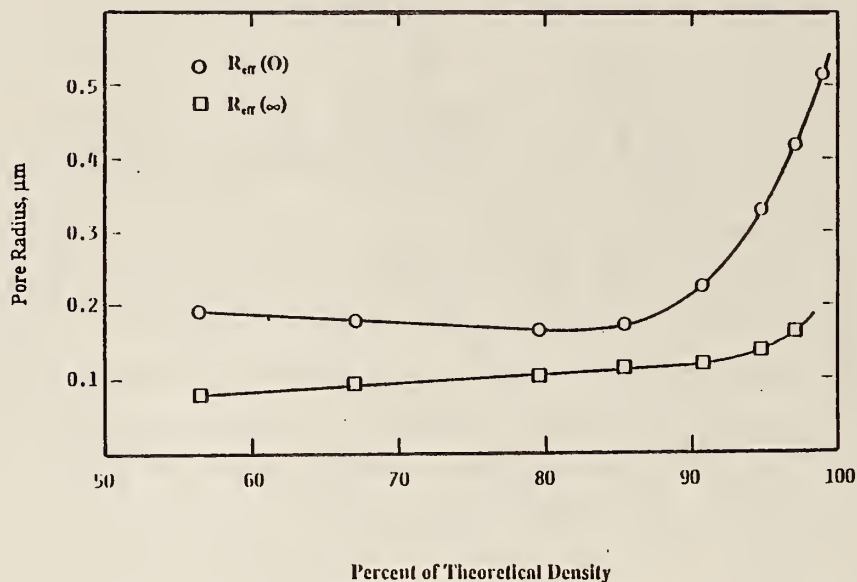


Figure 2. Effective pore radius (in micrometers) as a function of percent TD determined from the multiple scattering formalism (circles) and from the Porod analysis (squares).

This work was supported in part (GGL) by the U.S. Army Research Office under Grant No. 26123-MS.

References

- [1] Berk, N. F.; Hardman-Rhyne, K. A. Analysis of SAS DATA dominated by multiple scattering. J. Appl. Cryst. 21, 645-651 (1988).
- [2] Long, G. G.; Krueger, S. Multiple small angle neutron scattering characterization of the densification of ceramics: application to microporous silica. J. Appl. Cryst. (to be published).

NEUTRON SCATTERING AND ITS EFFECT ON REACTION RATES
IN NEUTRON ABSORPTION EXPERIMENTS

J. R. D. Copley

and

C. A. Stone
(Center for Analytical Chemistry)

In general there is a systematic error in the results of any inbeam neutron absorption experiment because of scattering in the sample [1]. The error is largest when scattering predominates over absorption, when the transmission of the sample is small, and when the lateral dimensions of the sample are large compared with its thickness. The ratio of the reaction rate in the sample (R), to the rate calculated ignoring both scattering and self-shielding due to absorption (\bar{R}), may be significantly less than or greater than unity, depending on the scattering properties of the sample and its size and shape.

These conclusions are derived from Monte Carlo calculations based on a very general expression for the rate of a neutron absorption reaction in a sample which scatters and absorbs neutrons. This expression is written as a sum over orders of scattering within the sample, as illustrated in figure 1, and was obtained using the technique adopted by Sears [2] in his study of multiple scattering effects in neutron scattering experiments. The first term in the series, R_0 , may be written as $\bar{R}c_0$, where \bar{R} is defined in figure 1 and c_0 is the self-shielding factor appropriate to neutron absorption experiments: for slab samples $c_0 = (1 - e^{-\tau}) / \tau$, where the optical thickness τ is the product of the slab thickness t and the total macroscopic cross section Σ_T . Each of the remaining terms R_j ($j \geq 1$) may be similarly written as $\bar{R}c_j$, where c_j is in general a $(4j + 3)$ -dimensional integral whose integrand is the product of j differential scattering cross sections (for the j scattering events), an overall attenuation factor, and a factor which expresses the departure of Σ_R from $(1/v)$ dependence. Complete details are given in reference [1].

In figures 2 and 3 we present the results of calculations of the correction factor $C = R/\bar{R}$, performed for slab samples of thickness t and lateral dimension ℓ , placed in a very narrow, monoenergetic, monodirectional neutron beam. The assumed scattering cross section was both isotropic and

$$R = \begin{array}{c} \text{---} \circ \text{---} \\ R_0 \end{array} + \begin{array}{c} \text{---} \circ \text{---} \\ R_1 \end{array} + \begin{array}{c} \text{---} \circ \text{---} \\ R_2 \end{array} + \begin{array}{c} \text{---} \circ \text{---} \\ R_3 \end{array} + \dots$$

$$\bar{R} = \begin{array}{c} \text{---} \circ \text{---} \\ \bar{R} \end{array} = \Phi V \Sigma_R$$

$$C = \frac{R}{\bar{R}}$$

Figure 1. The reaction rate R in a macroscopic sample is written as a sum of contributions from different orders of scattering. The first term, R_0 , represents neutrons which enter the sample and undergo the absorption reaction of interest. Subsequent terms R_j represent neutrons which are scattered j times and then undergo the reaction of interest. Attenuation of the beam, due to scattering and absorption, is included. The quantity \bar{R} is the reaction rate calculated in the approximation that both scattering and attenuation (by scattering and absorption) are ignored: ϕ is the mean incident neutron flux, V is the sample volume, and Σ_R is the macroscopic cross section for the reaction. The correction factor C is simply (R/\bar{R}) .

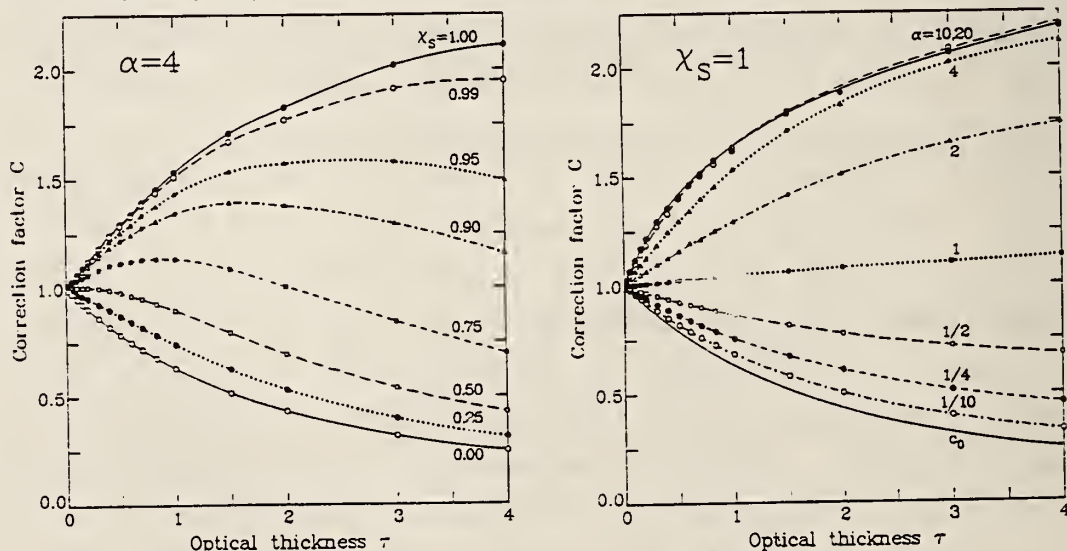


Figure 2. (left) Correction factors C for slab samples with aspect ratio $\alpha = 4$, for different values of the ratio $\chi_S = \Sigma_S/\Sigma_T$. The points represent the results of the Monte Carlo calculations whereas the lines are guides to the eye.

Figure 3. (right) Correction factors C for purely scattering slab samples with different aspect ratios α . The points represent the results of the Monte Carlo calculations whereas the lines are guides to the eye. The self-shielding factor c_0 is also shown.

static ("elastic" in the language of the thermal neutron scattering community), meaning that no change in neutron energy was permitted to occur within the sample. Figure 2 shows C as a function of τ , for different choices of the cross section ratio $\chi_S = (\Sigma_S/\Sigma_T)$, Σ_S being the total macroscopic scattering cross section of the sample. The calculations are for samples with $\ell = 4t$; i.e., samples with an aspect ratio $\alpha = \ell/t$ of 4. When $\chi_S = 0$, the only contribution to C is the self-shielding term c_0 , and the specific reaction rate (R/V) drops with increasing sample thickness. On the other hand (R/V) increases dramatically with increasing t in the limit that χ_S tends to unity. In this limit it is also very sensitive to χ_S at constant τ .

In figure 3 we show C as a function of τ , in the limit that χ_S tends to unity, for various choices of α . When α is much less than unity, i.e., for pencil-shaped samples, scattering mostly removes neutrons from the sample, so that C drops with increasing τ . In the opposite limit, that of a slab with infinite lateral dimensions, scattering increases the mean path length of neutrons in the sample and therefore enhances (R/V).

We are presently investigating the dependence of specific reaction rate on t , keeping ℓ fixed, in order to decide whether or not experimental measurements can be reliably extrapolated to zero thickness to correct for the effects of scattering (and absorption). We are also developing methods to calculate correction factors in samples of other shapes, such as disks and spheres. Our recent results suggest that extrapolations to zero thickness can be problematic, since C is a nonanalytic function of t .

In conclusion, we believe that changes in the mean distance travelled by a neutron, due to scattering, rather than changes in the mean reaction cross section, due to spectral moderation, are the principal cause of hitherto unexplained variations in observed reaction rates in largely hydrogenous samples.

References

- [1] Copley, J. R. D.; Stone, C. A. Nucl. Instrum. Meth. A281, 593 (1989).
- [2] Sears, V. F. Adv. Phys. 24, 1 (1975).

CHARACTERIZATION OF MOLECULAR NETWORK OF EPOXIES USING NEUTRON SCATTERING

W.-L. Wu
(Polymers Division)

Neutron scattering has been used extensively to study the chain conformation of thermoplastics in bulk and in solution. The basic scheme used is to blend deuterium labeled chains with the protonated chains. The conformation of individual chains can be extracted from the scattering results [1]. The first successful attempt to use neutron scattering to investigate the network structure in thermosets was made by Wu and Bauer [2]. The basic approach of their work was to have all the monomer partially deuterated. The material after cure or crosslink resembles, in a linear chain analogue, a multiple block copolymer of $(H - D)_N$, where H stands for the protonated portion of the monomer or repeating unit and D stands for the deuterated portion. The corresponding symbol for networks is therefore $\gg(H - D)_N\ll$, where the branches on each side of the monomer denote the multi-functionality nature of the junction point.

For a multi-block linear polymer in bulk, the scattering intensity has been modeled using the results of the random phase approximation (RPA) [3]. For linear and flexible chains, only a modest amount of change in scattering behavior is observed as the value of N increases from one to infinity. In other words, the scattering behavior of a di-block copolymer is almost the same as that of a multi-block one. This is not a surprising result since the position correlation between blocks of the same chain diminishes rapidly as the contour distance between these blocks increases. This is just the nature of a flexible chain. However, for multi-block rigid rod molecules, the width of the scattering peak gets narrower as the value of N increases, albeit the application of RPA to an ensemble of rigid rod molecules is rather questionable.

For thermosets, RPA calculations based on a simplified network model have been carried out [2]. The result indicates that the peak width depends strongly on the rigidity of the network. The early neutron scattering results of partially deuterated diglycidyl ether of bisphenol A (DGEBA) cured with Jeffamines can be fitted quantitatively with the RPA scheme. However, the presence of amines tends to muddle the experimental results; in the uncured mixtures the correlation hole peak from the partially deuterated DGEBA almost disappears due to the presence of amines. They also make the

data interpretation more complicated; e.g., the H portion in the notation $(H - D)_N$ for cured materials now denotes a combination of the amine and the protonated portion of DGEBA. Although the fit between the calculation and the neutron scattering results on Jeffamine/DGEBA is quite satisfactory [3], the question concerning the sensitivity of neutron scattering for elucidating the network structure still remains. In other words, if the starting monomers give rise to a clear correlation hole peak in scattering intensity, will crosslinking result in a significant change in this peak?

To answer this question, the following experiment was conducted. The partially deuterated DGEBA (d-DGEBA) was cured without any amines. It is well known that homopolymerization of DGEBA will occur at elevated temperature especially in the presence of some catalysts [4]. Piperidine (5 pph) was added to d-DGEBA at room temperature and served as a catalyst. The material was cured at 160 °C for 20 hours. Infrared results on the amplitude of the epoxide band at 915 cm^{-1} indicated that the cure was almost complete.

Neutron scattering measurements were conducted using the BT-6 spectrometer. With the analyzer crystal in front of the detector, only the elastic scattering component was recorded. The results for the monomer and the cured sample are given in figure 1. The thickness for both samples was identical (2 mm) and the beam apertures for these two measurements were also kept the same. Consequently a direct comparison can be made between these two scattering curves.

The most striking feature observed for these scattering results is the down shift of the peak position upon curing. This implies that the average radius of gyration of the monomer increases upon crosslinking. This result is rather surprising in light of our current understanding of rubber elasticity theory which was developed for materials with large molecular weight between crosslinks. In the present case, the length of the linkage between crosslinks is rather short, in the range of $\sim (10 - 20)\text{ \AA}$. The increase in monomer size upon crosslinking might be interpreted as the straightening effect of chain ends as they join at a crosslink point. This phenomenon is similar to what occurs in star shape molecules; the radius of gyration of an individual arm is larger than that of an equivalent free chain. This effect can be rather pronounced in star molecules with a large number of arms. In homopolymerized epoxy, the functionality of the junctions

can be rather high. Hence this chain end effect could play an important role in the increase in the monomer size upon crosslinking.

DEUTERATED DGEBA NEUTRON DATA

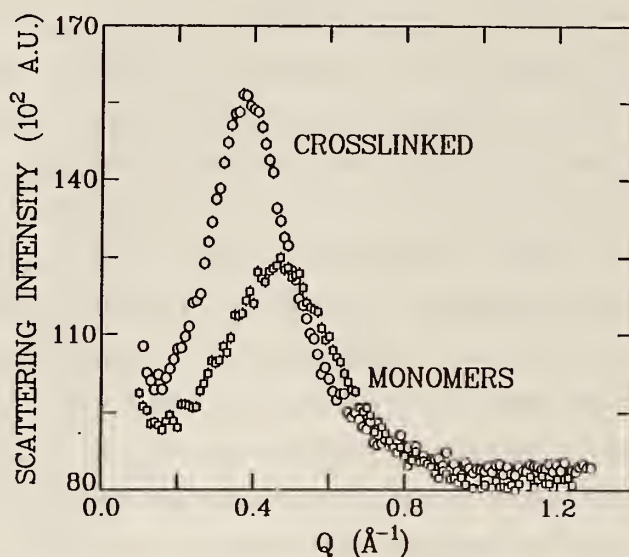


Figure 1. Neutron scattering results of partially deuterated DGEBA monomer and the crosslinked material.

The sharpening of the scattering peak is the other interesting feature caused by crosslinking. The half widths of the peaks shown in figure 1 are 0.25 \AA^{-1} and 0.36 \AA^{-1} for the cured sample and monomer, respectively. In addition, the ratios of the half-widths to the peak positions are 0.69 and 0.76 for the cured and the uncured materials, respectively. According to a calculation based on RPA, this ratio stays the same for linear chains of different size. In other words this sharpening effect cannot be attributed just to the increase in the radius of gyration of monomers. Therefore, this sharpening of the scattering peak suggests that the crosslinking results in additional changes which must be of an inter-monomer nature.

As demonstrated in the work by Wu and Bauer [3], for multi-block copolymer in bulk the half-width of the scattering peak decreases as the number of repeats N increase. This result has now been extended to crosslinked polymers to accommodate the observation mentioned above.

In summary, the crosslinking process in thermosets results in pronounced changes in the scattering behavior. These changes indicate 1) an increase in the radius of gyration of the monomer upon crosslinking, 2) an enhancement of the inter-monomer correlation.

References

- [1] For review article see: Wignall, G. D. Encyclopedia of polymer science and engineering. Second ed. Wiley-Interscience (1985).
- [2] Wu, W.; Bauer, B. J. Polym. Commun. 26, 39 (1985), Polym. 27, 169 (1986).
- [3] Wu, W.; Bauer, B. J. Macromol. 19(6), 1613 (1986).
- [4] Riew, C. K.; Rowe, E. H.; Siebert, A. R. Advances in chemistry series (ACS) No. 154, 326 (1976).

SHEARING APPARATUS FOR SANS: PRELIMINARY RESULTS FROM SHEARED COLLOIDAL SUSPENSIONS

G. C. Straty and H. J. M. Hanley
(Thermophysics Division)

and

C. J. Glinka

The apparatus. We have constructed and tested a couette-type concentric cylinder apparatus to investigate liquids at equilibrium and under shear. The apparatus is intended to be available to SANS users as a general purpose tool. Design features include a) versatility and a rugged construction, b) a wide range of shear rates and operating temperatures, and c) fully automated computer controlled and programmable functions.

An outline of the apparatus has been presented by Straty [1] and details will be provided in a forthcoming publication. The cell is a stationary cylindrical quartz glass stator surrounded by a rotating cylindrical quartz glass rotor. The cell used for testing has a mean diameter of 56.5 mm with an annular gap of 0.5 mm. Thermostating fluid is circulated within the stator for temperature control. The nominal operating temperature range is at present 245-373 K. The outer cylinder is driven by a dc brushless servo motor that is programmed to allow for any inputted combination of velocity, acceleration, direction of motion, delay, or other operating parameters.

Test results: shear-induced changes in the microstructure of polystyrene colloidal suspensions. An ongoing project at NIST is to try to understand why liquids behave as they do. A key to this understanding is to investigate the microstructure of liquids, particularly distortions in the

pair correlation function, or the structure factor, when the liquid is perturbed away from equilibrium [2]. Colloidal suspensions are attractive candidate systems for study because we have demonstrated the parallel between suspensions and simple atomic liquids [3], and it is well known that the structure factor of colloidal suspensions obtained by light, x-rays, or neutrons is relatively straightforward to interpret.

Solutions of 6% to 30% by weight 98 nm diam polystyrene suspensions in deionized H_2O and in H_2O/D_2O mixtures were prepared. The solutions were placed in the shearing cell and the neutron intensity-wave vector (Q) pattern observed for the systems at rest and when subjected to a shear. A dramatic difference in the intensity plots, and hence the structure factor, was evident. Typical results are shown in figure 1 for the 30% sample. The initial lattice structure is very evident. It is surmised that the colloidal crystal distorts under low shear allowing layers to slip relative to one another until, at sufficient shear, the slippage creates a liquid-like structure factor. Whether the suspension is actually a liquid is an open question. The temperature of the experiments was a nominal 22 K. One rpm is equivalent to a shear rate of about 6 Hz. The distortion sequence is reproducible and reversible.

SHEAR INDUCED MELTING OF
POLYSTYRENE COLLOIDAL SUSPENSIONS



Figure 1. Change in the neutron scattered intensity pattern for a sheared colloidal suspension as a function of shear-rate. Note the shear induced melting to a liquid structure.

References

- [1] Straty, G. C. J. Res. Natl. Inst. Stand. Technol. 94, 259 (1989).
- [2] Hanley, H. J. M. Lectures on thermodynamics and statistical mechanics. A. E. Gonzales and C. Varea, eds. World Scientific Press, 109 p. (1988).
- [3] Hanley, H. J. M.; Rainwater, J. C.; Clark, N. A.; Anderson, B. J. J. Chem. Phys. 79, 4448 (1983).

ANALYSIS OF SANS FROM CONTROLLED PORE GLASSES

N. F. Berk and C. J. Glinka

W. Haller
(Ceramic Division)

and

L. C. Sander
(Organic Analytical Research Division)

Small angle neutron scattering (SANS) measurements have been performed on several samples of silica controlled pore glasses with pore sizes ranging from roughly 70 to 300 Å. The scattering intensity is strongly peaked at small Q and shows approximate Porod law behavior at large Q . Contrast variation measurements have shown that the pore space in these samples is entirely interconnected and thus forms a bicontinuous microstructure. The scattering data have been analyzed using the leveled wave method based on an early scheme for representing two-phase microstructures resulting from spinodal decomposition. In this approach [1], interfaces are modeled by the contours of a stochastic standing wave composed of plane wave components propagating in random directions with random phases and having wave numbers distributed according to a given probability density, $P(k)$. We have determined model $P(k)$ functions by fitting the SANS data with the leveled wave scattering function and then used these to construct leveled wave images of the corresponding porous structures (fig. 1). The average pore sizes obtained by measuring chord lengths in the computer models turn out to agree with the values determined for these glasses by mercury porosimetry.

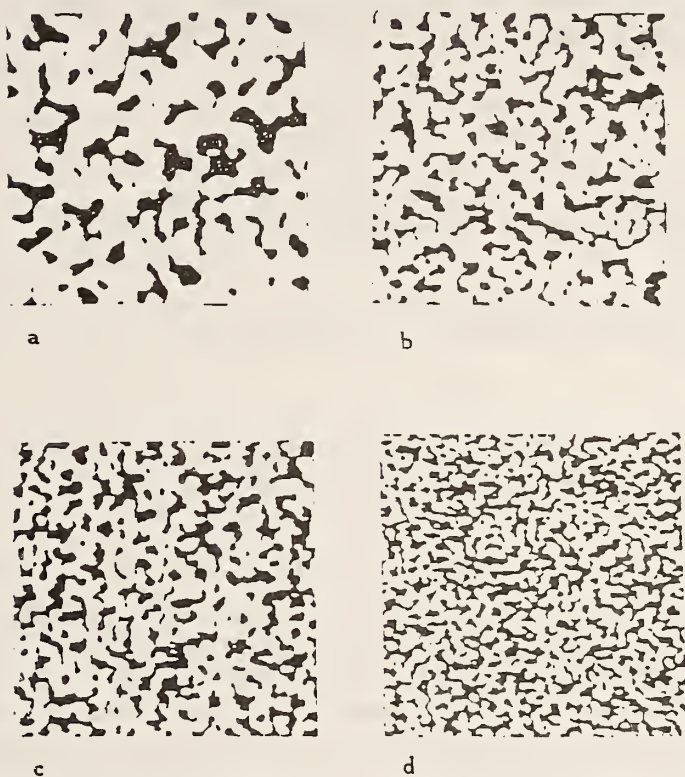


Figure 1. Simulated "TEM" views of controlled pore glass structure as determined from analysis of SANS using the leveled wave model. Each image corresponds to a particular porosity, ϕ , and average pore size, D , according to: a) $\phi = 68\%$, $D = 255 \text{ \AA}$; b) $\phi = 66\%$, $D = 156 \text{ \AA}$; c) $\phi = 63\%$, $D = 116 \text{ \AA}$; d) $\phi = 51\%$, $D = 70 \text{ \AA}$. The four views are shown on a constant length scale.

Reference

- [1] Berk, N. F. Scattering properties of a model bicontinuous structure with a well defined length scale. Phys. Rev. Lett. 58, 2718 (1987).

**PHYSICAL GELS OF AQUEOUS POLYVINYLSALCOHOL SOLUTIONS
- A SMALL ANGLE NEUTRON SCATTERING STUDY**

W.-L. Wu and L. D. Coyne
(Polymers Division)

M. Shibayama, H. Kurokawa, and S. Nomura
(Kyoto Institute of Technology, Kyoto, Japan)

S. Roy
(Polaroid Corporation, Norwood, MA)

and

R. S. Stein
(University of Massachusetts, Amherst, MA)

Physical gelation in various polymer solutions has been a subject of interest to many researchers. Poly(vinylalcohol) (PVA) in water is one of the physical gel systems studied rather extensively; after all, PVA fibers have been produced commercially from aqueous PVA solutions for many years. Compared to chemical gelation, the gelation process in physical gels has not been widely studied by scattering techniques. This does not imply that other transitions, e.g., liquid-liquid phase transitions in physical gels, have not been studied using scattering techniques. For instance, the spinodal transition in PVA-water has been determined via an elastic light scattering technique.

For the sol-gel transition problem the change in the cluster size or molecular weight distribution during gelation is an essential parameter to monitor. The sol-gel transition is defined as the point at which the average cluster size goes to infinity. To measure the molecular weight or the cluster size distribution with either chromatographic or scattering techniques, the material must be diluted. However, dilution will cause physical gels to be highly disturbed or even completely dissolved. Consequently, scattering and other techniques in which dilution is a prerequisite are applicable only in studying the sol-gel transition in chemical gels. However, as will be shown, it is possible to study certain aspects of physical gelation without resorting to a dilution scheme.

SANS data were collected on PVA gels as they were heated through their sol-gel transition temperature. The PVA solutions with concentration across ϕ^* , the concentration threshold at which the polymer chains start to overlap, were investigated. Mass fractal dimension and correlation length were

extracted from the SANS data. Very little change in these two quantities were observed for these solutions with their concentration greater than ϕ^* as they went through a sol-gel transition.

For the solution at ϕ^* concentration, a maximum was observed in both the correlation length and the zero-angle scattering intensity as it went through the transition temperature. The origin of this maximum is interpreted successfully in terms of a two-phase weak aggregate model.

SMALL ANGLE NEUTRON SCATTERING FROM BACTERIAL MAGNETITE

S. Krueger, G. J. Olson, and J. J. Rhyne,

and

R. P. Blakemore, Y. A. Gorby, and N. Blakemore
(University of New Hampshire, Durham, NH)

Magnetotactic bacteria were discovered and described by Blakemore [1]. The bacterial cells accumulate iron intracellularly, to a significant fraction of their dry weight (2-4%), in the form of membrane-bounded magnetite (Fe_3O_4) crystals [2], termed magnetosomes. The magnetosomes in *Aquaspirillum magnetotacticum*, the most thoroughly studied magnetotactic bacterium, are usually cuboidal to octahedral in shape, with a diameter of 400-500 Å, and are arranged in a chain that longitudinally traverses the cell [3]. An average of 20 single domain magnetic iron oxide particles form the chain, which carries a net magnetic dipole moment equal to the vector sum of the individual particle moments and which is sufficient to orient the cell in the geomagnetic field [4]. The feasibility of applying the small angle neutron scattering (SANS) technique for studies of metal accumulation or deposition by living cells was explored using *A. magnetotacticum* as a model system.

Aquaspirillum magnetotacticum strains MS-1 and MS-2 were grown at the University of New Hampshire in continuous culture [2]. Iron was supplied as ferric quinate (FeQ). The total background iron content of the medium (no FeQ added) was 0.35 μM , which was the concentration at which "low iron" cells of MS-1 were grown. "High iron" cells were grown in 40 μM FeQ, and "normal iron" cells in 20 μM . Cells were shipped cold to NIST where they were stored at 2 °C until analysis (within 2-3 days).

The scattering from MS-1, grown under "normal iron" conditions, was measured in both 100% D₂O and in 30% D₂O buffers in an applied horizontal magnetic field of 25 Gauss using a neutron wavelength, λ , of 6 Å with a wavelength spread $\Delta\lambda/\lambda = 0.25$. The results, in the form of constant intensity contour plots are presented in figure 1. In 100% D₂O (fig. 1a), the scattering from the bacterium itself is large compared to that from the magnetite particles. The scattering pattern is highly elliptical and extends to larger Q values, where $Q = 4\pi\sin(\theta)/\lambda$ and θ is the Bragg scattering angle. The elliptical shape of the intensity contours confirm that the bacteria are oriented by the magnetic field.

On the other hand, the scattering from MS-1 in 30% D₂O (fig. 1b) arises mainly from the magnetite particles themselves. While the pattern is still slightly elliptical, it is confined to much smaller Q. This scattering is a result of interaction of the neutron magnetic moment with that of the magnetite particles and can be described in the form [5]

$$I(Q, \alpha) = B(Q) \pm C(Q)\cos^2\alpha, \quad (1)$$

where α is the angle between the magnetic field direction in the plane of the detector and the scattering vector, Q. The negative sign applies for a ferromagnet and the positive sign for a super-paramagnetic system.

Additional SANS measurements were performed, in an applied magnetic field of 25 Gauss, on MS-1, grown under both "high iron" and "low iron" conditions, as well as on MS-2, grown under "normal iron" conditions. In all three cases, the solvent contained 30% D₂O, permitting studies of the magnetite particles in the living cells. Slightly elliptical intensity contours, similar to those shown in figure 1b, were obtained in each case. The intensity contours from both the "high iron" and "normal iron" samples had the major axis of the ellipse in the direction perpendicular to that of the magnetic field (negative sign in eq (1)), indicating that the magnetosomes behaved as ferromagnetic particles. On the other hand, the contours from the "low iron" sample showed elongation in the direction of the magnetic field (positive sign in eq (1)), consistent with a superparamagnetic system.

The data were averaged in sectors of width 30° about the horizontal (0°) and vertical (90°) directions. The transverse and longitudinal spin scattering components were separated as $B(Q) + C(Q)$ and $B(Q) - C(Q)$,

respectively [6]. Each component was fit to a Lorentzian plus Lorentzian squared equation of the form [6]

$$I(Q) = E/(Q^2 + \kappa_1^2)^2 + F/(Q^2 + \kappa_2^2), \quad (2)$$

corresponding to a spin correlation term $\langle S_i | S_j \rangle = \exp\{-\kappa r_{ij}\}$. The coefficients E and F as well as the inverse correlation lengths, κ_1 and κ_2 were found as given in table 1.

The longitudinal inverse correlation length, $\kappa_1(l)$, for the "low iron" sample as well as the transverse inverse correlation lengths, $\kappa_1(t)$, for all three samples are zero. Derived from the Lorentzian squared term, κ_1 describes static spin correlation lengths, $\xi_1(l)$ and $\xi_1(t)$, which are long range. However, since the amplitude coefficient E is nonzero, these correlation lengths and thus, the sizes of the magnetic domains, must be just beyond the resolution limits of the SANS instrument under the present experimental conditions, and are listed in table 1 as greater than 300 Å.

Values well within the resolution limits of the SANS instrument were obtained for $\kappa_2(l)$, in the "low iron" case, and for $\kappa_2(t)$ in all three cases. Since κ_2 is associated with the Lorentzian term describing the dynamic spin fluctuations, the results indicate dynamic spin correlation lengths, $\xi_2(l)$ and $\xi_2(t)$, on the order of 50 Å, which are superposed on a static magnetic cluster size several times larger.

Table 1. Summary of SANS results

Sample		<u>Lorentzian Squared Term</u>		<u>Lorentzian Term</u>	
		$E (10^{-8})$	$\xi_1 (\text{Å})$	$F (10^{-5})$	$\xi_2 (\text{Å})$
"high iron"	(t)	11.0	> 300	2.3	60 ± 10
"normal iron"	(t)	9.6	> 300	2.4	38 ± 4
"low iron"	(t)	2.5	> 300	0.9	38 ± 4
	(l)	3.2	> 300	3.1	20 ± 4

(t) ≡ transverse spin component
(l) ≡ longitudinal spin component

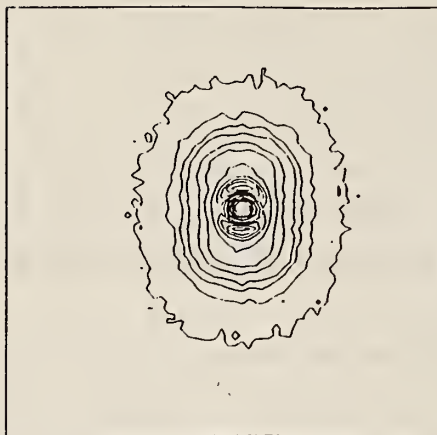


Figure 1a.

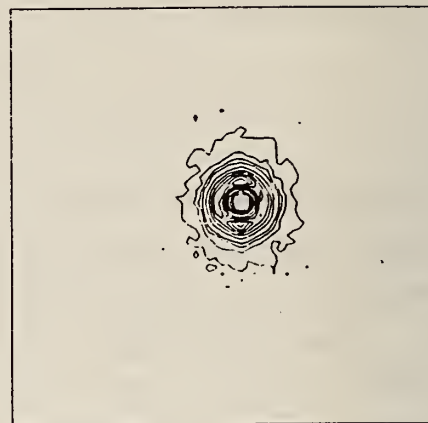


Figure 1b.

Figure 1. Constant intensity SANS contours from *A. magnetotacticum* with an applied horizontal magnetic field of 25 Gauss a) in 100% D₂O, where the bacteria themselves scatter strongly, and b) in 30% D₂O, where the scattering from the magnetite particles dominates.

References

- [1] Blakemore, R. P. Science 190, 377 (1975).
- [2] Blakemore, R. P.; Maratea, D.; Wolfe, R. S. J. Bacteriol. 140, 720 (1979).
- [3] Balkwill, D. L.; Maratea, D.; Blakemore, R. P. J. Bacteriol. 141, 1399 (1980).
- [4] Frankel, R. B. Ann. Rev. Biophys. Bioeng. 13, 85 (1984).
- [5] Cywinski, R.; Booth, J. G.; Rainford, B. D. J. Phys. F. 7, No. 12, 2567 (1977).
- [6] Rhyne, J. J. Physica B 130, 253 (1985).

SANS STUDY OF MIXED LECITHIN-BILE SALT MICELLES AND VESICLES

E. W. Kaler and J. F. Billman
(University of Washington, Seattle, WA)

We have carried out a series of experiments to investigate the effect of bile salt on lecithin vesicles and mixed micelles. One of the most straightforward ways to follow a micelle-to-vesicle structural transition in model bile is simply to dilute a mixed micelle solution with buffer. If a 5.0 g/dl mixture with a lecithin/taurodeoxycholate ratio of 0.4 (which is initially a mixed micellar solution) is diluted with 0.15 M NaCl buffer, a series of size changes is detected with quasielastic light scattering (QLS). Initially, the solution has an apparent radius of 42 Å. Apparent sizes in sequentially diluted samples increase monotonically until a 16x-diluted sample demonstrates a radius of 435 Å. Further dilution produces a monotonic decrease in size to an apparent radius of 118 Å after a 144 dilution. This progression of sizes has been postulated to be the result of micelle growth cumulating in micelle aggregation into rod-like structures (in samples demonstrating the largest sizes), followed by aggregate breakup and the formation of vesicles at the highest dilutions.

To test this hypothesis, we have made SANS measurements along such a path (fig. 1). Several features are clear. First, the scattering from the least dilute sample is consistent with that of mixed micelles as observed by us in other systems. Second, there is a qualitative difference between the form of the scattering curve of the least and most dilute samples; in particular the most dilute samples have substantial periodicity in the scattering curves and are consistent with the scattering from vesicles. Finally, it is clear that the periodicity increases as the dilution increases from 36 to 144. This last feature is consistent with a coexistence of vesicular and micellar aggregates. An example of the fit of a vesicle form factor to the 144 dilution data is shown in figure 2. Note that excellent agreement with QLS measurements is obtained along with new information about bilayer thickness. An exact fit of the data can be gotten after accounting for polydispersity of the vesicle population.

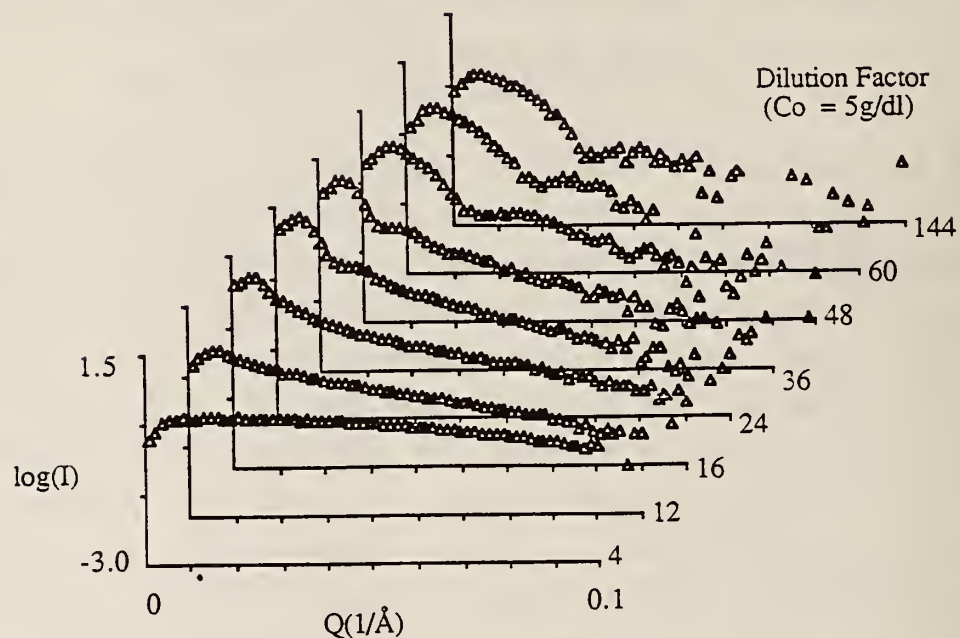


Figure 1. SANS patterns of samples generated by sequential dilution with 0.15 M NaCl buffer of a 5.0 g/dl mixture with a lecithin/taurodeoxycholate ratio of 0.4. The initial solution contains mixed micelles, and the final sample is vesicular.

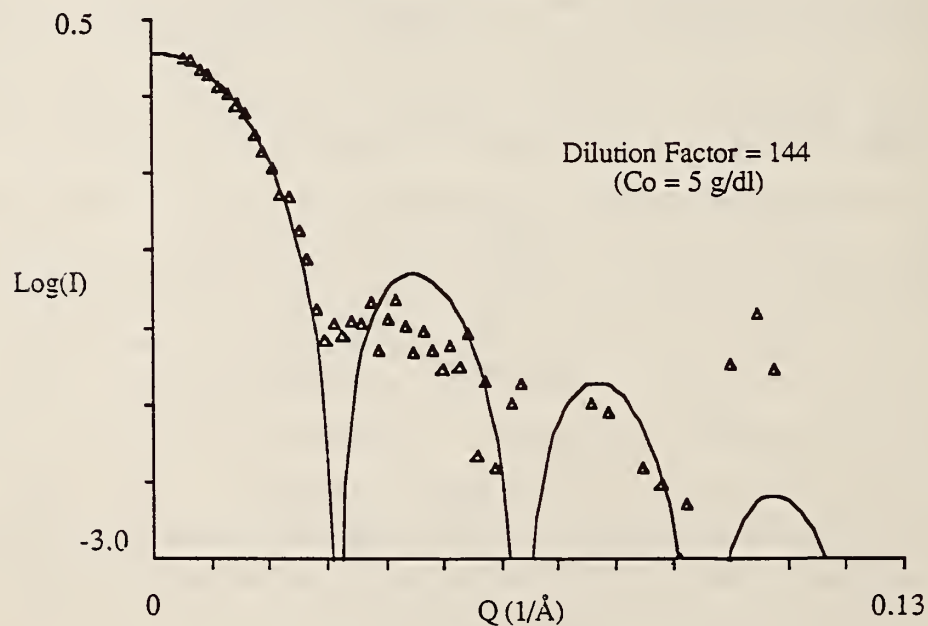


Figure 2. Fit of SANS pattern from the 144x dilution shown in figure 1. The solid line is the fitted value for a monodispersed population of vesicles with outer radii of 118 Å and bilayer thickness of 40 Å. The radius as determined by QLS is 118 Å.

NIST CRYSTAL DATA CENTER

A. D. Mighell and V. L. Himes

and

M. Mrose
(U.S. Geological Survey)

The NIST Crystal Data Center is concerned with the collection, evaluation and dissemination of data on solid-state materials. The data center maintains a comprehensive database with chemical, physical, and crystallographic information on all types of well-characterized substances. These materials fall into the following categories: inorganics, organics, organometallics, metals, intermetallics, and minerals. The data are made available to the scientific community through computer oriented modes of dissemination and through printed products. Two major databases are produced: NIST CRYSTAL DATA [1] and the NIST/Sandia/ICDD Electron Diffraction database [2]. These databases have many uses including materials design, materials characterization, and phase identification by neutron, x-ray, and electron diffraction.

During the year, work has focused on the following areas: the development of a new analytical tool by integrating the Electron Diffraction Database into the analytical electron microscopes that are marketed by several different commercial companies; the publication of a new book for phase identification of materials based on d-spacing/element type matching techniques; the production of a CRYSTAL DATA CD-ROM and accompanying software; the design of algorithms and software to be used in the automation of diffractometers with respect to accurate symmetry determination; and the preparation of the annual update to the master database (currently 142,000 entries).

As the databases now contain large collections of evaluated data, the development of efficient dissemination methods is critical to the utilization of the information for research and analysis. Recently, it has become apparent that three principal methods for the computerized delivery of scientific data are rapidly evolving. All three are now used by the data center with the first two being initiated during this year. The first is a desktop method in which the database on CD-ROM is used in conjunction with a PC. The second is the incorporation of the database into a scientific

instrument where the combination represents a new analytical tool. The third is the distribution of data through international on-line systems.

The on-line method permits the data center to provide rapidly the general scientific community with up-to-date data and with extensive software tools to retrieve and manipulate the information. All that is required to access the system is a terminal, a modem, and a local call. To build and maintain the on-line system in the most efficient manner, NIST and the National Research Council (Canada) have formally agreed to pool their resources. The objective is a long-term collaboration not only to broaden the scope of the existing CRYSDAT System (= on-line version of NIST CRYSTAL DATA), but also to expand the system to include databases in related fields to create an interdisciplinary materials database system. Such a system will utilize a high performance computer environment including supercomputing resources, networks, and the applications of new software technologies.

References

- [1] NIST CRYSTAL DATA (1989). A database of chemical, physical, and crystallographic data (142,000 entries). Compiled and evaluated by the NIST Crystal Data Center, National Institute of Standards and Technology, Gaithersburg, MD 20899.
- [2] NIST/Sandia/ICDD Electron Diffraction Database (1988). A database designed for phase characterization by electron diffraction. Prepared by the NIST Crystal Data Center (in collaboration with the Sandia National Laboratories and the International Centre for Diffraction Data), National Institute of Standards and Technology, Gaithersburg, MD 20899.

Both standard reference databases are leased to the scientific community in two forms: CD-ROM and magnetic tape.

A NEW METHOD FOR IDENTIFICATION OF SOLID-STATE MATERIALS

V. L. Himes and A. D. Mighell

As a result of a long-term basic research program supported by the Reactor Radiation Division and the Office of Standard Reference Data, the Crystal Data Center has developed a highly accurate analytical procedure that will greatly extend identification techniques, particularly for electron diffractionists. The method opens new opportunities in the identification of solid-state materials, in that crystalline samples in the size range of 10 μm to 10 \AA can be accurately characterized.

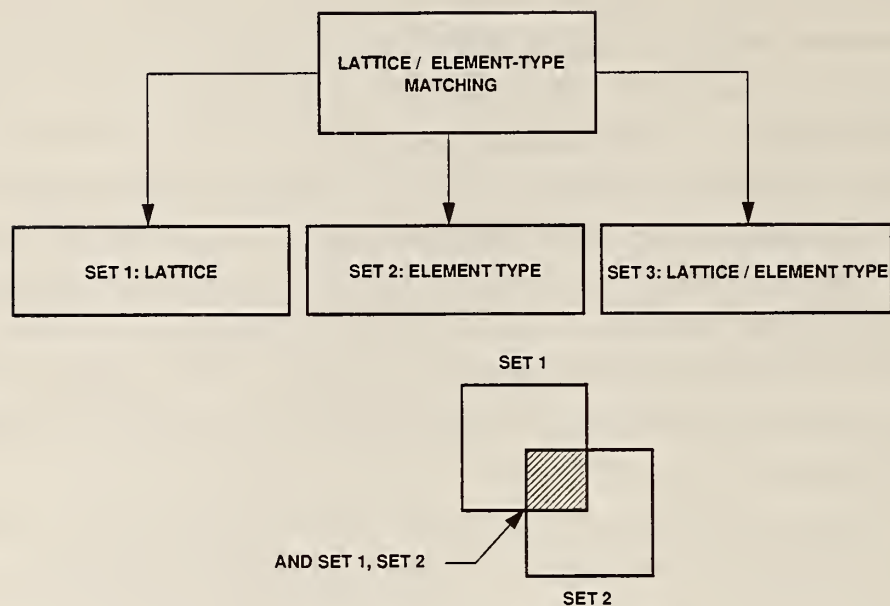
REACTOR RADIATION DIVISION AND COLLABORATIVE PROGRAMS

Research with NIST CRYSTAL DATA (a large database with chemical, physical and crystallographic data on solid-state materials) has proved that a material can be uniquely characterized on the basis of its lattice and chemical composition. To characterize a material, it is sufficient to determine any primitive cell of the lattice and the element types present. Using a modern analytical electron microscope (AEM), the experimentalist can collect the required data on an unknown sample. The lattice information is obtained by rotation of the sample to obtain two planes of data, from which a unit cell defining the lattice can be deduced. The chemical data are determined by energy dispersive spectroscopy (EDS) or electron energy loss spectroscopy (EELS).

Once the experimental data are measured, the unknown can be identified against the database of knowns using lattice/element-type matching techniques. The basic strategy consists of three steps (fig. 1). First, the unknown lattice is searched against the database to find all lattices that are the same or related; the results of this search are kept in SET 1. Second, the unknown is searched against the database to find all materials with the same or similar element types; the results of this search are kept in SET 2. Finally, SET 1 and SET 2 are combined using the BOOLEAN .AND. operation to obtain SET 3 which is the answer set. Experience has proved that the procedure is selective and accurate.

Rapid and accurate identification of the unknown against lattices in the database with 140,000 entries is due: a) to the development of a universal classification scheme for all lattices independent of crystal system and lattice centering; b) to theoretical work that has led to algorithms that can deduce the relationship, if it exists, between any pair of lattices; and c) to the creation of computer algorithms and search software to carry out lattice matching in an efficient manner when an extremely large number of lattices is involved.

Plans are under way to build this procedure directly into the work stations associated with commercial analytical electron microscopes through technology transfer with private-sector groups. This strategy, then, provides an automated identification technique since data collection, NIST CRYSTAL DATA, and the identification software will all be integrated into the same instrument. The methodology is also useful for the identification of unknowns by means of neutron and x-ray diffraction data.



SET 1 = The SET of compounds resulting from lattice matching.

SET 2 = The SET of compounds resulting from element-type matching.

SET 3 = AND SET 1, SET 2 = the compounds in the NIST CRYSTAL DATA file that have the same or related lattice/element-type as the unknown.

Figure 1. Phase identification by lattice/element-type matching.

AUTORADIOGRAPHY STUDY OF PAINTINGS

Y. T. Cheng and J. S. Olin

(Smithsonian Institution, Washington, DC and Reactor Radiation Division)

The first phase of autoradiography study on paintings of Thomas Wilner Dewing has been completed. A manuscript titled "Thomas Wilner Dewing: An Ebauche or Sketch of His Painting Technique" has been prepared and accepted by the "Smithsonian Studies in American Art" for publication. The work comprises the study on 11 of Dewing's paintings and is the result of a close collaboration among scientists, art historians and painting conservators. The collaboration is needed because the study is not only to reveal how the artist achieved his painterly effects, but also to seek the meaning which he purposed to convey. The autoradiographs suggest the technique that the artist employed in his creative process by registering brush marks, pigment distributions, and form changes. These radiographic images were analyzed in

conjunction with other analytical tools at our disposal such as the scanning electron microscope, gas chromatography mass spectrometer as well as more conventional means of painting examination--x-ray radiography, microscopy, and infrared photography. Extensive literature research and personal interviews have also contributed to the interpretation of the autoradiographs and understanding of each of the paintings. They often provided information about changes in the painting which were subsequently revealed in the autoradiographs.

Dewing is a good subject for such an investigation for in many ways he was a painter's painter, recognized in his own day for his technical ability. Not one to work routinely, Dewing varied his paint applications from picture to picture, blending his individual style with a repertory of images that he drew from sources as diverse as Jean-Baptiste-Simeon Chardin, Jan Vermeer, Gerard ter Borch, the American expatriate James McNeill Whistler, and the old masters. To our fascination, we find that throughout his career, Dewing continued to employ the classical ebauche that he had learned while a student in Paris. This technique ordained the method whereby he laid in his work, establishing its light and dark passages which were clearly revealed by the autoradiographs.

Gamma ray spectroscopy was conducted in parallel to the autoradiography process. Table 1 lists the surface density in mg/cm^2 of the various elements detected by neutron activation in Dewing's paintings.

The work to examine paintings of another American artists Albert P. Ryder by neutron activation autoradiography continued. Thus far, 10 of his works from the collections in the National Museum of American Art (NMAA), including his master work "Jonah", have been studied. Portions of the study have been included in the catalog, and will be on display during the Ryder exhibition to be inaugurated in 1990 at NMAA.

To more accurately analyze the radiographic information generated in the study, calibration references are being established. The calibration procedure involves first measuring the film responses of selected known materials that were subjected to the same painting neutron activation condition. The film responses as a function of time in the autoradiographic sequence are stored in computer and serve as standards against which one can compare the digitized results of painting autoradiographs.

REACTOR RADIATION DIVISION AND COLLABORATIVE PROGRAMS

Table 1. Surface density of the elements in Dewing's paintings as determined by neutron activation analysis

ELEMENT	PAINTING							
	ALMA THAYER	HOUSTON	LADY LISTENING	NECKLACE	NUDE	SPINET	LADY IN WHITE #1	LADY IN WHITE #2
SODIUM	0.67	0.11	0.16	0.97	0.07	1.79	0.12	0.17
MAGNESIUM	*	*	0.54	*	*	*	0.46	*
ALUMINIUM	0.57	0.35	0.40	0.38	0.35	0.82	0.43	0.95
CHLORINE	1.02	0.22	0.41	0.82	1.32	2.97	0.14	0.33
POTASSIUM	0.08	0.06	0.02	0.21	0.21	1.21	0.49	0.61
CALCIUM	6.45	1.54	7.44	3.65	3.73	14.89	7.58	2.80
CHROMIUM	0.02	0.10	0.31	0.22	0.02	0.08	*	0.03
MANGANESE	0.02	0.09	0.03	0.01	0.10	0.07	0.10	0.20
IRON	0.47	6.77	0.93	*	2.05	*	4.35	7.51
COBALT	0.02	0.11	*	*	0.09	*	*	0.01
COPPER	*	0.26	*	*	*	*	*	0.09
ZINC	1.62	0.38	9.40	7.81	0.34	2.95	5.11	16.26
ARSENIC	*	0.06	*	*	0.01	0.01	*	0.01
CADMIUM	0.16	0.57	0.08	0.09	*	0.65	0.17	0.08
ANTIMONY	0.02	0.25	0.30	*	0.02	0.12	*	*
BARIUM	1.75	0.26	0.07	1.61	0.03	3.01	*	0.97
MERCURY	0.55	1.14	0.29	0.34	*	21.16	*	0.02

* indicates element was not detected

REACTOR RADIATION DIVISION AND COLLABORATIVE PROGRAMS

COLD NEUTRON PROJECT

J. R. D. Copley, C. J. Glinka, J. A. Gotaas, G. Greene, W. Knill, J. LaRock, C. J. Majkrzak, C. O'Connor, D. Pierce, H. J. Prask, J. M. Rowe, S. Satija, I. G. Schroder, T. J. Udovic, and R. Williams

The neutron guide hall and office/laboratory building construction contract was awarded in the fall of 1987. The bids received indicated that the design package was good, and the successful bidder proved to be responsible and reliable; construction began in November 1987.

On January 12, 1989, the Cold Neutron Research Facility (CNRF) was officially dedicated by the Secretary of Commerce, C. William Verity. Among the many representatives of government, industry, and universities present were former Deputy Secretary of Commerce Clarence J. Brown and Acting Under-Secretary of Commerce for Technology, Ernest Ambler. Dr. Ambler, Raymond Kammer, Acting Director of NIST, and Institute for Materials Science and Engineering Director, Lyle Schwartz also spoke at the ceremonies.

In his address, Secretary Verity stressed that the CNRF represents the imminent arrival in this country of an important set of new tools for scientists and engineers, and that the development of new polymers, new ceramics, new catalysts, and better semiconductor devices all involve problems that may only be solved by cold neutron probes. He mentioned the report of the National Research Council, which placed the project at the top of its list of urgently needed improvements, and the economic importance of the tools that the project would provide. He also praised the cost effectiveness and rapidity of the construction and the foresight of the NIST scientists who designed the reactor and made provision for the addition of a large cold-neutron source.

The new office space associated with the CNRF was occupied in early March 1989, and the current state of facility construction is as follows. The neutron guide tubes are being fabricated by Cilas-Alcatel of France, with the first delivery in the spring of 1989, and all guides for NG 5, 6, and 7 now on-site; guides for NG 3 have been ordered. Penetration of the 7-m thick exterior wall for guide-tube installation began in late June, following the end of the last reactor cycle in early June. Fabrication of the guide support system is being done in the NIST shops, and is on schedule. Construction of the automatic shutter system began in early 1989; delivery of

the first (for testing) took place in May, and delivery of the remaining six is expected on schedule.

In the first stage of instrumentation, the three guides that run along the east side of the guide hall will be installed and developed. The remaining four guides will be installed later, possibly at the same time as a new cold source, which is presently being designed, is ready. This schedule has been chosen to minimize reactor down time, while allowing for an orderly development of the full complement of instruments. The layout of the initial three guides and instruments is shown in figure 1.

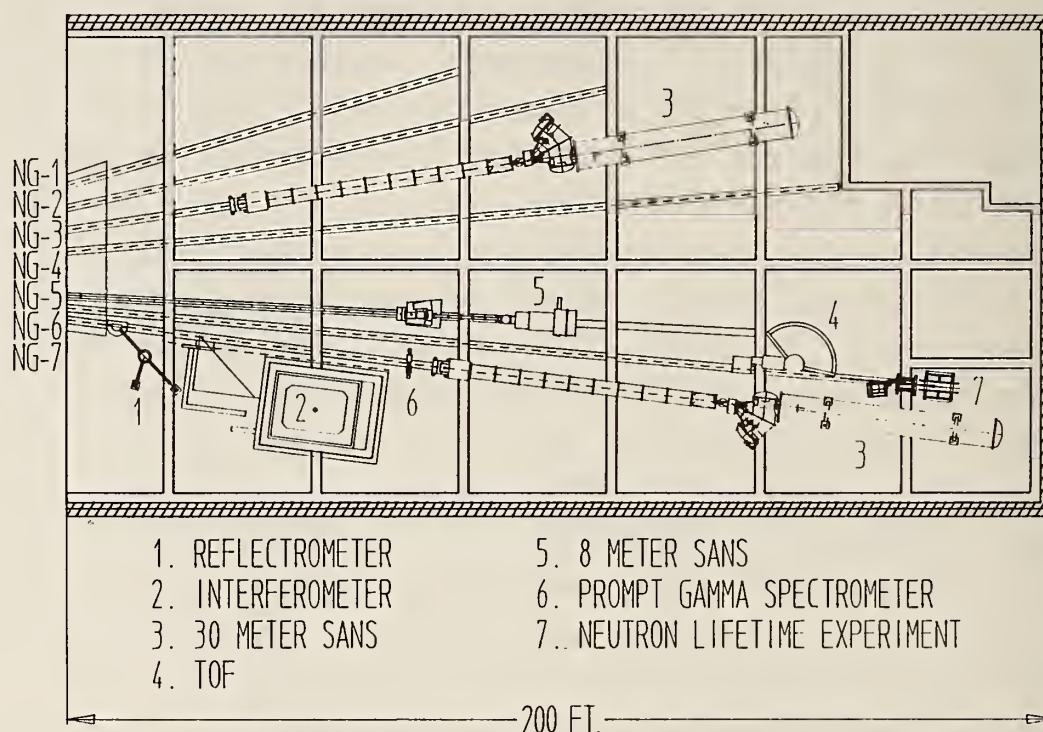


Figure 1. Cold Neutron Research Facility layout showing initial instrumentation complex.

The design and construction of the first instruments are under way, with different instruments at different stages. Two of the instruments shown, the 8-m small angle neutron scattering facility (SANS) and the time-of-flight (TOF) spectrometer, have been moved from the reactor building to the guide hall. As the new instruments come on line, these two will be replaced, but in the development stage, they will be available for research. The port previously allocated to the TOF machine in the reactor hall will be modified to become a new neutron depth profiling station, installation of which will follow immediately on guide installation. Within the guide hall, the

Exxon/NIST 30 m high-resolution SANS will be ready for installation early in 1990, as will the prompt gamma-ray activation analysis station. Also to be placed on-line at that time will be the neutron lifetime experiment--a University of Sussex(UK)/NIST collaboration.

Among the other instruments to be installed on the first three guides, fabrication of a cold neutron triple-axis spectrometer will begin soon, whereas a neutron reflectometer is entering the detailed-design stage. Both of these instruments should be completed in early 1990. A neutron interferometer is in the design and initial construction stage, with an expected installation date of 1992. Not shown on the floor plan is a second 30 m SANS and a spin-polarized crystal spectrometer, to be built under the National Science Foundation (NSF)/NIST sponsorship as described below; the fabrication of the SANS is now under way. Also in the design stage for commissioning in 1992 are a high resolution cold neutron time-of-flight spectrometer and a back-reflection spectrometer. Descriptions of the current state of development of some of the instruments are given in separate subsections of this report.

Relating to instrument development, the following major collaborations have been initiated in 1989. NIST and NSF have announced plans to develop a Center for High Resolution Neutron Scattering (CHRNS) for research in chemistry, physics, biology, and materials science at the CNRF. The Center, to be built around two state-of-the-art neutron research instruments to be designed and constructed by NIST with funding from NSF, will be managed as a national user facility, open to use by U.S. universities, industries, and government agencies. Proposals for research time will be evaluated on the basis of scientific merit by a program advisory committee. The new instruments will be a 30-m SANS spectrometer and a spin-polarized inelastic neutron scattering (SPINS) spectrometer.

The Organic and Electronic Materials Department of Sandia National Laboratories (SNL) has entered into a long-term cooperative research agreement with the CNRF. SNL will provide partial funding for development and support costs of the new high-resolution TOF and the new back-reflection spectrometer. SNL will also provide a post-doc to participate in instrument development and to perform research of interest to SNL and NIST.

In early March the initial members of the Program Advisory Committee for the CNRF were officially welcomed to the committee. Dr. David Price of

Argonne National Laboratory, Professor E. A. Schweikert of Texas A&M University, Dr. Sunil Sinha of Brookhaven National Laboratory, and Professor Hyuk Yu of the University of Wisconsin, have generously agreed to serve. The first PAC meeting is planned for the fall.

Two workshops were conducted during the reporting period. A workshop on Neutron Methods for High T_c Superconductors was held at NIST November 3-4, 1988. This workshop was designed to provide interested DARPA contractors with an in-depth view of neutron methods as applied to superconductor characterization. Presentations were made by NIST and guest scientists on total-profile analysis, SANS, inelastic neutron scattering, neutron activation analysis, and neutron microstructure characterization. A workshop on the Utilization of Cold Neutron Beams for Prompt Gamma Neutron Activation Analysis and Neutron Depth Profiling was held on May 22-23, 1989. It focussed on applications of neutron-induced nuclear reactions in chemical analysis, materials science, and physics research.

In May the first issue of the **Neutron Standard**, the Reactor Radiation Division and CNRF newsletter, was printed and sent to approximately 16,000 scientists and engineers from specialties which the CNRF could benefit. News of the dedication, facility development, and special events--such as workshops--was presented. A detailed description of instruments and a request for proposals is planned for inclusion in the next newsletter.

CENTER FOR HIGH RESOLUTION NEUTRON SCATTERING

J. J. Rhyne

The National Science Foundation provided a grant for a Center for High Resolution Neutron Scattering (CHRNS), which will include the development of two instruments in the Cold Neutron Research Facility. These instruments, a 30-m SANS and a Spin Polarized Inelastic Neutron Spectrometer (SPINS), to be jointly developed by NIST and NSF, will operate as a user facility open to qualified research workers from universities, national laboratories, and industry. The CNRF program committee will evaluate proposals for beam time.

The 30-m SANS will occupy an end-guide position in the guide hall and will provide the highest resolution available in the United States (minimum Q of 0.001 \AA^{-1} with a sample flux of approximately 10^4 n/sec on a 2 cm diam

sample), and will incorporate a high counting rate two-dimensional detector. The detector will move inside a 15-m evacuated flight path. Provision will be made for a second detector to move along an arc at a fixed radial distance of 1.5-m thereby extending the Q-range of the instrument to 1 \AA^{-1} . The plan is to provide for a polarized neutron capability using a polarizing filter or multilayer reflection crystals.

The neutron monochromator will be a variable pitch velocity selector providing wavelength tunability over the range 4 to 25 Å with a variable wavelength spread, $\Delta\lambda/\lambda$, from about 5 to 25%.

The design and procurement of electronic and mechanical components for the SANS instrument is under way, and it is anticipated it will be available for use in March 1991 with the SPINS, described in more detail below, available approximately a year later.

SPIN POLARIZED INELASTIC NEUTRON SCATTERING SPECTROMETER (SPINS)

C. F. Majkrzak

Design work on this new instrument for the NIST Cold Neutron Research Facility and CHRNS is currently under way. As described in detail elsewhere [1], the use of efficient broad-band polarizers and novel energy-dependent, spin-flipping devices will make it possible, in principle, to achieve high energy resolution without prohibitive restrictions on beam divergence. Measurement of energy transfers with a resolution approaching $10 \text{ } \mu\text{eV}$ should be obtainable. Because the actual efficiencies of the polarizers and flippers ultimately limit the performance of the instrument, priority is now being given to the development of these component devices. Various types of polarizers are being fabricated and tested, including supermirrors and curved Soller arrays of mirrors or benders. Detailed calculations of the performance of energy-dependent spin-flipping devices are also being done in order to determine the optimal spatial current distribution.

Reference

- [1] Majkrzak, C. F.; Glinka, C. J.; Satija, S. K. SPIE Conf. Proc. No. 983, p. 129, SPIE, Bellingham, WA, 1989.

COLD NEUTRON TRIPLE AXIS SPECTROMETER

S. F. Trevino
(ARDEC, Picatinny Arsenal, NJ and Reactor Radiation Division)

Two cold neutron triple axis spectrometers will be installed on guide tubes at the Cold Neutron Research Facility. The conceptual design of one of these instruments is completed and detailed engineering is in progress. We hope that the first of these instruments will be installed in the summer of 1990.

Capabilities common to the two instruments are:

- monochromator scattering angle from 30 to 150 deg;
- vertical focusing of the monochromator;
- shielded filters between monochromator and sample (cold Be and Pg);
- sample scattering angles from -150 to +150 deg;
- shielded filters between sample and analyzer;
- vertical focusing of the analyzer;
- interchangeable collimators with angular acceptance between 5 and 60 min of arc between monochromator-sample, sample-analyzer, and analyzer-detector;
- the sample environment includes temperature control from 3 mk to 2000 K deg., pressures to 10 kbar, and magnetic fields to 60 kgauss; and
- the mechanical support of the sample and analyzer tables will be accomplished with air pads.

One of the spectrometers will be capable of neutron polarization analysis of the beam before and after the sample by the use of either multi-layer or mirror technology or both.

The second machine will utilize the Drabkin resonance flipper for energy analysis (see C. F. Majkrzak in this report).

HIGH RESOLUTION TIME-OF-FLIGHT SPECTROMETER

J. R. D. Copley

The high resolution time-of-flight spectrometer will use two pairs of counter-rotating disk choppers to produce a pulsed beam of monochromatic neutrons at the sample position. Either two or three additional choppers will be used to remove higher orders, and to reduce the burst frequency in order to minimize frame overlap problems at the detector. We expect to award a contract in October for the design and construction of the complete chopper system, comprising motors, bearings, disks, vacuum housings, and a stand-alone microprocessor-based control system. The height of the slots in the choppers will be 100 mm whereas a choice of at least three distinct slot widths will be available, depending on the desired resolution. In order to increase the intensity on the sample under conditions of high resolution, we expect to (a) include an arrangement of two closely spaced slots in at least one of the pairs of counter-rotating choppers [1], and (b) use a multiply-channelled guide which restricts the lateral motion of the neutrons after they leave the first chopper pair [2].

The instrument will probably be located on guide NG-1, which will hopefully have supermirror-coated horizontal surfaces in order to increase the intensity at the sample. It is likely that we shall include an option to use an inclined multilayer-coated plate or plates, placed before the first chopper, to remove very long wavelength neutrons from the incident beam: this device will be particularly attractive if it turns out to obviate the need for a seventh chopper.

References

- [1] Copley, J. R. D. Nucl. Inst. Meth. A273, 67 (1988).
- [2] Copley, J. R. D. On the use of multiply channelled guides to increase intensity on the sample in a multiple disk chopper time-of-flight spectrometer, elsewhere in this report.

ANALYTICAL CALCULATIONS OF THE PERFORMANCE OF NEUTRON GUIDE SYSTEMS

J. R. D. Copley

Our previous work in this area [1] has been considerably extended over the past 12 months [2,3]. The emphasis lately has been on analytical calculations of the performance of moderately complicated straight-sided guide systems. Acceptance diagrams at various points within a guide system are computed and plotted using a computer program developed in collaboration with G. Greene of this Division. These diagrams show the y - β distribution of the neutrons at the location of interest, where y is the spatial coordinate normal to the direction of the guide, and β measures the angle between the neutron direction and the guide direction. The acceptance diagrams in turn enable us to compute integrated intensities and related properties.

In the following paragraphs we discuss some of the guide system problems which we have attacked using the analytical technique:

(1) It is likely that the horizontal surfaces of some of the guides in the new hall will have supermirror coatings. In contrast, all guide surfaces within the biological shield of the reactor will almost definitely be nickel-coated, because of uncertainties with regard to the long-term stability of supermirror coatings in high radiation fields. We have investigated the idea of tapering the nickel-coated guide section in order to increase the intensity of neutrons at the exit of the guide. Our results, shown in figure 1, show that the expected increase is of order 10 to 15% at long wavelengths.

(2) A supermirror-coated guide which is preceded by a nickel-coated guide is, in general, incompletely illuminated because of the lower critical angle of nickel. In addition the intensity of neutrons in the guide decreases with increasing distance from the source because the supermirror coating has less than 100% reflectivity above the nickel critical angle. These statements have been placed on a quantitative basis as illustrated in figure 2. We conclude that intensity gains of order 30 to 50% may be achieved, for wavelengths up to about 6 Å, using supermirror-coated guides which start just outside the biological shield of the reactor. These calculations are clearly of importance in view of the very significant additional cost of supermirror-coated guides.

(3) We have investigated the performance of a vertically curved monochromator placed in a neutron guide, with particular reference to effects

due to changes in the critical angle of the guide coating. The mosaic spread of the monochromator was appropriately convoluted into the acceptance diagram calculations. The results were independently confirmed by Monte Carlo calculations [4]. In figure 3 we show cumulative intensity distributions computed as a function of vertical distance from the sample center for various choices of mosaic spread η , for nickel- and supermirror coated guides. When η is small an increase in the critical angle of the guide results in an increase in the height of the beam at the sample. On the other hand a large mosaic spread has the effect of increasing the intensity at all points along the sample.

(4) One of the more important features of our calculational method is that we can track neutrons which are transmitted through a non-absorbing guide surface. This has enabled us to compute the filtering properties of the device illustrated in the inset to figure 4. Our results, shown in figure 4, are in good agreement with Monte Carlo calculations by Mezei [5] for the case that the inclined plate's critical angle is twice that of the guide. It is possible that a device of this sort will be placed before the first chopper of the high resolution time-of-flight spectrometer (see elsewhere in this report), in order to remove very long wavelength neutrons which might otherwise contaminate the beam at the sample. Note that the actual transmission will be somewhat reduced because the transmitted beam must pass through the inclined plate.

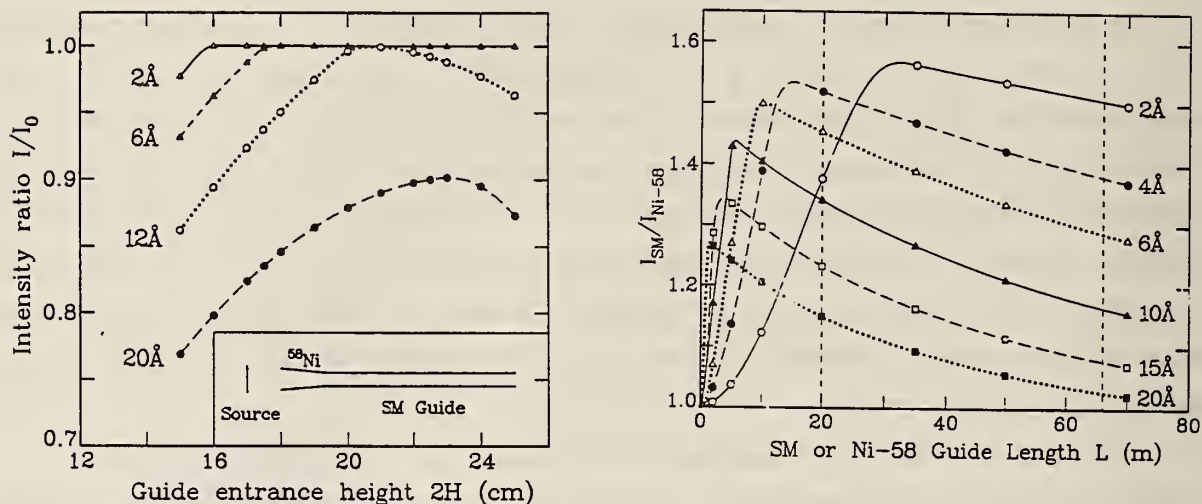


Figure 1. (left) Results of 2-dimensional calculations of the intensity at the exit of a long supermirror guide placed immediately following a converging ^{58}Ni guide, as shown in the inset. The supermirror guide is long in the sense that its acceptance angle (i.e., its height/length) is less than the critical angle for all wavelengths considered in the calculations. The ^{58}Ni guide entrance is 120 cm from the source and 160 cm long. The source is 30 cm high, the entrance height of the ^{58}Ni guide is $2H$, and its exit height is 15 cm. The supermirror guide height is 15 cm. The intensity I is expressed as a ratio to the maximum intensity I_0 which is obtained if the supermirror guide is fully illuminated. In these calculations the critical wave vectors Q_C for ^{58}Ni and for the supermirror material were 0.025 and 0.042 \AA^{-1} respectively. The supermirror was assumed to have 100% reflectivity up to the critical wave vector.

Figure 2. (right) Calculated ratios of the intensities I_{SM} and I_{Ni-58} at the exits of guides of length L coated with supermirror material and with ^{58}Ni respectively. In both cases the guide is preceded by a parallel 160 cm long ^{58}Ni guide whose entrance is 120 cm from the source (cf the inset to fig. 1). The source is 30 cm high and the guides are 15 cm high. The ^{58}Ni has a critical wave vector Q_C of 0.025 \AA^{-1} whereas the reflectivity of the supermirror is 100% up to 0.021 \AA^{-1} (the critical wave vector of natural Ni), falling gradually to 85% at 0.042 \AA^{-1} : thereafter, it is zero. The vertical dashed lines indicate, very approximately, values of L corresponding to the closest and most distant positions where beams can be extracted from guides in the guide hall.

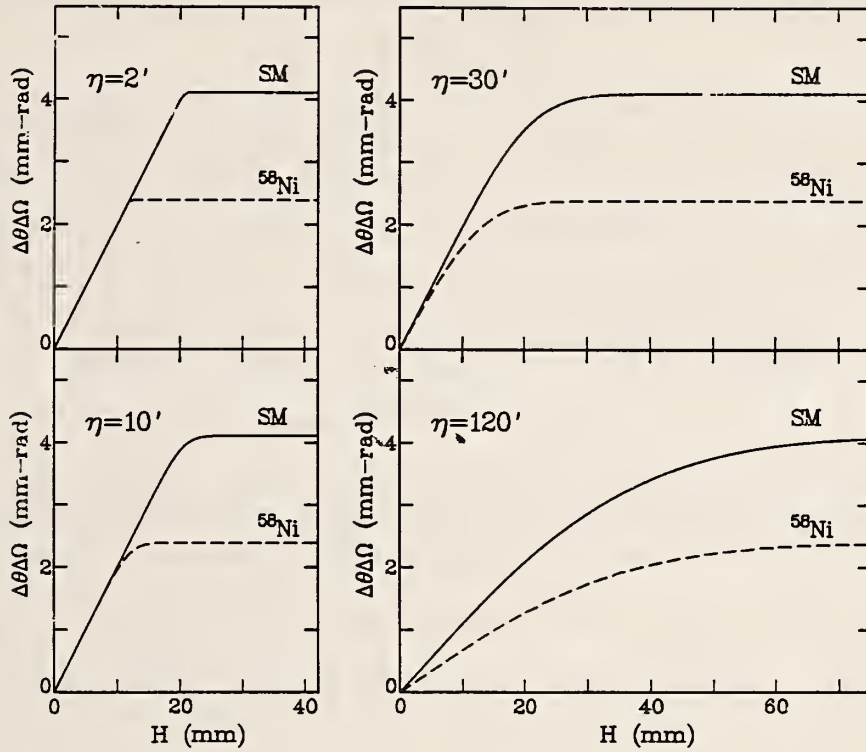


Figure 3. Cumulative intensity distributions in the focal plane of a vertically curved monochromator crystal placed in a guide. The neutron wavelength is 4 Å, the monochromator d-spacing is 3.35 Å, and its radius of curvature is 1.791 m. The focal plane (for neutrons in the guide) is therefore 1.50 m from the monochromator. The full height of the guide (and monochromator) is 15 cm, and it is coated either with ^{58}Ni ($Q_C = 0.025 \text{ Å}^{-1}$) or with supermirror material ($Q_C = 0.043 \text{ Å}^{-1}$). The ordinate is proportional to the integrated intensity on a sample of half-height H . Its maximum value, when H is large, is the product $(2H_G)(2\theta_C)$ where $2H_G$ is the height of the guide and θ_C is its critical angle.

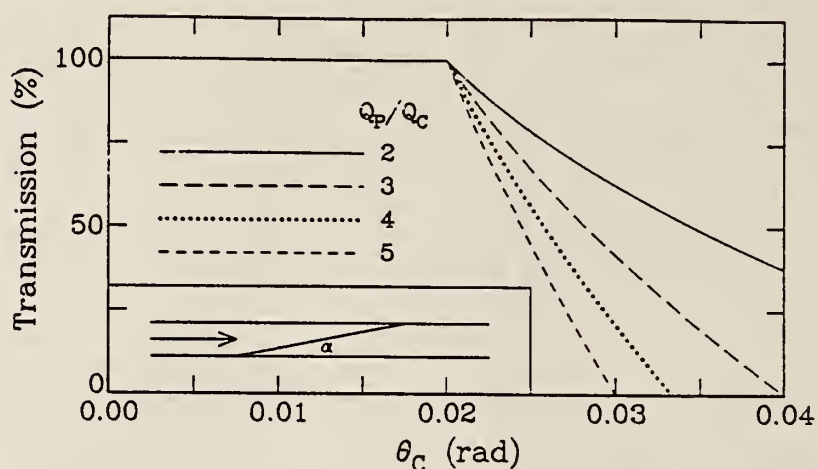


Figure 4. The calculated transmission of the device shown in the inset, which is basically a plate inclined at an angle α to the mean beam direction, coated with material of critical wave vector Q_p . The critical wave vector of the guide, Q_c , is 0.025 \AA^{-1} , i.e., that of ^{58}Ni , and the filter is designed to have 100% transmission up to 10 \AA , i.e., for $\theta_c \leq 0.02$. This is achieved by making α equal to $0.02 (1 + Q_p/Q_c)$.

References

- [1] Copley, J. R. D. NIST Tech. Note 1257, O'Connor, C., ed. p. 151 (1989).
- [2] Copley, J. R. D. Advanced Neutron Sources, Physics Conference Series Vol. 97, Institute of Physics Publishing, London, 1989 (in press).
- [3] Copley, J. R. D. Nucl. Instrum. Meth. (submitted).
- [4] The Monte Carlo calculations were performed by D. A. Neumann.
- [5] Mezei, F. Thin-film optical devices: mirrors, supermirrors, multilayer monochromators, polarizers, and beam guides. Majkrzak, C. F., ed. Proc. SPIE 983, 10 (1989).

ON THE USE OF MULTIPLY CHanneled GUIDES TO INCREASE INTENSITY
ON THE SAMPLE IN A MULTIPLE DISK CHOPPER TIME-OF-FLIGHT SPECTROMETER

J. R. D. Copley

A conventional direct geometry inelastic scattering time-of-flight spectrometer (at a reactor) necessarily has at least two choppers: the first pulses the beam and the second selects a wavelength from the pulsed beam. If disk choppers are used, significant advantages accrue when each of the two choppers is replaced by a pair of counter-rotating choppers, as illustrated in figure 1. A neutron guide is generally placed before, between, and sometimes following the chopper pairs, in order to increase the intensity of neutrons on the sample. (In a real instrument there are additional choppers, to remove unwanted orders and to reduce frame overlap, but these choppers are of no concern to us in the present discussion.)

The intensity distribution immediately following the first chopper pair, for the setup illustrated in figure 1, is a triangular function of the transverse spatial coordinate y . It rapidly develops into a roughly rectangular distribution as the neutrons progress down the guide, as illustrated in figure 2 for the case that $2W_1 = 2W_G$ (see the caption to fig. 1). In what follows, we shall assume that the intensity in any guide placed between the chopper pairs of a time-of-flight (TOF) spectrometer is independent of y by the time the neutrons reach the second chopper pair.

The transmission of the second chopper pair, integrated over time, is again a triangular function of y , and the number of neutrons which pass through the second chopper pair, per pulse, is given by

$$I_2 = (dI_1/d\lambda) (W_2/W_G) (h/mL) (W_2/v), \quad (1)$$

where the number of neutrons transmitted by the first chopper pair, per pulse, per unit wavelength interval, is

$$(dI_1/d\lambda) = \Phi_0 (2 W_1^2/v) (2H_G) (2 \theta_c)^2. \quad (2)$$

In these equations Φ_0 is the intensity of the incident beam before the first chopper pair (typically expressed in units of neutrons/cm²/sec/ster/Å), v is the tangential velocity of the choppers, $2H_G$ is the height of the guide (and of the slots in the choppers), θ_c is the (wavelength-dependent) critical

angle of the guide material (assumed identical for all surfaces), L is the distance between the chopper pairs, h is Planck's constant, and m is the mass of the neutron.

Suppose that it were possible to completely prevent motion of neutrons in the y direction, so that the intensity distribution just before the second chopper pair was still triangular (rather than rectangular). In this case the transmitted intensity I_2 , for the special case that $2W_1 = 2W_2 = 2W_G$, would be increased to $(4/3)$ of its value in the absence of the constraint on y . The increase occurs because a greater proportion of the neutrons are located close to the guide centre, where the transmission of the second chopper pair is relatively high. This result suggests the use of multiply channeled guides to restrict the lateral motion of the neutrons, and thereby increase the intensity on the sample, in a multiple disk chopper spectrometer. This concept is illustrated in figure 3. Calculated gains for several choices of chopper slot width and number of channels are presented in table 1. Note that gains are particularly dramatic when the chopper slot widths are much smaller than the guide width. This is the case when an instrument is in its higher resolution modes of operation, under circumstances where any method of increasing intensity on the sample is particularly welcome.

In order to decide whether multiply channeled guides should be used in a given instrument we must determine their effect on its resolution. We will then be able to estimate intensity gains at constant resolution. This work has just been started. Our preliminary calculations indicate that intensity gains at constant resolution can still be significant, though somewhat less dramatic than the numbers given in table 1.

The gain in intensity in any practical realization of this concept will clearly be somewhat smaller than the theoretical gain, because of the finite thickness of the channel plates, losses due to misalignments, and reflectivity losses due to the increased number of reflections. Nevertheless, we believe that significant overall gains can result, and we are likely to incorporate this concept into the design of the new high resolution TOF spectrometer (described elsewhere in this report).

Table 1. Calculated gains for various choices of the ratios (W_1/W_G) and (W_2/W_G) as a function of N , the number of channels into which the guide is (equally) divided. The relative intensity per pulse (R.I.), in the third column, is in units of $[\Phi_0 (2 W_G^2/v) (2H_G) (2 \theta_C)^2 (h/mL) (W_G/v)]$. Note that (for symmetry reasons) there is no gain if $N = 2$

(W_1/W_G)	(W_2/W_G)	R.I.	Gains, relative to $N = 1$				
			$N = 3$	$N = 4$	$N = 8$	$N = 16$	$N = \infty$
1.0	1.0	1	1.222	1.250	1.313	1.328	1.333
1.0	0.5	1/4	1.556	1.500	1.625	1.656	1.667
0.5	0.5	1/16	2.389	2.000	2.500	2.625	2.667
0.5	0.25	1/64	2.667	2.000	3.000	3.250	3.333
0.25	0.25	1/256	3.000	2.000	4.000	5.000	5.333

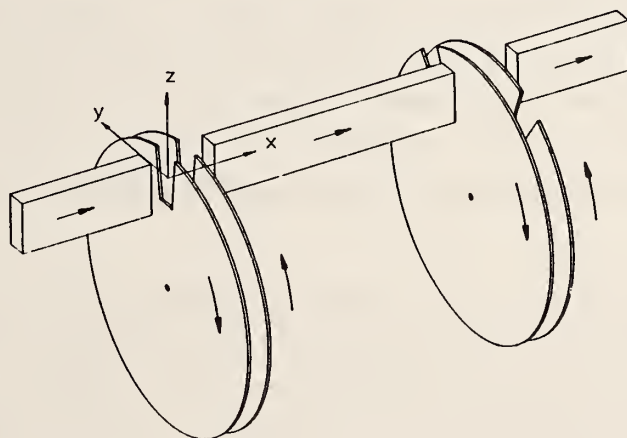


Figure 1. Two closely spaced counter-rotating chopper pairs arranged to pulse and monochromate a beam of neutrons in a guide tube of width $2W_G$ and height $2H_G$. The slots in the choppers have linear velocity v , and the distance between chopper pairs is L . The widths of the slots in the first and second chopper pairs are $2W_1$ and $2W_2$, respectively. The height of all slots is $2H_G$. The coordinate system is indicated.

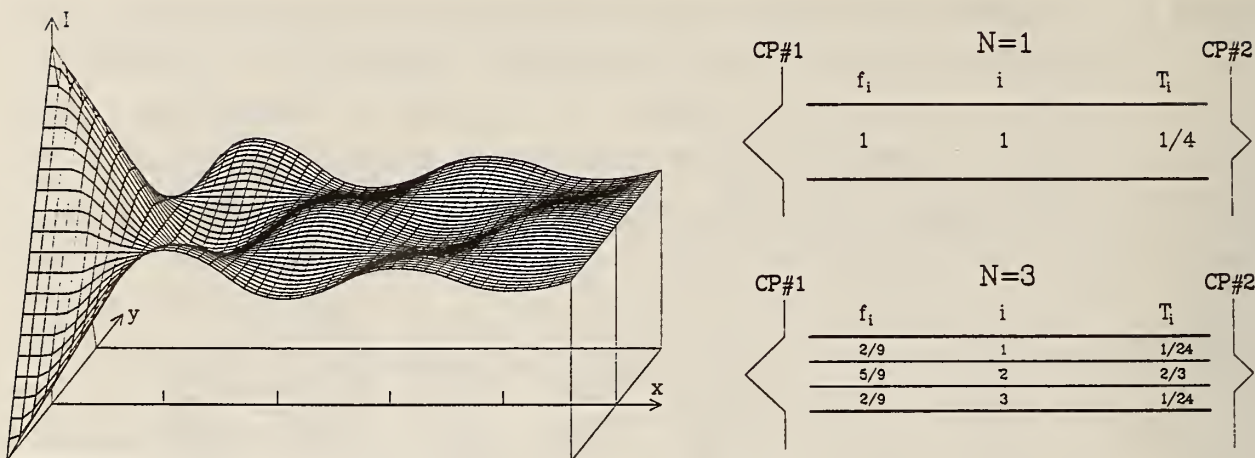


Figure 2. (left) A three-dimensional plot illustrating the evolution of an initially triangular spatial neutron distribution with base width $2W$ (at $x = 0$), as it progresses along a guide of the same width and critical angle θ_C . The distribution is flat, i.e., independent of y , at the nodes $x = (nW/\theta_C)$ where n is a positive integer: these positions are indicated by the tick marks along the x axis. At the antinodes, $x = (nW/\theta_C)$ with $n = 1/2, 3/2, 5/2$, etc., the extremum values of the intensity are $I_{\text{mean}}(1 \pm 1/4n)$ where I_{mean} is the mean intensity. The underside of the surface is not shown.

Figure 3. (right) The concept of a channeled guide is illustrated with reference to the case that $(W_1/W_G) = 1$ and $(W_2/W_G) = 1/2$. To the left and right of the guide are shown relative intensity distributions transmitted by the first and second chopper pairs (CP#1 and CP#2) respectively. The quantity f_i is the fraction of the intensity transmitted by the first chopper pair, $(dI_1/d\lambda)$, which enters channel i . The quantity T_i is the mean transmission of the second chopper pair for neutrons in channel i , relative to the peak transmission at $y = 0$. The number of neutrons per pulse after the second chopper pair may be written as $[(dI_1/d\lambda) \{ \sum_i (f_i T_i) \} \Delta\lambda_2]$, where $(dI_1/d\lambda)$ is defined in the text and $\Delta\lambda_2 = (h/mL) (2W_2/v)$ is the maximum wavelength interval transmitted by the second chopper pair (at $y = 0$). The gain of the three-channel arrangement is the ratio of the sums $\sum_i (f_i T_i)$, i.e., $[(7/18)/(1/4)] = (14/9)$ (cf. Table 1).

FOCUSED NEUTRON BEAMS FOR MATERIALS ANALYSIS

D. F. R. Mildner
(Center for Analytical Chemistry)

The Cold Neutron Research Facility at NIST combined with advanced research in neutron optics offers the possibility for developing an analytical microprobe for techniques which are dependent only on the reaction rate, not on the collimation, such as prompt-gamma activation analysis and neutron depth profiling analysis. Previous work involving converging guides of nickel-titanium supermirrors [1] looks promising, though there are problems with undulations of the layer profile as the film thickness increases. However, intensity gains are only about three in one dimension, caused by the increase of the angle that the neutron makes with the device axis on successive reflections.

Stacked curved microguides overcome this limitation of any mirror system by the superposition of outputs from many individual elements each of which point to a focus. Their ends slightly overlap each other, rather like a shifted stack of playing cards. The device is best understood by analogy with a strong focusing optical lens. The maximum intensity gain with the smallest possible focal area is obtained with a large number of microguides, each with a large radius of curvature and a short focal length. The thickness of the microguides relative to their length requires some optimization, though it may be dictated by practical considerations.

The principle was first demonstrated with 45 overlapping nickel coated glass mirrors, over a meter long, giving a gain of nearly two [2]. In another effort, 100 layers of alternating aluminum (3200 Å) and nickel (500 Å) were placed on a convex surface of length about 1 cm [3]. This device demonstrated the bending of neutrons, but no attempt was made to measure any intensity gain, if any. Surprisingly, this idea has remained dormant until last year at Jülich, where 10 bilayers of aluminum (10,000 Å) and nickel (1000 Å), of length 11 mm, were used to focus a beam of dimensions $0.01 \times 25 \text{ mm}^2$ into a circular spot of 3 mm half width at a distance of 23 cm.

The method to be adopted at NIST uses 25 μm thick, 5 cm diam nickel coated silicon wafers. Single crystal silicon has about the same neutron properties as aluminum for the substrate for the nickel. Silicon wafers of a thickness of about .001 in are now commercially available, and can easily be coated with nickel (1000 Å) on one side. The wafers will be loaded into a

cassette, fabricated to ensure overlapping, and to enable a small curvature to be maintained.

A method using acceptance diagrams [4] has been developed for analyzing the transmission properties of continuous curved neutron guides [5], such as beam benders and microguides. The method allows analytic expressions for the intensity and spatial and angular distributions of neutrons transmitted along a one-dimensional guide. The acceptance area for curved guides is parabolic in shape, and shows the asymmetry in the spatial distribution. From these formulations the average number of reflections can be determined as a function of wavelength. This is important for the microguides since reflectivity losses increase with the average number of reflections in the exponent.

References

- [1] Copley, J. R. D.; Majkrjak, C. F. Thin-film neutron optical devices: mirrors, supermirrors, multilayer monochromators, polarizers and beam guides. C. F. Majkrjak, ed. SPIE Proc., pp 93-104, August 1988, San Diego.
- [2] Friedmann, M.; Rauch, H. Nucl. Instrum. Meth. 86, 55-59 (1970).
- [3] Marx, D. Nucl. Instrum. Meth. 94, 533-536 (1971).
- [4] Carpenter, J. M.; Mildner, D. F. R. Nucl. Instrum. Meth. 196, 341-348 (1982).
- [5] Mildner, D. F. R. Nucl. Instrum. Meth. (submitted).

DESIGN STUDIES FOR THE PROMPT GAMMA-RAY ACTIVATION ANALYSIS INSTRUMENT

C. A. Stone and R. Zeisler
(Center for Analytical Chemistry)

Development of the prompt gamma-ray instrument has focused attention on the neutron and gamma-ray background near the instrument. Characteristics of the background were studied using the prompt gamma-ray instrument at the ELLA Cold Neutron Research Facility, KFA Jülich. Experiments showed that much of the background activity is due to neutrons which scatter off of the samples and are captured by materials which can be viewed by the detectors. An especially important experiment showed that the gamma-ray background due to boron in the neutron guides will degrade the performance of the instrument.

In these experiments a gamma-ray detector and a piece of borated glass were placed outside of the neutron beam such that the detector could view both the glass and a sample which was placed in the neutron beam. When a sample which scattered neutrons, i.e., an hydrogenous sample, was placed in the neutron beam, a very intense boron peak was observed in the prompt gamma-ray spectra. Moreover, the intensity of the boron peak was a function of the total neutron scattering cross section of the sample. An important concern here lies in the placement of the NIST prompt gamma-ray instrument at a mid-point along the NG-7 neutron guide. The neutron guide is split at the instrument with a neutron guide continuing to the SANS instrument: prompt gamma-ray analyses are thus performed underneath this continuing guide. As a result of these studies, the neutron guide near the prompt gamma-ray instrument has been designed using boron-free glass.

Support and shielding materials were shown to contribute significantly to the prompt gamma-ray instrument at KFA Jülich. Neutron capture in the aluminum from the sample supports, from the table which supported the detector, and from other miscellaneous components all contributed to the background in the gamma-ray spectra. Another major source of background was from the lead used to shield the detectors from the background! Although lead itself has a low neutron-capture cross-section, it is large for the impurities within the lead (antimony, for example). Thus an important part of the shielding for the prompt gamma-ray instrument includes quickly attenuating neutrons which scatter from the sample and thereby preventing them from striking material surrounding the instrument.

One promising material for neutron shielding is ^6Li -containing glass. Samples of this glass have been fabricated with up to 37 mole-percent of $^6\text{Li}_2\text{O}$. The primary component of this glass is SiO_2 (59 mole-percent) but it also contains small amount of Al_2O_3 as a stabilizer. This glass is easily made and can be ground into any desired shape. The large ^6Li concentration gives the glass the ability to quickly absorb the neutrons: 1 mm is sufficient to attenuate 85% of the neutron beam. Plates of this glass will be incorporated into the shielding of the detectors and the general shielding in the instrument.

COLD NEUTRON DEPTH PROFILING

G. P. Lamaze, R. G. Downing, J. K. Langland, and B. L. Grazman
(Nuclear Methods Group)

The design of the new Cold Neutron Depth Profiling (CNDP) Facility has been completed and the major components have been ordered. This includes a new 61 cm diam stainless-steel chamber, vacuum system, detectors, electronics, and data acquisition system. The new depth-profiling chamber will be capable of operating at UHV pressures and incorporates many design features that enhance the capabilities that currently exist at the thermal depth-profiling instrument at BT-3. The chamber will have an XY positioning system that will allow computer controlled scanning of up to 15 cm diam samples. The computer will also be capable of rotating both the sample and the detectors to adjust the sensitivity of the depth-profiling probe. The ability to use time-of-flight depth profiling techniques has also been incorporated into the chamber design. An electron gun for in-situ surface etching of samples will also be available.

The cold neutron beam will be filtered by 24 cm of single crystal sapphire to remove most of the fast neutrons. The expected neutron fluence rate at the sample position is $7 \times 10^9 \text{ n cm}^{-2} \text{ s}^{-1}$ with a cadmium ratio of about 10^{-4} . The peak energy of the beam is calculated to be 5.6 meV, which, for a $1/v$ cross-section reaction gives an effective cross section of 1.9 times the thermal value. This yields an increased sensitivity of about 20 times that of the present facility at BT-3 for the same efficiency particle detectors. Pancake type uranium fission chambers will be used for monitoring the neutron fluence. Both the beam and the target chamber are expected to be available in early October 1989.

A second chamber is being designed that will be placed downstream from the above chamber. This will have a computer-controlled sample changing capability for processing of batches of study materials. While this chamber will be less sophisticated than the chamber described above, it will allow higher sample throughput for routine analyses. This chamber will also be operated at UHV pressures and in-situ surface etching may also be available. This chamber is expected to be available in the spring of 1990.

REACTOR RADIATION DIVISION AND COLLABORATIVE PROGRAMS

HIGH RESOLUTION SMALL ANGLE SCATTERING SPECTROMETER

C. J. Glinka, J. Moyer, and A. Heald

and

S. K. Sinha

(Exxon Research and Engineering Company, Annandale, NJ)

Much of the vacuum flight path for the 30-m long, high resolution SANS spectrometer, being built jointly by NIST and the Exxon Research and Engineering Co., has been constructed and assembly of the instrument is now under way. The 15-m long post-sample section of the flight path, shown in figure 1, is designed to house two large area position-sensitive detectors; one that can be positioned within the main cylindrical section of the flight path at any distance from 4 to 15 m from the sample, and a second identical detector that moves along a circular arc at a fixed distance of 2 meters from the sample. Together the two detectors will span a Q-range from roughly 0.001 to 1 \AA^{-1} . The 15-m long pre-sample flight path, which is still under construction, has provision for the insertion of neutron guide sections to allow the effective source-to-sample distance to be varied in steps from 5 to 15 m to match the beam collimation to the chosen sample-to-detector distance.

The neutron velocity selectors, purchased for the instrument from the Central Institute for Physics in Budapest, Hungary, have been received and tested and do meet all of their design specifications. In particular, the wavelength bandpass of these selectors has been measured by time-of-flight and can be varied from 10 to 25% ($\Delta\lambda/\lambda$ FWHM) by inclining the axis of the rotor to the beam direction.

A novel feature of this instrument will be the use of a doubly curved, grazing incidence mirror, 2.4 m long, to focus the incident beam onto the detector. If successful, such a mirror would provide up to a fourfold increase in flux on the sample, for a given minimum Q-value, over what can be obtained with either single or multi-beam converging pinhole collimation. As currently planned this mirror will consist of eight, 30 cm long x 5 cm high, concave cylindrical segments that will be aligned tangent to an arc 1700 m in radius. Each segment will be slightly bent to conform approximately to this 1700 m arc to achieve focusing in the horizontal plane. We recently received and tested the first 30 cm segment of the planned mirror which had a measured

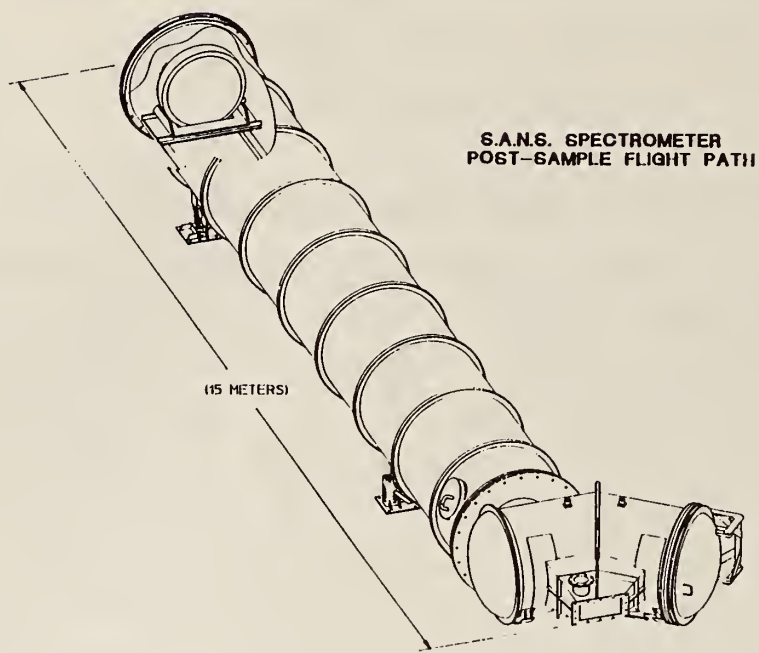


Figure 1. Isometric view of the post-sample vacuum flight path for the NIST/Exxon high resolution SANS spectrometer. The flight path will house two detectors, one that is moveable along the axis of the long cylindrical section and another within the angled section near the sample to extend the angular range of the instrument.

surface roughness of between 5 to 10 Å (rms). The profile of a slit-collimated neutron beam reflected from the surface of this mirror was observed to be free of any stray scattering due to the residual surface roughness at least to the 10^{-3} level which was the signal-to-noise limit of the measurement. Based on these results, we are proceeding to order the remaining sections needed for the full mirror.

The NIST/Exxon SANS instrument is expected to begin operation during the early part of 1990 with implementation of all of its planned features, including the focusing mirror and polarized beam options, continuing throughout next year.

DESIGN OF A COLD NEUTRON BACKSCATTERING SPECTROMETER

D. A. Neumann

The cold neutron backscattering spectrometer will be the first ultra-high energy resolution spectrometer to be built in the United States. This excellent resolution ($\approx 0.5 \mu\text{eV}$) is achieved by reflecting the neutrons from perfect Si monochromator and analyzer at a Bragg angle of $\approx 90^\circ$. The major drawback of this approach is the low intensity due to the narrow energy slice which is accepted and to the small divergence of the incident beam imposed by the guide. Since the narrow energy slice is necessary to obtain the desired resolution, the only way to improve the intensity is to increase the divergence of the incident beam. Several features are planned in order to accomplish this. First the instrument will be placed on a ^{58}Ni guide with the possibility still open of having supermirror coatings on the top and bottom of the guide. There will also be a converging supermirror nose to compress the beam from $6 \times 15 \text{ cm}^2$ to the sample size which will probably be $3 \times 3 \text{ cm}^2$, necessary because the sample size has a second-order effect on the resolution.

The most novel feature intended to increase the divergence of the incident beam is the implementation of the phase-space transform idea of Schelten and Alefeld [1]. Here a crystal with a relatively large mosaic is placed on a disk chopper so that the crystal moves perpendicularly to the average scattering vector. Then neutrons that have larger Bragg angles than the nominal one are Doppler shifted to larger energies and vice versa; i.e., neutrons that are moving too slowly are sped up and those moving too fast are slowed down. Simulations [2] have shown that a gain of a factor of 5-6 can be realized using this technique. We are preparing tests to determine if the crystal can be spun fast enough to realize this anticipated gain in practice. Another possible problem with using this technique is that the sample must be placed next to the direct beam which leads to concerns about the background. Since it is not possible to accurately gauge the severity of this problem, the instrument will be built so that the beam can be deflected away from the main beam before striking the phase-space chopper.

Another important feature planned for the backscattering spectrometer which will reduce the counting time for some experiments is a hydraulic Doppler drive for varying the incident energy distribution. This device,

pioneered at Jülich, allows the experimenter to vary the incident energy distribution so that the majority of time can be spent in a region of particular interest; e.g., in the vicinity of a rotational tunneling line. In addition, this device will extend the dynamical range of the instrument out to at least 100 μeV , if the experimenter chooses to do so. With the inclusion of these features which should increase the neutron current density on the sample to 10^5 n/sec-cm^2 and provide a great deal of flexibility to the user, this spectrometer will open up a wide range of experiments in condensed matter chemistry and physics that are at present impossible to perform in the United States.

References

- [1] Schelten, J. and Alefeld, B.; in Proc. Workshop on Neutron Scattering Instrumentation for SNQ, Maria Laach, 3-5 September 1984, Scherm, R. and Stiller, H. H., eds. report JÜ1-1954 (1984).
- [2] Neumann, D. A.; in NBS Reactor: Summary of Activities July 1987 Through June 1988, O'Connor, C., ed. NIST Tech Note 1257, p. 141.

SUPERMIRROR DEVELOPMENT

C. F. Majkrzak, D. A. Neumann, and J. R. D. Copley

The program of systematic development of supermirror coatings for neutron guide tubes, described in last year's report, continues. Significant progress has been made. Two private companies have been fabricating the supermirrors which are evaluated by us here at the NIST reactor. Specifically, to overcome the progressive roughening of layers which typically occurs in the conventional Ni-Ti supermirrors [1], a number of amorphous alloy multilayer systems such as $\text{Ni}_x\text{C}_{1-x} - \text{Ti}_y\text{Mn}_{1-y}$ have been investigated and improved supermirror reflectivities have in fact been obtained. However, because the companies involved in the research will probably bid for a contract to coat some of the guide tubes in the new NIST Cold Neutron Research Facility, the actual neutron reflectivity profiles, as well as detailed information regarding the deposition processes, are of a proprietary nature and cannot be revealed at this time.

Reference

- [1] Keem, J. E. et al. Neutron and X-ray Scattering and TEM studies of Ni-Ti multilayers. Proc. of the SPIE, Vol. 983, C. F. Majkrzak, ed. SPIE, Bellingham, WA, 1989, p. 38.

B. NON-RRD PROGRAMS

NEUTRON INTERACTIONS AND DOSIMETRY GROUP

J. A. Grundl
(Ionizing Radiation Division)

The Neutron Interactions and Dosimetry Group develops and applies well-characterized neutron fields and related capabilities for neutron dosimetry methods evaluation and standardization, for detector development and calibration, and for reaction cross-section measurements. Involvement with outside organizations, both in the federal and private sectors includes many types of research and technology assistance programs as well as leadership roles on national and international standards and radiation policy making bodies.

A selection of accomplishments for FY 89 with emphasis on NIST reactor related activities are outlined below in titled paragraphs grouped under four projects.

DOSIMETRY FOR MATERIAL PERFORMANCE ASSESSMENT. (E. D. McGarry, D. Gilliam, C. Eisenhauer, and G. Lamaze). Dosimetry methods for monitoring the degradation of materials in high fluence neutron exposures are diverse. This project provides some form of measurement assurance, standardization, or methods development for nearly every approach to materials dosimetry employed in the United States. Interlaboratory measurement cooperation with substantial International participation are an important feature of this project.

NIST/Nuclear Regulatory Commission (NRC) Contract. The 1977 Rancho Seco Reactor incident demonstrated that it was possible for a nuclear pressure vessel subjected to thermal shock to also experience significant pressure loading. This was of particular importance to subsequent studies that showed that relatively small flaws subject to pressurized thermal shock (PTS) could lead to failure of the pressure vessel. The possibility of small flaw development increases with hardening and loss of ductility of the pressure vessel, which takes place in carbon steels subjected to neutron irradiation. By law, Title 10 of the Code of Federal Regulations, Appendix G and H require that a program, involving irradiation of metallurgy test specimens and dosimeters, be carried out for the surveillance of pressure

NON-RRD PROGRAMS

vessel embrittlement damage. Consequently, the NRC in late 1977 identified the need for improved surveillance of reactor pressure vessels. In practice this means more and better fast neutron dosimetry and improved fluence calculational capability. Improvement implies better methods as well as better assessment of the uncertainties of derived parameters. The NRC carried out an 11-year international program (1977-1988), the Light Water Reactor Pressure Vessel Surveillance Dosimetry Improvement Program (LWR-PV-SDIP), dedicated to this task. NIST participated in activities to benchmark reference dosimetry measurements and calculations, and continues as consultant to the NRC.

NRC Regulatory Guide Preparation. A regulatory guide to provide guidance for improving and benchmarking neutron transport calculations is being drafted. The guide is in the form of instructions on important aspects of calculations, on dosimetry needed to validate the calculations, and on the reconciliation of differences between measurement and calculation including the assignment of uncertainties. NIST is a major participant in the formulation of this document, the preparation of which will continue into FY 90.

Neutron surveillance dosimetry measurements are generally made in special capsules containing dosimeters and metallurgy test samples. They are located in the water between the reactor core and the pressure vessel. Calculations are necessary to extrapolate results from these capsules to the one-quarter thickness of the pressure vessel, the established point of interest for reactor licensing. The extrapolation is carried out after the calculations have been confirmed by, or normalized to, the measurements in the surveillance capsule.

ASTM Benchmark Standard Balloted. Another draft of an ASTM Standard Guide for benchmark referencing of neutron dosimetry for reactor pressure vessel surveillance, E706IIIB [1], was prepared by NIST and was accepted for ballot after revision by the ASTM E10.05 Subcommittee meeting in Orlando, Florida, January 1989. A revised draft was balloted at the June 1989 E10.05 Meeting in Scottsdale, Arizona.

NIST/Westinghouse Cooperative Agreement. Measurement assurance activities with respect to Solid State Track Recorders (SSTRs) developed by Westinghouse Science and Technology Center (formerly Westinghouse Research) continues. The trend in the nuclear power industry to implement SSTR

dosimetry in ex-vessel cavities also continues. The bulk of these interests centers around work taking place in Westinghouse PWRs and in the B&W Owner's Group Davis Besse Dosimetry Benchmark Experiment. NIST is specifically interested in problems associated with establishing reliable masses for the SSTR fissionable deposits which are in the pico-gram to nano-gram range.

Generally, mass uncertainties in conventional dosimeters are not significant. At the picogram and nanogram level in SSTR dosimeters, however, the amount of material and the uniformity of the fissionable deposit present difficulties. The latter, in particular, is not always distinguishable from the effects of neutron fluence gradients. Westinghouse has largely circumvented the latter problem by using a readout system that provides two and three dimensional graphics of the fission track density over the whole surface of the SSTR. The problem of total mass is less easily solved. NIST has taken on the task of providing a basis for establishing mass scales of ^{237}Np , ^{235}U , ^{238}U , and ^{239}Pu ultra-lightweight deposits in Westinghouse SSTR dosimeters. This involves exposing the heavier of the lightweight deposits to known neutron fluences. These irradiations are carried out in the ^{235}U Cavity Fission Source at the NIST Reactor to an accuracy of about 2.5% (1σ). Initial results for ^{238}U suggest that there is a 5% discrepancy between masses assigned on this basis and those determined at Westinghouse by spiking and alpha counting techniques.

The IAEA Advisory Group Meeting on Nuclear Data for Radiation Damage Assessment and Related Safety Aspects will meet in September 1989 in Vienna, Austria. NIST will co-author a paper with Westinghouse Research entitled, "Benchmark Referencing of Ultra Low-Mass, Solid State Track Recorder Neutron Dosimeters in NIST Standards Neutron Fields."

Calibration of BELGIAN Cavity Fission Source. NIST personnel traveled to Mol, Belgium in December 1988 to re-establish the tie between the NIST and CEN/SCK fission neutron fluences in their respective ^{235}U Cavity Fission Sources. The basic calibration measurements were made with a NIST dual fission chamber containing fissionable deposits identical to those used in the calibration accomplished at Mol by NIST (then NBS) in 1983. Measured fission rates agreed to about $\pm 1\%$ (1σ). This is a significant result because in the interim NIST had to repair and re-calibrate the run-to-run monitor used to maintain the absolute fluence scale of the Belgian Cavity Fission Source.

NON-RRD PROGRAMS

The calibration of the Belgian ^{235}U fission field also affects the NIST ^{235}U Cavity Fission Source calibration because of complementary features of the two sources. The NIST ^{235}U fission source strength is almost two orders of magnitude higher than the Belgian source but the volume available for experiments is much smaller. The larger experimental volume in the Belgian source is more appropriate for NIST fission chambers and hence the direct fission chamber calibration in Belgium may be transferred back to the NIST source with some reduction in uncertainty. This cycle of calibration was completed in December 1988.

VENUS Benchmark Participation. The most active use of the Belgian Cavity Fission Source for the past several years has been to calibrate miniature fission chambers for active dosimetry in the Belgian LWR-PV Benchmark Experiment, VENUS, at their CEN/SCK Laboratory in Mol, Belgium. The VENUS series of PV benchmark experiments confirm neutron transport calculations of dosimetry measurements in the vicinity of fuel corners and out through the pressure vessel into the ex-vessel cavity. Additional checks involve ex-core calculations associated with matters of high fuel burnup. The VENUS experiments started in 1983 and have just been completed this year. The primary NIST function has been to provide supplementary benchmark calibrations and "hands-on" verification of the CEN/SCK benchmark referencing.

VENUS Absolute Power Calibrations. NIST became involved in the VENUS power determination when the ^{235}U mass of in a commercial miniature fission chamber was determined at the reactor thermal column [2]. These small sealed fission chambers make it possible to probe down in between the fuel plates in a low-power core and, without disturbing the thermal fluence rate, make vertical and horizontal scans of the absolute fission rate over the core volume. This powerful technique for determining absolute core-power levels was first employed in pool critical assembly (PCA) [3]. The reported ^{235}U mass of $4.72 \pm 2\% \mu\text{g}$ was determined by comparing fission rates with a known-mass deposit from the NIST inventory.

Corrections for gradients, relative spatial locations, and thermal fluence perturbations have made this measurement the subject of extensive discussions on both sides of the Atlantic. The matter was of some importance because the chambers involved were also used to determine the absolute core power of the earlier benchmark, PCA, operated at Oak Ridge National Laboratory (ORNL).

NON-RRD PROGRAMS

Now, after 8 years of additional work in which the Belgians have considerably advanced the state-of-the-art in the determination of absolute power levels in experimental reactor facilities, the "4.72 μg ^{235}U mass" stands as the constant that links three expensive VENUS campaigns to PCA. The reason is that through 10 years of effort the NIST calibrated miniature fission chamber was the common instrument used in all experimental configurations.

Dosimetry Methods Development for Reactor Support Structures. An NRC priority effort in the Heavy Section Steel Technology (HSST) Program this year was evaluation of the implication of low-temperature low-fluence-rate embrittlement on reactor vessel support structures. This issue arose from findings of higher than expected embrittlement in the High Flux Isotope Reactor (HFIR), at ORNL, and in the reactor shield tank from the Shippingport Reactor. The HSST staff studied and categorized all LWRs [4] into support structure types, and then selected two specific plants for detailed review. One aspect of this review will be to obtain dosimetry measurements and neutron transport calculations near critical support structures in two operating reactors. NIST is responsible for consultation and contracting for the dosimetry measurements and for benchmarking these measurements against NIST standard neutron fields. The benchmarked dosimetry will be used to adjust the calculations at the dosimeter locations. The calculations will be used then to specify the radiation damage exposure at the support structures.

Dosimetry at the Trojan Reactor. Two commercial power reactor installations have been selected for plant-specific evaluation of major reactor support integrity. They are the Trojan Reactor in Oregon and the Turkey Point Reactor in Florida. Current preparations for ex-vessel dosimetry experiments in Trojan are under NIST direction and will include a measurement assurance component. The plan is to place dosimetry packages as close as possible to a support structure buried in the concrete of the biological shield. These measurements will then be used to normalize or adjust neutron transport calculations used to predict cumulative exposures at critical flaw depths in the support structure. Contracts will be let for the dosimetry in FY 89 and the irradiation will take place in 1990. All dosimeter-evaluation systems must be benchmarked prior to obtaining the Trojan measured results in 1991.

PUD Neutron Sensors for Out-of-Core Reactor Dosimetry. Second only to the fission of ^{237}Np for good spectrum coverage of neutron with energies $E > 1.0$ MeV, ^{238}U is the desirable reaction for PV surveillance dosimetry. However, in such partially thermalized spectra, the fission in small concentrations of ^{235}U remaining in depleted ^{238}U can require a significant correction. Avoiding this correction by using highly depleted uranium is expensive and the material is becoming scarce. The Paired Uranium Detector (PUD) dosimetry technique was developed at NIST to circumvent the need for the highly depleted ^{238}U material and to obtain a measure of the $^{235}\text{U}/^{238}\text{U}$ fission ratio, an important neutron spectrum index.

The technique involves simultaneous irradiation of moderately depleted uranium (approximately 200 pm ^{235}U) along with natural uranium as the ^{235}U detector. Both materials are readily available. The small concentration of ^{235}U in natural uranium (0.7%), with low self-absorption, gives the ^{235}U response correction for the depleted uranium detector and a reasonable value of the $^{235}\text{U}/^{238}\text{U}$ spectral index. The ^{238}U detector of the PUD pair can be directly calibrated in the ^{235}U fission neutron spectrum of the Cavity Fission Source at the NIST Reactor and the quality assurance of the depletion can be checked in a thermal neutron beam. The uncertainty enhancement associated with the composite response in each detector has been documented.

Energy Response of Innovative Electronic-Hardware Dosimeter. The Nuclear Effects Directorates (NED) at the Aberdeen Proving Ground has been evaluating a new personnel dosimetry system for battlefield use by the Army. Special NIST neutron-field facilities were used to establish the neutron energy sensitivity of this semiconductor device. Multiple irradiations were performed for NED in a thermal neutron beam, in the 2-keV scandium filtered beam, in the 24-keV iron filtered beam, and at the 144-keV silicon filtered beam, all at the NIST Reactor, and at several Van de Graaff beams, and finally at the NIST ^{252}Cf source.

Applications of PUDs in Benchmark Experiments. PUD detectors, furnished by NIST, were first employed in the ORNL/PSF Surveillance Capsule Perturbation Experiment and in the ORNL/SDMF-4 Dosimetry-Method Comparison Experiment [4]. In the latter experiment, detector pairs, furnished by NIST, were placed along with conventional single isotope radiometric fission detectors front, back, and inside of a pressure vessel wall simulator. The results are reasonably consistent among the three fission products counted,

NON-RRD PROGRAMS

including the sometimes troublesome ^{103}Ru fission product activity. The observed spectral indexes ($^{238}\text{U}/^{235}\text{U}$) indicate an expected spectrum hardening in going from the front water/steel interface to the vessel quarter thickness as epithermal neutrons from the water are absorbed. Continued degradation of the spectrum occurs deeper in the steel as inelastic scattering in iron transfers neutrons to below the ^{238}U response threshold.

Following these ORNL pressure-vessel simulator benchmarks, PUDs were used to back up SSTR measurements in the first low-level leakage core measurements at the H. B. Robinson commercial power plant. The NIST/PUD measurements were made in both the surveillance capsule and in the ex-vessel cavity to confirm generic through-wall transport calculations and decreased fluence-rates in low-leakage cores.

Following these benchmark measurements, PUDs have become useful as ex-vessel cavity fluence dosimeters in commercial power plants. These include the Diablo Canyon, Turkey Point, and the Zion reactors. All of this is carried out as part of the NIST/Westinghouse cooperative agreement.

PERSONNEL DOSIMETRY (R. Schwartz, C. Eisenhauer, J. Coyne, and E. Boswell). Standard neutron fields are used to calibrate radiation protection instrumentation and to investigate and test new types of dose measuring techniques. Responsibilities in national and international dosimetry methods research focuses on tissue dose modeling, and tissue equivalent proportional counter (TEPC) measurements, and the development of written standards.

Calibration Service. Approximately 60 neutron radiation protection instruments were calibrated this year. Although the majority of the calibrations were done for commercial nuclear power plants, our "customers" also included institutions as diverse as Redstone Arsenal and the M. D. Anderson Cancer Center. For the past year we have also been performing tests of the "electronics package," before performing the actual neutron calibration. This allows us to detect nonlinearities or instabilities which are difficult to pin down using neutron sources alone.

Performance Tests of "Bubble Dosimeter." The new "bubble," or super-heated drop detectors represent a new and promising approach to neutron dosimetry. We are involved in a joint project to determine the relevant properties of these detectors. The other "players" include the Naval Surface

Warfare Center, the U.S. Naval Academy, the Naval Research Laboratory, and the National Physical Laboratory (NPL) in England.

While we still have many data to analyze, it so far appears that the "bubble dosimeter" (supplied by Bubble Technology, Inc., (BTI)) has high sensitivity, a good dose equivalent response, and is quite linear up to the point where the bubbles can no longer be accurately counted. Fewer data have been analyzed for the SDD-P (a pen-sized neutron personnel dosimeter supplied by Apfel Enterprises, Inc.,) but this device also seems to have a good dose equivalent response. Although intrinsically less sensitive than the "bubble dosimeter," it is much easier to read. We are currently analyzing the large amount of energy response data taken at a recent visit to NPL, and will shortly be measuring the response as a function of temperature for several of these devices.

TEPC Dose Measurement for Neutron RBE. The Armed Forces Radiobiology Research Institute (AFRRI) recently obtained very surprising results in experiments which examined the relative biological efficiency (RBE) for lethality in mice exposed to reactor radiations. In brief, the experiments indicated that a slight (5%) addition of neutron dose, into a pure gamma-ray field, decreased the lethal dose for the mice by almost 40%. The neutron and gamma-ray dose components were determined by conventional AFRRI ion chamber dosimetry. In an effort to shed some light on this totally unexpected result, we measured the linear energy transfer (LET) spectra in some of the AFRRI fields, using a tissue-equivalent proportional counter (TEPC). The results of this measurement disagreed with the AFRRI ion chamber dosimetry. Specifically, our results indicated that the supposedly 5% neutron field actually had a neutron dose approximately equal to the gamma-ray dose; i.e., the field was \approx 50% neutrons. If the dosimetry derived from our TEPC results is used to interpret the data from the "mouse experiments," then there are no longer any surprises. It should be pointed out that since the efficiency of the TEPC is very high, the reactor had to be run at very low power, and our experiments were limited to measurement of the neutron-gamma ratios for various configurations similar to those used in the mouse experiments. There was no attempt made to determine the absolute doses used in the actual experiments. We are currently trying to understand this difference in dosimetry, and, in particular, we are running the TEPC in known neutron,

NON-RRD PROGRAMS

gamma-ray, and mixed neutron-gamma fields to establish the accuracy and reliability of the system.

Catalog of Neutron Spectra for AFRRRI. A catalog of neutron spectra requested by the Armed Forces Radiobiological Research Institute has been completed. This catalog gives tabulations and plots of calculated fluence spectra, plots of calculated and measured energy deposition spectra, reaction rates measured with neutron activation foils and neutron fission chambers, neutron kerma rates measured with ionization chambers, and comparisons of measured and calculated quantities.

ICRU Publication on Practical Determination of Dose Equivalent. In a landmark publication ("Determination of Dose Equivalents Resulting from External Radiation Sources," ICRU Report 39 (February 1, 1985)), the International Commission on Radiation Units and Measurements (ICRU) recommended a new system for determining the dose equivalents resulting from exposure to external radiation sources. The advantages of the new system included a uniform approach to dose equivalent determination and reporting for gamma-rays, electrons, and neutrons, as well as a close link with the fundamental limiting quantity, effective dose equivalent (as defined in ICRP Publication 26). ICRU 39 is, however, a very terse document, giving little more than the definitions of the new dose equivalent quantities. Accordingly, another report committee was set up by the Commission to produce a document on practical determination of dose equivalents; i.e., how one uses the new quantities in practical radiation protection measurements and calibrations. In the rather short time--as these things go--of just over 2 years from our first organizational meeting, an "almost-final" draft was submitted to the Commission for its preliminary approval. Unfortunately, it does appear that we are shooting at a moving target. At a recent meeting, the Commission decided that the document should be split into two separate reports: the first on gamma-rays and electrons, and a second, separate publication on neutrons. This, despite the fact that one of the advantages of the new system was the unification of the dose equivalent definitions for the three types of radiations, and the fact that the draft text was carefully crafted to emphasize this unification. In addition, some Commission members are questioning the definitions of some of the quantities, and the phantom, specified in ICRU 39. We anticipate further interesting developments.

NON-RRD PROGRAMS

Radiation Protection Policy Committee Work. C. Eisenhower serves as chairman of a subpanel of the Science Panel of the Committee on Interagency Radiation Research and Policy Coordination (CIRRPC). The subpanel has produced a report on the desirability of planning for research on human health effects in the event of a nuclear accident. The subpanel recommended a follow-up effort to recommend ways of implementing such planning.

RESEARCH AND TECHNOLOGY ASSISTANCE (all group members). Research and technology assistance are strongly coupled in neutron dosimetry. A multiplicity of institutional involvements, drawn to the group by the availability of unique irradiation facilities and measurement capabilities, encourages a variety of attractive projects and unavoidable responsibilities.

Neutron Lifetime--Absolute Neutron Counting. An overview of the NIST involvement in measurement of the free neutron lifetime is given in the Fundamental Physics section of the NON-RRD program reports. The paragraphs in this section will discuss only one aspect of the experiment--the improvements in the absolute neutron counting under development for the upcoming new phase of the project at the NIST guide hall. In the measurements made at the Institut Laue-Langevin during the past year, the neutron density determination was made by employing a B-10(n, $\alpha\gamma$) detector whose mass-thickness had been determined by isotope dilution mass spectrometry. In the new phase of the project at NIST, calibration of the neutron monitor will be made by two new methods which do not depend on either the B-10 sample mass nor the B-10 reaction cross section. The new methods are alpha-gamma coincidence and calorimetry.

A new alpha-gamma coincidence counter for thermal and cold neutrons has been built [2], based on the counting of prompt gamma rays from a boron target which totally absorbs the impinging neutrons. In the calibration of the gamma detectors, the totally-absorbing B-10 target is replaced by a thin B-10 target and the alpha-gamma coincidence method is employed to establish the efficiency of the gamma detectors. Alternatively, the gamma efficiency can be determined by calibration with a standard alpha source with reference to the well-known branching ratio for the B-10(n, $\alpha\gamma$) reaction. Both of the calibration methods are believed to have the potential for approaching the 0.1% accuracy level, and a comparison of these two calibration techniques

will provide a test of consistency in assessing the accuracy actually achieved. Figure 1 shows a photograph of the new apparatus.

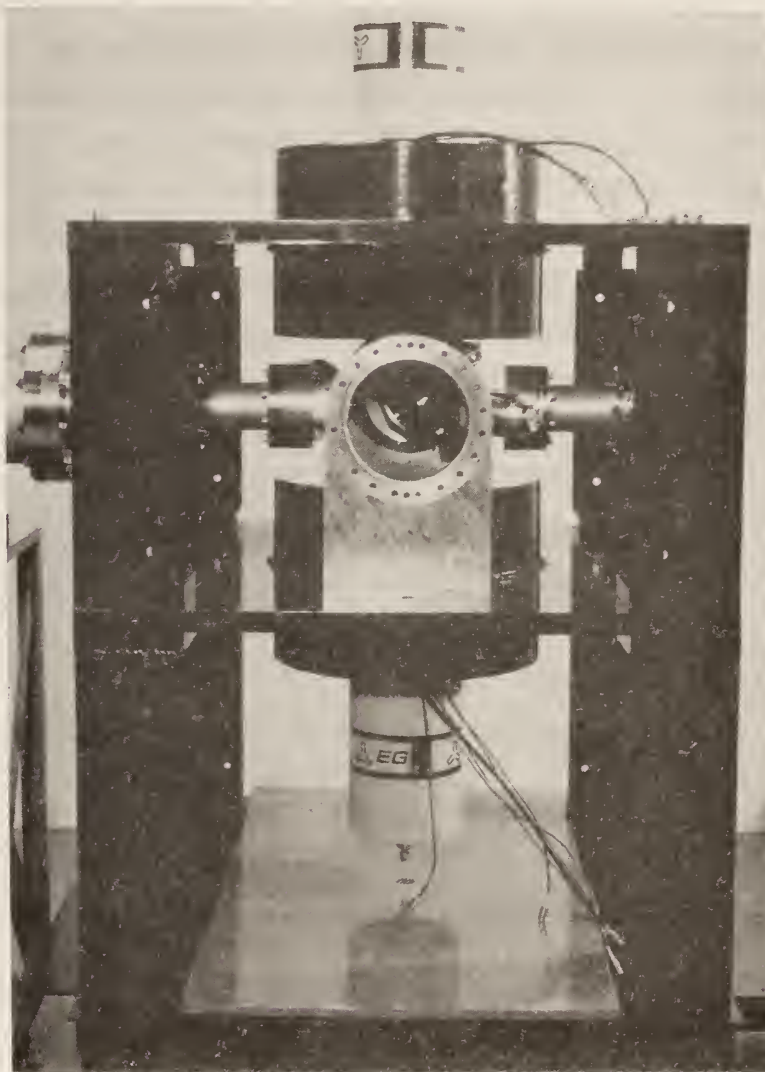


Figure 1. The new alpha-gamma coincidence system.

In collaboration with scientists from Los Alamos National Laboratory (LANL) and Harvard University, a Li-6 calorimeter was given initial testing in a beam from the thermal column. This neutron counter operates by measuring the heat derived from totally absorbing a beam of neutrons in a Li-Pb target. The observed thermal power and derived neutron flux were compared with the flux derived from fission chamber measurements. These results were found to agree within the $\pm 3\%$ uncertainty of the fission chamber measurements. Future intercomparisons at more demanding accuracy levels are planned with respect to the alpha-gamma coincidence method.

Benchmark Measurements for Criticality Safety. In collaboration with the Department of Energy sponsored groups at LANL and ORNL, an experimental program has been undertaken to improve the understanding of neutron leakage from aqueous systems which are representative of situations occurring in chemical processing of isotopes for nuclear weapons production. There has been a long-standing difficulty in the field of criticality safety analysis in calculating criticality of systems composed of multiple subcritical assemblies. One possible explanation for the difficulty is that the calculations are incorrectly predicting the neutron leakage from the individual assemblies. The present program compares calculations by two of the best Monte Carlo codes with state-of-the-art measurements for spherical aqueous systems driven by ^{252}Cf neutron sources. Fission ionization chambers with fissionable deposits from the NIST collection of Fissionable Isotope Mass Standards (FIMS) are employed to make the neutron leakage measurements. Working deposits from the FIMS collection are calibrated with respect to the reference deposits by comparisons made in beams from the reactor thermal column and in other NIST neutron fields.

Measurements have been completed at one of two prescribed radii outside a water-filled sphere of 4-in (10.16 cm) diam, including fission rates for four different nuclides: ^{235}U , ^{238}U , ^{239}Pu , and ^{237}Np . It has been possible to determine the ratios of count rates for the water-filled sphere relative to the count rates for the empty sphere to an accuracy of the order of 1%, because these ratios are independent of uncertainties in the source strength, the deposit masses, and the detector positions (so long as they remain fixed). The calculations and experiments are in good agreement for these wet/dry counting ratios for ^{238}U and ^{237}Np . However, for ^{235}U and ^{239}Pu , these wet/dry ratios are calculated to be 5 to 8% (respectively) higher than measured. These results must be considered as preliminary until perturbation studies of temperature variations and geometrical uncertainties have been completed; but if sustained, these results could provide valuable guidance in improving criticality safety calculations.

Radiation Shielding Calculations for NIST Cold Neutron Research Facility (CNRF). Calculations have been made to determine shielding necessary for two shutters to be installed at the CNRF. The first shutter will be placed at the exterior face of the biological shield. Calculations

were made for G. Lamaze using the discrete ordinates method, (ANISN computer code.) Various combinations of iron, tungsten, borated polyethylene, and lead were explored to determine an optimum configuration. The final configuration was designed by G. Lamaze on the basis of these calculations and the criterion that the dose equivalent rate due to neutrons and photons emerging from the shield be less than 100 mrem/h.

The second type of shutter will be placed at the wall of the reactor room. Calculations were made for I. Schröder using both the discrete ordinates and Monte Carlo methods. One area of concern in this case is the area near the shutter when the shutter is closed and acts like a beam stop. Another area of concern is the area on the other side of the wall, which is the interior face of a wall in the Guide Hall. Monte Carlo calculations were used when the geometry was critical and discrete ordinate calculations for thick-shield calculations. These calculations were used to design shield in both areas.

Neutron Penetration in Slabs of Finite Extent. Monte Carlo calculations of neutron transmission through slabs have been performed to help the U.S. Navy estimate shielding of personnel on submarines carrying nuclear missiles. These calculations demonstrate that neutron and gamma-ray penetration is insensitive to the position of a slab between a localized (point) source and detector. Furthermore, an angular parameter can be specified such that the relative contribution of neutrons or photons within that angle is also insensitive to the slab position. This is equivalent to quantifying the increase in scattered particles as one moves from a narrow-beam to a broad-beam configuration. A paper on this subject will be submitted for publication in Nuclear Science and Engineering.

Nuclear Energy Exhibit at National Atomic Museum. The National Atomic Museum in Albuquerque, NM, is developing a nuclear energy exhibit around an operating replica of Lady Godiva, an early experimental nuclear reactor and nuclear historic landmark. The aim of the exhibit, summed up in its title: Lady Godiva and the Realities of Nuclear Energy, is to engage public perception of nuclear energy by means of an eminently displayable and historically important nuclear reactor. A group member with unique experience in this area of nuclear technology is a consultant for the exhibit. Efforts this year have focused on the preparation and review of texts for exhibit labeling and an introductory video.

IRRADIATION AND CALIBRATION FACILITIES (E. D. McGarry, J. Grundl, C. Eisenhauer, and E. Boswell). Well-characterized neutron fields built and maintained as permanent irradiation facilities, provide certified fluences of pure fission neutrons, sub-MeV distributions, monoenergetic keV beams, and thermal neutrons. Passive and active detectors are exposed in these neutron fields for response calibrations, for cross-section measurements, and for the investigation of new measurement techniques. A multi-purpose fission rate measurement capability is centered around the NIST "go anywhere" double fission chambers and the NIST set of fissionable isotope mass standards (FIMS). The Manganous Sulfate Bath is the primary neutron source strength calibration facility for the United States. Absolute neutron fluences for all fission-neutron-driven standard neutron fields at NIST are derived from source strength calibrations at this facility.

Fission Neutron Irradiation Operations. Spreadsheets and test reports for certified fission neutron fluence irradiations have been reworked and updated and are now on PC computers. The new general purpose shield cave for storing high- and intermediate-level radioactive components is moving toward completion. The shield walls and top section are finished and on the reactor floor. Hardware for the rolling door is in hand. When complete, this shield cave will greatly simplify irradiation operations at the reactor thermal, not only for the cavity fission source but also for the Intermediate-Energy Standard Neutron Field (ISNF).

References

- [1] McElroy, W. N.; McGarry, E. D., eds. LWR-PV-SDIP: service laboratory procedures: verification and surveillance capsule perturbations. NUREG/CR-3321, WHC-EP-0205, NRC, Washington, DC, December 1988.
- [2] McGarry, E. D. Determination of the effective mass of ^{235}U in the fission chambers used for absolute core-power measurements in PCA. Light Water Reactor Pressure Vessel Irradiation Surveillance Program, Quarterly Progress Report for the April, May, June 1980 Quarter.
- [3] McElroy, W. N., ed. LWR-PV-SDIF: PCA experiments, blind test, and physics-dosimetry support for the PSF experiments. NUREG/CR-3318, HEDL-TME 84-1, NRC, Washington, DC, September 1984.
- [4] Cheverton, R. D.; Pennell, W. E.; Robinson, G. C.; Naust, R. K. Impact of radiation embrittlement on integrity of pressure vessel supports for two PWR plants. NUREG/CR-5320, January 1989.

NUCLEAR METHODS GROUP: OVERVIEW

R. R. Greenberg
(Center for Analytical Chemistry)

The development and application of nuclear analytical techniques for greater accuracy, higher sensitivity, and better selectivity are the goals of the Nuclear Methods Group. A high level of competence has been developed in both instrumental and radiochemical neutron activation analysis (INAA and RNAA). In addition, the group has the unique capability of using neutron beams as analytical probes for both prompt gamma activation analysis (PGAA) and neutron depth profiling (NDP). NDP determines elemental (isotopic) concentrations versus depth profiles within the first few micrometers of a surface by the energy analysis of the prompt charged-particles emitted during neutron bombardment. PGAA, on the other hand, measures the total amount of an analyte present throughout a sample by the analysis of the prompt gamma-rays emitted during neutron capture. These techniques (INAA, RNAA, PGAA and NDP) provide a powerful combination of tools to address a wide variety of analytical problems of great importance in science and technology.

The group has continued to contribute to the Standard Reference Material (SRM) certification effort; this year's efforts include multielement determinations performed on a number of SRMs including: Total Diet, Apple Leaves, Peach Leaves, Oyster Tissue, Coal, and Marine Sediment. Group members are serving as Technical Champions for many of these new SRMs, and as such are responsible for scientific decisions made throughout the production and certification processes of these materials. Additionally, RNAA measurements are currently under way to determine Hg in Bovine Serum and Se in Buffalo River Sediment. This will allow the certification of two additional, highly-important elements in these existing SRMs. A homogeneity study has been completed on the new Apple and Peach Leaves SRMs which showed that many elements were homogeneous to about 1% in 100 mg samples. In collaboration with members from other groups in the Inorganic Analytical Research Division, a study of these leaf materials has been undertaken to identifying problems in the dissolution of these materials which can lead to analytical errors during the certification analyses. A new ability to quantify nitrogen in biological samples will result from this year's research in developing an RNAA-liquid scintillation beta counting technique which exploits the thermal neutron reaction $^{14}\text{N}(n,p)^{14}\text{C}$, and measures the activity

of (radioactive) CO_2 upon sample processing. This project is being done in collaboration with the University of Illinois.

The International Conference on Nuclear Analytical Methods in the Life Sciences, held at NIST from April 17-21, 1989, was organized by members of the Nuclear Methods Group. At this conference, 144 participants from 32 countries presented papers and posters detailing recent advances of nuclear analytical methodology in the life sciences. The conference pointed to the continuing, essential role of nuclear methods in the life sciences, and provided new emphasis for the group's research program in this field.

Recent applications of Neutron Activation Analysis (NAA) in the life sciences by the group include "nonclassical" detection and determination of "tags" associated with biological macromolecules such as proteins, enzymes, and antibodies. In one application, an activatable tag has been attached to an antibody used in a medical diagnostic test. The INAA determination of the activatable tag is then used as the detection step of the diagnostic analysis. Research is continuing on the polyacrylamide gel electrophoresis neutron activation analysis technique (PAGE-NAA). The activation and subsequent determination of phosphorus in phosphoproteins has already been demonstrated. Research to extend this technique to the determination of other elements in specific macromolecules is under way. Such advanced uses of NAA in the life sciences may open a wide variety of applications for nuclear analytical chemistry.

The Biomonitoring Specimen Bank Research Project continued its research support for other agencies' monitoring programs. These programs included the Environmental Protection Agency's human liver project, the National Oceanic and Atmospheric Administration (NOAA)'s National Status and Trends (NS&T) program, the National Cancer Institute's micronutrient program, the International Atomic Energy Agency (IAEA)/NIST/Food and Drug Administration (FDA)/U.S. Department of Agriculture (USDA) Total Diet Study, and most recently, the NOAA Alaska Marine Mammal Project. Research has centered on specimen banking protocols and improved analytical methodology. The group's participation in intercalibration exercises with the project participants and the development of QA materials for various marine analyses helped to enhance the quality of the analytical results used in the assessment of the environmental health of the nation. Of major importance this year has been the analysis of samples from 30 NOAA NS&T sites. Both essential and

pollutant elements have been studied to assess the effects of anthropogenic inputs to the environment.

The joint NIST/FDA/USDA study of trace elements in human diet, sponsored by the IAEA, has completed its fifth year. A total of 120 diets from different countries have been analyzed to date for minor and trace elements. Nine diets from different regions of the United States have also been collected, and thus far, six have been analyzed. The data obtained from the U.S. diet composites have confirmed daily intake results for some of the elements investigated by the FDA (based on individual food analysis), as well as established reliable daily dietary intakes for additional elements including B, Cr, Cs, Li, and Sn. In the case of Li, the observed intake values are considerably lower than earlier published results. The group has taken an active role in the NIST program on high-temperature superconductivity research, both in the measurement of impurities in starting materials and final products, and the determination of the actual stoichiometry of the metallic constituents. The effort this year has centered on the development of accurate, rapid measurements of these materials by both NAA and PGAA. An effort to establish an accurate, monitor activation analysis technique for further study of high-temperature superconductors at NIST is under way.

Nearly a decade ago, a systematic error for PGAA was observed in which elemental sensitivities (counts/ $\mu\text{g-s}$) increased with increasing hydrogen concentration. Sensitivities in hydrogenous samples have been observed to increase by up to approximately 25% relative to samples with little H. This error was handled previously by matching H concentrations in samples and standards without any real understanding of the problem. During the last year, substantial progress has been made in understanding the problem on a theoretical level. In addition, systematic, experimental solutions to this problem are currently under investigation. The sensitivity enhancement seems to be caused predominantly by neutron scattering. This scattering can increase the neutron path length within the sample for some sample geometries, and thus may enhance the probability of neutron absorption. Measurements have been made which demonstrate this sensitivity enhancement as a function of H concentration for 11 elements in samples of constant size and shape. In a second set of measurements made on a series of disk-shaped pellets with constant H concentration but varying thicknesses (shapes),

elemental sensitivities were observed to increase with decreasing sample thickness. These general trends have been predicted by theoretical calculations. Our current understanding of this problem indicates that effects of scattering on sensitivities can be minimized or perhaps eliminated by irradiating spherical samples. A final series of measurements made on spherical samples with constant H concentration, and varying diameters (and thus masses), has indicated that the use of a spherical geometry greatly reduces, and perhaps eliminates, this problem.

A novel technique of PGAA analysis of gas samples has been developed using both the currently available thermal neutron beam at the NIST reactor and the ELLA Cold Neutron Facility at KFA, Jülich. Feasibility studies involving noble gases and gas mixtures indicate that sensitivities in the sub-ppm range for a number of elements should be achievable using the new NIST cold-source PGAA instrument which will be operational in FY 90. The development of a nuclear technique for gas analysis will establish an independent analytical method for reference material certification.

During the past year, a large part of the group's efforts has been directed at the exploitation of the analytical applications of cold neutrons. These efforts are needed to take full advantage of the guided beams of cold neutrons soon to be available at the new Cold Neutron Research Facility (CNRF). Plans are under way to include both PGAA and NDP experimental systems in the first phase of implementation. The group's involvement includes the design and construction of state-of-the-art instruments for both PGAA and NDP. Last year, the cold source itself was installed and became operational, and construction of the guide hall was completed during the first part of this year. The group's efforts have been aided substantially by its ability to use the existing cold neutron beams at the KFA Jülich facility. A major grant from the Eastman Kodak Company is contributing to the timely development of the NDP cold-neutron instrument. In order to introduce these new instruments to the potential user community outside of NIST, the Nuclear Methods Group organized a workshop on Analytical Measurements with Cold Neutron Beams, which was held May 22-23, 1989. This was the third in an ongoing series of workshops on the uses of cold neutrons organized by NIST.

Research on the new recoil-nucleus time-of-flight NDP technique has focused on the problem of detecting (with good energy resolution) the low

energy heavy nuclei which are emitted along with the light nuclei used in conventional NDP. These heavy nuclei can be used to provide very high resolution depth profiling capabilities in the sample region very close to the surface. Initial measurements appear to have validated this approach, and efforts are under way to determine how closely the actual depth resolution measured will approach the calculated values.

A long-range program to explore and develop the analytical applications of focused beams of cold neutrons has been initiated within the group. The ultimate goal of this research is to produce beams of neutrons which have intensities several orders of magnitude greater than previously available. Such beams will greatly enhance the capabilities of both PGAA and NDP, and may ultimately lead to a neutron milliprobe or even microprobe. The neutron microguide appears to be the most promising approach to achieve analytically useful focused neutrons, and as a first approach, a device will be developed and tested using a stack of nickel-coated single-crystal silicon wafers as focusing elements.

The strong interaction with industrial scientists using NDP, PGAA, and NAA has continued this year with a growing number of guest workers, research associates, and joint publications. An important development has been the demonstration of two-parameter coincidence spectroscopy (in NDP) for thin samples, in collaboration with the NDP group at the University of North Carolina and with Eastman Kodak. For appropriate samples, this technique provides an increase in sensitivity equivalent to more than a tenfold increase in reactor neutron flux. The measurement of distributions of lithium and boron in metals, glasses, and polymers continues to produce important results.

The Nuclear Methods Group is collaborating with scientists from the NIST Center for Atomic Molecular and Optical Physics, the NIST Center for Radiation Research, and the University of Sussex in a new measurement of the neutron lifetime. The goal of this research is to provide a new value for the neutron lifetime with an uncertainty of less than 0.3%. The current uncertainty for the neutron lifetime is about 0.6%. The technique used involves detecting the protons which decay in a neutron beam passing through a superconducting-magnet proton trap. Such measurements have been made with a cold neutron beam at the Institut Laue-Langevin in Grenoble, and additional measurements will be made at the new NIST CNRF next year.

During the coming year the group will continue to improve the accuracy, productivity, and sensitivity of nuclear methods as applied to elemental measurements. Problems to be addressed include those inherent in sample preparation, irradiation, radiochemical separation, counting, and data reduction, with the goal of minimizing and quantifying various sources of random and systematic errors in analysis by nuclear methods. Maintaining full accuracy at high count rates using current-generation data-acquisition electronics is the goal of our count-rate-dependent studies. Accurate quantification of gamma-ray self-absorption and measurement of the shape of the efficiency curve are required for accuracy in monitor activation analysis (since matching of sample with primary standards is not done). The development of monitor activation analysis is part of the high-temperature superconductivity effort to achieve rapid sample turnaround with minimum sacrifice of accuracy; however, the approach will also provide good quality control when used in parallel with traditional primary standard NAA.

INAA HOMOGENEITY MEASUREMENTS ON THE NEW NIST LEAF REFERENCE MATERIALS

D. A. Becker
(Center for Analytical Chemistry)

The first natural matrix, widely distributed reference material was Bowen's kale, produced and evaluated by Humphrey J. M. Bowen of Reading University, U. K. [1]. This material demonstrated to the scientific community the usefulness of such reference materials, and shortly afterwards the National Bureau of Standards (NBS) brought forth the first such material to be certified for trace elemental content [2]. Eventually, SRM 1571 Orchard Leaves was certified by NBS for 25 elements, with information values and/or compiled literature values for 42 additional elements [3], for a total of 67 elements. The Orchard Leaves SRM has been out of stock for a number of years, and was replaced by SRM 1572, Citrus Leaves. The Citrus Leaves were certified by NBS for 22 elements, with information values and/or compiled literature values for 35 additional elements, for a total of 57 elements.

NIST has obtained and prepared a new "orchard leaves" reference material to be certified for elemental content. Actually, the previous orchard leaves are being replaced by two new leaf materials: Apple Leaves, SRM 1515 and Peach Leaves, SRM 1547. These two materials have been obtained and prepared

for certification work, and this paper discusses some of the work on these materials to date.

Since the intent was to improve these new leaf SRMs in relation to the old leaf SRMs as well as other currently available botanical reference materials, a number of new or revised procedures were developed to better evaluate the SRM preparation procedures. These included the following: handpicking of the apple leaves followed by washing prior to grinding, to help remove dirt and siliceous material (a significant problem with the Orchard Leaves; washing was not done with the peach leaves, to determine differences, if any); jet milling and air-classification to obtain very small particle size, to allow evaluation of homogeneity at smaller sample sizes; a detailed moisture content and moisture uptake evaluation, along with weight loss measurements during drying; and, a dissolution study to help establish both the "insolubles" content of the leaves, if any, plus evaluate the ability of different dissolution techniques to totally solubilize the leaf materials. The space available here is not sufficient to present all of the information; however, the instrumental neutron activation analysis (INAA) homogeneity data are presented in tables 1 and 2, and fluence monitor data documenting the constant fluence rates in the RT-4 pneumatic tube facility are presented in figure 1.

Since these leaf materials were ground to extremely fine particle sizes through use of a jet-mill, it was expected that a very high degree of homogeneity would be obtained. The homogeneity study was thus designed to establish whether smaller than the usual 250 mg sample size could be specified while still maintaining appropriate certification uncertainties. The homogeneity study was made by INAA, with a sample size of 100 mg.

Experimental conditions are as follows: short half-life isotopes were measured after a 60 second irradiation at $2 \times 10^{13} \text{ n} \cdot \text{cm}^{-2} \cdot \text{s}^{-1}$ fluence rate (RT-4 at 15 MW power level), with four counts usually at 2, 9, 22, and 60 minutes decay. Counting geometries were always at or greater than 10 cm for these counts, and data were corrected for differences in irradiation time (using copper foil fluence monitors), decay time before counting, live time of count, decay during counting period, pulse pileup, and for weight losses during drying. For these preliminary results, the elements determined under these conditions were aluminum, calcium, manganese, potassium, sodium, and chlorine.

NON-RRD PROGRAMS

Activation products with half-lives of one day or more were determined after a second irradiation on these same samples, this time for four hours at a fluence rate of $6 \times 10^{13} \text{ n} \cdot \text{cm}^{-2} \cdot \text{s}^{-1}$ (RT-1 at 15 MW power level). Samples were counted twice, after approximately 6 days and 30 days. These 4 hours irradiations were actually two 2-hour irradiations. After the first irradiation, each rabbit was immediately flipped end-for-end, and irradiated for an additional 2 hours. With the specific configuration of the NIST reactor pneumatic tubes, this exactly corrects for the linear fluence dropoff in these tubes, providing all samples with exactly the same neutron exposure (within measurement uncertainties of $\pm 0.25\%$). For these preliminary results, the elements lanthanum, scandium, cobalt, iron, chromium, samarium (apple leaves only) and bromine (peach leaves only) were measured under these conditions.

In addition to those corrections specified above, conditions were monitored as closely as possible to eliminate or minimize all sources of error in these analyses.

The results for SRM 1515, Apple Leaves are contained in table 1, and results for SRM 1547 are contained in table 2. The measured homogeneity of both these materials is very good, with "Additional Variance" requirements of up to about 2% for most elements measured. It should be noted that the "Additional Variance" value includes all experimental uncertainties in the entire measurement process (preparation, irradiation, counting, and data reduction) except for the counting statistics (σ).

In order to evaluate the effect of the copper foil fluence monitor correction on the short half-life measurements, potassium values shown in table 1 for Apple Leaves were recalculated without using the fluence monitor correction factor. The copper foil data had an experimentally observed standard deviation of 1.014% (1s) for 42 irradiations ($n = 42$) over a 56 day period, while the counting statistics for this data (σ) averaged 0.11% (fig. 1). Without the copper foil fluence correction factor, the Apple Leaf potassium values had $s = 1.07\%$, $\sigma = 0.56\%$ (since counting statistics are the same), and an "Additional Variance" of 1.00%. Since use of the fluence normalization factors reduced the experimentally observed variability (s) from 1.07 to 0.55%, this demonstrates the need for such fluence monitoring when high precision data is required, and when irradiations are performed over a relatively long period of time. Further, the above data was

NON-RRD PROGRAMS

calculated with only 13 data points for the non-fluence corrected potassium values because one irradiation was known to be about 12% longer than the others due to operator error. However, when the fluence monitor correction was applied this value was indistinguishable from the other 13 values, and thus was included in the fluence corrected data in table 1.

In conclusion, the data in tables 1 and 2 indicate that these two new SRMs are homogeneous at the 100 mg sample size to better than $\pm 1.5\%$ at the 1s confidence level for at least six elements, plus better than $\pm 3.0\%$ for at least three additional elements.

Table 1. Homogeneity results for SRM 1515, Apple Leaves
Excess Variance^c Additional^d

Element	n	s ^a	σ^b	Observed?	Variance
Potassium	14 ^e	0.55%	0.56%	No	0.0%
Manganese	14	0.63%	0.16%	Yes	0.62%
Aluminum	15	0.72%	0.61%	No	0.42%
Calcium	13 ^f	0.92%	0.91%	No	0.30%
Lanthanum	15	1.07%	0.26%	Yes	1.07%
Samarium	14	1.33%	0.10%	Yes	1.37%
Sodium	14	5.41%	1.90%	Yes	5.20%
Chlorine	14	1.44%	0.68%	Yes	1.30%
Scandium	15	1.91%	0.81%	Yes	1.72%
Cobalt	14	2.95%	1.68%	Yes	2.31%
Iron	15	5.58%	2.74%	Yes	4.46%
Chromium	15	12.82%	9.61%	No	5.00%

^a s about unweighted mean (in % relative).

^b A priori uncertainty based only on counting statistics (in % relative).

^c Determination of excess variance based upon agreement between s and σ (i.e., whether s fell between 5-95% probability for a normal population).

^d Additional variance required to bring "probability of exceeding" to $50 \pm 2\%$ for a normal population. For the elements scandium, cobalt, iron, and chromium, this "Additional Variance" must include an estimated 2% random uncertainty due to the very close counting geometry. All other analytical uncertainties including any inhomogeneity are also located in the "Additional Variance" column as well.

^e One homogeneity sample was lost for all determinations except aluminum, lanthanum, scandium, iron, and chromium.

^f A second sample was counted at a different geometry, thus could not be directly compared to the others.

NON-RRD PROGRAMS

Table 2. Homogeneity results for SRM 1547, Peach Leaves

<u>Element</u>	<u>n</u>	<u>s</u> ^a	<u>σ</u> ^b	Excess Variance ^c	Additional ^d
				<u>Observed?</u>	<u>Variance</u>
Potassium	15	1.03%	0.45%	Yes	0.95%
Manganese	15	0.74%	0.10%	Yes	0.76%
Aluminum	15	1.44%	0.61%	Yes	1.35%
Calcium	15	0.89%	0.91%	No	0.0%
Lanthanum	15	0.79%	0.17%	Yes	0.74%
Bromine	15	0.90%	0.39%	Yes	0.84%
Sodium	15	3.34%	2.35%	Yes	2.43%
Chlorine	15	1.83%	1.04%	Yes	1.59%
Scandium	15	2.62%	0.64%	Yes	2.58%
Cobalt	15	2.43%	1.13%	Yes	2.11%
Iron	15	2.87%	1.08%	Yes	2.69%
Chromium	15	5.56%	4.09%	Yes	2.92%

^a s about unweighted mean (in % relative).

^b A priori uncertainty based only on counting statistics (in % relative).

^c Determination of excess variance based upon agreement between s and σ (i.e., whether s fell between 5-95% probability for a normal population).

^d Additional variance required to bring "probability of exceeding" to $50 \pm 2\%$ for a normal population. For the elements scandium, cobalt, iron, and chromium, this "Additional Variance" must include an estimated 2% random uncertainty due to the very close counting geometry. All other analytical uncertainties including any inhomogeneity are also located in the "Additional Variance" column as well.

NON-RRD PROGRAMS

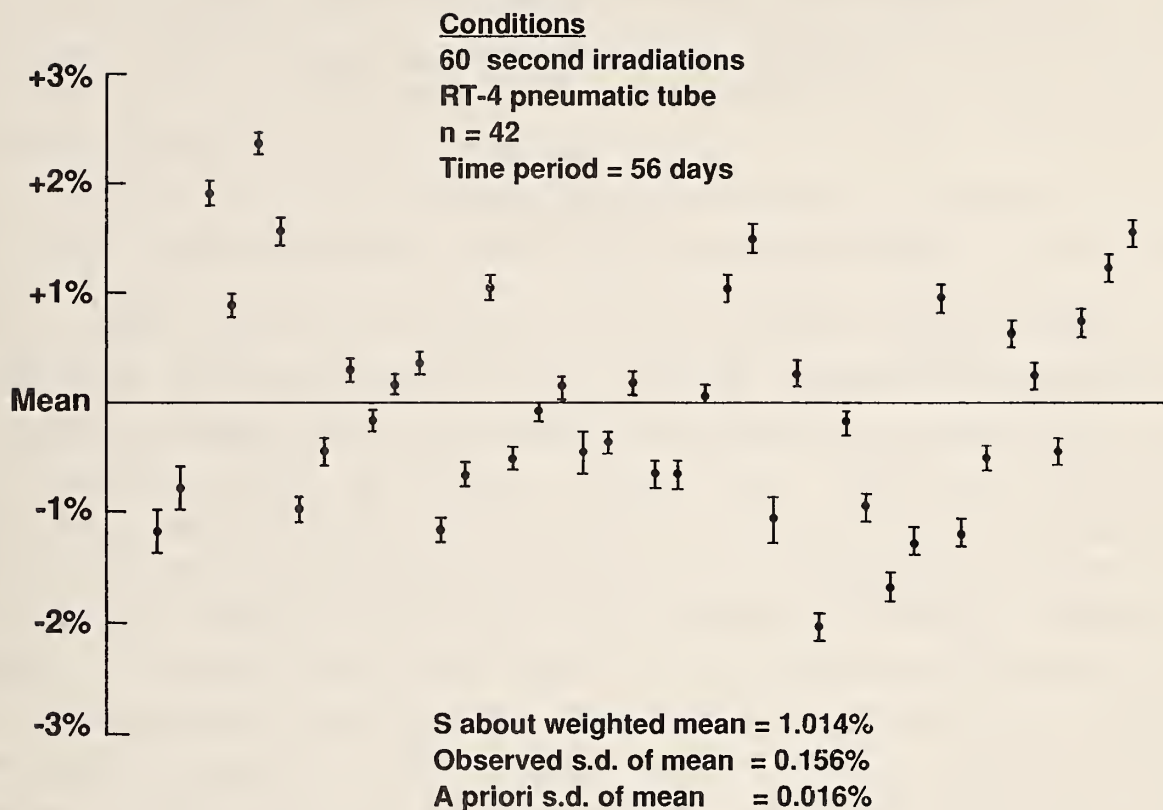


Figure 1. Copper foil fluence monitor data.

References

- [1] Bowen, H. J. M.; Cawse, P. A. Production of a homogeneous biological material for intercomparison of elementary analyses by different laboratories in Activation analysis: principles and applications, Lenihan, J. M. and Thompson, S. J., eds. Academic Press (1965).
- [2] Smith, G. W.; Becker, D. A. Preparation of an NBS biological SRM for trace elemental analysis, in Nuclear activation techniques in the life sciences. IAEA, Vienna (1967).
- [3] Gladney, E. S. et al. Compilation of elemental concentration data for NBS clinical, biological, geological, and environmental SRMs, Natl. Bur. Stand. (U.S.) Tech. Note 260, 1987. 111 p.

PROMPT GAMMA ACTIVATION ANALYSIS OF GASEOUS SAMPLES

R. Zeisler, C. A. Stone, W. D. Dorko
(Center for Analytical Chemistry)

and

M. Rossbach
(Nuclear Research Center (KFA), Jülich, FRG)

Neutron-capture prompt gamma-ray activation analysis (PGAA) is an instrumental multielemental technique that has been successfully applied to the analysis of a wide variety of sample types. Environmental, geological and biological samples are routinely analyzed at thermal neutron PGAA facilities. An advantage of the PGAA technique is that there is in principle no limit to the sample size or type and its physical form. The PGAA technique has been applied primarily to the analysis of small solid samples, but in only a few instances has it been applied to the analysis of liquid samples. It appears that PGAA has not been applied to the analysis of gaseous samples. Although modern analytical chemistry of gases utilizes very sensitive methods such as gas chromatography and mass spectrometry, a nuclear technique based on PGAA will establish an independent analytical method for reference materials certification. In addition, the technique may be sufficiently sensitive to determine lower concentrations of certain elements than is nowadays possible. In this contribution we present results from the analysis of chlorine in nitrogen using the thermal neutron facility at NIST. This work has been expanded to include measurements with a high flux, large diameter guided beams of cold neutrons at the ELLA Cold Neutron Research Facility of the Nuclear Research Center (KFA), Jülich. The prospect of performing analyses using cold neutrons dramatically increases the applicability of this novel technique. Briefly, the NIST PGAA instrument [1] has a thermal neutron beam (2.5 cm diam, 3.5×10^8 neutrons/cm²s flux) which strikes a sample approximately 50 cm from a collimated Ge spectrometer. The ELLA PGAA instrument [2] is located at the end of a cold neutron guide (5 x 10 cm area, 2.6×10^8 neutrons/cm²s flux) with the sample position 20 cm away from the detector. The gas samples used in these analyses were contained in a specially designed thin-walled Teflon sample cell which had a volume of 2000 cm³. Measurements were performed by placing this cell in the neutron beams. Since the cell was larger than the two neutron beams, the neutron

beam and the viewing angle of the detectors defined the sample volume. The effective sample size was approximately 24 cm^3 at NIST and 190 cm^3 at ELLA. A section of a typical prompt gamma spectrum of nitrogen containing a chlorine compound is shown in figure 1.

Studies at NIST involved determining the count rate of chlorine lines for dilute samples of vinylchloride in nitrogen. Figure 2 shows the measured count rates for a series of dilutions between 100 and 5000 (volume) ppm. These results show good reproducibility at each dilution and an excellent correlation of the count rate with dilution. Background measurements included gas samples of pure nitrogen, helium, argon, and ambient air; there was no detectable blank contribution to the data. Other gases measured included hydrogen (as methane) in helium and in argon. Initial measurements at ELLA have focused on determining concentration of hydrogen as methane in nitrogen gas. Background measurements included pure nitrogen, helium and ambient air samples. Although the hydrogen background at the ELLA facility is much lower than at the NIST (thermal) facility, it was significant enough to limit measurements to the 1000 ppm level. Painted lead bricks and boroplastic shielding materials were identified as major sources of the hydrogen background. Changes are currently under way to eliminate the

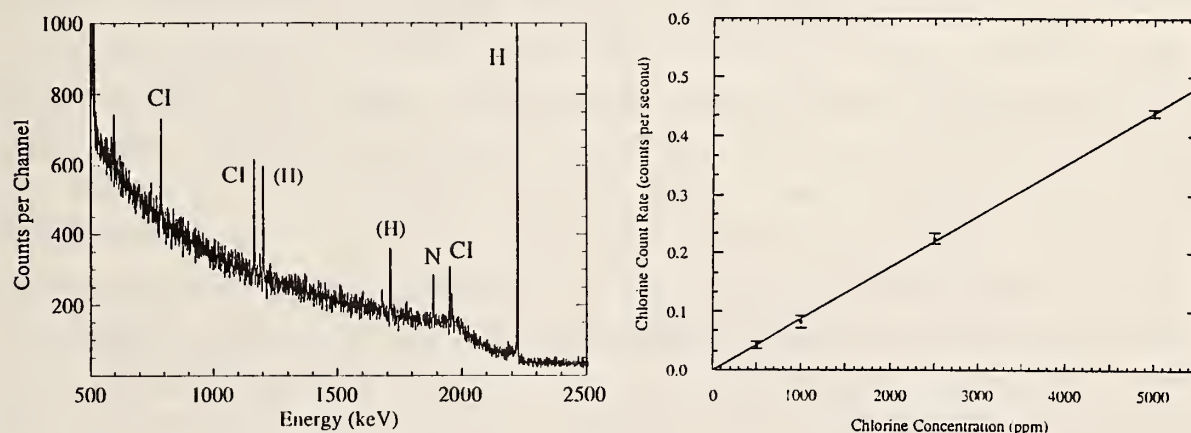


Figure 1. (left) Prompt gamma spectrum of nitrogen containing 5000 ppm vinylchloride from 500 to 2500 keV. The gas sample was counted 1 hour at the NIST instrument. The hydrogen peak is a background contribution to the spectra.

Figure 2. (right) Count rate of chlorine (as vinylchloride) in nitrogen at various concentrations. The correlation between count rate and concentration is excellent ($R = 0.99973$).

hydrogen background. Experiments will also be performed to determine chlorine in nitrogen to directly compare results from both facilities. There are several attractive features about using PGAA as a gas analysis technique. It is a relatively simple technique requiring no sample preparation. Since the samples are much less dense than either the solid or liquid samples, self shielding and self absorption effects are insignificant. There are few physical parameters in the PGAA analysis and these are well-determined, which lends it to absolute determinations. This application of PGAA is suitable to in situ analysis of gas reactions, process control monitoring as well as for basic studies of neutron capture gamma-ray emission rates.

References

- [1] Failey, M. P.; Anderson, D. L.; Zoller, W. H.; Gordon, G. E.; Lindstrom, R. M. *Anal. Chem.* 51 2209-2220 (1979).
- [2] Lindstrom, R. M.; Zeisler, R.; Rossbach, M. J. *Radioanal. Nucl. Chem.* 112, 321-330. (1987).

INSTRUMENTAL NEUTRON ACTIVATION ANALYSIS OF MARINE SAMPLES

S. F. Stone, B. J. Koster, and R. Zeisler
(Center for Analytical Chemistry)

The National Biomonitoring Specimen Bank (NBSB) at NIST has been involved in the National Status and Trends program since 1985. Each year, samples are collected and banked from approximately 20% of the sites from both the Mussel Watch and Benthic Surveillance programs. In this way, a complete archive of the sites will be created by 1991. Precise sampling protocols have been developed to ensure that the samples are not contaminated during collection and processing [1]. "B" sections of a small number of the samples were used for the determination of inorganic and organic real-time and trend monitoring data. For analysis, the samples were cryogenically homogenized. The respective "A" sections were banked undisturbed. Analytical procedures focus on instrumental nuclear methods. A sequential analysis approach has been developed, that allows the same 200 mg sub-sample of the homogenized specimen to be taken through a number of procedures.

NON-RRD PROGRAMS

These procedures include x-ray fluorescence (XRF-BFP), prompt gamma activation analysis (PGAA), and instrumental neutron activation analysis (INAA) [2] for the bivalve samples, PGAA and INAA for the sediment samples [3], and INAA alone for the fish tissue samples.

During the 3 years of collection, analysis has been completed on sediment, fish muscle, and fish liver samples from 12 sites in the Benthic Surveillance project; and, sediment and bivalves from 18 sites in the Mussel Watch project. All sample types have been a challenge to the applied procedures due to the greatly varying concentrations of trace elements among the sites. Nevertheless, the applied nuclear methods have shown their flexibility in providing accurate measurements for elements that may vary two to three orders of magnitude among the samples. An extension of this work was the determination of over 30 elements in Standard Reference Material (SRM) 1941, "Organics in Marine Sediment". The results for the SRM are given in table 1. Concentrations for these elements will be included for information on the SRM certificate.

The composition of this material appears unusual in many respects, containing high levels of many of the elements, including S, Fe, Ti, Sc, many of the rare earths, and U. This unusual composition, in addition to the normal complexity of a sediment spectra, meant that great care was necessary during the analysis, and when considering interferences. However, these interferences must always be considered in similar materials, such as those analyzed in the NS&T program.

References

- [1] Lauenstein, G. G.; Calder, J. A. Progress in environmental specimen banking. Wise, S. A.; Zeisler, R. and Goldstein, G. M., eds. Natl. Bur. Stand. Spec. Publ. 740, 1988, pp. 19-30.
- [2] Zeisler, R.; Stone, S. F.; Sanders, R. W. Anal. Chem, 60, 2760-2765 (1988).
- [3] Stone, S. F.; Koster, B. J.; Zeisler, R. Biol. Trace Element Res. (in press).

NON-RRD PROGRAMS

Table 1. Instrumental neutron activation analysis results. Element concentrations in mg/kg, dry weight basis

Element	Gamma Energy	SRM 1941		IAEA-SD-N-1/2	
	Used	Mean	Uncertainty ²	Value	Uncertainty
B ¹	477	75.5	1.7	87.7	1.5
Na	1368, 2754	12910	290	10740	120
Al	1778	64800	2400	37290	650
Si ¹	3539, 4933	222000	8000	272000	11000
S ¹	841	16410	840	3000	1000
Cl	1642, 2167	16400	400	9460	120
K ¹	770	15800	120	15200	580
Sc	889	34.34	0.42	6.913	0.060
Ti	320	17220	310	2812	93
V	1434	812	31	79.0	1.3
Cr	320	634.5	9.7	150.8	2.4
Mn	846	787.8	9.5	856.1	5.7
Fe	1099, 1292	105400	1000	36230	380
Co	1173, 1332	27.48	0.14	11.455	0.074
Zn	1115	1012	43 ⁴	437.6	6.5
As	559	75.4	4.0	56.30	0.44
Se	264	10.11	0.50	1.76	0.27
Rb	1076	92.1	1.3	69.6	2.2
Ag	657	1.24	0.47	1.54	0.25
Sb	1691	15.20	0.42	3.55	0.061
Cd ¹	558	2.32	0.29	12.30	0.52
Cs	795	4.78	0.13	4.36	0.10
La	1596	359	12	29.11	0.29
Ce	145	271.8	3.6	54.77	0.77
Sm ¹	333	25.69	0.40	5.52	0.20
Eu	778	2.184	0.060	1.065	0.042
Tb	298	2.19	0.40	0.669	0.0010
Gd ¹	182	15.16	0.37	5.43	0.35
Hf	482	22.43	0.29	8.48	0.12
Ta	1221	16.43	0.45	0.990	0.12
Th	311	25.63	0.25	6.73	0.10
U	(1596)	(22)		≤6.6	

¹ PGAA

² $t_{s/\sqrt{n}}$ for $P = 0.05$

³ 1 s counting statistics

⁴ includes an allowance for uncertainties in peak integration

DETERMINATION OF B AND Li IN DIETARY SAMPLES USING NA-MS

G. V. Iyengar and R. G. Downing
(Center for Analytical Chemistry)

W. B. Clarke
(McMaster University, Hamilton, Canada)

and

J. T. Tanner
(Food and Drug Administration, Washington DC)

An international human nutrition project sponsored by the International Atomic Energy Agency in Vienna, and jointly supported by the National Institute of Standards and Technology, the U.S. Food and Drug Administration, and the U.S. Department of Agriculture is in its fifth year. Under this program, diets from different countries including the United States are being analyzed for a number of minor and trace elements. In view of the emerging interest on the role of lithium and boron in animal and human nutrition, analytical work on the diets was extended to include Li and B. As a first step, diets from the United States were selected for preliminary studies. A combination of neutron activation (NA) and mass spectrometry (MS) was used for the simultaneous determinations of B and Li. This technique developed by Clarke et al. [1] has the required detection limit (< 10 ng/g) to measure the natural levels of these two elements in biomaterials. The method has been successfully used to quantify B and Li in several biological and dietary reference materials. This report deals with the application of NA-MS to determine B and Li in mixed total human diets prepared as described earlier [2]. These food composites represent the U.S. diet based on the Food and Drug Administration's Total Diet Study, and reflect the daily consumption of foods by 25-30 year old adult males. Until now, five collections belonging to Southeast (Georgia, Texas, West Virginia), North Central (Ohio, Iowa, Kansas), Northeast (New York, Pennsylvania, Rhode Island), South (Alabama, Louisiana, Texas), and West (Arizona, California, Oregon) have been analyzed. The concentrations (dry weight basis) in these collections range from 50 ± 0.6 to 124.3 ± 1.2 $\mu\text{g/kg}$ for Li, and 2.5 ± 0.2 to 3.6 ± 0.3 mg/kg for B. Based on initial estimates, the average intake amounts to 1.5 ± 0.25 (range 1.3 - 1.8) mg of B, and 37.35 ± 14.61 (range 25 - 62) μg of Li. Since the weights of the 201 individual components remain the same in all

composites, the changes observed in the composition may be linked to changes within a food item; e.g., fat content in meat and factors susceptible to geographical variations. Movement of foods across the country is a factor that needs to be considered in interpreting these findings. Analysis of future collections and more background information on the origin of foods should clarify this situation. The daily intake of Li calculated from the present study is the lowest in comparison with earlier published results [3,4], and is comparable with the recent findings reported for Canada [5]. For B, the intake is in the same range as observed in Canada [5] and Finland [6], and lower than that reported from the United Kingdom [4].

References

- [1] Clarke, W. B.; Koekebakker, M.; Barr, R. D.; Downing, R. G.; Fleming, R. F. Appl. Radiat. Isot. 38, 735 1987.
- [2] Iyengar, G. V.; Tanner, J. T.; Wolf, W. R.; Zeisler, R. Sci. Total Environ. 61, 235 (1987).
- [3] Reference Man. ICRP-23, Pergamon Press, New York, (1975).
- [4] Hamilton, E. I. The chemical elements and man. Wiley, NY (1979).
- [5] Clarke, W. B.; Gibson, R. S. J. Food Comp. Analysis (in press).
- [6] Acta Agriculturae Scandinavica. Supplement 22, (1980).

EXHUMATION CONFIRMS LEAD ANALYSES RESULTS

Neutron Activation Analysis Unit
(Federal Bureau of Investigation, Washington, DC)

Investigation of a drug-related double murder in the Northeast section of Washington, DC, produced no suspects after 2 years until an acquaintance of the perpetrators came forward with information which implicated three of the areas most notorious hoodlums. Investigators set out to gather the corroborative evidence necessary for prosecution.

A search of the suspects residence revealed a spent bullet in the basement which appeared to be the same caliber as the three bullets removed from one of the victims. Neutron activation analyses of these bullets and an additional fragment of lead removed from the victim revealed that the lead

NON-RRD PROGRAMS

fragment was slightly different in elemental composition from the bullets, thereby indicating that the victim had been shot four times. To make the matter more interesting, this fragment was the only specimen from the victim with exactly the same elemental composition as the bullet found in the suspect's basement.

After convincing prosecutors of the probable fourth bullet, the body was exhumed and reautopsied. A fourth bullet was recovered from the jawbone. Neutron activation analysis was used to show that the composition of this bullet was identical to the composition of the bullet from the suspects basement. This dramatic evidence was critical in establishing the credibility of the prosecution's case.

The accused were found guilty of murder.

INSTRUMENTAL NEUTRON ACTIVATION ANALYSIS OF MICROSCOPIC SAMPLES

R. M. Lindstrom
(Inorganic Analytical Research Division)

and

D. J. Lindstrom
(NASA Johnson Space Center, Houston, TX)

The high intrinsic sensitivity of neutron activation analysis has been widely employed for the determination of low concentrations in centigram-sized samples. By extending the standard measurement conditions to intense neutron irradiation and low-background, high-efficiency gamma ray counting, three orders of magnitude improvement in efficiency can be gained, and compositional measurements can be obtained in submicrogram samples.

Under a microscope, samples ranging from 0.2 to 1000 ng were picked with a tungsten probe and heat sealed separately in high-purity quartz tubes 0.1-0.2 mm in diam and 5-10 mm long. Sets of samples and standards were sealed in an outer envelope and irradiated with a thermal neutron fluence of 2×10^{20} n/cm².

The sample vials were cleaned in nitric acid and the induced radioactivity was assayed with high-efficiency solid and well-type Ge detectors with very low background. Detectors were operated in a counting room 20 m underground (Johnson Space Center) or a dedicated low-background laboratory

(NIST). An optimized thickness of low-background lead was used for detector shielding.

In the analysis of such small quantities of material, measuring sample weights and assuring homogeneous standards are major sources of analytical uncertainty. For the smallest samples, too small to weigh accurately, normalization to a major element like iron provides accurate concentration ratios. Well-prepared synthetic silicate glasses have proven to be homogeneous at 10 μg sample size. Since the size of these samples is smaller than or comparable to the 10 μm range of recoil fission fragments, large errors can be incurred in determining uranium-235 unless the sample is counted inside an irradiation container which is thick-walled enough to retain the fission products.

Detection limits for many elements are well below picogram levels and some approach femtograms. Because the method is nondestructive (though some sample handling is required), the samples are available with little compromise for further characterization by microprobe or other techniques after instrumental neutron activation analysis is completed.

LOW-BACKGROUND GAMMA RAY ASSAY LABORATORY FOR ACTIVATION ANALYSIS

R. M. Lindstrom and J. K. Langland
(Inorganic Analytical Research Division)

In activation analysis, as in environmental monitoring and measuring of cosmic-ray activation products, there is at times a need to reduce the background of a germanium gamma-ray detector as low as possible, for example instrumental neutron activation analysis (INAA) of very pure materials such as semiconductor silicon, INAA of very small samples such as individual grains of cosmic dust, and radiochemical activation analysis of ultratrace concentrations. Although it is not easy to achieve truly low backgrounds at a laboratory in close proximity to a reactor or laboratories in which millicurie quantities of radioactivity are handled, with care the background achievable can be remarkably good.

Many sources of gamma-ray background need to be guarded against. In most counting rooms on most days the dominant radioactivity is environmental potassium, uranium, thorium, and their daughters in concrete and other materials of construction of the building. Radioactivity may be present in

NON-RRD PROGRAMS

the detector itself or its shield. Radiochemical laboratories may be sources of detectable radioactivity at levels far below health physics significance. At a research reactor, the atmosphere inside the counting room may contain ^{41}Ar from irradiated air. Cosmic rays set the ultimate limit to the background unless the counting room is moved deep underground.

The chances for contamination were lessened by installing the detectors in a dedicated room, as far away from radiochemical work, irradiation facilities, and sample changers as practicable. We used a prefabricated environmental chamber 2.74 m x 4.57 m inside, installed in a high-bay area with only a 10 cm concrete roof overhead. A wall-mounted air conditioner removes the heat of the counting equipment and keeps a slight positive pressure in the room. Traffic is discouraged by keeping the air temperature cooler than most people find comfortable. A sticky floor mat at the entrance keeps shoe-borne dirt out. The smoke detector in the room is the optical type instead of ionizing, since the latter may contain 1 to as much as 100 μCi of ^{241}Am or ^{226}Ra .

Two detectors are used for low-background measurements, a Ge well detector in a cylindrical shield and a large solid detector in a shield made of stacked lead bricks. The specifications of the two detectors are as follows:

<u>Detector identification</u>	<u>Ty</u>	<u>Anne</u>
EG&G Ortec model no.	GEM-40195	GWL-180210-S
Crystal geometry	cylinder	closed-end well
Ge type	p	n
Cryostat	upright dipstick	upright dipstick
Low-bkg modifications	yes	no
Crystal size, dia x length	60 x 79 mm	60 x 74 mm
Well dimensions (room T)	none	10 dia x 51 mm deep
Standard efficiency @ 25 cm	45%	30%
Resolution @1333 keV	1.76 keV	2.01 keV

The well detector, named Anne, is housed in a cylindrical shield, built twenty years ago to house a scintillation coincidence gamma spectrometer at the Naval Radiological Defense Laboratory [1] and subsequently transferred to NIST. The walls and roof of this shield are 10 cm of selected lead, clad in stainless steel. The dimensions are large enough to

NON-RRD PROGRAMS

house the detector in its Dewar with 25 cm of clearance above the crystal can. The Dewar rests on a disk of lead 5 cm thick, which in turn rests clear of the walls on rubber blocks. The shield thus provides excellent vibration damping, an especially important consideration for a well detector with large microphonic sensitivity.

The solid detector "Ty" incorporated the manufacturer's low-background modifications: a magnesium end cap, charcoal cryosorber, and 3 cm of old lead between the crystal and the preamplifier. This detector was housed in a shield made of new 2" x 4" x 8" bricks of low-activity lead [2] from an ore body with a low radiogenic ^{206}Pb component and hence a low content of other radium daughters. By neutron activation analysis we have found lead from this source to be unusually low in trace impurities. Except for degreasing with ethanol, the bricks were not specially cleaned before use. The shield arrangement is shown in figure 1. The supporting structure is made of welded aluminum to avoid the possibility of ^{60}Co contamination in steel. Beneath the table is a 10 cm shadow shield of nonselected lead to absorb radiation from the concrete floor.

The optimum thickness of the shield was determined by experiment, balancing background against bulk and expense. Once the decay gamma rays from natural radioactivity are reduced (by a factor 10^4 in 15 cm), increasing thickness gives an increasing background from the buildup of tertiary cosmic ray particles. As figure 2 shows, the positron annihilation peak increases slowly with increasing thickness of the lead roof. The final dimensions were 6" (15 cm) walls and a 4" (10 cm) roof. To ensure a tight fit, the lead bricks were stacked snugly together with the aid of a mallet and the outer wall courses were offset from the inner by 6 mm.

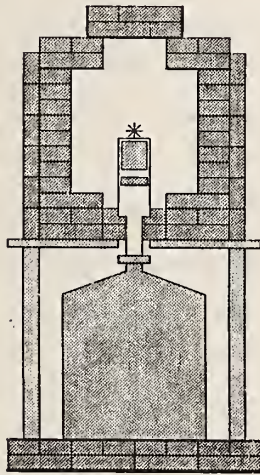
The lead shield was lined with material of lower atomic number to absorb the Pb fluorescent x-rays. A commonly used lining is 1 mm Cd with 0.1 mm Cu inside. While Cd is an excellent absorber for lead K x-rays, its large cross section for radiative neutron capture is undesirable when neutrons are an important contributor to the background. When the solid detector was experimentally surrounded by Cd sheet inside the shield, the count rate of the 559 keV capture line was 0.003 c/s. At NIST it has been the practice to replace Cd with 6 mm or more of copper, which absorbs the x-rays equally well, reacts less with neutrons, cost less, is nontoxic, and can also be used structurally. The present shield was accordingly lined with 12 mm of OFHC

NON-RRD PROGRAMS

copper, whereupon the continuum background increased by a third over that in the unlined lead, and new peaks appeared in the spectrum from decay of the levels of the copper-63 and -65, excited by inelastic scattering of high-energy cosmic ray neutrons. In the near future, the copper will be removed and replaced by thin tin.

Background lines from excited Cu

<u>Energy</u>	<u>c/s</u>	<u>Isotope</u>
669.6	0.0017	63
770.6	0.0004	65
962.1	0.0024	63
1115.5	0.0008	65
1327.0	0.0006	63
1412.0	0.0002	63
1481.8	0.0003	65



Effect of Roof Thickness for 8" Walls

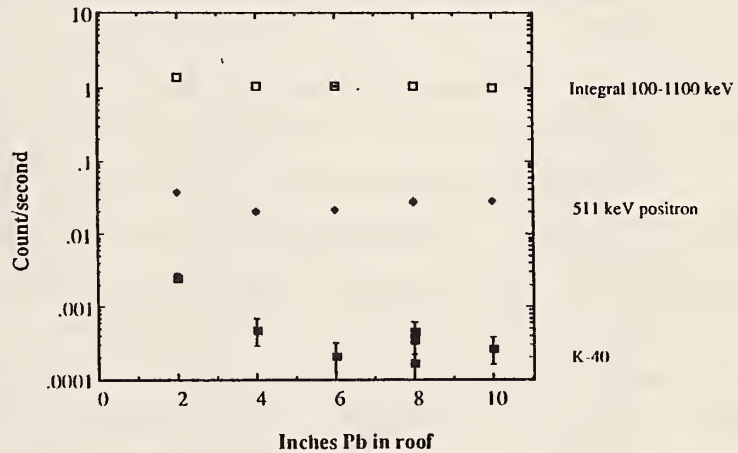


Figure 1. (left) Low-background shield for Ty detector.

Figure 2. (right) Background vs. roof thickness for 8" thick walls. The cosmic-ray positron peak at 511 keV and the integral background increase with increasing thickness beyond 4".

It was originally intended to install a thick inner lining of low-Z plastic material to reduce low-energy x-rays still further and inhibit bremsstrahlung from charged particles. Experiment showed that this was not desirable. To test the effect of adding large quantities of hydrogen, the detector was surrounded by 12 L of water in 2-L polyethylene bottles. The

effect of the hydrogen in moderating high-energy cosmic-ray neutrons was dramatic. The hydrogen capture line at 2223 keV appeared at 0.020 c/s (count per second), and on prolonged counting the characteristic lines at 596.4 and 868.4 keV from capture of the thermalized neutrons in the germanium detector itself were visible at 0.005 and 0.002 c/s, respectively. With a 1-L Marinelli beaker the hydrogen capture line was 0.003 c/s, whether or not the detector and Marinelli were surrounded by Cd sheet either outside or inside the lead. From the measured counting efficiency in the Marinelli geometry the thermal neutron flux is estimated to be $0.02 \text{ n/cm}^2\text{s}$. The shield will finally be lined with thin sheets of acrylic, whose only purpose is to provide an easily cleanable or replaceable hedge against contamination.

In the unlined lead shield, the background shows only 511-keV positron annihilation radiation, products of cosmic-ray neutron interactions with the germanium of the detector itself [3,4], excitation lines of $^{207,206}\text{Pb}$, radon daughters, ^{40}K , and ^{60}Co , in that order of importance (table 1). Only the annihilation line is higher than 5 c/hr. Except for a trace of ^{60}Co , no lines are detected which can be attributed with certainty to long-lived radioactivity in the materials of which the detector or the shield are constructed. The remaining radon activity will be reduced by flushing the shield continuously with nitrogen boiling off from the Dewar.

The background spectrum of the detector in the unlined lead shield is shown in figure 3. The conspicuous broad peaks extending upward from 596 and 693 keV result from inelastic scattering of fast cosmic-ray neutrons on ^{74}Ge and ^{72}Ge , respectively [3]; an enlarged view of this portion of the spectrum can be seen in the accompanying section of this report concerned with cold fusion. From the 693-keV line, produced with an 80 mb cross section, the fast neutron flux is estimated to be $0.02 \text{ n/cm}^2\text{s}$ and the energy about 1 MeV [5]. The integral background from 100 to 2400 keV is 1.54 c/s.

The influence of the NIST reactor (located 60 m from the shields) was insignificant. No difference in either continuum or peaked background was visible whether or not the reactor was operating. In particular, ^{41}Ar from irradiated air, small amounts of which are easily measurable in a laboratory adjacent to the pneumatic tubes, is rarely detectable. The air from the reactor confinement building and radiochemistry laboratories is discharged from a 30-m stack 70 m from the counting room; under most weather conditions

NON-RRD PROGRAMS

the air inlet for the building is well away from where the plume reaches ground level.

Having shown that the main source of residual background in these detectors is cosmic radiation, we conclude that the greatest additional improvements to background will require either deep burial of the counting room or active (anticoincidence) shielding.

Table 1. Gamma rays in residual background

Energy (keV)	Nuclide	Count rate, c/s Ty	Anne
53.5	^{73m}Ge	0.0005	
66.6	^{73m}Ge	0.003	0.001
72.8	Pb $K\alpha 2$	(0.003)	
75.0	Pb $K\alpha 1$		0.015
84.4	Pb $K\beta 1'$	(0.0004)	0.009
87.3	Pb $K\beta 2'$		
139.9	^{75m}Ge	0.002	0.001
159.7	^{77m}Ge	0.001	
197.9	^{71m}Ge	0.002	0.002
238.6	$^{212}\text{Pb}(\text{Th})$	0.0005	0.017
295.2	$^{214}\text{Pb}(\text{U})$	0.0002	0.002
511.0	annihilation	0.03	0.025
569.6	$^{207*}\text{Pb}$	0.0003	
583.1	^{208}Tl		0.006
596.1	$^{74}\text{Ge}(\text{n}, \text{n}')$	0.010	0.03
693.4	$^{72}\text{Ge}(\text{n}, \text{n}')$	0.009	0.02
609.3	^{214}Bi	0.002	0.003
803.3	$^{206*}\text{Pb}$	0.001	0.001
1173.2	^{60}Co	0.0003	0.001
1332.5	^{60}Co	0.0002	0.001
1460.8	^{40}K	0.0004	0.002

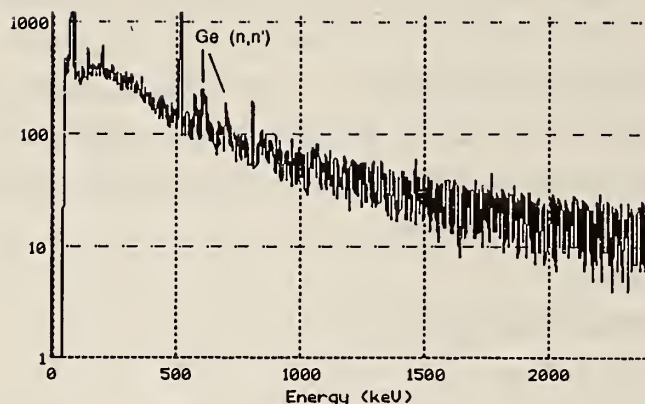


Figure 3. Background spectrum (140 h counting time) of the Ty detector in the unlined low-background shield. Except for Pb x-rays, the 511-keV annihilation line, and inelastic scattering of fast neutrons from germanium and lead, the background spectrum is nearly featureless.

References

- [1] Euler, B. A.; Covell, D. F.; Yamamoto, S. Nucl. Instr. Meth. 72, 143 (1969).
- [2] Doe Run lead, Division Lead Co., Summit, IL.
- [3] Chasman, C.; Jones, K. W.; Ristinen, R. A. Nucl. Instr. Meth. 37, 1 (1965).
- [4] Roy, J.-C.; Cote, J.-E.; Durham, R. W.; Joshi, S. R. J. Radioanal. Nucl. Chem. 130, 221 (1989).
- [5] Chasman, C.; Jones, K. W.; Ristinen, R. A. Phys. Rev. Lett. 15, 245 (1965).

INVESTIGATION OF REPORTED COLD NUCLEAR FUSION

R. M. Lindstrom
(Inorganic Analytical Research Division)

To sustain the thesis of Fleischmann and Pons's (University of Utah) and Jones et al. (Brigham Young University (BYU)) that nuclear fusion has been induced by electrochemical methods [1,2], the observation of neutrons is a necessary confirmation. Four signatures of the fusion process are measurable: tritium generation, helium-3 generation, neutron generation, and energy generation. Neither paper claims to have measured an increase in tritium or ^3He , although the Utah group has made tritium measurements in the

electrolyte and has collected gas samples. Only the Utah group reports the generation of heat. The well-known thermodynamics of the d-d reaction (2×10^{12} neutrons/s per watt) make the heat generated inconsistent, by a factor of 10^9 , with the neutron intensity observed. The only unambiguous diagnostic marker of the fusion process reported is therefore the generation of 2.5 MeV neutrons.

Mere qualitative observation of neutrons is not sufficient to confirm fusion. Only a quantitative measurement statistically and temporally above background can establish that fact. There is quantitative evidence, on the contrary, that the reported observations can be explained simply by cosmic rays and other sources of background. The Utah group detected neutrons by observing the characteristic prompt gamma rays emitted on neutron capture in hydrogen, while the BYU group detected the energetic neutrons directly.

To test the claims of the Utah group, a large (31.4% efficiency relative to 3" x 3" NaI) high-resolution germanium gamma-ray detector was set up at NIST without shielding adjacent to a 70-L cylindrical tank of water. The gamma-ray spectrum (fig. 1) clearly showed the characteristic neutron capture line of hydrogen-1 at 2223.3 keV at 0.0015 ± 0.0002 counts per second (s.d.). This peak, clearly visible after only ten hours counting, was adjacent to a background line at 2204.1 keV at 0.0143 ± 0.0004 c/s from ^{214}Bi , a daughter of ^{238}U through radon.

Judging from a published photograph [3], the geometry of this experiment is comparable to that of the Utah measurement, and differs chiefly in the absence of Utah's electrochemical cell. Figure 1A of the Utah paper [2] is a gamma-ray spectrum showing this region of the spectrum. Their spectrum was obtained with a sodium iodide scintillation spectrometer with a resolution of 50 keV fwhm (measured from the figure): this is very good for NaI, perhaps a record, but still twenty times worse than the NIST Ge detector and insufficient to resolve the hydrogen capture line from ^{214}Bi . The count rate is 0.017 c/s, coincidentally the same as the background observed at NIST for the sum of the two lines. The caption to this figure states that the background is featureless in this region; on the other hand it also appears to say that the background is four times higher than the signal. Internal inconsistencies aside, it appears that it is not necessary to invoke nuclear fusion to explain the "neutron" signal in the Utah paper.

Recent NIST measurements with a low-background gamma detector described elsewhere in this report allow an estimation of the cosmic-ray neutron intensity and energy. From the counting rate of $\text{Ge}(n,n')$ inelastic scattering lines [4] in the background (fig. 2), the neutron flux was found to be $0.02 \text{ n/cm}^2\text{s}$; from the width of these peaks [5] the energy is estimated to be about 2 MeV, just the value of the neutrons produced by the d,d reaction. These fast cosmic-ray neutrons become thermalized and captured in a modest amount of water; the effective thermal flux in a 1-L Marinelli beaker on the detector is $0.02 \text{ n/cm}^2\text{s}$, as measured by the intensity of the 2223 keV capture line.

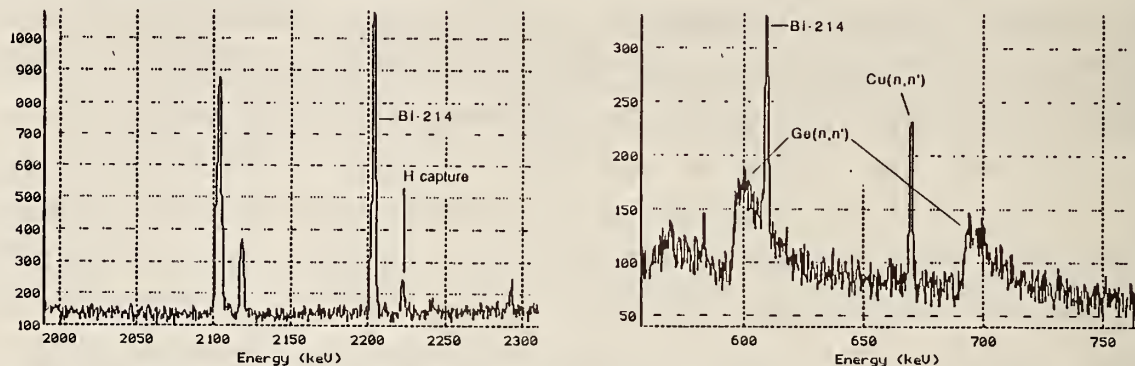


Figure 1. (left) Background spectrum (109 h counting time) of an unshielded high-resolution gamma detector adjacent to a 70-liter tank of tap water. The 2223-keV line from the capture of cosmic-ray neutrons is visible next to the much more intense 2204-keV line from the radon daughter Bi-214.

Figure 2. (right) Broad peaks in the background of a well-shielded gamma-ray detector, caused by inelastic scattering of cosmic-ray neutrons. The width of the peaks gives information on the neutron energy.

The BYU group reports a measured neutron counting rate (their run 6, assuming 0.5 neutrons/fusion) of $4 \times 10^{-3}/\text{s}$ (this number is 100 times larger in the published paper than in the widely circulated preprint version). Their detector has a 150 cm^2 cross section, so the integral cosmic background at Provo should be greater than 3 c/s. They report a background in the 2 MeV region of 10^{-3} c/s , implying excellent energy discrimination. The net signal is thus only twice background. The cosmic-ray neutron flux is highly variable [6]. The neutron flux in Colorado has been observed to rise 500% above normal following a large solar flare. Since we are now beginning a period of high solar activity, one may conclude by Occam's principle that the most likely interpretation of the BYU measurement as well is variability in the neutron detector background, not nuclear fusion.

References

- [1] Jones, S. E.; Palmer, E. P.; Czirr, J. B.; Decker, D. L.; Jensen, G. L.; Thorne, J. M.; Taylor, S. F.; Rafelski, J. *Nature* 338, 737 (1989).
- [2] Fleischmann, M.; Pons, S. J. *Electroanal. Chem.* 261, 310 (1989).
- [3] Pool, R. *Science* 243, 1661 (1989).
- [4] Chasman, C.; Jones, K. W.; Ristinen, R. A. *Nucl. Inst. Meth.* 37, 1 (1965).
- [5] Chasman, C.; Jones, K. W.; Ristinen, R. A. *Phys. Rev. Lett.* 15, 245 (1965).
- [6] Forbush, S. E. *Handbuch der Physik*, Springer-Verlag, Berlin 1966, v. XLIX/1, p. 159.

FACILITIES FOR ACTIVATION ANALYSIS

R. M. Lindstrom and J. K. Langland
(Inorganic Analytical Research Division)

Beginning in 1977, the group has implemented a flexible network of computers to acquire and process data from 21 gamma-ray and charged particle spectrometers (see fig. 1). The system is now in its third generation of multiuser computers, centered on a VAX 11/730 file and peripheral server with a network linking it with two more microVAXs in the group, three additional computer-based multichannel analyzers, nine stand-alone analyzers, and 11 personal computers, with each unit in the system used for the part of the analytical process for which it is best suited. Data are acquired and partially processed on the computer-based analyzers and the VAX, and the data transferred to microcomputers for further statistical interpretation, graphics, and report writing. The group's network is part of a building-wide Ethernet system with seven more minicomputers (operated by the Reactor Radiation Division) and which in turn is linked to the NIST-wide fiber optic data trunk. Two of the group's multichannel analyzers are directly connected to the Ethernet. Progressive growth of the computer capabilities over the past decade has occurred without ever experiencing a break in the group's ability to acquire and process data, and without forcing users to new technology before they are ready to do so.

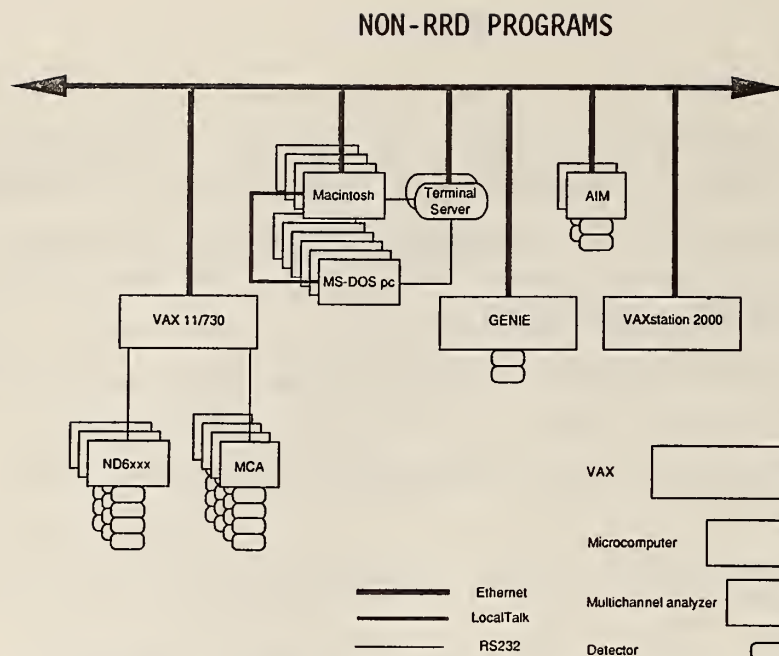


Figure 1. Schematic diagram of the data acquisition and processing network used by the Nuclear Methods Group.

ATMOSPHERIC, ENVIRONMENTAL BIOLOGICAL STUDIES BY INSTRUMENTAL AND NEUTRON-CAPTURE PROMPT γ -RAY ACTIVATION ANALYSIS

G. E. Gordon and J. M. Ondov
(University of Maryland, College Park, MD)

We continue to make considerable use of instrumental neutron activation analysis (INAA) and neutron-capture prompt γ -ray activation analysis (PGAA) for development and testing of the methods themselves and to determine concentrations of about 40 elements in particles, gases, rain, and fog from the atmosphere, in related source materials such as crustal dust and coal fly ash, and in standards appropriate for use in this field. By measuring concentrations of such a large number of species, we are able to identify contributions from certain types of air-pollution sources to the atmospheric burden at ambient sampling sites, a technique now known as "receptor modeling." Also, we are beginning to use neutron activation analysis to observe several isotopes of Zn to determine the presence of a stable isotope tracer in samples from humans. Examples of these studies are briefly discussed in the following sections.

Our activities at the reactor have not been as extensive this year as in the past for two major reasons: (1) the reduced operating schedule of the reactor in connection with installation of the cold neutron facility, and (2)

the fact that an unusually large number of our students had either recently graduated or were writing theses. Over the past 2-1/2 years, nine students have written theses (5 Ph.D. and 4 M.S.). All but one of these students made much use of the reactor during their time in our department, so the reactor has served a vital role in our graduate research program. We are pleased to report that a new group of students is about to begin heavy use of the reactor when the present shutdown ends.

EFFECTS OF NEUTRON SCATTERING BY HYDROGEN ON NEUTRON-CAPTURE PROMPT γ -RAY ACTIVATION ANALYSIS (PGAA)

E. Mackey and G. E. Gordon
(University of Maryland, College Park, MD)

In a continuing effort to improve accuracy in PGAA, we are investigating the effects of neutron scattering by H on PGAA elemental sensitivities. Previous work by Anderson and Cunningham [1] and by Kitto [2] performed at the NIST/University of Maryland PGAA facility [3] has shown increasing elemental sensitivities with increasing H content. Kitto's results indicated that each element is affected differently, with sensitivity enhancements ranging from 1.8 to 4.3% enhancement per wt. % H. The first phase of the present work was designed to measure sensitivity enhancements as a function of H content. The second phase was designed to measure elemental sensitivities in hydrogenous samples as a function of sample size or, equivalently, as a function of the absolute amount of scatterer. The third phase, now in progress, is designed to measure sensitivity vs. sample shape.

Sensitivities for 11 elements were measured over a broad range of H concentrations. For each element, an aqueous and a D₂O standard solution were prepared from a salt of the element. A series of samples ranging in H concentration from 0 to 11% H (i.e., 100% D₂O to 100% H₂O) were prepared by mixing appropriate amounts of the two stock solutions. Sample volume and shape were constant (400 μ L in a 1.5- x 1.5-cm Teflon bag). Gamma rays emitted by the samples were collected during irradiations of up to 3 hrs. The results, shown in table 1, indicate that most elements studied undergo about the same amount of enhancement. The most notable exception is Sm, for which the enhancement is only about one-fourth that of the other elements studied. If neutron scattering results in a slight shift of the energy

distribution towards lower energy, the effective absorption cross section for Sm would be decreased due to the broad absorption resonance at 0.09 eV in ^{149}Sm . This provides a possible explanation for the anomalous enhancement behavior of Sm, although further investigation is needed.

Table 1. Enhancement of elemental sensitivities in PGAA with increasing hydrogen concentration

Element	% Enhancement/wt. %H	Element	% Enhancement/wt. %H
B	1.90 ± 0.15	Ag	1.65 ± 0.20
Na	2.47 ± 0.29	Cd	1.43 ± 0.17
Cl	1.73 ± 0.20	I	1.90 ± 0.18
K	2.13 ± 0.13	Sm	0.54 ± 0.074
Mn	2.90 ± 0.26	Gd	1.57 ± 0.14
Br	2.18 ± 0.20		

In the second phase of study, a series of disk-shaped pellets of 1.27-cm diam and varying thickness were prepared from each of several hydrogenous Standard Reference Materials (SRM 1571 Orchard Leaves, SRM 912 Urea, SRM 922 Tris-hydroxymethylaminomethane). Thicknesses ranged from 0.5 to 10 mm. Spectra of these samples were collected during irradiations of up to 6 h. Results from these experiments indicate that sensitivities increase with decreasing sample thickness as shown, for example, for B in SRM 1571 in figure 1. Similar behavior is observed for K and H in SRM 1571, and for H in both SRM 912 and 922. These findings are consistent with the theoretical work of Copley and Stone [4]. By use of Monte Carlo calculations, they show that, in a scattering matrix, the mean path length of the neutron is increased relative to the path length in a non-scattering matrix.

Preliminary work in the third phase of this study has indicated that the use of spherical samples may eliminate scattering-induced sensitivity enhancement. A comparison was made between sensitivities obtained for Cl in spherical and in disk-shaped samples of the same material. Sensitivities decrease with increasing sample size for the disk-shaped samples of constant diameter and ranging in thickness from approximately 0.1 to 1 cm. However, sensitivity is constant within $\pm 2\%$ for spherical samples ranging in mass from 0.25 to 1.6 g (or, in diam, from 0.8 to 1.4 cm). Further work in this area is in progress.

NON-RRD PROGRAMS

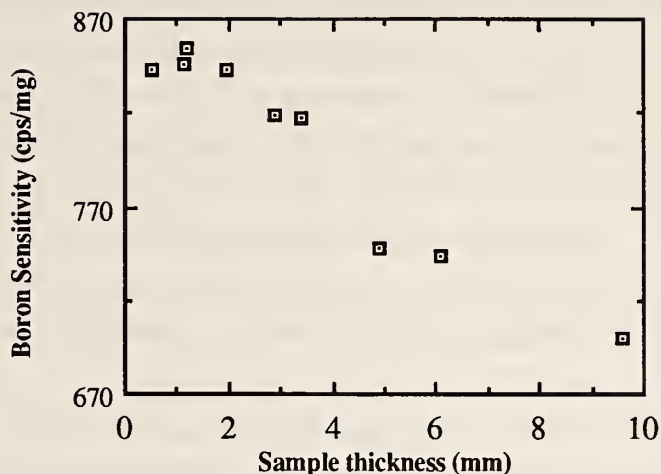


Figure 1. Boron sensitivity in SRM 1571 Orchard Leaves as a function of sample thickness.

References

- [1] Anderson, D. L.; Cunningham, W. C. Presented at the International Conf. on Nuclear Analytical Methods in the Life Sciences, Natl. Inst. Stand. Technol., Paper A47, April 1989. Biol. Trace Elem. Res. (submitted for publication).
- [2] Kitto, M. E., Ph.D. thesis, Department of Chemistry and Biochemistry, University of Maryland, College Park, 1987.
- [3] Anderson, D.L.; Failey, M. P.; Zoller, W. H.; Walters, W. B.; Gordon, G. E.; Lindstrom, R. M. J. Radioanal. Chem. 63, 97-119 (1981).
- [4] Copley, J.; Stone, C. Nucl. Instrum. Meth (submitted for publication).

SUBMICROMETER SIZE DISTRIBUTIONS OF AIRBORNE PARTICLES BEARING VARIOUS TRACE ELEMENTS

J. M. Ondov, J. A. Dodd, and G. Tuncel
(University of Maryland, College Park, MD)

Knowledge of the composition and size distributions of atmospheric fine particles is important because these parameters govern respirability, deposition, nucleation of water vapor, and light scattering. Submicrometer particles are of special interest, as they are respirable, have long atmospheric residence times, and are frequently enriched in potentially toxic species. Trace elements borne by these particles are also useful for apportioning sources and tracking air masses over long distances.

Despite the importance of this information, reliable measurements of the distributions of major, minor, and trace constituents of the submicrometer aerosol have been limited. Most ambient sampling is done with either "whole" filter samples or with dichotomous samplers, which fractionate particles into "fine" and "coarse" particles (typically, < 2.5 - and 2.5 - to 10 - μm diam groups, respectively [1]). Chemical characterization of size-segregated submicrometer particles has been limited to measurements of sulfate, carbon, major ions such as sulfate and ammonium, and a few elements that can be observed with x-ray fluorescence (XRF).

The lack of high quality elemental composition data for size-classified submicrometer aerosol has been due in part to the lack of reliable samplers capable of providing sufficient quantities of size-segregated particles in this range for detailed analysis. Fractionation into several size groups is usually done with cascade impactors. For some time, they were limited to sizing particles above about 0.4 - μm in diam. This limit was extended to ~ 0.05 μm by operation at greatly reduced pressures, but at the expense of high (near sonic) jet velocities conducive to particle bounce [2-4]. Despite this advance, applications have been limited because of impractical pumping requirements, low flow rate, and particle-bounce problems.

In 1981 Kuhlmei et al. developed an impactor capable of sizing submicrometer particles at modest pressure drops (i.e., about 250 Torr for 0.06 - μm minimum size cut) and modest jet velocities (127 m/s for 0.09 - μm cut) using micro-orifice technology [5]. The impactor's low-pressure drop and 28 -L/min flow rate permit collection of samples suitable for trace analysis with a standard air-sampling pump.

We have tested the micro-orifice impactor (MOI) by field collections of particles at a rural site in Western Maryland near Deep Creek Lake, as part of a larger study of air pollution during the summer of 1983 [6]. Most samples were collected between August 1-31, 1983, with sampling periods ranging from 6 to 24 h. The MOI was horizontally configured and equipped with a cyclone pre-collector and an external 37 -mm after-filter as described by Kuhlmei et al. [5]. Cutoff diameters for the stages ranged from about 1.0 to 0.08 μm and the cyclone removed particles down to 3 - μm diameter.

Impactor collection surfaces and the after-filters from seven out of the 60 sample sets were analyzed by INAA at the NBS reactor using a combination of 10-min followed by 3-h irradiations, each followed by taking of two γ -ray

spectra of samples and appropriate flux monitors and standards irradiated along with the samples using Ge detectors [7].

Concentrations of a minimum of 26 elements, including Al, As, Br, Ca, Ce, Cl, Co, Cr, Fe, K, La, Mg, Mn, Na, Se, Sb, V, Ti, and Zn could be detected on at least three of five submicrometer impactions stages, i.e., enough data to estimate the mean diameters and standard deviations of the size distributions of particles bearing those elements. Examples of the "raw" size distributions for Al and V resulting from six experiments are shown in figure 2. There are clear differences in these distributions, as expected, since Al mostly arises from crustal sources, whereas V often has additional high temperature such as oil-fired power plants and steel plants.

Only because of the high sensitivity of instrumental neutron activation analysis (INAA) with the large flux of the NIST reactor was it possible to observe so many elements with a total fine particle loading of only 180 μg . Detection on more stages was generally achieved with loadings of 240 to 400 μg . However, evidence for particle bounce was observed when loadings were > 1 mg. Despite the use of thin, high purity Teflon impaction surfaces, detection of Ag, Cu, Gd, Hf, I, In, Nd, Sc, Sm, Ta, Th, W, and Yb was frequently limited by their concentrations in substrate blanks in polyethylene packaging materials used in the analyses. Bromine loss during sample storage and extended neutron irradiation is also evident. The results of these analyses demonstrate the feasibility of determining size-distribution functions for many important minor and trace elements present in ambient aerosol. We anticipate that similar or better results will be achievable in more polluted urban areas with shorter sampling times.

A manuscript describing the experimental work has been submitted for publication [8]. We are now applying deconvolution procedures to the raw size spectra to remove the effects of the nonsharp collection-efficiency curves to obtain the inherent size distributions, which will be published later.

NON-RRD PROGRAMS

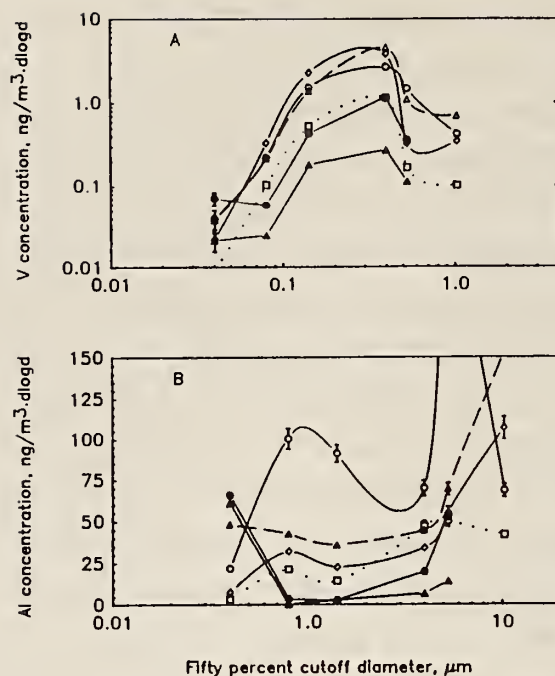


Figure 2. Size-distribution functions for Al and V obtained by irradiation of collection surfaces and after-filter from micro-orifice impactor experiments.

References

- [1] Dzubay, T. G; Stevens, R. K.; Gordon, G. E.; Olmez, I.; Sheffield, A. E.; Courtney, W. J. Environ. Sci. Technol. 22, 46-52 (1988).
- [2] McFarland, A. R; Nye, H. S.; Erikson, C. H. Development of a low pressure impactor. U.S. Environmental Protection Agency Report No. EPA-650/2-74-014.
- [3] Pilat, M. J.; Powell, E. B.; Carr, R. C. APCA J. 4, 35 (1977).
- [4] Hering, S. V.; Flagan, R. C.; Friedlander, S. K. Environ. Sci. Technol. 12, 667 (1978).
- [5] Kuhlmei, G. A.; Liu, B. Y. H.; Marple, V. A. Amer. Indust. Hyg. Assn. J. 42, 790 (1981).
- [6] Vossler, T. L.; Lewis, C. W.; Stevens, R. K.; Dzubay, T. G.; Gordon, G. E.; Tuncel, S. G.; Russwurm, G. M.; Keeler, G. J. Atmos. Environ. 23, 1535 (1989).
- [7] Germani, M. S.; Gökmen, I.; Sigleo, A. C.; Kowalczyk, G. S.; Olmez, I.; Small, A.; Anderson, D. L.; Failey, M. P.; Gulovali, M. C.; Choquette, C. E.; Lepel, E. A.; Gordon, G. E.; Zoller, W. H. Anal. Chem. 52, 240-245 (1980).
- [8] Ondov, J. M.; Dodd, J. A.; Tuncel, G. Nuclear analyses of trace elements in size-classified submicrometer aerosol particles from a rural airshed. Aerosol Sci. Technol. (submitted for publication).

CALIFORNIA AIR RESOURCES BOARD AIR-FILTER SAMPLES

M. Han, A. Mizohata, and G. E. Gordon
(University of Maryland, College Park, MD)

To test the quality of our analyses, we occasionally participate in "blind, round-robin" analyses of new standards or particular kinds of samples. Recently we analyzed six air filters containing atmospheric particles collected in California and three blank filters. This study was done for the California Air Resources Board (CARB) to check on laboratories that were doing x-ray fluorescence (XRF) analyses of large numbers of samples collected as part of a major study of air pollution in the Los Angeles airshed. Four laboratories had analyzed most of the same samples by XRF before we received them, but we did not receive their results until we reported our values. We were the only group to do instrumental neutron activation analysis (INAA).

Table 2 shows a representative comparison of four sets of results for a sample containing particles with diam $< 10 \mu\text{m}$, i.e., fine and coarse particles. Most XRF analysts do not report data for elements as light as Na and Mg because corrections for self-absorption of their very soft x-rays are large and uncertain; thus, the agreement for those reported is surprisingly good. Corrections even for Al are large and only the EPA/NSI XRF result agrees with our INAA value, which should be quite accurate. We don't measure S well, as indicated by the large assigned error. There was considerable spread in the Cl values, possibly because of variable losses of volatile Cl species. Our Ca value is not very precise and appears to be lower than the XRF values.

Iron and K should be measurable with comparable reliability by both INAA and XRF. Except for the EPA/NSI data, the XRF values are greater than ours outside of the quoted errors. This may reflect a concern that was a major reason for having us perform INAA: the dichotomous sampler, with which these samples were collected, produces a nonuniform deposit with greater deposition in the center of the filter. Furthermore, some XRF instruments have a greater x-ray intensity in the center of the irradiating beam. The combination of nonuniform deposits and beams would yield greater apparent masses of elements on the filters. The fact that Fe and K XRF values are greater than ours suggests that this was a problem, as INAA is a bulk measurement, not dependent on the uniformity of the deposit.

NON-RRD PROGRAMS

Table 2. Comparison of CARB INAA and XRF results for filter MK-948

Element	This Work		(ng/filter)					ARB-NEA-STI	EPA/NSI
			NEA	DRI					
Na	10000 ±	500						No	7215 ± 914
Mg	2950 ±	1250						Errors	2597 ± 179
Al	6800 ±	700	9600 ±	1450	18201 ±	5349			5262 ± 298
S	66000 ±	23000	14100 ±	900	13670 ±	73	13872		13824 ± 702
Cl	1500 ±	250	2230 ±	200	1501 ±	433	952		1376 ± 82
K	3000 ±	400	4900 ±	260	4464 ±	866	3810		3473 ± 178
Ca	5900 ±	1000	11800 ±	600	11217 ±	1799	8571		9658 ± 507
Ti	1000 ±	165	2200 ±	115	1539 ±	77	1520		1635 ± 105
V	31.7 ±	2.0	73 ±	25	81 ±	107	96		<90
Cr	85 ±	6	160 ±	15	140 ±	10	115		910 ± 57
Mn	210 ±	12	330 ±	23	304 ±	13	250		<250
Fe	8700 ±	600	14000 ±	730	11063 ±	42	11121		10967 ± 693
Cu	380 ±	80	425 ±	25	345 ±	7	241		321 ± 106
Zn	400 ±	90	980 ±	50	788 ±	9	683		772 ± 139
As	8.5 ±	0.7	<70		<200	0			330 ± 150
Se	20 ±	4	24 ±	6	18 ±	5	29		<1600
Br	140 ±	15	245 ±	15	200 ±	7	144		<430
Sb	19.6 ±	1.1	<230		<185				<6600

INAA values for Ti, V, and Cr were lower than the XRF values in most samples. We would be most surprised if we were wrong on these elements, especially V and Cr. In previous comparisons we have made with XRF on the same samples [1-3], we have often found that XRF yields higher apparent values than INAA for trace elements whose x-rays fall among those of minor and major elements, here K, Ca, and Fe. Perhaps software used to extract net peak areas does not completely remove tails of the large peaks. In addition, there are specific interferences between elements, e.g., L lines of Br, Ba, and Pb fall under the K lines of Al, V, and As, respectively. There is usually enough Pb in atmospheric samples that one cannot measure As reliably. The problem of Ba interference with V is subtle in that the interference can be significant even when the Ba K line cannot be measured reliably.

Although the agreement for Mn is not outstanding for the example in table 2, it is surprisingly good for most samples. Some of the As, Se, and Sb XRF values also agree reasonably well with INAA, despite their low concentrations. As in previous comparisons, [1-3] our INAA values for Br are lower than those from XRF, which are usually reliable. We have previously speculated that there are slow losses of volatile Br species to the gas phase. Since we are always the last group to analyze the samples, if this

hypothesis is correct, the samples contain less Br by the time we get them. However, it is also possible that we lose Br during irradiations.

This exercise strengthens our belief that one should occasionally participate in blind, round-robin comparisons. As the present exercise did not include other INAA studies, we were unable to check the masses of many additional elements for which XRF provided no values. Furthermore, when there were disagreements, it wasn't always clear which group(s) were wrong. The exercise should have been more valuable to the XRF groups. Not only did they often disagree with our values, but they often have disagreements with each other well outside of their stated errors. In the past, they have often done intercomparisons using standards that are ideal for XRF, e.g., very thin, uniform films with only one or two elements per standard [4], for which various XRF analysts obtain much better results than for the "real world" samples analyzed here.

References

- [1] Dzubay, T. G.; Stevens, R. K.; Gordon, G. E.; Olmez, I.; Sheffield, A. E.; Courtney, W. J. Environ. Sci. Technol. 22, 46-52 (1988).
- [2] Tuncel, S. G.; Olmez, I.; Parrington, J. R.; Gordon, G. E.; Stevens, R. K. Environ. Sci. Technol. 19, 529-537 (1985).
- [3] Hermann, D.; Ph.D. thesis, Department of Chemistry and Biochemistry, University of Maryland, College Park, 1988.
- [4] Dzubay, T. G.; Morosoff, H.; Whitaker, G. L.; Yasuda, H.; Bazan, F.; Bennett, R. L.; Cooper, J.; Courtney, W. J.; Frazier, C. A.; Gatti, R. C.; Germani, M.; Gordon, G.; Hanamura, S.; Kellogg, R. B.; Rhodes, J. R.; Schindler, J. S. J. Trace and Microprobe Tech. 5, 327-341 (1988).

STABLE ISOTOPE TRACING OF ZINC IN INFANTS

S. H. Harrison, O. J. Chitale, T. Quinn, and G. E. Gordon
(University of Maryland, College Park, MD)

Much has been learned about the absorption and subsequent behavior of trace elements in human beings by administration of radioactive tracers, which can be observed both in vivo and in samples collected from the body, e.g., feces, urine, and blood. However, because of the radiation exposure, these convenient, definitive tracers cannot be used for study of some of the most important population groups at risk of trace element deficiencies: pregnant women and infants. For this reason, enriched stable isotope tracers

have come into wide use during the past decade. One administers a sample of the element in which a minor isotope has been enriched to nearly 100%. The appearance of the tracer is observed by an increase of the abundance ratio of the tracer isotope relative to another stable isotope. Isotopic ratios are normally measured by mass spectrometry, but in favorable cases one can observe two or more isotopes via their neutron irradiation products. We have been doing tracer studies of Zn using stable ^{70}Zn , whose natural abundance is about 0.6%, for which enrichments up to about 80% are used as the tracer. Three stable Zn isotopes have observable neutron irradiation products: ^{244}d ^{65}Zn , 14-h $^{69\text{m}}\text{Zn}$, and 4-h $^{71\text{m}}\text{Zn}$ from stable ^{64}Zn , ^{68}Zn , and ^{70}Zn , respectively. In earlier work involving the NIST reactor, we verified the use of stable ^{70}Zn tracer by simultaneously using it with radioactive ^{65}Zn in vivo tracer in adult volunteers. This work has been submitted for publication [1,2].

Over the past 2 years, we have been using the method to study Zn nutrition in various classes of newborn infants: pre-term, normal, and low birth-weight full-term. This study is being conducted in cooperation with Drs. K. Sivasubramanian and M. Wastney of Georgetown University Medical Center, using subjects from Georgetown's neonatal unit. Depending on how the infant is being fed, the ^{70}Zn is administered orally or intravenously. Samples of urine, feces, red blood cells (RBC), and plasma are collected at various times after administration. Because of the enormous activities of irradiation products of Na, K, Cl, and Br that would be formed by irradiation of the raw samples, we must perform extensive pre-irradiation chemistry to produce reasonably pure Zn samples in which γ rays of 14-h $^{69\text{m}}\text{Zn}$ and 4-h $^{71\text{m}}\text{Zn}$ can be observed soon after irradiations.

Studies of infants are much more difficult than those of adults. Although the amounts of feces available are usually adequate, very small quantities of the others, especially RBC and plasma, are available. Typically 1 mL of blood is taken per sample vs. 10 mL from adults. Careful attention by nurses is needed to prevent mixing of urine and feces. Usually samples can be collected only as long as the infant remains in the neonatal unit (typically 1 week), whereas adult volunteers can be asked to provide samples for as long as the experiment requires.

Despite these difficulties, we have begun to obtain results. Tracer experiments have been conducted with seven infants, of which final results

are available for two infants. Results obtained from the feces samples from two cases are shown in figure 3. The fraction of tracer appearing versus the days following administration are shown. For the first case, the only significant amount outside of errors appears on Day 5, about 1.5% of the tracer, at which time the experiment was terminated when the infant was released. Results for Case 2 were much better, as several samples contained significant amounts of tracer, the maximum being 10% in one sample from the second day. Many additional samples have been separated and are awaiting start-up of the reactor for irradiation. Dr. Wastney is subjecting the results to kinetic analyses as they are obtained.

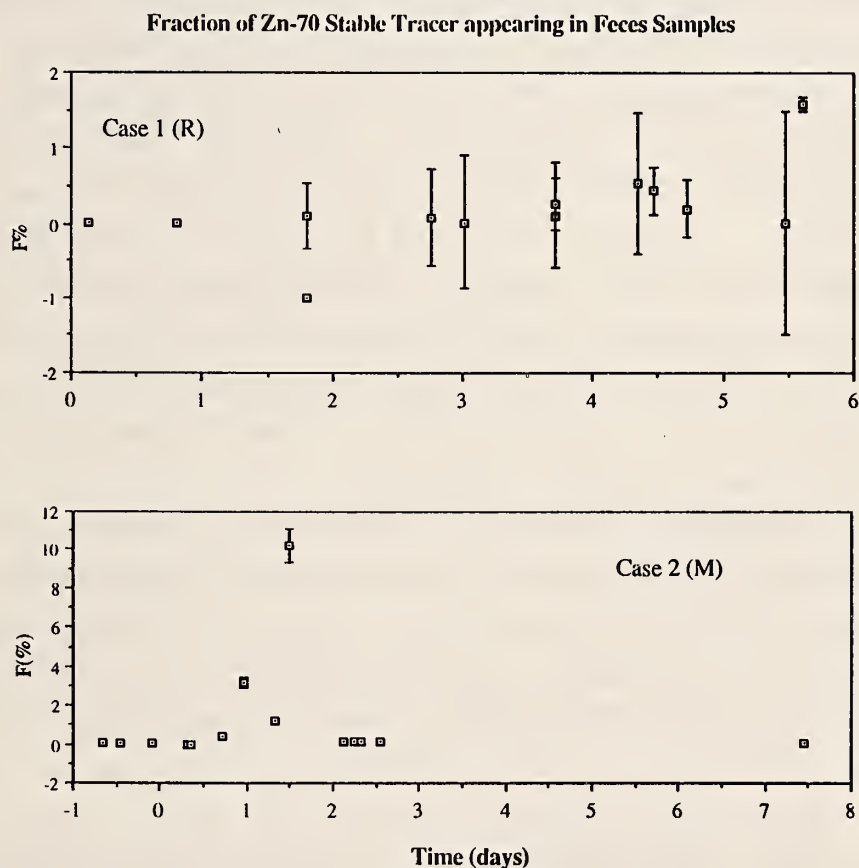


Figure 3. Fraction of stable ^{70}Zn tracer appearing in feces from two infants vs. day.

References

- [1] Gökmen, I. G.; Aras, N. K.; Gordon, G. E.; Wastney, M. E.; Henkin, R. I. Anal. Chem. (in press).
- [2] Wastney, M. E.; Gökmen, I. G.; Aamodt, R. L.; Rumble, W. F.; Henkin, R. I.; Gordon, G. E. Am. J. Physiol. (submitted for publication).

INVESTIGATION OF THE GAMMA-RAY SPECTRUM FOR THE
 $^{128}\text{Te}(\text{n},\text{g})$ and $^{130}\text{Te}(\text{n},\text{g})$ REACTIONS

C. Ford, P. F. Mantica, Jr., B. E. Zimmerman, and W. B. Walters
(University of Maryland, College Park, MD)

and

C. A. Stone
(Center for Analytical Chemistry)

We have made an initial attempt to determine the spectrum of gamma rays following neutron capture on the two heavy stable Te nuclides, ^{128}Te and ^{130}Te . Te is an element whose isotopes do not have large cross sections for neutron capture and is not generally observed in trace element analysis. The structure of the daughter nuclides ^{129}Te and ^{131}Te has been studied in numerous radioactive decay investigations and in a variety of transfer reaction measurements, but still has not been fully accounted for in theoretical models. Literature concerning the spectrum of capture-gamma rays is also sparse and quite incomplete. At low energies, both nuclides have $1/2^+$ levels that are populated rather strongly in (n,γ) reactions by cascades through levels in the 2 to 3 MeV range. Consequently, these nuclides are important candidates for determination in prompt gamma ray activation analysis (PGAA) using coincidence techniques.

The use of coincidence techniques for determining additional elements in PGAA would be important for elements that are not now regularly determined by singles counting. For the technique to be suitable, the element under study should have one or two major cascades of two or three gamma rays from the capture state to the ground. Important factors in determining the sensitivity of the method will be the detection efficiencies and gamma-ray intensities. Because these nuclides have both high and low energy gamma rays that appear to carry significant portions of the decay, these measurements to make a better accounting for the capture-gamma-ray spectrum itself are a first step in developing possible coincidence methods for their determination by coincidence counting in PGAA.

NON-RRD PROGRAMS

FUNDAMENTAL PHYSICS

Dr. Geoffrey Greene
(Center for Atomic, Molecular, and Optical Physics)

The Fundamental Neutron Physics Program at the NIST Cold Neutron Research Facility includes research in particle physics, basic nuclear physics, and neutron interferometry. It is a collaborative effort involving personnel from the Reactor Radiation Division, as well as from other organizational units within the National Measurement Laboratory, including the Quantum Metrology Division, Center for Atomic, Molecular, and Optical Physics; and the Neutron Interactions and Dosimetry Group, Center for Radiation Research. This work has a strong collaborative character with contributions from other institutions including the University of Missouri, Los Alamos National Laboratory, the University of Sussex (U.K.), and Harvard University. In addition, this work receives support from the Department of Energy and NATO.

This year considerable effort has gone into the design and initial construction of the Neutron Interferometry Position at the Cold Neutron Facility. This work has included detailed analysis of the vibration isolation system as well as the completion of the design for the first stage of seismic isolation.

In the area of nuclear and particle physics, significant work has gone into an experimental effort to determine the half-life of the neutron. Very successful preliminary runs were carried out at the Institut Laue Langevin in Grenoble, France. This experiment will be installed on guide #6 at the NIST facility as the initial instrument on the fundamental physics end position.

NEUTRON ACTIVATION ANALYSIS AT THE FOOD AND DRUG ADMINISTRATION

D. L. Anderson, W. C. Cunningham, and E. A. Mackey
(U.S. Food and Drug Administration, Washington, DC)

The Food and Drug Administration (FDA) maintains a neutron activation analysis (NAA) facility in the reactor building of NIST. This facility is directed by FDA's Center for Food Safety and Applied Nutrition and provides agency-wide analytical support for special investigations and applications research. NAA complements other analytical techniques used at FDA and serves

NON-RRD PROGRAMS

as a reference technique and confirmatory quality assurance (QA) tool. Instrumental, neutron-capture prompt- γ , and radiochemical NAA procedures (INAA, PGAA, and RNAA, respectively) continue as the prime analytical approaches. This combination of nuclear techniques enables diverse multielement information to be obtained for foods and related materials.

Methods development and applications research is a continuing FDA effort to improve overall analytical capabilities. During this past year approximately 30 food and biological standards were analyzed to continue accumulation of general analytical information on foods and related materials. The standards were from NIST, Japanese National Institute for Environmental Studies (NIES), International Atomic Energy Agency (IAEA), and U.S. Department of Agriculture (USDA). Related work included efforts to promote the generation of biological reference material. FDA's NAA facility participated in certification of 13 food reference materials in collaboration with USDA, Agriculture Canada, and NIST. Matrices included a mixed diet and 12 individual biological materials. In a cooperative effort between FDA, the University of Maryland, and NIST, several PGAA experiments have been designed to characterize matrix effects due primarily to the presence of hydrogen. During the past year, the relationship between boron sensitivity and hydrogen content was measured for several matrices. As shown in figure 1, B sensitivity (i.e., c/s-mg) increases with increasing weight percent H for both solid and liquid prepared standards.

Other matrix-effect studies using standard H_2O/D_2O solutions were carried out to show the sensitivity behavior of H, Cl, K, Na, I, Br, Mn, Ag, Cd, Sm, and Gd as a function of hydrogen content. Enhancements are also observed for these elements, but the degree of enhancement (for a given H concentration) varies significantly.

PGAA and INAA freeze-drying loss studies on mixed food composite materials were initiated during the past year. These composites are mixtures of a large number of foods and beverages derived from either the FDA Total Diet Study or the USDA Mixed Diet Study. Two of the composite materials studied are also being issued by NIST in dried form as reference materials. These are RM 8431a Mixed Diet from the USDA Mixed Diet Study and SRM 1548 Total Diet from the FDA Total Diet Study. The possibility of element loss during the freeze-drying of these previously dried materials was studied here relative to the QA value of these matrices. Because the neutron flux used

for PGAA is very low, radiation damage is negligible and the technique is essentially non-destructive. Analytical portions can be analyzed, freeze-dried, and then re-analyzed to monitor for element losses. In work done so far, no freeze-drying losses are observed for B, C, N, Na, S, Cl, and K in either RM 8431a or SRM 1548. Preliminary measurements for wet diet composites, however, indicate that approximately 30% of the boron is lost during the freeze-drying process. Thus, it appears that none of these elements are lost after the initial freeze-drying; i.e., with subsequent freeze-drying of previously dried material. On the other hand, the initial freeze-drying operation appears to result in potential boron loss. Because freeze-drying may be widely employed, it is important to understand such losses in order to accurately reflect the elemental content of original wet-weight samples. NAA and additional PGAA are under way to explain these findings and to look for other element losses.

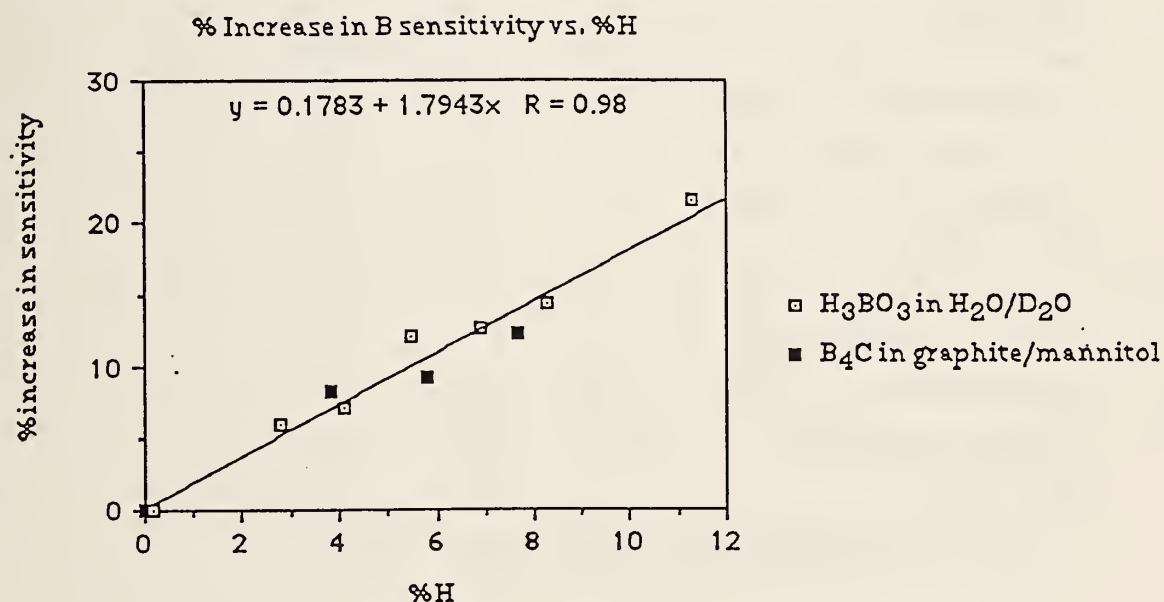


Figure 1. Effect of hydrogen content on Boron sensitivity.

GERMANIUM DETECTOR OPTIMIZATION OF MDA FOR EFFICIENCY VS. LOW INTRINSIC BACKGROUND^[1]

D. R. Brown and L. A. Slaback
(Occupational Health and Safety Division)

The efficiency and minimum detectability characteristics of four intrinsic germanium (InGe) detectors were evaluated as a function of sample type; e.g., small point, a 200 ml cylindrical container, and two marinelli geometries (1 liter and 3.5 liter). Of particular interest is the performance of these detectors in determining reactor activation and fission products in environmental samples. The detectors and shields used are shown in tables 1 and 2.

Table 1. Detector characteristics

Detector Parameters	HP1	HP2	Ty*	HP3
Nominal Efficiency	21%	45%	45%	30%
Ge Crystal Diam (mm)	56	68	59	54
Ge Crystal Length (mm)	41	61	79	70
Ge Dead Layer (mm)	1	.6	.7	.7
End Cap Material	Al	Al	Mg	Al
End Cap Thickness (mm)	0.5	1	1	1
End Cap - Crystal (mm)	5	5	3	3
End Cap Diam (mm)	75.0	86.5	86.5	75.0
Low Bkg Construction	No	No	Yes	No
Shield Used	A	B	C	B

*has added background reducing design features

Table 2. Shield parameters

Shield	Lead Sides	Top	Liner	Design
A	6"	6"	.06" Cu	cube, cast lead,
B	4"	4"	.06" Cd, .06" Cu	cylindrical, cast lead
C	6"	4"	.5" Cu	stacked lead bricks

NON-RRD PROGRAMS

The efficiency was determined and the minimum detectable activity (MDA) was calculated for all geometries and over a range of energies from 80 keV to 1.6 MeV. For bulk environmental samples, e.g., the Marinelli geometries, the MDA results were notable for their similarity. Most important is the need to optimize the sample geometry for the particular detector being used. A properly sized sample container of the 20% detector out-performed the 45% detectors.

Reference:

- [1] Brown, D. R.; Slaback, L. A. Germanium detector optimization of MDA for efficiency vs. low intrinsic background. Proceedings of Topical Meeting on Instrumentation, 4-8 December, 1988, Health Phys. Soc. pp. 46-52.

C. REACTOR OPERATIONS AND ENGINEERING SERVICES

REACTOR OPERATIONS AND SERVICES

T. Raby, J. Torrence, J. Ring, and N. Bickford

Construction of the new Cold Neutron Research Facility continues to require significant reactor shutdowns that will extend into the coming years. Accordingly, this year the reactor was on-line 56% of the time equivalent to 48% full power operation which comprised essentially all available operating time. Operations were the smoothest of any year with no unscheduled shutdowns of any significance.

The repair of the thermal shield cooling system using a new leak sealing method developed by the National Nuclear Corporation of England was partially successful. The method requires repeated applications of the sealant, on the average of twice a year, for the sealant to hold in a high radiation environment and to withstand temperature fluctuations. All past repairs were scheduled so as not to interfere with reactor operation.

The existing main heat exchangers continue to require extreme care and careful maintenance. As yet, a very small leak, on the order of a few drops a minute, could not be found. New, more reliable heat exchangers are in the procurement stage and are not expected to be ready before the end of 1990.

Extensive negotiations with the Department of Energy (DOE) were undertaken to assure future supplies of both nuclear fuel and heavy water. Nuclear fuel is now on an accelerated fabrication schedule that will guarantee a current reserve of at least 5 years. Immediate heavy water needs will be met by DOE. However, future supplies will have to await further negotiations with DOE and the Canadian Government since heavy water is in critically short supply.

The small operating staff continues to perform double duties, operation and engineering. The latter includes design, installation, quality control, testing, repair, and maintenance. Of the total 16 operators at the beginning of the year, 15 held senior operator licenses, and one trainee also qualified and obtained a senior license making the NIST reactor the only reactor in its class with all operators holding a senior level license. More recently one senior operator transferred to the Health Physics Group but will continue to maintain his license. A new trainee was just hired to replace him.

REACTOR OPERATIONS AND ENGINEERING SERVICES

A summary of the operating statistics for the past year follows. Fuel utilization continues to be the best in the country.

No. of equivalent days at 20 MW	175
Equivalent on-line time at 20 MW	48%
Average U-235 burnup	66%
No. of irradiations	1160
Hours of irradiations	4900
Hours per irradiation	4.2

The same program of reactor irradiations continued. Irradiation services were provided to many organizations from within and outside NIST covering wide areas of research, applications, and standards.

REACTOR OPERATIONS AND ENGINEERING

J. H. Nicklas and R. S. Conway

Design and engineering services were provided, on a regular basis, to reactor operations and the research groups throughout the year. They included successful resolution of several complex problems that occurred which otherwise would have resulted in lengthy delays. An example of this was the timely determination of the cause of malfunction during testing of control rod drive No. 2 which was extremely hard to locate or even duplicate. The corrective steps taken assured reliable operation and permitted the reactor to start-up on schedule.

There were nine major projects that were undertaken in addition to regular engineering services. These include:

Specifications for Replacement Heat Exchangers. The specifications for more reliable heat exchangers for the primary and auxiliary systems were computed using the latest in design materials, fabrication, testing and quality assurance innovations and techniques. The new design will assure a close to zero leakage as possible over the lifetime of the units. Procurement will begin later this year.

REACTOR OPERATIONS AND ENGINEERING SERVICES

Nuclear Fuel Fabrication. The first group of advanced heavier loaded fuel elements were qualified and accepted. Accordingly, all future elements will further improve fuel utilization by at least 10% and as much as 20% a significant cost saving in addition to reducing the number of refueling outages.

Control Rod Fabrications. The NBSR control rods are the only ones of their kind in the United States with a very unusual design. The original components were hand-crafted at Argonne National Laboratory. Since the shutdown of CP-5 a decade ago, the only expertise left resides with the current engineering staff at the reactor. As a consequence, an ambitious program was undertaken to have enough complete control rod assemblies, ready for installation, to last for the term of the current license or until 2004. This program will be completed over the next 2-3 years prior to the expected retirement of the principals involved. Less experienced engineers are also being trained to assume this responsibility in the future.

Thermal Shield Cooling System. Together with Reactor Operations, extensive maintenance and repair were carried out on this system. Initially 40 of 200 tubes suspected of leaks were treated using the special method developed by the National Nuclear Corporation of England. The treatment was repeated on 25 tubes and will be repeated again several times in the future. Experience has shown that several applications are needed to fully seal the leaks, however, improvements were noted with each application.

Secondary Auxiliary and Experimental Cooling System. A complete redesign of this system to provide for significantly increased cooling capacity was completed. The current capacity is inadequate because of the increased number of components served by the system. The new design separates this system from the main cooling system, thereby improving the main system's cooling capacity as well.

Monitors. Back-ups to two existing crucial monitors were designed and are in the process of being installed. A second N-16 monitor was incorporated into a complete redesign of the secondary coolant monitoring system. The new design will return possibly contaminated water back to the system rather than discharging it to the environment and will provide redundancy in the early detection of heat exchanger leaks during reactor operation. A second extended range stack effluent radiation monitor was designed and installed. The new monitor will not only serve as a back-up to

REACTOR OPERATIONS AND ENGINEERING SERVICES

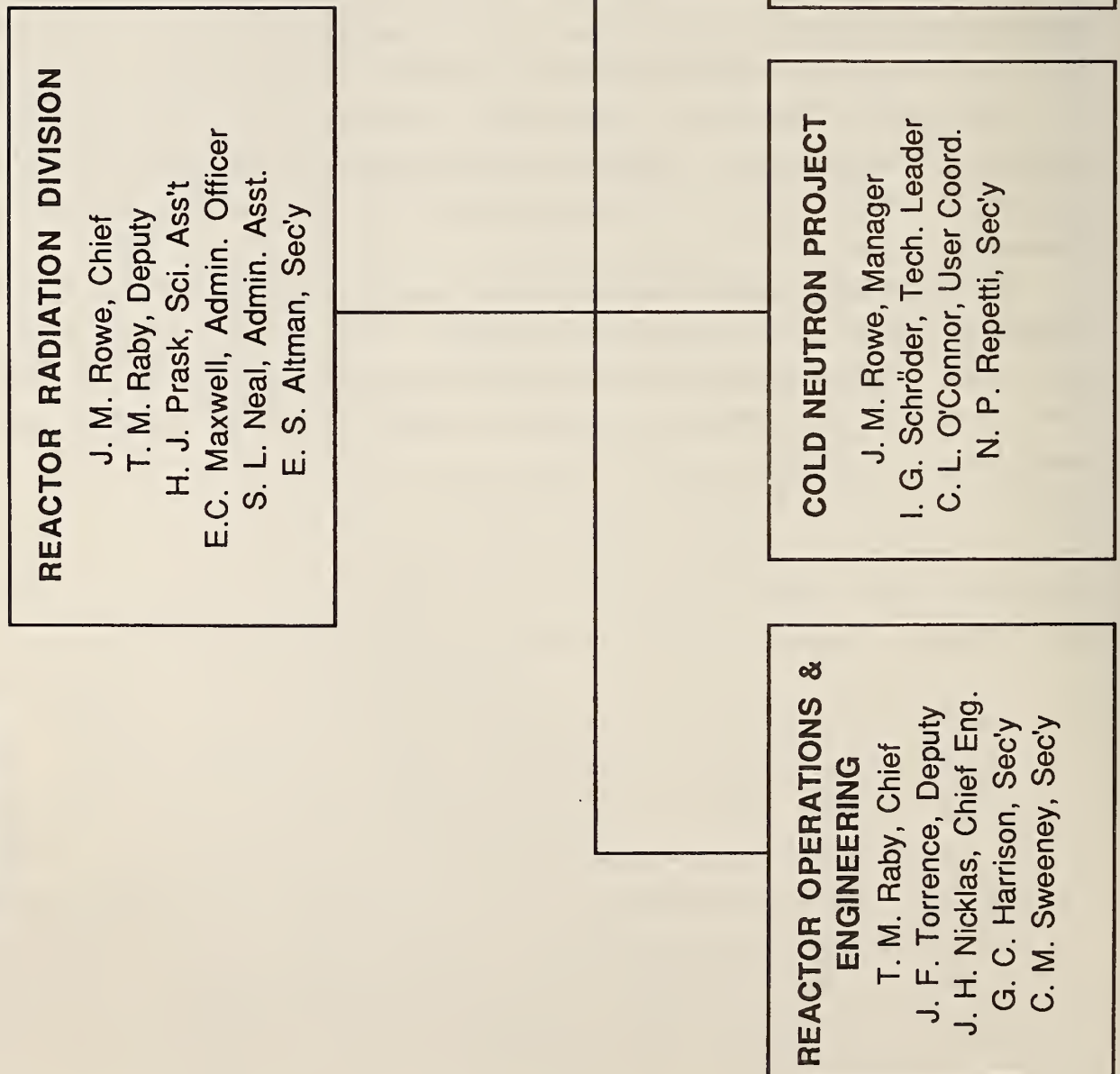
the existing stack monitor, but would also, because of its extended range, be the principal instrument used for emergency action in the case of a radiation emergency.

Automatic Control System. The current automatic control system for the reactor is one of a kind and 25 years old, and can no longer be easily maintained or repaired. The system was completely redesigned employing the latest advances in technology. A mockup of the system was tested in the laboratory for several months and was found superior in reliability and performance. The new system will be installed next year after further testing.

Reactor Control Room. A comprehensive study of control room instrumentation and controls was made over the last year by a visiting engineering specialist and members of the instrumentation group. A detailed plan was developed for future upgrade and modernization of the system using up-to-date design features and equipment. Although many components were upgraded whenever possible over the years, the bulk of the system remains as originally installed at the time of construction of the reactor more than 25 years ago.

Emergency Power Supply System. Design and specifications for a back-up emergency power supply system were completed. The system will be installed next year. The new system will guard against unnecessary reactor shutdowns since the reactor cannot be operated without a source of emergency power available at all times.

D. PERSONNEL ROSTER



PERSONNEL ROSTER

Research and Engineering Staff

- | | |
|-----------------|---|
| N. F. Berk | <ul style="list-style-type: none">o Condensed matter theoryo SANS theory for microstructure analysiso Computer software for graphics and data analysis |
| R. C. Casella | <ul style="list-style-type: none">o Theory of neutron scattering from light-atom defects in metalso Group theory analyses of neutron scattering from condensed mattero Elementary particle theory, especially as related to reactor generated experiments |
| R. Conway | <ul style="list-style-type: none">o Electronic engineeringo Nuclear instrumentation |
| J. R. D. Copley | <ul style="list-style-type: none">o Time-of-flight spectrometer developmento Neutron instrumentation conceptual designo Solid state physics |
| R. W. Erwin | <ul style="list-style-type: none">o Magnetic materialso Phase transformationso Spin echo techniqueso Cryogenics |
| C. J. Glinka | <ul style="list-style-type: none">o SANS microstructure of metals and porous mediao Magnetic materialso Cold neutron instrument development |
| J. Gotaas | <ul style="list-style-type: none">o Low temperature phase transformationo SANS microstructure studieso Magnetism |
| G. Greene | <ul style="list-style-type: none">o Develops system and user software for cold neutron instrumentationo Interfaces spectrometers with data acquisition systems |
| V. Himes | <ul style="list-style-type: none">o Crystal database developmento X-ray crystallography |
| P. A. Kopetka | <ul style="list-style-type: none">o Mechanical engineeringo Cold Source designo Electro-mechanical systems |
| S. Krueger | <ul style="list-style-type: none">o Small angle neutron scattering instrumentationo Microstructure of materialso Biological problems |
| J. LaRock | <ul style="list-style-type: none">o Mechanical engineeringo Neutron instrumentation design |
| H. Layer | <ul style="list-style-type: none">o Electronics and data processingo Advanced instrumentationo Fundamental physics |

PERSONNEL ROSTER

- | | |
|----------------|---|
| C. F. Majkrzak | <ul style="list-style-type: none">o Condensed matter physicso Polarized neutron scatteringo Polarizing and monochromating devices |
| A. Mighell | <ul style="list-style-type: none">o Crystallographic database developmento Single crystal diffractiono Theory of crystal lattices |
| B. Mozer | <ul style="list-style-type: none">o Structure and microstructure of metallic glasseso Dynamics of liquidso NDE of alloys |
| D. Neumann | <ul style="list-style-type: none">o Two-dimensional materialso Solid state physicso Neutron and x-ray scattering instrumentation |
| J. H. Nicklas | <ul style="list-style-type: none">o Mechanical engineeringo Reactor fuel designo Reactor engineering support |
| D. Pierce | <ul style="list-style-type: none">o Mechanical engineeringo Neutron instrumentation design |
| H. J. Prask | <ul style="list-style-type: none">o Residual stress measuremento Neutron NDE of hardwareo Neutron NDE instrumentation |
| E. Prince | <ul style="list-style-type: none">o Structural properties of alloys, catalysts, and mineralso Advanced crystallographic refinement methodso Software for materials structure analyses |
| T. M. Raby | <ul style="list-style-type: none">o Reactor operationso Nuclear engineeringo Reactor standards |
| J. J. Rhyne | <ul style="list-style-type: none">o Properties and transformations of high technology magnetic materialso Structure of amorphous solidso Data acquisition and analysis system |
| J. M. Rowe | <ul style="list-style-type: none">o Orientationally disordered solidso Hydrogen in metalso Cold neutron research and instrumentation |
| J. J. Rush | <ul style="list-style-type: none">o Catalysts and molecular materialso Hydrogen in metalso Two-dimensional systemso Inelastic scattering methods |
| A. Santoro | <ul style="list-style-type: none">o Structure of electronic and structured ceramicso Theory of crystal latticeso Powder diffraction methods |

PERSONNEL ROSTER

S. Satija	<ul style="list-style-type: none">o Low-dimensional molecular systemso Fractal aspects of microporous mediao Neutron reflectometry
I. G. Schröder	<ul style="list-style-type: none">o Cold neutron instrumentation developmento Nuclear and engineering physicso Optical devices for neutron transport
F. Shorten	<ul style="list-style-type: none">o Physical measuremento Safety
J. Stalick	<ul style="list-style-type: none">o Neutron and x-ray diffractiono Inorganic chemistryo Crystal database development
J. Sturrock	<ul style="list-style-type: none">o Design engineeringo Nuclear systems and components
M. Suthar	<ul style="list-style-type: none">o Design engineeringo Nuclear systems and components
J. F. Torrence	<ul style="list-style-type: none">o Reactor supervisiono Reactor maintenanceo Nuclear engineering
T. J. Udovic	<ul style="list-style-type: none">o Neutron time-of-flight instrumentationo Properties of catalystso Spectroscopy of surfaces

Technical Staff

Reactor Operations

Richard D. Beasley
Myron H. Bell
Nathan A. Bickford
Mark G. Cassells
Forest C. Clark
Howard W. Dilks
Daniel J. Flynn
Larry T. Lindstrom
Michael J. McDonald
William W. Mueller
Thomas J. Myers
John H. Ring
Ricky P. Sprow
Robert F. Stiber
Attila L. Toth
Daniel P. Wilkison

Neutron Research

George M. Baltic
Donald H. Fravel
Wayne C. Knill
Hugh L. McConaghy
Michael J. Rinehart
William H. Rymes
Thuan Thai
Robert H. Williams

Reactor Engineering

James A. Beatty
Richard P. Hayes

PERSONNEL ROSTER

NON-RRD NBS STAFF LOCATED AT REACTOR

Occupational Health
and Safety Division (354)

D. Brown
C. Campbell
J. Clark
I. Jensen
F. Moore
D. Nelson
J. Shubiak
L. Slaback

Ionizing Radiation
Division (536)

E. Boswell
C. Eisenhower
D. Gilliam
J. Grundl
E. McGarry
R. Schwartz
J. Coyne

Inorganic Analytical
Research Division (551)

D. Becker
G. Downing
K. Fitzpatrick
B. Grazman
R. Greenberg
G. Iyengar
G. Lamaze
J. Langland
R. Lindstrom
J. Maki
D. Mildner
B. Norman
C. Stone
S. Stone
R. Zeisler

GUEST WORKERS AND COLLABORATORS

INSTITUTE FOR MATERIALS
SCIENCE AND ENGINEERING (400)

J. Cahn

Ceramics Division (420)

E. Fuller
R. Krause
G. Long
S. Malghan
C. Ostertag
W. Haller

Polymers Division (440)

B. Bauer
R. Briber
F. Brinkman
T. Chang
J. Clark
L. Coyne
T. Davis
C. Han
S. Krueger
A. Nakatani
G. Olsen
W. Wu

Metallurgy Division (450)

F. Biancaniello
R. Fields
F. Gayle
C. Johnson
D. Lashmore
R. Shaefer

Surface Science Division (541)

R. Cavanagh

Organic Analytical
Division (552)

B. Koster
L. Sander
S. Wise

Gas and Particulate
Science Division (553)

W. Dorko
C. Poston
J. Small

Center for Atomic, Molecular
and Optical Physics (570)

M. Arif
R. Deslattes
S. Dewey
G. Greene

PERSONNEL ROSTER

Semiconductor Electronics

Division (727)

J. Ehrstein
J. Marshall
J. Suehle

Thermophysics Division (774)

H. Hanley
J. Straty

Armed Forces Institute of Pathology

D. Nagarajan

Army Armament Research, Development and Engineering Center

C. Choi
S. Trevino

Army Ballistics Research Lab

D.-R. Chang
B. Rice
L. Vandekieft

Federal Bureau of Investigation

R. Bilko
R. Halberstam
K. Hargadon
J. Havekost
J. Inga
K. Lundy
R. Rebbert
J. Riley
P. Sanderson

Food and Drug Administration

D. Anderson
W. Cunningham
J. Tanner

Geological Survey

M. Mrose

NASA

D. Lindstrom

National Institutes of Health

R. Finn
R. Nossal

National Oceanic and Atmospheric Administration

G. Lauenstein

Naval Research Laboratory

D. Collins
K. Grabowski
P. Skeath
C. Roland
C. Trask

Naval Surface Weapons Center

G. Riel
M. Spano

Smithsonian Institution

R. Bishop
M. Blackman
Y. Cheng
R. Cunningham
E. Myers
J. Olin

Argonne National Laboratory

T. Brun
J. Jorgensen
J. Liu
P. Thiyagarajan
K. Vandervoort

Battelle Pacific Northwest Laboratories

F. Brauer
G. Dudder
G. Endres
M. Failey

Boris Kidric Inst., Belgrade, Yugoslavia

M. Davidovic
D. Djordjevic

Brookhaven National Laboratory

R. DiNardo
L. Passell

C.E.C.M./C.N.R.S. Grenoble, France

M. Bessiere
Y. Calvayrac
M. Cornier-Quiquandon
D. Gratias
S. Lefebvre
M. Marezio
S. Miraglia
A. Quivy

C.E.N. Saclay, France

R. Bellissent

PERSONNEL ROSTER

Paul Scherrer Inst.
Villigen, Switzerland
I. Anderson

Energy Research Foundation
(The Netherlands)
J. Woittiez

Hahn-Meitner Institute
(Berlin)
D. Behne

Institut Laue-Langevin
Grenoble, France
A. Magerl
D. Richter
C. Vettier

Instituto se Pesquisas
Energeticas Nucleares, Sao Paulo, Brazil
M. Saiki

KFA Jülich, Germany
H. Grimm
R. Hempelmann
M. Rossbach
M. Stoepler

Korean Inst. of Sci. & Tech.
H. Kim

Lawrence Berkeley Lab.
D. Morris
R. Sid

Los Alamos National Laboratory
T. Bowles
S. W. Cheong
J. Eckert
Z. Fisk
H. Robertson
R. Robinson
T. Sosnick
J. Trewhella
J. Wilkerson
J. Yethiraj

Oak Ridge National Laboratory
J. Cable
J. Fernandez-Baca
J. Hayter
G. Ludtka
H. Mook
R. Nicklow
B. Sales
H. Smith

Risø National Laboratory
J. Bohr

Alfred University
R. Snyder
R. Zhou

Auburn University
B. Taterchuck

Chalmers University of Technology
L. Sjölin

College of William and Mary
E. Schoe
R. Wright

Colorado School of Mines
N. Wada

Florida International U.
W. Jones

Goethe University
W. Bauer
A. Bienok

Harvard University
T. Chupp
J. Richardson
E. Wasserman

Iowa State University
A. Goldman
R. Barnes

John Carroll University
J. Trivisonno

PERSONNEL ROSTER

Johns Hopkins University

C. L. Chien
M. Creplak
A. Ganrin
D. Musser
F. Streitz
G. Xiao

Kyoto Institute of Technology

H. Kurokawa
S. Nomura
M. Shibayama
Q. Tran-Cong

Kyoto University (Japan)

H. Hasegawa
T. Hashimoto
H. Jinnai
S. Sakurai

Lehigh University

A. Klein
L. Sperling
S. Yang
J. Yoo

M.I.T.

J. Didiskein
M. Dresselhaus
M. Green
S. Haile
J. Speck
B. Wuensch

McMaster University

W. Clarke
R. Barr

Miami University (Ohio)

J. Cantrell

Michigan State University

T. D. Brewer
Y. Fan
H. Kim
A. Moini
T. Pinnavaia
S. Solin
M. S. Wang

Nagoya University

H. Choshi
Y. Matsushita
Y. Mogi
K. Mori
Y. Muroga
M. Nagasawa
I. Nodo
R. Saguchi
Y. Takahashi

Northwestern University

A. Allen
J. Barker
J. Weertman

Oregon State Graduate School

P. Davis

Penn State University

L. Pilione
J. Yehoda

Purdue University

A. Overhauser

Rutgers University

R. Gerhardt
T. Madey

San Jose State University

P. Englert
A. Ling

Scottish Universities Research Reactors

R. Scott

Temple University

J. Crow
C.-S. Jee
A. Kebede
T. Mihalisin

Texas A&M University

E. Schweikert

University of Annecy (France)

J. Bouillot

University of Antwerp (Belgium)

K. Michel

University of California (Davis)

P. Klavins
R. Shelton

PERSONNEL ROSTER

University of California (Irvine)

V. Guinn

University of California (Santa Barbara)

S. Cox

J. Fint

D. Klingensmith

C. Levi

R. Odette

G. Stucky

University of California (San Diego)

J. Arnold

J. Ferreira

B. Lee

B. Maple

J. Neumeier

K. Nishiizumi

K. Yang

University of Delaware

J. Beamish

W. Dubner

University of Exeter (U.K.)

R. Slade

University of Florida

S. Nagler

University of Houston

W.-K. Chu

D. Gray

University of Illinois

J. Ankner

J. Borchers

B. Boyle

R. Du

J. Dura

C. Flynn

J. Kordas

A. Matheny

G. Moore

M. Salamon

F. Tsui

H. Zabel

University of Illinois (Chicago)

M. Said

J. Kouvel

University of Maryland

H. Ammon

O. Chitale

T. Clinton

F. Divita

J. Dodd

C. Ford

G. Gordon

M. Han

W. Li

Z. Lin

J. Lynn

E. Mackey

F. Mantica

A. Mizohata

J. Nicol

J. Ondov

C. Purdy

T. Quinn

S. Regdos

S. Skanthakumar

G. Tuncel

J. Valette-Silver

W. Walters

S. Wight

Z. Wu

H. Zhang

B. Zimmerman

University of Massachusetts

A. Hanyu

L. Jong

R. Stein

University of Milan (Italy)

M. Zocchi

University of Michigan

D. Vincent

R. Fleming

University of Missouri

R. Berliner

W. Ching

B. Hammouda

H. Kaiser

S. Werner

D. Worcester

University of Nancy (France)

C. Dutour

P. Mangin

G. Marchal

M. Verghat

PERSONNEL ROSTER

University of New Hampshire

N. Blakemore
R. Blakemore
Y. Gorby

University of North Carolina

E. Frye
N. Parikh
M. Swanson

University of Notre Dame

J. Furdyna
T. Giebultowicz
P. Klosowski
H. Luo
N. Samarth

University of Pennsylvania

P. Davis

University of Pittsburg

W. Goldberg

University of Sussex, U.K.

J. Byrne
P. Dawber
J. Spain

University of Vermont

T. Flanagan

University of Virginia

T. Williamson

University of Washington

J. Billman
B. Heckel
E. Kaler
E. Mader
K. Mottet
W. Zoller

University of West Virginia

R. Kannan
M. Seehra

University of Wisconsin

D. Huber

Utah State University

T. Isenhour

Yale University

J. Flanagan

AT&T Bell Laboratories

F. Bates
R. Cava
G. Fredrickson
J. Mitchell
D. Murphy
W. Rhodes
J. Riley
J. Rosedale
L. Schneemeyer
S. Sunshine
J. Waszazak
S. Yegnasubramanian

Aerospace Corporation

R. Bowman
J. Knudsen

Allied Signal Corporation

T. Barden
G. Fish
A. Maeland
C. Parker

Atomic Energy of Canada, LTD

W. Lennard

Bell Communications Research Laboratories

P. Barboux
M. Giroud
L. Greene
G. Hull
P. Miceli
J. Tarascon

CARB

A. Svensson

Charles Evans & Assoc.

R. Fleming

CIDTECH

J. Carbone
M. Wadsworth

Directed Technologies, Inc.

N. Chesser

E. I. DuPont de Nemours Co.

J. Parise
M. Subramanian

PERSONNEL ROSTER

Eastman Kodak

T. Hossain
M. Landry
J. Levine
J. O'Reilly
C. Swanson
J. Tritten
H. Yang

Exxon

B. Ables
R. Busch
L. Fetters
J. Huang
J. Hughes
M. Kim
K. Liang
M. Lin
D. Lohse
R. Overfield
E. Sheu
S. Sinha
E. Sirota

GEN Corp.

I. Hargis
S. Aggarwal

GTE Laboratories

G. Hamill

W. R. Grace

R. Wormsbecker

Hughes, Malibu

R. Wilson

IBM (San Jose)

G. Hadziioannou
T. P. Russell
S. H. Anastasiadis

Imperial Chemical Industries

J. Howard
H. Stanley

Intel Corporation

N. Cox

Lockheed EMSCO

D. Lindstrom

Optoline Corp.

J. Bradshaw

Polaroid Corp.

S. Roy

Research Triangle

N. Wadlen

Southwest Research Inst.

R. Page

SRI, Inc.

S. Johnson

Westinghouse-Hanford Corp.

W. McElroy

E. PUBLICATIONS

- Ables, B.; Yang, L.; Leta, D.; Majkrzak, C. F. "Fast Diffusion of Interstitial Deuterium in Amorphous Silicon," Proceedings of the 12th Int'l. Conf. on Amorphous and Liquid Semiconductors, Prague, 24-28 August 1987.
- Ammon, H. L.; Choi, C. S.; Reddy, S. "Crystal Structure of 1,4-diiodocubane," Acta Cryst. C44, 1671-1672 (1988).
- Ammon, H. L.; Choi, C. S.; Bashir-Hashemi, B.; Moriarty, R. M.; Khosrowshahi, S. J. "Structure of 1-adamantanylammonium Trinitromethide," Acta Cryst. C45, 319-321 (1989).
- Ammon, H. L.; Choi, C. S.; Damvarapu, R. S.; Iyer, S.; Alster, J. "Crystal Structure of Cubane-1,4-diammonium Bis-(trinitromethide)," Acta Cryst., in press.
- Anastasiadis, S. H.; Russell, T. P.; Satija, S. K.; Majkrzak, C. F. "Neutron Reflectivity Studies of the Surface Induced Ordering of Diblock Copolymer Films," Phys. Rev. Lett. 62, 1852 (1989).
- Anastasiadis, S. H.; Russell, T. P.; Satija, S. K.; Majkrzak, C. F. "Neutron Reflectivity Studies of Thin Diblock Copolymer Films," Proceedings of the National Meeting of the American Chemical Society, Dallas, Texas, April 1989, p. 14.
- Anastasiadis, S. H.; Russell, T. P.; Satija, S. K.; Majkrzak, C. F. "A Neutron Reflectivity Study of the Order-Disorder Transition in Thin Film Diblock Copolymer Films," Proceedings of the MRS Symposium on Neutron Scattering for Materials Science, Boston, MA, 1989 (to be published).
- Anastasiadis, S. H.; Russell, T. P.; Satija, S. K.; Majkrzak, C. F. "The Morphology of Symmetric Diblock Copolymers as Revealed by Neutron Reflectivity," J. Chem. Phys. (to be published).
- Ankner, J. F.; Zabel, H.; Neumann, D. A.; Majkrzak, C. F. "Grazing-Incidence Neutron Diffraction from Si (110)," Phys. Rev. B, in press.
- Ankner, J. F.; Zabel, H.; Neumann, D. A.; Majkrzak, C. F. "Grazing-Angle Neutron Diffraction," Phys. Rev. B40, 792 (1989).
- Ankner, J. F.; Zabel, H.; Neumann, D. A.; Majkrzak, C. F.; Dura, J. A.; Flynn, C. P. "Grazing-Angle Neutron Diffraction," Les Editions de Physique (in press).
- Ankner, J. F.; Zabel, H.; Neumann, D. A.; Majkrzak, C. F.; Matheny, A.; Dura, J. A.; Flynn, C. P. "Neutron Reflectivity Study of Gd-Y Interface," Proceedings of the MRS Symposium on Neutron Scattering for Materials Science, Boston, MA, 1989 (to be published).
- Bates, F. S.; Rosedale, J. H.; Fredrickson, G. H.; Glinka, C. J. "Fluctuation-Induced First-Order Transition of an Isotropic System to a Periodic State," Phys. Rev. Lett. 61, 2229-2232 (1988).

PUBLICATIONS

- Bauer, B. J.; Briber, R. M.; Han, C. C. *Macromol.* 22(2), 940, (1989).
- Bauer, W. H.; Bieniok, A.; Shannon, R. D.; Prince, E. "Neutron Powder Diffraction Study and Thermogravimetry of Sodium Cesium Zeolite Rho," *J. Solid State Chem.* (in press).
- Berk, N. F.; Hardman-Rhyne, K. A.; "Analysis of SAS Data Dominated by Incoherent Multiple Scattering," *J. Appl. Cryst.* 21 645-651 (1988).
- Bohr, J.; Gibbs, J.; Moncton, D. E.; D'Amico, K. L.; Majkrzak, C. F.; Mohanty, K. "Synchrotron X-Ray Scattering Studies of Rare-Earth Metals", *Proc. of the Workshop on X-Ray and Neutron Scattering from Magnetic Materials*, November 1987, Argonne, IL, *Physica B* 159, 93 (1989).
- Borchers, J. A.; Nieuwenhuys, G. J.; Salamon, M. B.; Flynn, C. P.; Du, R.; Erwin, R. W.; Rhyne, J. J. "Magnetic Structure and Magnetostriction of Epitaxial Er Films," *J. Phys. Colloque* C8, Suppl. #12, 49, 1685 (1988).
- Borchers, J.; Salamon, M. B.; Du, R.; Flynn, C. P.; Erwin, R. W.; Rhyne, J. J. "Characterization of Structural and Magnetic Order of Er/Y Superlattices," *Superlattices and Microstructures Vol. 4/5*, Academic Press, 1988, pp. 439-442.
- Boumazouza, D., Mangin, P.; George, B.; Louis, P.; Brand, R. A.; Rhyne, J. J.; Erwin, R. W. "Comment on the Paper 'Magnetism in $\text{Au}_{82.5}\text{Fe}_{17.5}$ '," *Phys. Rev.* 39, 749 (1989).
- Briber, R. M.; Bauer, B. J. *Macromol.* 21(11), 3296, (1988).
- Buchenau, U.; Monkenbusch, M.; Stamm, M.; Majkrzak, C. F.; Nucker, N. "Neutron Scattering Study of Relaxations and Vibrations in Molten Polyethylene," *Proc. of the Workshop on Polymer Motion in Dense Systems*, 1988.
- Cahn, J. W.; Gratias, D.; Mozer, B. "A 6-D Structural Model for the Icosahedral $(\text{Al}_1\text{Si})\text{-Mu}$ Quasicrystal," *J. Phys. (France)* 49, 1225 (1988).
- Cahn, J. W.; Gratias, D.; Mozer, B. "Patterson-Fourier Analysis of the Icosahedral $(\text{Al}_1\text{Si})\text{-Mu}$ Alloy." *Phys. Rev.* B38, 1638 (1988).
- Carr, M. J., Chambers, W. F., Melgaard, D., Himes, V. L., Stalick, J. K.; Mighell, A. D. "NIST/Sandia/ICDD Electron Diffraction Database: A Database for Phase Identification by Electron Diffraction." *J. Res. Natl. Inst. Stand. Technol.* 94, 15-20 (1989).
- Casella, R. C. "Comparison of Interplanar-Boson-Exchange Models of High-Temperature Superconductivity--Possible Experimental Tests", *Appl. Phys. Lett.* (in press).

PUBLICATIONS

- Casella, R. C. "Dependence of T_c on the Number of CuO_2 Planes per Cluster in Interplanar-Boson-Exchange Models of High- T_c Superconductivity", *Solid State Commun.* 70, 75-77 (1989).
- Casella, R. C. "Theoretical Models For High-Temperature Superconductivity," *Nuovo Cimento* D10, 1439-1448 (1988).
- Cava, R. J.; Marezio, M.; Krajewski, J. J.; Peck, W. F., Jr.; Santoro, A.; Beech, F. "Neutron Powder Diffraction Study of $\text{Pb}_2\text{Sr}_2\text{YCu}_3\text{O}_8$, the Prototype of a New Family of Superconductors," *Physica C*, 157, 272-278 (1989)
- Chien, C. L.; Xiao, G.; Cieplak, M. Z.; Musser, D.; Rhyne, J. J.; Gotaas, J. A. "Superconductivity in Orthorhombic and Tetragonal $\text{YBa}_2(\text{Cu}_{1-x}\text{A}_x)_3\text{O}_y$ Systems (A = Zn, Ga, Al, and Co)," *Superconductivity and Its Applications*, Kwok, H. S.; Shaw, D. T., eds., Elsevier Publishing, 1988, pp 110.
- Choi, C. S.; Prask, H. J. "Orientation Distribution of Fiber-Axes and Neutron Powder Diffraction Profiles." Eighth International Conference on Texture of Materials, Kallend, J. S.; Gottstein, G., eds. The Metallurgical Society, Inc., Publications, 215-221 (1988).
- Choi, C. S.; Prask, H. J.; Ostertag, C. P. "Texture Study of Magnetically Aligned $\text{YBa}_2\text{Cu}_3\text{O}_7$ -type Materials by Neutron Diffraction." *J. Appl. Cryst.* (in press).
- Copley, J. R. D. "An Analytical Method to Characterize the Performance of Multiple Section Straight-Sided Neutron Guide Systems," *Nuclear Instrument Methods in Phys. Res. A* (submitted).
- Copley, J. R. D. "On the Use of Acceptance Diagrams to Calculate the Performance of Multiple Section Straight-Sided Neutron Guide Systems," Advanced Neutron Sources, Physics Conference Series vol. 97, Institute of Physics Publishing, London, 1989 (in press).
- Copley, J. R. D. "On the Use of Multiple Slot Multiple Disk Chopper Assemblies to Pulse Thermal Neutron Beams," *Nuclear Instruments and Methods in Phys. Res.* A273, 67-76 (1988).
- Copley, J. R. D. "The Effect of Chopper Jitter on the Time-Dependent Intensity Transmitted by Multiple-Slot Disk Chopper Systems," in Advanced Neutron Sources, Physics Conference Series Vol. 97, Institute of Physics Publishing, London, 1989 (in press).
- Copley, J. R. D. "The Significance of Multiple Scattering in the Interpretation of Small Angle Neutron Scattering Experiments," *J. Appl. Cryst.* 21, 639-644 (1988).

PUBLICATIONS

- Copley, J. R. D.; Majkrzak, C. F. "Calculations and Measurement of the Performance of Converging Neutron Guides," in Thin-Film Optical Devices: Mirrors, Supermirrors, Multilayer Monochromators, Polarizers and Beam Guides, Majkrzak, C. F., ed. Proc. SPIE 983, 93-104 (1989).
- Copley, J. R. D.; Stone, C. A. "Neutron Scattering and Its Effect on Reaction Rates in Neutron Absorption Experiments," Nuclear Instruments and Methods in Phys. Res. A281, 593 (1989).
- DiNardo, R. P.; Majkrzak, C. F.; Neumann, D. A. "Fabrication of Neutron Polarizing Multilayers by Sputtering," SPIE Proceedings Vol. 983, ed. C. F. Majkrzak, SPIE, Bellingham, WA, 149 (1989).
- DiNardo, R. P.; Majkrzak, C. F.; Neumann, D. A. "Fabrication of Neutron Polarizing Fe-Si Multilayers by Sputtering," in Thin Film Neutron Optical Devices: Mirrors, Supermirrors, Multilayer Monochromators, Polarizers, and Beam Guides, ed. C. F. Majkrzak, SPIE, Bellingham, WA, 149 (1988).
- DiNardo, R. P.; Takacs, P. Z.; Majkrzak, C. F.; Stefan, P. M. "Sputter Deposition System for Controlled Fabrication of Multilayer Mirrors," Proc. of the 29th SPIE Int'l. Tech. Symposium, August 1985, San Diego, CA. Vol. 563, p. 30.
- Endoh, Y.; Majkrzak, C. F. "Polarized Neutron Diffraction Studies of Magnetic Multilayer Structures," Chapter in a book on metallic superlattices, Shinjo, T.; Takada, T., eds. Elsevier Science Publications (1989).
- Erwin, R. W.; Rhyne, J. J.; Borchers, J.; Du, R.; Salamon, M. B.; Flynn, C. P. "Magnetoelasticity in Rare-Earth Superlattices and Films," Physica B (to be published).
- Erwin, R. W.; Rhyne, J. J.; Borchers, J.; Salamon, M. B.; Du, R.; Flynn, C. P. "Structure of Er|Y Superlattices," J. de Phys. Colloque C8, Suppl. #12, 1631 (1988).
- Fan, Y. B.; Solin, S. A.; Neumann, D. A.; Sabel, H.; Rush, J. J. "Elastic Neutron Scattering Studies of the Structure of Graphite Intercalated With Potassium and Ammonia," Phys. Rev. B36, 3386 (1989).
- Fernandez-Baca, J. A., Rhyne, J. J.; Erwin, R. W.; Fish, G. E. "Neutron Scattering Study of the Magnetic Correlations of Iron-Rich Fe-Ni-Zr Glasses," J. Phys. Colloque C8, Suppl. #12, 1207 (1988).
- Fernandez-Baca, J. A.; Lynn, J. W.; Rhyne, J. J.; Fish, G. E. "Low temperature Spin Waves in Amorphous $\text{Fe}_{90-x}\text{Ni}_x\text{Zr}_{10}$," J. Appl. Phys. 63, 3749 (1988).
- Fischer, R.; Baur, W.; Shannon, R.; Parise, J.; Faber, J.; Prince, E. "New, Different Forms of Ammonium Loaded, and Partly Deammoniated Zeolite Rho Studied by Neutron Powder Diffraction," Acta Crystallogr. Sect. C. (1988) in press.

PUBLICATIONS

- Flynn, C. P.; Borchers, J. A.; Demers, R. T.; Du, R.-R.; Dura, J. A.; Klein, M. V.; Kong, S. H.; Salamon, M. B.; Tsui, T.-F.; Yadavalli, S.; Zhu, X.; Zabel, H.; Cunningham, J. E.; Erwin, R. W.; Rhyne, J. J. "Growth and Properties of Superlattices with Antiferromagnetic Rare Earths," (to be published).
- Flynn, C. P.; Tsui, F.; Salamon, M. B.; Erwin, R. W.; Rhyne, J. J. "Dependence of Magnetic Coupling on Growth Direction in Epitaxial Dy-Y Superlattices," Phys. Lett. F (submitted for publication).
- Flynn, C. P.; Tsui, F.; Salamon, M. B.; Erwin, R. W.; Rhyne, J. J. "Anisotropic Response of Rare Earths in Superlattices," (to be published).
- Forano, C.; Slade, R. C. T.; Andersen, E. K.; Andersen, I. G. K.; Prince, E. "Neutron Diffraction Determination of Full Structures of Anhydrous Li-X and Li-Y Zeolites," J. Solid State Chem. (in press).
- Giebultowicz, T. M.; Rhyne, J. J.; Ching, W. Y.; Huber, D. L.; Furdyna, J. K.; Lebech, B.; Galazka, R. R. "Harmonic Magnons in $\text{Zn}_{1-x}\text{Mn}_x\text{Te}$ and $\text{Cd}_{1-x}\text{Mn}_x\text{Te}$," Phys. Rev. B39, 6857 (1989).
- Giebultowicz, T. M.; Holden, T. M. "Neutron Scattering Studies of Magnetic Ordering and Magnetic Dynamics of Diluted Magnetic Semiconductors," in Diluted Magnetic Semiconductors, Furdyna, J. K.; Kossut, J., eds., in the series Semiconductors and Semimetals, Vol. 25, p. 120, Academic Press, Boston, MA 1988.
- Giebultowicz, T. M.; Klosowski, P.; Rhyne, J. J.; Udovic, T. J.; Furdyna, J. K.; Giritat, W. "Magnetic Exchange Interactions in Co-based II-VI Diluted Magnetic Semiconductors: $\text{Zn}_{1-x}\text{Co}_x\text{S}$," Phys. Rev. B (in press).
- Giebultowicz, T. M.; Rhyne, J. J.; Seehra, M. S.; Kannan, R. "Neutron Diffraction in $\text{Co}_p\text{Mg}_{1-p}\text{O}$ Solid Solutions," J. Phys. Colloque C8, 49, 1105 (1988).
- Giebultowicz, T. M.; Rhyne, J. J.; Furdyna, J. K.; Galazka, R. R. "Neutron Diffraction Studies of $\text{Cd}_{1-x}\text{Mn}_x\text{Te}$ and $\text{Zn}_{1-x}\text{Mn}_x\text{Te}$ Single Crystals," J. Phys. Colloque C8, 49, 1199 (1988).
- Glinka, C. J. "Workshop on Microstructure and Macromolecular Research with Cold Neutrons," J. A. Gotaas and C. O'Connor, J. Res. Natl. Inst. Stand. Technol. 93(6), 667-669 (1988).
- Goldman, A.; Gao, Y.; Ting, S.-T.; Crow, J. E.; Li, W.-H.; Lynn, J. W. "Crystal Electric Fields in Rare Earth-Ba-Cu-Oxide Superconductors," J. Mag. Mag. Mater. 76-77, 607 (1988).
- Gotaas, J. A.; Rhyne, J. J.; Wenger, L. E.; Mydosh, J. A. "Magnetic Structure of $\text{Y}_{0.97}\text{Er}_{0.03}$," J. Phys. (Paris) 49, C8-365-366 (1988).

PUBLICATIONS

- Gotaas, J. A.; Said, M. R.; Kouvel, J. S.; Brun, T. O. "Magnetic Structure of Cubic $Tb_{0.3}Y_{0.7}Ag$ ", J. Phys. (Paris) 49, C8-345-346 (1988).
- Gratias, D.; Cahn, J. W.; Bessiere, M.; Calvayrac, Y.; Lefebvre, S.; Quivy, A.; Mozer, B. "N-dimensional Crystallographic Description of the Icosahedral Phases; The Example of the $Al_{73}Mn_{21}Si_6$ Quasiperiodic Structure," Proc. of the NATO Conference, Acquafredda, Plenum (1988).
- Gratias, D.; Cahn, J. W.; Mozer, B. "Six-Dimensional Fourier Analysis of Icosahedral $Al_{73}Mn_{21}Si_6$ Alloy," Phys. Rev. B38, 1643 (1988).
- Grimm, H.; Stiller, H.; Majkrzak, C. F.; Ruppoecht, A. "Neutron Scattering Study of the Hydration Hull of DNA by H_2O/D_2O Exchange," Proceedings of the Int'l. Conf. on Neutron Scattering, Grenoble, France, July 1988, Physica B 156 and 157, 464 (1989).
- Grimm, H.; Stiller, H.; Majkrzak, C. F.; Rupprecht, A.; Dahlborg, U. "Observation of Acoustic Umklapp Phonons in Water-Stabilized DNA by Neutron Scattering," Phys. Rev. Lett. 59, 1780 (1987).
- Heise, W. H.; Lu, K.; Kuo, Y-J; Tatarchuk, B. J.; Udovic, T. J.; Rush, J. J. "Neutron Scattering Study of Hydrogen on Ruthenium Sulfide," J. Phys. Chem. 92, 5184 (1988).
- Himes V. L.; Mighell, A. D.; Stalick, J. K.; Young, S.; Carr, M.; Anderson, R.; Holomany, M.; Jenkins, R.; Lyman, C. "Elemental and Interplanar Spacing Index for Phase Identification by Electron and X-Ray Diffraction," published jointly by NIST and the International Centre for Diffraction Data (1989).
- Himes, V. L.; Mighell, A. D. "NBS Crystal Data: Compound Identification and Characterization Using Lattice-Formula Matching Techniques," Metallurgical Society (publisher), Chapter in Computerized Metallurgical Databases, pp. 153-168 (1988).
- Horton, J. C.; Squires, G. L.; Boothroyd, A. T.; Fetters, L. J.; Rennie, A. R.; Glinka, C. J.; Robinson, R. A. "Small Angle Neutron Scattering From Star-Branched Polymers in the Molten State," Macromol. 22, 681-686 (1989).
- Krueger, S.; Zaccai, G.; Wlodawer, A.; Langowski, J.; O'Dea, M.; Maxwell, A.; Gellert M. "Neutron and Light Scattering Studies of DNA Gyrase and Its Complex With DNA," (1989) (submitted for publication).
- Krueger, S.; Lynn, J. W.; Russell, J. T.; Nossal, R. "Small Angle Neutron Scattering Method for *in situ* Studies of the Dense Cores of Biological Cells and Vesicles: Application to Isolated Neurosecretory Vesicles," J. Appl. Crystallogr. (to be published).
- Krueger, S.; Olson, G. J.; Rhyne, J. J.; Blakemore, R. P.; Gorby, Y. A.; Blakemore, N. "Small Angle Neutron and X-Ray Scattering From Magnetite Crystals in Magnetotactic Bacteria," J. Mag. Mag. Mater. (to be published).

PUBLICATIONS

- Kwo, J.; Hong, M.; Hsieh, T. C.; Fleming, R. M.; McWhan, D. B.; Yafet, Y.; Majkrzak, C. F.; Gibbs, D.; Boni, P.; Goldman, A. I.; Cable, J. W.; Bohr, J.; Grimm, H. "Rare-Earth Magnetic Superlattices," International Conference on Magnetism, Paris, France, July 1988, J. Phys. Colloque C8, 49, 1651 (1988).
- Lee, E.; Elminger, M.; Passell, L.; Majkrzak, C. F. "The Brookhaven Neutron Reflection Spectrometer," (to be published).
- Li, W.-H.; Lynn, J. W.; Mook, H. A.; Sales, B. C.; Fisk, Z. "Long Range Antiferromagnetic Order of the Cu in Oxygen-Deficient, $R\text{Ba}_2\text{Cu}_3\text{O}_{6+x}$," Phys. Rev. B37 (*Rapid Communications*), 9844 (1988).
- Li, W.-H.; Lynn, J. W.; Stanley, H. B.; Udovic, T. J.; Shelton, R. N.; Klavins, P. "Antiferromagnetic Structure and Crystal Field Splittings in the Cubic Heusler Alloys HoPd_2Sn and ErP_2Sn ," J. Phys. (Suppl.) 49, C8-373 (1988).
- Li, W.-H.; Lynn, J. W.; Stanley, H. B.; Udovic, T. J.; Shelton, R. N.; Klavins, P. "Crystal-Field Splittings in the Cubic Heusler Alloys HoPd_2Sn ," Phys. Rev. B39, 4119 (1989).
- Long, C. G.; Krueger, S. "Multiple Small Angle Neutron Scattering Characterization of the Densification of Ceramics: Application to Microporous Silica," J. Appl. Crystallogr. (in press).
- Long, C. G.; Krueger, S.; Gerhardt, R. A. "Small Angle Neutron Scattering Characterization of Microporous Silica," Proc. Symp. on Adv. Characterization Tech. for Ceramics, 24-26 October 1988.
- Lynn, J. W.; Li, W.-H. "Magnetic Order in $R\text{Ba}_2\text{Cu}_3\text{O}_{6+x}$," J. Appl. Phys. 64, 6065 (1988).
- Lynn, J. W.; Li, W.-H.; Mook, A.; Sales, B. C.; Fisk, Z. "Nature of the Magnetic Order of Cu in Oxygen Deficient $R\text{Ba}_2\text{Cu}_3\text{O}_{6+x}$," Phys. Rev. Lett. 60, 2781 (1988).
- Lynn, J. W.; Li, W.-H.; Mook, H. A.; Sales, B. C.; Fisk, Z. "Antiferromagnetic Order of the Cu in $R\text{Ba}_2\text{Cu}_3\text{O}_{6+x}$," J. Phys. 49, C8-1, 2153 (1988).
- Lynn, J. W.; Li, W.-H.; Trevino, S. F.; Fisk, Z. "Pressure Dependence of the the Cu Magnetic Order in $\text{NdBa}_2\text{Cu}_3\text{O}_{6+x}$," Phys. Rev. B460, (1989) (to be published).
- Lynn, J. W.; Skanthakumar, S.; Clinton, T. W.; Kebede, A.; Jee, C.-S.; Crow, J. E.; Mihalisin, T. Phys. Rev. B40 (*Rapid Communications*), (1989) (to be published).

PUBLICATIONS

- Majkrzak, C. F.; Neumann, D. A.; Copley, J. R. D.; DiNardo, R. P. "Fe-W Supermirrors for Polarizing Neutrons," Proc. MRS Fall 1988 Symposium D, 103, 115 (1988).
- Majkrzak, C. F. "Multilayer and Supermirror Polarizers for Neutrons," Proceedings of the Workshop on X-Ray and Neutron Scattering From Magnetic Materials, ANL, November 1987, Physica B 159, 143 (1989).
- Majkrzak, C. F. "Polarized Neutron Diffraction Studies of Synthetic Superlattices," Metallic Multilayers and Epitaxy, Hong, M.; Wolf, S.; Gubser, D. C., eds. The Metallurgical Society, Pittsburgh, PA; 1988.
- Majkrzak, C. F. "Polarized Neutron Scattering: Methods and Studies Involving Artificial Superlattices," Proc. of the Int'l Conf. on Neutron Scattering, Grenoble, France, July 1988, Physica B, 156-157, 619 (1989).
- Majkrzak, C. F. "Summary of the Recent Conference on Thin-Film Neutron Optical Devices," Proc. of ICANS-X, Los Alamos, NM, October 3-7, 1988 (in press).
- Majkrzak, C. F.; Berk, N. F. "Neutron Flux Enhancement Using Spin-Dependent Interaction Potentials," Phys. Rev. B40, 371 (1989).
- Majkrzak, C. F.; Cox, D. E.; Lehmann, M. S. "Neutron Diffraction," to appear as a chapter in Physical Methods of Chemistry, Rossiter and Hamilton, eds. John Wiley and Sons, Inc. (to be published).
- Majkrzak, C. F.; Gibbs, D.; Kwo, J.; Hong, M.; Yafet, Y.; Bohr, J.; Chien, C. L. "Magnetic Rare Earth Superlattices," Adv. Phys. (to be published).
- Majkrzak, C. F.; Gibbs, D.; Kwo, J.; Hong, M.; Yafet, Y.; Bohr, J.; Chien, C. L. "Magnetic Rare Earth Superlattices," Adv. Phys. (to be published).
- Majkrzak, C. F.; Glinka, C. J.; Satija, S. K. "Applications of Mirrors, Supermirrors, and Multilayers at the NBS Cold Neutron Research Facility," SPIE Proc. Vol. 983, Majkrzak, C. F., ed. SPIE, Bellingham, WA, 1989 p.129.
- Majkrzak, C. F.; Neumann, D. A.; Copley, J. R. D.; DiNardo, R. P. "Fe-W Supermirrors for Polarizing Neutrons," Proc. of the 1987 Fall Meeting of the Mater. Res. Soc., Vol. 103, p. 115.
- Majkrzak, C. F.; Satija, S. K.; Neumann, D. A.; Rush, J. J.; Lashmore, D.; Johnson, C.; Bradshaw, J.; Passell, L.; DiNardo, R. "Determination of Hydrogen Density Profiles in Thin Films and Multilayers by Neutron Reflection," Proc. of the MRS Symposium on Neutron Scattering for Materials Science, Boston, MA, 1989 (to be published).
- Mangin, P.; Boumazouza, D.; George, B.; Rhyne, J. J.; Erwin, R. W. "Static and Dynamic Properties of the $(\text{Fe}_x\text{Cr}_{1-x})_{75}\text{P}_{15}\text{C}_{10}$ Reentrant Spin Glass Amorphous Alloy," Phys. Rev. B (to be published).

PUBLICATIONS

- Matsushita, Y.; Nakao; Saguchi, R.; Mori, K.; Chosi, H.; Muroga, Y.; Noda, I.; Nagasawa, K.; Chang, T.; Glinka, C. J.; Han, C. C. "Phase Contrast Matching in Lamellar Structures Composed of Mixtures of Labeled and Unlabeled Block Copolymers for Small Angle Neutron Scattering," *Macromol.* 21, 1802-1806 (1988).
- Miceli, P. F.; Tarascon, J. M.; Bagley, B. G.; Greene, L. H.; Barboux, P.; Hull, G. W.; Giroud, M.; Rhyne, J. J.; Neumann, D. A. "Magnetic Properties of Some High T_c Compounds," in the Proc. of the 10th Winter Meeting on Low Temperature Physics of High Temperature Superconductivity, World Scientific Publishing, (in press).
- Miceli, P. F.; Tarascon, J. M.; Barboux, R.; Greene, L. H.; Bagley, B. G.; Hull, G. W.; Giroud, M.; Rhyne, J. J.; Neumann, D. A. "Magnetic Transitions in the System $\text{YBa}_2\text{Cu}_{2.8}\text{Co}_{0.2}\text{O}_{6+y}$," *Phys. Rev.* B39, 12375 (1989).
- Miceli, P. F.; Tarascon, J. M.; Greene, L. H.; Barboux, P.; Giroud, M.; Neumann, D. A.; Rhyne, J. J.; Schneemeyer, L. F.; Waszczak, J. V. "Antiferromagnetic Order in $\text{YBa}_2\text{Cu}_{3-x}\text{Co}_x\text{O}_{6+y}$," *Phys. Rev.* B38, 9209 (1988).
- Miceli, P. F.; Tarascon, J. M.; Greene, L. H.; Barboux, P.; Jorgensen, J. D.; Rhyne, J. J.; Neumann, D. A. "Charge Transfer and Bond Lengths in $\text{YBa}_2\text{Cu}_{3-x}\text{M}_x\text{O}_{6+y}$," *Proc. Mater. Res. Soc.* (in press).
- Mighell, A. D.; Himes, V. L. "A New Method for Phase Identification for Electron Microscopists," *J. Elect. Microsc. Techn.* (submitted for publication).
- Minor, W.; Giebultowicz, T. M. "Studies of fcc Heisenberg Antiferromagnets by Monte Carlo Simulations on Large Spin Arrays," *J. Phys. Colloque* C8, 49, 1551 (1988).
- Neumann, D. A.; Zabel, H.; Morkoc, H. "Terracing in Strained-Layer Superlattices," *J. Appl. Phys.* 64, 3024 (1988).
- Neumann, D. A.; Zabel, H.; Fan, Y. B.; Solin, S. A.; Rush, J. J. "Neutron Scattering Study of Phonon-Libron Coupling in Potassium-Ammonia Intercalated Graphite," *Phys. Rev.* B37, 8424 (1988).
- Neumann, D. A.; Zabel, H.; Magerl, A.; Fan, Y. B.; Solin, S. A. "Neutron Spectroscopy of Rotational Tunneling of NH_3 in Graphite," in Graphite Intercalation Compounds: Science and Applications, Endo, M.; Dresselhaus, M. S.; Dresselhaus, G., eds. *Mater. Res. Soc.* 9 (1988).
- Nicol, J. M.; Eckert, J.; Howard, J. "The Dynamics of Molecular Hydrogen Adsorbed in CoNa-A Zeolite," *J. Phys. Chem.* 92, 7117 (1988).
- Nicol, J. M.; Rush, J. J.; Kelley, R. D. "Inelastic Neutron Scattering Studies of the Interaction of Hydrogen With Palladium Black," *Surface Sci.* 197, 67 (1988).

PUBLICATIONS

- Parise, J. B.; McCarron, E. M.; Sleight, A. W.; Prince, E. "Refinement of the Structure of β' -MoO₃," *Matls. Sci. Forum* 27/28, 85-88 (1988).
- Parise, J. B.; Torardi, C. C.; Subramanian, M. A.; Gopalakrishnan, J.; Sleight, A. W.; Prince, E. "Superconducting Tl_{2.0}Ba_{2.0}CuO_{6+δ}: A High Resolution Neutron Powder and Single Crystal X Ray Diffraction Investigation," *Phys. C* 159, 239-244 (1989).
- Prince, E. "Principles of Rietveld Refinement," *Proc. of the International Workshop on the Rietveld Method*, Petten, The Netherlands. (in press, 1989)
- Prince, E. "The Crystal Structure of Ammonium Paradodecatunstate Tetrahydrate by Neutron Diffraction," Howard T. Evans, *Acta Cryst. Sect. C*. (in press, 1989)
- Prince, E. "The Maximum Entropy Distribution Consistent with Observed Structure Amplitudes," *Acta Crystallogr. Sect. A* A45, 200-203 (1988).
- Prince, E. "Phase Extension by Combined Entropy Maximization and Solvent Flattening," *Acta Crystallogr.* A44, 216-222 (1988).
- Prince, E. "An Alternative Approach to the Hauptman-Karle Determinantal Inequalities," *Acta Crystallogr. Sect. A* A45, 144 (1988).
- Prince, E.; Slade, R. C. T.; Ramanan, A.; West, B. C. "The Structure of V₉Mo₆O₄₀ Determined by Powder Neutron Diffraction," *J. of Solid State Chemistry* (in press).
- Rhyne, J. J. "Highlights from the Exotic Phenomena of Lanthanide Magnetism," Chapter 76, *Handbook on the Physics and Chemistry of Rare Earths*, Vol. 11, Gschneidner, K. A.; Eyring, L., eds. North Holland Publishing, Amsterdam, 1988, pp. 293-322.
- Rhyne, J. J.; Erwin, R. W.; Borchers, J.; Salamon, M. B.; Du, R.; Flynn, C. P. "Exchange and Magnetostrictive Effects in Rare Earth Superlattices," *J. Less Com. Metals* 148, 17 (1989).
- Rhyne, J. J.; Erwin, R. W.; Borchers, J.; Salamon, M. B.; Du, R.; Flynn, C. P. "Magnetic Multilayers," *Physica Scripta* (to be published).
- Rhyne, J. J.; Erwin, R. W.; Borchers, J.; Salamon, M. B.; Du, R.; Flynn, C. P. "Magnetic Ordering in Rare Earth Multilayers Studied by Neutron Diffraction," *Metallic Multilayers and Epitaxy*, Hong, M.; Wolf, S.; Gubser, D. C., eds. Metallurgical Soc. Inc., Warrendale, PA, 1988, pp. 11-32.
- Rhyne, J. J.; Erwin, R. W.; Borchers, J.; Salamon, M. B.; Du, R.; Flynn, C. P. "Neutron Scattering Studies of Magnetic Multilayers," *Physica* B159, 111 (1989).

PUBLICATIONS

- Rodgers, J. R.; Mighell, A. D. "Numeric Databases in Materials and Biological Sciences," Editors of a Special Issue of the J. Res. Natl. Inst. Stand. Technol. 94, 1-94 (1989).
- Rodgers, J. R.; Mighell, A. D. For a Special Issued (on Numeric Databases in Materials and Biological Sciences) of the J. Res. Natl. Inst. Stand. Technolo. 94, 1-94 (1989).
- Rush, J. J. "Research Opportunities and Planned Facilities at the Advanced Neutron Source," A.N.S. Trans. 57, 290 (1988).
- Rush, J. J.; Flanagan, T. B.; Craft, A. P.; Clewley, J. D.; Sakamoto, Y. "The Optic Mode Frequencies and Solubilities of Hydrogen in Ordered and Disordered Rd_3Mn ," J. Phys. F (in press).
- Rush, J. J.; Udovic, T. J.; Hempelmann, R.; Richter, D.; Driesen, G.; "Hydrogen Sites in Amorphous $Pd_{85}Si_{15}J_x$ Probed by Neutron Vibrational Spectroscopy," J. Phys.: Condensed Matter 1, 1061-1070 (1989).
- Santoro, A. "Crystallography of Superconductors," in High-Temperature Superconductivity, J. W. Lynn, ed., Springer-Verlag publishers, (in press, 1989).
- Santoro, A. "Crystal Chemistry of Superconductors and Related Compounds," in Chemistry of Superconducting Materials, Vanderah, T. A., ed., Noyes Publications (in press, 1989).
- Santoro, A. "Defective Structures of $Ba_2YCu_3O_x$ and $Ba_2YCu_{3-y}M_yO_z$ ($M = Fe, Co, Ni, Al, Ga, \dots$)," in Chemistry of Superconducting Materials, Vanderah, T. A., ed., Noyes Publications (in press, 1989).
- Santoro, A.; Beech, F.; Marezio, M.; Cava, R. J. "Crystal Chemistry of Superconductors. A Guide to the Tailoring of New Compounds," Physica C156, 693-700 (1988).
- Satija, S. K.; Majkrzak, C. F.; Anastasiadis, S. H.; Russell, T. P. "The Morphology of Symmetric Diblock Copolymers as Revealed by Neutron Reflectivity," Proc. of the MRS Symposium on Neutron Scattering for Materials Science, Boston, MA 1989 (to be published).
- Schwarzenbach, D.; Abrahams, S. C.; Flack, H. D.; Gonschorek, W.; Hahn, T.; Marsh, R. E.; Prince, E.; Robertson, B. E.; Rollett, J. S.; Wilson, A. J. C. "Report of the International Union of Crystallography Subcommittee on Statistical Descriptors," Crystallogr. Sect. A., A45 63-75 (1989).
- Seehra, M. S.; Giebultowicz, T. M. "Magnetic Structures of fcc Systems with Nearest-Neighbor and Next-Nearest Neighbor Exchange Interactions," Phys. Rev. B38, 11898 (1988).

PUBLICATIONS

- Sjolin, L.; Svensson, L.; Prince, E.; Sundell, S. "Phase Improvement in the Structure Interpretation of Fragment TR₂C from Bull Testis Calmodulin Using Combined Entropy Maximization and Solvent Flattening," Acta Crystallogr. B (in press).
- Skanthakumar, S.; Zhang, H.; Clinton, T. W.; Li, W-H.; Lynn, J. W.; Fisk, Z.; Cheong, S-W. "Magnetic Phase Transitions and Structural Distortion in Nd₂CuO₄," Physica C (to be published).
- Spano, M. L.; Gotaas, J. A.; Rhyne, J. J. "Neutron Scattering Study of Magnetic Order in a Tb_{0.5}Dy_{0.5} Single Crystal," J. Phys. Colloque C8, Suppl. 12, 345 (1988).
- Tarascon, J. M.; Miceli, P. F.; Barboux, P.; Hwang, D. M.; Hull, G. W.; Giroud, M.; Greene, L. H.; Le Page, Y.; McKinnon, W. R.; Tselepis, E.; Pleizier, G.; Eibschutz, M.; Neumann, D. A.; Rhyne, J. J. "Structure and Magnetic Properties of Doped Co and Fe-Bi₂Sr₂Cu_{1-x}M_xO_y Phases," Phys. Rev. B39, 11587 (1989).
- Torardi, C. C.; Reiff, W. M.; Prince, E. "Topochemical Li-ion Insertion into FeClMoO₄ and Fe₂(MoO₄)₃: Structure and Magnetism of LiFeClMoO₄ and Li₂Fe₂(MoO₄)₃," Matls. Sci. Forum 27/28, 223-228 (1988).
- Tran Qui, D.; Hamdoune, S.; Soubeyroux, J. L.; Prince, E. "Neutron Powder Diffraction Study of Solid Solution Li_{1+x}Ti_{2-x}In_xP₃O₁₂," J. Solid State Chem. 72, 309-315 (1988).
- Udovic, T. J.; Nicol, J. M.; Cavanagh, R. R.; Rush, J. J. "Hydrogen Adsorbate-Adsorbate Interactions on Transition Metal Surfaces as Studied by Incoherent Inelastic Neutron Scattering," 196th National Meeting of the American Chemical Society, Los Angeles, CA, September 28, 1988.
- Udovic, T. J.; Rush, J. J.; Sander, L. C. "Neutron Scattering Study of the Vibrations and Dynamics of Trimethylsilyl Adsorbates on Silica," 63rd American Chemical Society Colloid and Surface Science Symposium, Seattle, WA, June 20, 1989.
- Vergnat, M.; Houssaini, S.; DuFour, C.; Brunson, A.; Marchal, G.; Mangin, Ph.; Erwin, R. W.; Rhyne, J. J.; Vettier, C. "Evidence of Hydrogen Modulation in Si/Si:H Amorphous Multilayers," Phys. Rev. B (to be published).
- Yafet, Y.; Kwo, J.; Hong, M.; Majkrzak, C. F.; O'Brien, T. "Interlayer Exchange in Magnetic Superlattices," J. Appl. Phys. 63, 3453 (1988).
- Yethiraj, M.; Robinson, R. A.; Rhyne, J. J.; Gotaas, J. A.; Buschow, K. H. J. "Magnetic and Crystallographic Properties of UNiSn," J. Mag. Mag. Mater. (to be published).

PUBLICATIONS

- Yoo, J. N.; Sperling, L. H.; Glinka, C. J.; Klein, A. "Characterization of Film Formation from Polystyrene Latex Particles Via SANS," Macromol. (submitted for publication).
- Yu, S.C.; Lynn, J.W.; Rhyne, J.J.; Fish, G.E. "Spin Wave Excitations in Amorphous $\text{Fe}_{78}\text{B}_{13}\text{Si}_9$," J. Appl. Phys. 63, 4083 (1988)
- Zabel, H.; Neumann, D. A. "Neutron Scattering Studies of Potassium-Ammonia Layers in Graphite," Can. J. Chem. 66, 666 (1988).
- Zabel, H., Neumann, D. A. "Neutron Scattering Studies of Potassium-Ammonia Layers in Graphite," Can. J. Chem. 66, 666 (1988).

INDEPENDENT PROGRAMS

- Banerjee, I.; Frost, M.; Davies, P.; Cox, J. N. and Downing, R. G., "SIMS and NDP Studies of SiO_2 ; Si_3N_4 / SiO_2 /Si Structures," Proc. SIMS VII Conf., John Wiley and Sons (submitted for publication).
- Becker, D. A. "Fast Neutron INAA: Nickel Sensitivities and Fluence Variations at Three Reactors," Trans. Am. Nucl. Soc. 56, 193 (1988).
- Becker, D. A. "Homogeneity and Evaluation of the New NIST Leaf CRMs," J. Radioanal. Nucl. Chem. (in press).
- Becker, P. R.; Koster, B. J.; Wise, S. A. and Zeisler, R., "Alaskan Marine Mamal Tissue Archival Project," Biol. Trace Elem. Res. (submitted for publication).
- Blackman, M. J., Ceramic Technology and Problems of Social Evolution in Southwestern Iran. Proceedings of the Materials Research Society. Pittsburg, PA, 1988.
- Blackman, M. J. Chemical Characterization of Ceramics, Unfired clay Artifacts, and Source Clays from Tell Leilan, Syria. Ninevite 5 Symposium Volume. ed. Harvey Weiss, Yale University Press, New Haven, CT (in press).
- Blackman, M. J.; Mery, S.; Wright, R. P. Production and Exchange of Ceramics on the Oman Peninsula from the Perspective of Hili. J. Field Archaeology (1988).
- Burger, G.; Schwartz, R. B. Guidelines on Calibration of Neutron Measuring Devices. Technical Reports Series No. 285, International Atomic Energy Agency, Vienna, Austria, 1988.
- Carpenter, J. M.; Mildner, D. F. R.; Cudrnak, S. S.; Hilleke, R. O. "The Neutron Transmission of Single Crystal MgO Filters," Nucl. Instrum. Meth. A278, 397-401 (1989).

PUBLICATIONS

- Caswell, R. S.; Coyne, J. J. "Effects of Track Structure on Neutron Microdosimetry and Nanodosimetry, Nuclear Tracks and Radiation Measurements," (in press).
- Caswell, R. S.; Coyne, J. J. "Microdosimetry of Radon and Radon Daughters," Radiation Protection Dosimetry (submitted for publication).
- Coyne, J. J.; Caswell, R. S.; Zoetelief, J. "Calculations of the Relative Effectiveness of Alanine for Neutrons with Energies up to 17.1 MeV," Radiation Protection Dosimetry (submitted for publication).
- Coyne, L. D.; Wu., W. "An Examination of Mechanisms Responsible for Incoherent Scattering of Subthermal Neutrons by Polymers," *Polymer Comm.* (in press).
- Eisenhauer, C. M.; Hunt, J. B. "Anisotropic Neutron Emission from a ²⁵² Cf Source," *Radiation Protection Dosimetry* 22(4), 253-258 (1988).
- Germani, M. S.; Zoller, W. H. "Vapor-Phase Concentrations of As, Se, Br, I and Hg in the Stack of a Coal-Fired Power Plant," *Environ. Sci. Technol.* 22, 1079-1085 (1988).
- Gilliam, D. M.; Greene, G. L.; Lamaze, G. P. "Absolute Neutron Counting Based on B-10 Alpha-Gamma Coincidence Methods," *Nucl. Instru. Methods*, (in press).
- Gilliam, D. M.; Hocken, D. G.; Humphreys, J. C.; Lamaze, G. P. "Neutron Sensitivity of LiF Chip Gamma Dosimeters at Megagray Doses," *Reactor Dosimetry, Methods, Applications, and Standards*, American Society for Testing and Materials, Spec. Tech. Publ. STP1001, 206 (1989).
- Gokmen, I. G.; Aras, N. K.; Gordon, G. E.; Wastney, M. E.; Henkin, R. I. "Radiochemical Neutron Activation Analysis of Zinc Isotopes in Human Blood, Urine and Feces for *In Vivo* Tracer Experiments," *Anal. Chem.* (submitted for publication).
- Grazman, B.; Troutner, D. E. "Rh-105 As a Potential Radiotherapeutic Agent." *Applied Radiation and Isotopes*, *International J. Radiation Applic. Instrum. Part A. Applied Radiation and Isotopes* 39:257, (1988).
- Greenberg, R. R. "Evaluation of Precision and Accuracy of Selenium Measurements in Biological Materials Using Neutron Activation Analysis," *Trans. of the Am. Nucl. Soc.* 56, 148-9 (1988).
- Greenberg, R. R.; Zeisler, R. "A Radiochemical Procedure for Ultratrace Determination of Chromium in Biological Materials," *J. Radioanal. Nucl. Chem.* 124, 5-20 (1988).
- Greenberg, R. R. "Analysis of Atmospheric Particulate Samples Via Instrumental Neutron Activation Analysis," *Proc. of Conf. on Recent Developments in Monitoring Methods for Toxics in the Atmosphere*, (in press).

PUBLICATIONS

- Greenberg, R. R.; Fleming, R. F.; Linstrom, R. M. "Elemental Characterization of Four Coal Standard Reference Materials via Instrumental Neutron Activation Analysis and Neutron-Capture Prompt Gamma Activation Analysis," (to be submitted to Anal. Chem.)
- Greenberg, R. R.; Kingston, H. M.; Zeisler, R.; Woittiez, J. R. W. "Neutron Activation Analysis of Biological Samples with a Pre-Irradiation Chemical Separation," (to be submitted to Biol. Trace Elem. Res.).
- Greenberg, R. R.; Stone, S. F.; Zeisler, R. "The Determination of Trace Elements in Human Livers," Proc. 10th U.S.-German Seminar of State and Planning on Environmental Specimen Banking, Virginia Institute of Marine Sci., Gloucester Point, VA, October 6-8, 1986, NBS Spec. Publ. 740, 82-90 (1988).
- Greenberg, R. R.; Zeisler, R.; Malozowski, S. "Investigation of Natural Chromium Levels in Human Blood," Trace Eelemnt Analytical Chemistry in Medicine and Biology, 5, Bratter, P.; Schramel, P., eds. 220-228 (1988).
- Greenberg, R. R.; Zeisler, R.; Kingston, H. M.; Sullivan T. M. "Neutron Activation Analysis of the NIST Bovine Serum Standard Reference Material Using Chemical Separations," Fresenius Z. Anal. Chem. 332, 652-656 (1988).
- Hastie, D. R.; Schiff, H. I.; Whelpadale, D. M.; Peterson, R. E.; Zoller, W. H.; Anderson, D. L. "Nitrogen and Sulphur over the Western Atlantic Ocean," Atmos. Environ. 22, 2381-2392 (1988).
- Hastie, D. R.; Schiff, H. I.; Whelpdale, D. M.; Peterson, R. E.; Zoller, W. H. Anderson, D. L.; Church, T. M. "Description and Intercomparison of Techniques to Measure N and S Compounds in the Western Atlantic Ocean Experiment," Atmos. Environ. 22, 2393-2400 (1988).
- Hunt, J. B.; Champlong, P.; Chemtob, M.; Kluge H.; Schwartz, R. B. "International Intercomparison of Neutron Survey Instrument Calibrations," Radiation Protection Dosimetry 27, 103-110 (1989).
- Iyengar, G. V.; Behne, D. "Appropriate Reference Parameters for the Evaluation of Elemental Analysis Data from Biomedical Specimens," J. Res. Natl. Bur. Stand. (US) 93, 326-328 (1988).
- Iyengar, G. V.; Gopal-Ayengar, A. R. "Human Health and Trace Elements Including Effects on High Altitude Populations," Ambio 17, 31-35 (1988).
- Iyengar, G. V.; Iyengar, V. "Clinical Samples. In, Quantitative Trace Analysis of Biological Materials," McKenzie, H. A.; Smythe, L. E., eds., Elsevier Science Publishers, Amsterdam, 1988, pp. 401-417.
- Iyengar, G. V.; Woittiez, J. R. W. "Trace Elements in Human Clinical Specimens: Evaluation of Literature Data to Identify Reference Values," Clin. Chem. 34, 474-481 (1988).
- Iyengar, G. V. "Biological Trace Element Research: A Multi-disciplinary Science," Sci. Total Environ. 71, 1-5 (1988).

PUBLICATIONS

- Iyengar, G. V. "Elemental Analysis of Biological Systems: Biomedical, Compositional, Environmental and Methodological Aspects," Vol. I. CRC Publishers, Boca Raton, FL, 1989.
- Iyengar, G. V. "Nutritional Chemistry of Chromium," *Sci. Total Environ.* 1989, (in press).
- Iyengar, G. V. "The Role of Neutron Activation Analysis in Nutritional Biomonitoring Programs," *Trans. Am. Nucl. Soc.* 56, 233-234 (1988).
- Iyengar, G. V. "Trends in the Daily Intake of Trace Elements by Human Subjects: An Analytical Appraisal," *Proc. of International Conf. of Bioavailability 88*, The Royal Society of Chemistry, London, 1989, (in press).
- Iyengar, G. V.; Clarke, W. B.; Downing, R. G.; Tanner, J. T. "Boron and Lithium in Biological Materials," *Trace Element Analytical Chemistry in Medicine and Biology*, Vol. 5, Braetter, P.; Schramel, P., eds., Walter de Gruyter, Berlin, 1988, pp. 267-269.
- Iyengar, G. V.; Tanner, J. T.; Tanner, W. R.; Wolf; Zeisler, R. "Development of Multi-Purpose Biological Reference and Materials," *J. Res. Natl. Bur. Stand. (US)* 93, 360-362 (1988).
- Iyengar, G. V.; Wolf, W. R.; Tanner, J. T. "Multipurpose Reference Materials," *Fres. Z. Anal. Chem.* 332, 549-551 (1988).
- Joel, E. C.; Olin, J. S., Blackman, M. J.; Barnes, I. L. "Lead Isotope Studies of Spanish, Spanish Colonial and Mexican Majolica," *Proc. 26th International Archaeometry Symposium*, Toronto, Canada, 1989, pp.188-195.
- Kitto, M. E.; Anderson, D. L. "The Use of Whatman-41 Filters for Particle Collection," *Atmos. Environ.* 22, 2629-2630 (1988).
- Kitto, M. E.; Anderson, D. L.; Zoller, W. H. "Simultaneous Collection of Particles and Gases Followed by Multielement Analysis Using Nuclear Techniques," *J. Atmos. Chem.* 7, 241-259 (1988).
- Lamaze, G. P.; Grundl, J. A. "Activation Foil Irradiation by Reactor Cavity Fission Sources," *NBS Measurement Services, Spec. Publ.* 250-14 (1988).
- Lamaze, G. P.; Grundl, J. A. "Activation Foil Irradiation with Californium Fission Sources," *NBS Measurement Services, Spec. Publ.* 250-14, (1988).
- Lamaze, G. P.; Eisenhauer, C. M.; Grundl, J. A.; McGarry, E. D.; Schima, F. J.; Spiegel, V. "Cross-Section Measurements in the Intermediate-Energy Standard Neutron Field," *International Conference on Nuclear Data for Science and Technology*, Mito, Japan, (1988).
- Lamaze, G. P.; Eisenhauer, C. M.; Grundl, J. A.; McGarry, E. D.; Schima, F. J.; Spiegel, V. "Cross-Section Measurements in the Intermediate-Energy Standard Neutron Field," *Proc. of the International Conference on Nuclear Data for Science and Technology*, Mito, Japan, May 30-June 3, 1988, pp. 1033-1036, 1988 JAERI.

PUBLICATIONS

- Lamaze, G. P.; Gilliam, D. M.; Williams, A. P. "Prompt Gamma as a Fluence Rate Monitor in Neutron Beam Experiments," *J. of Radioanalytical and Nuclear Chemistry* 123(2), 551-559 (1988).
- Lamaze, G. P.; Schima, F. J.; Eisenhauer, C. M.; Spiegel, V. "Spectrum-Averaged Cross-Section Measurement of $^{103}\text{Rh} (n,n')^{103\text{m}}\text{Rh}$ in the ^{252}Cf Fission Neutron Spectrum," *Nuclear Science and Engineering* 100, 43-47 (1988).
- Lindstrom, D. J.; Zolensky, M. E.; Lindstrom, R. M. "Procedures for Instrumental Neutron Activation Analysis of Individual Cosmic Dust Particles," *Abstr. XXth Lunar and Planet. Sci. Conf., Lunar and Planet. Inst. Houston, 1989*, pp. 574-575.
- Lindstrom, R. M. "Analytical Standards in Silicon Analysis," *Proc. IAEA Consultants' Meeting on the Need for Intercomparison and Reference Materials for Characterization of Silicon, (Gaithersburg, MD, 1987: IAEA-TECDOC) (to be published by International Atomic Energy Agency, Vienna, Austria, 1989)*.
- Lindstrom, R. M. "Measurement of Superconductor Stoichiometry by Prompt and Delayed Neutron Activation," *Trans. Am. Nucl. Soc.* 56, 231 (1988).
- Lindstrom, R. M. "Neutron Activation Analysis in Electronic Technology," T. J. Shaffner and D. K. Schroder (eds.), *Diagnostic Techniques for Semiconductor Materials and Devices*, (PV 88-20), *Electrochem. Soc.*, Pennington, NJ, 1988, pp 3-14.
- Lindstrom, R. M.; Fleming, R. F.; Rook, H. L. "Neutron Microprobe: Prospects and Potential Applications," Newbury, D. E., ed. *Microbeam Analysis--1988*, San Francisco Press, 1988, pp. 407-408.
- McGarry, E. D. "1988 NIST Annual Report: LWR Pressure Vessel Surveillance Dosimetry Improvement Program," in *Compilation of Contract Research for the Materials Engineering Branch, Division of Engineering Technology, Annual Report for FY 88, USNRC Report NUREG-0975, Vol. 7, April 1989*.
- McGarry, E. D.; Rogers, J.; Prillinger, I. G.; Hawthorne, R. J. "Consideration of Calculated Experimental Neutron Dosimetry for Out-of-Core Metallurgy Irradiation Experiments at the Buffalo Reactor," *Proc. of 14th International Conference on the Effects of Radiation on Materials*, N. Pachen Ed. ASTM STP 1014, American Society for Testing and Materials, Philadelphia, PA (in press).
- Moody, J. R.; Greenberg, R. R.; Pratt, K. W.; Rains, T. C. "Recommended Inorganic Chemicals for Use as Calibrants," *Anal. Chem.* 60, 1203a-18a, (1988).
- Olin, J. S.; Blackman, M. J. "Compositional Classification of Mexican Majolica Ceramics of the Spanish Colonial Period," *Archaeological Chemistry IV*, Allen, R., ed., American Chemical Society, Washington, DC, pp. 87-112, 1989.

PUBLICATIONS

- Olmez, I.; Gulovali, M. C.; Gordon, G. E.; Henkin, R. I. "Trace Elements in Human Parotid Saliva," *Trace Elem. Res.* 22, 259-270 (1988).
- Ondov, J. M.; Choquette, C. E.; Zoller, W. H.; Gordon, G. E.; Biermann, A.H.; Heft, R. E. "Atmospheric Behavior of Trace Elements Emitted From a Coal-Fired Power Plant," *Atmos. Environ.* (in press).
- Ondov, J. M.; Dodd, J. A.; Tuncel, G. "Nuclear Analyses of Trace Elements in Size-Classified Submicrometer Aerosol Particles from a Rural Airshed," *Aerosol Sci. Technol* (submitted for publication).
- Parikh, N. R.; Frey, E. C.; Hofsaass, H. C.; Swanson, M. L.; Downing, R. G.; Hossain, T. Z.; Chu, W-K. "Neutron Depth Profiling by Coincidence Spectrometry," *Nucl. Instr. Methods* (submitted for publication).
- Perks, C. A.; Devine, R. T.; Harrison, K. G.; Goodenough, R. J.; Hunt, J. B.; Johnson, T. L.; Riel, G. L.; Schwartz, R. B. "Neutron Dosimetry Studies Using the New Chalk River Nuclear Laboratories Bubble-Damage Detector," *Radiation Protection Dosimetry* 23, 131-134 (1988).
- Prillinger, I. G.; McGarry, E. D.; Hawthorne, R. J. "Neutron Spectra Calculations for Ex-Core Irradiation Experiments At The Buffalo Reactor," *Proc. of 14th International Conference on the Effects of Radiation on Materials*, N. Packen, Ed. ASTM STP 1014, American Society for Testing and Materials, Philadelphia, PA (in press).
- Rossbach, M.; Scharpf, O.; Kaiser, W.; Graf, W.; Schirmer, A.; Faber, W.; Duppich, J.; Zeisler, R. "The Use of Focusing Supermirror Neutron Guides to Enhance Cold Neutron Fluence Rates," *Nucl. Instrum. Meth.* B35, 181-190 (1988).
- Rossbach, M.; Zeisler, R.; Lindstrom, R. M. "PGNAA With Cold Neutrons--A Challenge for Chemical Analysis," Multipurpose Research Reactors, (Proc. Symp. Grenoble: IAEA-SM-300/16), International Energy Agency, Vienna, 1988.
- Rothman, M. J.; Blackman, M. J. "Instrumental Neutron Activation Analysis of Sealing Clays from Tepe Gawra, Nineveh, Arpachiyah, and Tell Brak, Northern Mesopotamia," *MASCA Journal* (in press).
- Schraube, H.; Chartier, J. L.; Cosack, M.; Delafield, H. H.; Hunt, J. B.; Schwartz, R. B. "Calibration Procedures for Measuring the Radiation Response Characteristics of Neutron Measuring Devices Used for Radiation Protection," loc. cit., 217-222.
- Schuhmacher, H.; Kunz, A.; Menzel, H. G.; Coyne, J. J.; Schwartz, R. B. "The Dose Equivalent Response of Tissue-Equivalent Proportional Counters to Low-Energy Neutrons," *Radiation Protection Dosimetry* (submitted for publication).
- Schuhmacher, H.; Kunz, A.; Menzel, H. G.; Coyne, J. J.; Schwartz, R. B. "The Dose Equivalent Response of Tissue-Equivalent Proportional Counters to Low Energy Neutrons," *Radiation Protection Dosimetry* (in press).

PUBLICATIONS

- Shibayama, M.; Roy, S.; Wu, W.; Kurokawa, H.; Nomura, S.; Stein, R. S. Macromol. (in press).
- Sköld, K.; Price, D. L.; Mildner, D. F. R. (Book Review), "Neutron Scattering," parts A, B, and C, "Methods of Experimental Physics," Volume 23, Skold, K.; Price, D. L. and Mildner, D. F. R., eds., Nucl. Instrum. Meth. B35, 199-201 (1988).
- Stone, C. A.; Faller, S. H.; Walters, W. B. "Structure of Odd-Odd ^{132}Sb ," Phys. Rev. C39, 1963 (1989).
- Stone, C. A. guest editorialist, Scientific Computing and Automation, February, 1989.
- Stone, S. F.; Becker, D. A.; Koster, B. J.; Pella, P. A.; Sleater, G.; Tillekeratne, M. P. M.; Zeisler, R. "Inorganic Analytical Methods and Results for Marine Bivalves and Sediments," in Progress in Environmental Specimen Banking, NBS Spec. Publ. 740, U.S. Government Printing Office, Washington, DC, 1988, pp. 62-73.
- Stone, S. F.; Koster, B. J.; Zeisler, R. "Instrumental Neutron Activation Analysis of SRM 1941". "Organics in Marine Sediment, Element Content and Homogeneity," Biol. Trace Elem. Res. (submitted for publication).
- Stone, S. F.; Zeisler, R.; Gordon, G. E. "Quantitative Determination of Proteins Using Polyacrylamide Gel Electrophoresis and Neutron Activation," in Trace Element Analytical Chemistry in Medicine and Biology, Vol. 5, Bratter, P., Schramel, P., eds., Walter de Gruyter, Berlin/New York, 1988, pp. 157-166.
- Stone, S. F.; Zeisler, R.; Gordon, G. E. "Application of Polyacrylamide Gel Electrophoresis/Neutron Activation for Protein Determinations," Biol. Trace Ele. Res. (submitted for publication).
- Stone, S. F.; Zeisler, R.; Koster, B. J. "Neutron Activation Analysis of Major, Minor and Trace Elements in Marine Sediments," Trans. Am. Nucl. Soc. 56, 228-229 (1988).
- Tuncel, G.; Zoller, W. H. "Iridium in the South Pole Atmosphere: Estimation of a Meteoritic Component," Nature 329, 703-705 (1987).
- Vossler, T. L.; Lewis, C. W.; Stevens, R. K.; Dzubay, T. G.; Gordon, G. E.; Tuncel, S. G.; Russwurm, G. M.; Keller, G. J. "Composition and Origin of Summertime Air Pollutants at Deep Creek Lake, Oakland, MD," Atmos. Environ. (in press).
- Wastney, M. E.; Gokmen, I. G.; Aamodt, R. L.; Rumble, W. F.; Henkin, R. I.; Gordon, G. E. "Kinetic Analysis of Zinc Metabolism in Humans following Simultaneous Administration of ^{65}Zn and ^{70}Zn ," Am. J. Physiol (submitted for publication).
- Williamson, T. G.; Lamaze, G. P.; Gilliam, D. M.; Eisenhauer, C. M., NIST, Gaithersburg, Nuclear Science and Engineering, "Iron and Cadmium Capture Gamma Ray Photofission Measurements," (in press).

PUBLICATIONS

- Williamson, T. G.; Lamaze, G. P.; Gilliam, D. M.; Eisenhauer, C. M. "Iron and Cadmium Capture Gamma-Ray Photofission Measurements," Nuclear Science and Engineering, (in press).
- Williamson, T. G.; Lamaze, G. P.; Gilliam, D. M. "Calibration of a Neutron Driven Gamma Ray Source," Reactor Dosimetry, Methods, Applications, and Standards, American Society for Testing and Materials, Spec. Tech. Publ., STP1001, 751 (1989).
- Wise, S. A.; Koster, B. J.; Zeisler, R. "Status of Specimen Banking Activities at the National Bureau of Standards," Progress in Environmental Specimen Banking, NBS Spec. Publ. 740, U.S. Government Printing Office, Washington, DC, 1988, pp. 10-18.
- Wise, S. A.; Koster, B.J.; Parris, R. M.; Schantz, M. M.; Stone, S. F.; Zeisler, R. "Experiences in Environmental Specimen Banking," Intern. J. Environ. Anal. Chem., 1989 (in press).
- Wise, S. A.; Zeisler, R.; Goldstein, G. M., Eds. "Progress in Environmental Specimen Banking," NBS Spec. Publ. 740, U.S. Government Printing Office, Washington, DC, 1988, pp. 217.
- Woittiez, J. R. W.; Iyengar, G. V. "The Use of Neutron Activation in Dietary Reference Material Analysis," Fresenius Z. Anal. Chem. 332, 657-661 (1988).
- Woittiez, J. R. W.; Iyengar, G. V. "Trace Elements in Human Clinical Specimens," Proc., Trace Element Analytical Chemistry in Medicine and Biology. Braetter, P. and Schramel, P., eds., Walter de Gruyter, Berlin, 1988, pp. 267-269.
- Wu, W. Mat. Res. Soc. Symp. Proc. December 1988, Boston, MA.
- Wu., W. "Characterization of Molecular Network Epoxies Using Neutron Scattering," ANTEC 89 Proc. December 1988, Boston, MA.
- Wu., W.; Hu, J.; Hunston, D. L. Poly. Eng. and Sci. (submitted for publication).
- Wu., W.; Shibayama, M.; Roy, S.; Kurokawa, H.; Coyne, L. D.; Nomura, S.; Stein, R. S.; Macromol. (submitted for publication).
- Wu., W.; Stillie, J. K.; Tsang, J. W.; Perker, A. J. Mat. Res. Soc. Symp. Proc. December 1988, Boston, MA.
- Zaider, M.; Dicello, J.; Coyne, J. J. "The Effects of Geometrical Factors on Microdosimetric Probability Distributions of Energy Deposition," Nucl. Instrum. & Methods Phys. Research B40/41, 1261-1265 (1989).
- Zeisler, R.; Greenberg, R. R. "Determination of Baseline Platinum Levels in Biological Materials," in Trace Element Analytical Chemistry in Medicine and Biology, Volume 5, Bratter, P., Schramel, P., eds. Walter de Gruyter, Berlin/New York, 1988, pp. 297-303.

PUBLICATIONS

- Zeisler, R.; Greenber, R. R.; Stone, S. F. "Radiochemical and Instrumental Neutron Activation Analysis Procedures for the Determination of Low Level Trace Elements in Human Livers," J. Radioanal. Nucl. Chem. 124, 47-63 (1988).
- Zeisler, R.; Greenberg, R. R.; Stone, S. F. "The Determination of Trace Elements in Human Livers," in Progress in Environmental Specimen Banking, NBS Spec. Publ. 740, U.S. Government Printing Office, Washington, DC, 82-90 (1988).
- Zeisler, R.; Greenberg, R. R.; Stone, S. F.; Sullivan, T. M. "Selenium Determinations for the Assessment of Sample Stability in Specimen Banking," Trans. Am. Nucl. Soc. 56, 153-154 (1988).
- Zeisler, R.; Greenberg, R. R.; Stone, S. F.; Sullivan, T. M. "Long-Term Stability of the Elemental Composition of Biological Materials," Fresenius Z. Anal. Chem. 332, 612-615 (1988).
- Zeisler, R.; Stone, S. F.; Sanders, R. W. "Sequential Determination of Biological and Pollutant Elements in Marine Bivalves," Anal. Chem. 60, 2760-2765 (1988).
- Zeitsoff, P. M.; Hossain, T. Z.; Boisvert, D.; Downing, R. G. "Measurement and Control of the Boron and Phosphorous Concentration in LPCVD Borophosphosilicate Glass (BPSG)," J. Electrochemical Soc. (submitted for publication).
- Zeman, G. H.; Dooley M.; Eagleson, D. M.; Goodman, L. J.; Schwartz, R. B.; Eisenhauer, C. M.; McDonald, J. C. "Intercomparison of Neutron Dosimetry Techniques at the AFRRI TRIGA Reactor," loc. cit., 317-320.
- Zolensky, M. E.; Lindstrom, D. J.; Thomas, K. L.; Lindstrom R. M.; Lindstrom, M. M. "Trace Element Compositions of Six 'Chondritic' Stratospheric Dust Particles," Abstr. XXth Lunar and Planet. Sci. Conf., Lunar and Planet. Inst., Houston, TX, 1989, pp. 1255-1256.

U.S. DEPT. OF COMM. BIBLIOGRAPHIC DATA SHEET (See instructions)	1. PUBLICATION OR REPORT NO. NIST/TN-1272	2. Performing Organ. Report No.	3. Publication Date December 1989
4. TITLE AND SUBTITLE <p>NIST Reactor: Summary of Activities July 1988 Through June 1989.</p>			
5. AUTHOR(S) <p>Carol O'Connor, Editor</p>			
6. PERFORMING ORGANIZATION (If joint or other than NBS, see instructions) <p>NATIONAL INSTITUTE OF STANDARDS AND TECHNOLOGY (formerly NATIONAL BUREAU OF STANDARDS) U.S. DEPARTMENT OF COMMERCE GAITHERSBURG, MD 20899</p>		7. Contract/Grant No.	8. Type of Report & Period Covered July 1988 through June 1989
9. SPONSORING ORGANIZATION NAME AND COMPLETE ADDRESS (Street, City, State, ZIP) <p>Same as item #6 above.</p>			
10. SUPPLEMENTARY NOTES <p><input type="checkbox"/> Document describes a computer program; SF-185, FIPS Software Summary, is attached.</p>			
11. ABSTRACT (A 200-word or less factual summary of most significant information. If document includes a significant bibliography or literature survey, mention it here) <p>This report summarizes all those programs which use the NIST reactor. It covers the period for July 1988 through June 1989. The programs range from the use of neutron beams to study the structure and dynamics of materials through nuclear physics and neutron standards to sample irradiations for activation analysis, isotope production, neutron radiography, and nondestructive evaluation.</p>			
12. KEY WORDS (Six to twelve entries; alphabetical order; capitalize only proper names; and separate key words by semicolons) activation analysis; cold neutrons; crystal structure; diffraction; isotopes; molecular dynamics; neutron; neutron radiography; nondestructive evaluation; nuclear reactor; radiation.			
13. AVAILABILITY <input checked="" type="checkbox"/> Unlimited <input type="checkbox"/> For Official Distribution. Do Not Release to NTIS <input checked="" type="checkbox"/> Order From Superintendent of Documents, U.S. Government Printing Office, Washington, D.C. 20402. <input checked="" type="checkbox"/> Order From National Technical Information Service (NTIS), Springfield, VA. 22161			14. NO. OF PRINTED PAGES 324 15. Price

NIST *Technical Publications*

Periodical

Journal of Research of the National Institute of Standards and Technology—Reports NIST research and development in those disciplines of the physical and engineering sciences in which the Institute is active. These include physics, chemistry, engineering, mathematics, and computer sciences. Papers cover a broad range of subjects, with major emphasis on measurement methodology and the basic technology underlying standardization. Also included from time to time are survey articles on topics closely related to the Institute's technical and scientific programs. Issued six times a year.

Nonperiodicals

Monographs—Major contributions to the technical literature on various subjects related to the Institute's scientific and technical activities.

Handbooks—Recommended codes of engineering and industrial practice (including safety codes) developed in cooperation with interested industries, professional organizations, and regulatory bodies.

Special Publications—Include proceedings of conferences sponsored by NIST, NIST annual reports, and other special publications appropriate to this grouping such as wall charts, pocket cards, and bibliographies.

Applied Mathematics Series—Mathematical tables, manuals, and studies of special interest to physicists, engineers, chemists, biologists, mathematicians, computer programmers, and others engaged in scientific and technical work.

National Standard Reference Data Series—Provides quantitative data on the physical and chemical properties of materials, compiled from the world's literature and critically evaluated. Developed under a worldwide program coordinated by NIST under the authority of the National Standard Data Act (Public Law 90-396). NOTE: The Journal of Physical and Chemical Reference Data (JPCRD) is published quarterly for NIST by the American Chemical Society (ACS) and the American Institute of Physics (AIP). Subscriptions, reprints, and supplements are available from ACS, 1155 Sixteenth St., NW., Washington, DC 20056.

Building Science Series—Disseminates technical information developed at the Institute on building materials, components, systems, and whole structures. The series presents research results, test methods, and performance criteria related to the structural and environmental functions and the durability and safety characteristics of building elements and systems.

Technical Notes—Studies or reports which are complete in themselves but restrictive in their treatment of a subject. Analogous to monographs but not so comprehensive in scope or definitive in treatment of the subject area. Often serve as a vehicle for final reports of work performed at NIST under the sponsorship of other government agencies.

Voluntary Product Standards—Developed under procedures published by the Department of Commerce in Part 10, Title 15, of the Code of Federal Regulations. The standards establish nationally recognized requirements for products, and provide all concerned interests with a basis for common understanding of the characteristics of the products. NIST administers this program as a supplement to the activities of the private sector standardizing organizations.

Consumer Information Series—Practical information, based on NIST research and experience, covering areas of interest to the consumer. Easily understandable language and illustrations provide useful background knowledge for shopping in today's technological marketplace.

Order the above NIST publications from: Superintendent of Documents, Government Printing Office, Washington, DC 20402.

Order the following NIST publications—FIPS and NISTIRs—from the National Technical Information Service, Springfield, VA 22161.

Federal Information Processing Standards Publications (FIPS PUB)—Publications in this series collectively constitute the Federal Information Processing Standards Register. The Register serves as the official source of information in the Federal Government regarding standards issued by NIST pursuant to the Federal Property and Administrative Services Act of 1949 as amended, Public Law 89-306 (79 Stat. 1127), and as implemented by Executive Order 11717 (38 FR 12315, dated May 11, 1973) and Part 6 of Title 15 CFR (Code of Federal Regulations).

NIST Interagency Reports (NISTIR)—A special series of interim or final reports on work performed by NIST for outside sponsors (both government and non-government). In general, initial distribution is handled by the sponsor; public distribution is by the National Technical Information Service, Springfield, VA 22161, in paper copy or microfiche form.

U.S. Department of Commerce
National Institute of Standards and Technology
(formerly National Bureau of Standards)
Gaithersburg, MD 20899

Official Business
Penalty for Private Use \$300